






Universitat Autònoma de Barcelona

ADVERTIMENT. L'accés als continguts d'aquesta tesi queda condicionat a l'acceptació de les condicions d'ús establertes per la següent llicència Creative Commons:  http://cat.creativecommons.org/?page_id=184

ADVERTENCIA. El acceso a los contenidos de esta tesis queda condicionado a la aceptación de las condiciones de uso establecidas por la siguiente licencia Creative Commons:  <http://es.creativecommons.org/blog/licencias/>

WARNING. The access to the contents of this doctoral thesis it is limited to the acceptance of the use conditions set by the following Creative Commons license:  <https://creativecommons.org/licenses/?lang=en>



Universitat Autònoma de Barcelona

Departament de Microelectrònica i Sistemes Electrònics

GRAPHENE MICROTRANSISTORS:
A WIDE-BANDWIDTH
TECHNOLOGY FOR RECORDING
BRAIN FIELD POTENTIALS

Eduard Masvidal Codina

Memòria de Tesi
presentada per optar al títol de

DOCTOR EN ENGINYERIA ELECTRÒNICA I DE
TELECOMUNICACIÓ

Juny 2021



Universitat Autònoma de Barcelona



Dr. Anton Guimerà Brunet, Consejo Superior de Investigaciones Científicas, Prof. Jose Antonio Garrido Ariza, ICREA Research Professor, i Dr. Francesc Serra Graells, Professor Titular del Departament de Microelectrònica i Sistemes Electrònics,

Certifiquen

que la Memòria de Tesi *Graphene microtransistors: a wide-bandwidth technology for recording brain field potentials* presentada per Eduard Masvidal Codina per optar al títol de Doctor en Enginyeria Electrònica i de Telecomunicació s'ha realitzat sota la seva direcció a l'Institut de Microelectrònica de Barcelona pertanyent al Centro Nacional de Microelectrónica del Consejo Superior de Investigaciones Científicas i ha estat tutoritzada en el Departament de Microelectrònica i Sistemes Electrònics de la Universitat Autònoma de Barcelona.

Directors	Dr. Anton Guimerà Brunet
	Prof. Jose Antonio Garrido Ariza
Tutor	Dr. Francesc Serra Graells

....., a de de

*Als meus pares Eduard i Lluïsa,
al Marc, la Marina
i l'Aida*

Resum

Els registres d'activitat neuronal d'alta densitat en i entre regions cerebrals són vitals en la investigació enfocada a descobrir els processos subjacents de funcions cerebrals complexes i de patologies; tenen aplicacions en el diagnòstic mèdic, el pronòstic i el seguiment del tractament i són la base de neuropròtesis assistencials. Tot i això, les tecnologies de registre actuals no poden satisfer tots els requisits necessaris per a una interfície neuronal fiable i d'alta fidelitat.

En aquesta tesi doctoral es desenvolupen interfícies neuronals basades en transistors de grafè d'efecte de camp modulats per electròlit (gSGFETs), s'avalua la seva viabilitat per al registre *in vivo* de potencials de camp cerebral i es compara amb tecnologies de registre d'última generació. S'han dissenyat sondes neuronals de superfície flexible que contenen matrius de gSGFETs i s'han desenvolupat procediments de microfabricació que permeten una producció a escala d'oblies reproduïble i amb un alt rendiment. Una àmplia caracterització elèctrica ha demostrat que les matrius de gSGFET fabricades tenen un guany constant en un ampli ample de banda (de CC a diversos kHz), una alta homogeneïtat i un soroll intrínsec comparables a les tecnologies estàndard. Atès que el registre de senyals cerebrals amb una configuració de transistor no és una tècnica habitual, s'ha desenvolupat i validat una metodologia d'adquisició i postprocessament complet que permet registrar senyals de tensió amb alta fidelitat. A més, s'han estudiat les capacitats de registre dels gSGFET *in vivo* en rosegadors. S'han obtingut enregistraments aguts d'activitat espontània i evocada en rates anestesiades mitjançant gSGFET epicorticals amb una qualitat similar als microelectrodes d'última generació. S'ha estimat la relació senyal-soroll dels registres fets amb gSGFET d'activitat espontània i epileptiforme, confirmant les excel·lents capacitats de registre. A més, s'ha dut a terme un estudi crònic pilot que mostra l'estabilitat de les matrius de gSGFET durant tota la durada de l'implant, fins a cinc mesos, suggerint un límit inferior a les capacitats de registre crònic dels gSGFET.

Una limitació actual de les matrius de microelèctrodes és que per inestabilitats electroquímiques relacionades amb el material sensor el registre de l'activitat infralenta (ISA, $\approx <0.1\text{Hz}$) és complicat. Tot i que en el passat s'havia considerat que els senyals infralents eren sorolls no desitjats, actualment es considera que reflecteixen processos neuronals importants que són rellevants tant per a la cognició com per a estats patològics. Per tant, vam explorar si la tecnologia gSGFET podria tenir avantatges sobre les tecnologies actuals per al registre d'ISA. Per estudiar les capacitats de registre ISA es va escollir la ona de depressió cortical (CSD), un fenomen neurofisiològic que s'associa amb un empitjorament dels pronòstic en

múltiples patologies neurològiques incloses l'epilèpsia, la migranya i l'ictus. Els resultats obtinguts mostren que els gSGFET registren CSD, amb una fidelitat més alta que els microelectrodes metàl·lics, i de manera similar a les micropipetes de vidre, tot superant les seves limitacions de mapatge.

Les excelents capacitats de mapatge d'ISA dels gSGFETs van ser explotades per a la investigació en neurociència. En combinació amb la modulació optogenètica de l'activitat cerebral, es van utilitzar gSGFETs per caracteritzar els efectes electrofisiològics de la CSD en ratolins desperts. A més, es va desenvolupar una metodologia experimental que facilita les investigacions sobre les CSD. Més enllà de la CSD, també es descriu i es discuteixen les aplicacions de la tecnologia gSGFET per registrar altres potencials cerebrals patològics relacionats amb l'ISA, com ara canvis en el potencial extracel·lular basal degut a crisis epilèptiques. Per ampliar encara més les aplicacions dels gSGFETs i accelerar les investigacions sobre ISA, es demostra la compatibilitat dels gSGFETs amb tècniques d'imatge cerebral d'última generació mitjançant experiments multimodals que combinen gSGFETs amb imatge per ultrasons funcionals o imatges mesoscòpiques de fluorescència d'indicadors codificats genèticament.

En resum, els resultats presentats en aquesta tesi de doctorat demostren que la tecnologia de gSGFETs supera les limitacions de les tecnologies actuals de microelectrodes passius per al mapatge de potencials de camp cerebral d'alta fidelitat i resolució espacial en un ampli ample de banda de freqüència que inclou tant els potencials de camp locals clàssics com els canvis del potencial basal. Per tant, els resultats presentats indiquen la tecnologia gSGFET com una alternativa superior a les matrius de microelectrodes per al registre d'ISA. La tecnologia gSGFET desenvolupada és madura i està llesta per ser adoptada per laboratoris de recerca, amb un potencial especial per a la investigació translacional bàsica i preclínica. Un desenvolupament tecnològic addicional enfocat a la translació clínica dels dispositius podria aportar als pacients els avantatges d'un millor monitoratge de la fisiologia cerebral.

Abstract

High density recordings of neural activity within and across brain regions are vital in research focused to uncover the underlying processes of complex brain functions and pathophysiology; have applications in medical diagnosis, prognosis and treatment monitoring and are the base of assistive neuroprosthesis. However, current recording technologies are unable to meet all the requirements of a reliable, high fidelity neural interface.

In this PhD dissertation, neural interfaces based on graphene solution-gated field-effect transistors (gSGFETs) are developed and their feasibility for in vivo brain field potential recording is evaluated and benchmarked against state-of-the-art technologies. Flexible surface neural probes containing arrays of gSGFETs have been designed and microfabrication procedures developed allowing reproducible wafer-scale production with high yield. Extensive electrical characterization has shown that the fabricated gSGFET arrays have a constant-gain over a wide bandwidth (from DC to several kHz), high homogeneity and intrinsic noise comparable to standard technologies. Since recording brain signals with a transistor configuration is not a common technique, a full acquisition and post-processing methodology has been developed and validated allowing to record voltage signals with high fidelity. Furthermore, in vivo gSGFET recording capabilities have been studied in rodents. Acute recordings of spontaneous and evoked activity in anesthetized rats were obtained using epicortical gSGFETs with similar performance than state-of-the-art microelectrodes. The signal-to-noise ratio of gSGFET recordings of spontaneous and epileptiform activity in awake mice was determined, confirming the excellent recording capabilities. In addition, a pilot chronic study was conducted showing stability of the gSGFET arrays for the whole implant duration, up to five months, suggesting a lower bound of gSGFET chronic recording capabilities.

A current limitation of microelectrode grids is that due to material-related electrochemical unstabilities the recording of infraslow activity (ISA, $\approx < 0.1\text{Hz}$) is hampered. Although infraslow signals have been regarded as unwanted noise in the past, there is now increasing appreciation that they reflect important neural processes that are relevant to both normal cognition and disease states. We therefore explored if gSGFET technology could have advantages over current technologies for ISA recording. Cortical spreading depression (CSD), a neurophysiological phenomenon that is associated with worsening outcomes in multiple neurological pathologies including epilepsy, migraine and stroke was chosen to study ISA recording capabilities. Results obtained demonstrate that gSGFETs record CSD, with higher fidelity than metal microelectrodes, and similarly than gold-standard single-

point glass micropipettes while overcoming their spatial sampling limitations.

The excellent ISA mapping capabilities of gSGFETs were exploited for neuroscience research. In combination with optogenetic modulation of brain activity, gSGFETs were used to characterize the electrophysiological effects of CSD in awake mice. Moreover, an experimental methodology that facilitates investigations into CSDs was developed. Beyond CSD, the applications of gSGFET technology to record other ISA-related pathological brain potentials such as epileptic ictal baseline shifts are also reported and discussed. To further extend the applications of gSGFETs and accelerate investigations into ISA, the compatibility of gSGFETs with state-of-the-art brain imaging techniques is demonstrated by multimodal experiments combining gSGFETs with functional ultrasound or mesoscopic imaging of genetically encoded indicators.

Overall, the results presented in this PhD dissertation demonstrate that gSGFET technology overcomes the limitations of current passive microelectrode technologies for mapping with high fidelity and spatial resolution brain field potentials in a wide frequency bandwidth that includes both classical local field potentials as well as infraslow oscillations and baseline potential shifts. Therefore, the presented results state gSGFET technology as a superior alternative to microelectrode grids for ISA recording. The gSGFET technology developed is mature and ready to be adopted by research laboratories, holding special potential for basic and preclinical translational research. Further technology development towards clinical translation of the devices could bring to patients the benefits of improved brain monitoring.

Thesis Framework

The work presented in this PhD dissertation has been developed in the framework of the European Commission Graphene Flagship Core1 and Core2 projects and the BrainCom project. Work has been done at the Institut de Microelectrònica de Barcelona (IMB-CNM, CSIC), taking advantage of its micro- and nanofabrication clean-room facilities, within the Biomedical Applications Group led by Dra. Rosa Villa, under the supervision of Dr. Anton Guimerà Brunet and in close collaboration with the Advanced Electronic Materials and Devices group led by professor Jose A. Garrido from the Institut Català de Nanociència i Nanotecnologia (ICN2). In vivo experiments have been performed with the collaboration of Maria V. Sanchez-Vives group at Institut d'Investigacions Biomèdiques August Pi i Sunyer (IDIBAPS) and Rob Wykes group at Institute of Neurology, University College London (UCL). Further research on the applications of graphene transistor neural probes in neuroscience is ongoing under the European Commission Graphene Flagship Core3 and BrainCom projects.

Acknowledgements

Són moltes les persones que d'alguna forma o altre han fet possible aquesta tesi doctoral. Per començar m'agradaria donar les gràcies als meus dos directors. A l'Anton Guimerà, per a ser un mestre excel·lent durant els meus primers anys al CNM, ser en bona part el responsable de que m'embarques en la tesi doctoral, i per la continua supervisió i ajuda incessant durant tot el trajecte, esdevenint molt més que un director. A Jose Garrido le quiero agradecer sus investigaciones en el campo de los transistores de grafeno que forman en buena parte los fundamentos de esta tesis doctoral, así como su liderazgo de proyectos internacionales que me ha permitido realizar la tesis doctoral en el marco de proyectos como el Graphene Flagship i el BrainCom viajando por toda Europa en las reuniones de proyecto. También por la agudeza de sus preguntas siempre que he tenido la oportunidad de presentarle mis investigaciones así como su visión única para dar el impacto que merecen a los resultados de las investigaciones. També vull recordar la tutora d'aquesta tesi doctoral, l'Elena Valderrama per estar disponible sempre que ha fet falta.

En l'aspecte laboral vull agrair a tots els membres del GAB l'ambient excel·lent de treball i suport mutu. A Rosa Villa quiero agradecerle el liderazgo, soporte y confianza recibidos durante mi estada en el CNM, especialmente al principio cuando las cosas parecían no salir aun trabajando duro, así como por el modo de celebrar las buenas noticias. Al Xavi Illa per haver estat un mestre en l'art de la microfabricació i per les incontables hores a la Sala Blanca del CNM. A l'Eli Prats, per donar-me una canya i ensenyar-me a pescar grafè i ser la química de referència durant tota la tesi. A tots els membres del GAB: la Gemma, la Mar, el Javi, la Lucia.. Als companys de camí de tesis doctoral: al Jose, l'Anna, Pau, Miguel, Fernando. També vull agrair a tots els membres del grup del J. Garrido: Andrea, Damià, Ramon, Nathan, Jose, Elena, Clement per compartir aprenentatges en el camí. Vull estendre també els agraïments a tot els membres del CNM: administració, personal de laboratoris i sala blanca, etc; per la facilitat que he tingut per a desenvolupar aquesta tesi doctoral.

Voldria agrair també als col·laboradors sense els quals la major part d'aquestes investigacions interdisciplinars no hagués estat possible. A la Dr. Mavi Sánchez-Vives líder del grup de l'IDIBAPS, i a l'Àlex, el Miguel i la Almudena amb els que vaig iniciar-me a l'experimentació in vivo. To Rob Wykes for his believe and commitment to advance graphene transistor technology, inexhaustible energy and knowledge, as also his tradition to celebrate successful experiments. The 3 months

stay at UCL Institute of Neurology under his supervision were a great pleasure. I want to thank also the European Molecular Biology Organization (EMBO) for granting me a Short-Term Fellowship that allowed the stay at UCL in Rob's lab to be possible. Also I want to acknowledge Martin Smith for the interesting discussions (not only related to work) and valuable comments from who I've learnt a lot. Also I want to acknowledge Daman Rathore for the combined calcium imaging and parylene-C gSGFET arrays experiments and Diep Nguyen for the combined fUS and gSGFET experiments. Also I would like to thank g.tec and Multichannel system companies for supplying customized recording instrumentation.

Finalment, en aquestes línies vull aprofitar per agrair a tots aquells que amb el seu suport i estima m'han ajudat a tirar endavant. A l'Aida per acompanyar-me en aquest camí. Als amics i familiars per donar-me suport incondicional i en especial als meus pares per conduir-me a fer el que m'agrada.

Contents

Motivation and objectives	1
1 Background	5
1.1 Introduction	5
1.2 Brain field potentials	10
1.2.1 Mammalian brain macro- and microstructure	10
1.2.2 Brain activity	13
1.2.3 Extracellular field potentials	16
1.3 Principles of extracellular potential recording	19
1.3.1 Components of a recording system	19
1.3.2 Considerations for electrophysiological recordings	25
1.3.3 Passive and active recording technologies	28
1.3.4 Assessing recording quality	29
1.4 Voltage probes for mapping brain field potentials	33
1.4.1 Microelectrodes	33
1.4.2 Microtransistors	33
1.5 Graphene field-effect solution-gated transistor	36
1.5.1 Graphene	36
1.5.2 Graphene-electrolyte interface	38
1.5.3 gSGFET working principle	39
1.6 Summary	42
2 Flexible gSGFET arrays for brain recording	43
2.1 gSGFET electrical characteristics	45

2.2	Considerations for designing gSGFET arrays	49
2.3	Array design	54
2.4	Microfabrication considerations	56
2.5	Methods	61
2.5.1	Fabrication details	61
2.5.2	Instrumentation for electrical characterization	64
2.5.3	Electrical characterization details	65
2.5.4	Data Analysis	66
2.6	Results and discussion	67
2.7	Conclusions	79
3	Recording brain activity with gSGFETs	81
3.1	Considerations for brain recordings with gSGFETs	83
3.1.1	Operation of gSGFET arrays for neural recordings	83
3.1.2	Calibration of gSGFET recordings	84
3.2	Methods	86
3.3	Results	90
3.3.1	Recording brain activity under anesthesia	90
3.3.2	Recording activity in the awake brain	92
3.3.3	Recording of evoked potentials	95
3.3.4	Chronic recordings	96
3.3.5	Assessing recording fidelity of gSGFETs	98
3.4	Discussion	103
3.5	Conclusions	105
4	Mapping infraslow activity with gSGFETs	107
4.1	Introduction	108
4.2	Methods	111

4.3	Results and discussion	116
4.3.1	In vivo wide-band recordings with gSGFETs	116
4.3.2	ISA recording capabilities with gSGFETs and microelectrodes	119
4.3.3	Mapping cortical spreading depression with gSGFETs	125
4.4	Conclusions	128
5	Graphene transistors for CSD research	131
5.1	Introduction	132
5.2	Materials and methods	133
5.3	Results	142
5.3.1	Optogenetic CSD model in awake head-fixed mice	142
5.3.2	Comparison with more invasive CSD induction methodologies	147
5.3.3	CSD waveform analysis	149
5.3.4	Pharmacological suppression of CSD in awake mice	152
5.3.5	Investigation of CSD induction	154
5.3.6	Through skull detection of CSD	156
5.4	Discussion	158
5.5	Conclusion	162
6	gSGFETs for neuroscience research	163
6.1	Baseline potential shifts of the brain	164
6.2	Recording baseline potential shifts	166
6.2.1	Infraslow activity	166
6.2.2	Seizure-related baseline potential shifts	167
6.2.3	Seizures and spreading depolarization waves	170
6.2.4	Pharmacological baseline potential shifts	172
6.2.5	Terminal depolarization	174
6.3	Combination of gSGFETs with brain imaging techniques	176

6.3.1	gSGFETs and functional ultrasound	176
6.3.2	gSGFETs and Ca^{2+} imaging	178
6.4	Conclusion	182
Conclusions		183
Appendices		193
Appendix A Modelling gSGFETs		195
A.1	Modelling the graphene-electrolyte interface	195
A.2	Modelling current in gSGFETs	196
A.3	Modelling pH and ion strength sensitivity of gSGFETs	197
Appendix B Noise geometrical dependence		199
Appendix C Graphene production and characterization		201
C.1	Graphene production	201
C.2	CVD Graphene characterization	203
C.2.1	Optical Microscopy	203
C.2.2	Scanning electron microscopy	203
C.2.3	Raman Spectroscopy	204
C.2.4	Atomic Force Microscopy	204
Appendix D Fabrication details		205

List of Acronyms

4-AP 4-Aminopyridine	170
AFM atomic force microscopy	204
AP anterior-posterior	89
BMI brain-machine interfaces	7
BPF band-pass filtered	64
BPS baseline potential shifts	163
CMRR common-mode rejection ration	23
CNP charge neutrality point	49
CNS central nervous system	15
CVD chemical vapor deposition	38
CSD cortical spreading depression	108
ECoG electrocorticography	7
EDLC electrical double layer capacitance	20
EEG electroencephalography	6
EFP extracellular field potential	42
EPSP excitatory post-synaptic potentials	13
FET field-effect transistor	33
FFT fast Fourier transform	89
fMRI functional magnetic resonance imaging	6

gSGFET graphene solution-gated field-effect transistor.....	65
HOPG highly ordered pyrolytic graphite	201
IPSP inhibitory post-synaptic potentials	13
LED light emitting diode.....	89
LFP local field potential	16
LPF low-pass filtered.....	64
LSCI laser speckle contrast imaging.....	113
MAD median absolute deviation.....	69
MEA microelectrode array.....	88
MEG magnetoencephalography	6
ML medio-lateral.....	89
MUA multiunit activity.....	16
OECT organic electrochemical transistor.....	34
OHP outer Hemholtz plane.....	197
OSFET oxide-semiconductor field-effect transistor.....	34
PBS phosphate buffer saline.....	65
PCA principal component analysis	88
PCB printed circuit board	64
PDMS polydimethylsiloxane.....	8
PEDOT:PSS poly(3,4-ethylenedioxythiophene) polystyrene sulfonate	41
PMMA polymethyl methacrylate	58
PSD power spectral density	45

PTX picrotoxin	168
rCBF regional cerebral blood flow	113
ROI region of interest	113
RMS root mean square	26
SE secondary electron	203
SEM scanning electron microscopy	62
SNR signal-to-noise ratio	1
SGFET solution-gated field-effect transistor	40
TC transfer curve	98
UVO ultraviolet ozone	60
ZIF zero insertion force	54

Motivation and objectives

The human brain is one of the most elaborate biological structures in nature. It integrates information from the internal state of the body as well as from the environment through the senses and directs higher cognitive functions such as speech and sophisticated purposeful control of behavior. Malfunction due to injury or disease can cause devastating loss of autonomy and associated quality of life. However, despite significant advances, current treatment of brain diseases and disorders is limited and therefore, further research is warranted in order to improve the understanding of brain function at molecular, cellular, and system levels as well as to unravel the pathogenesis of complex brain diseases [1].

A highly practical route to monitor brain function is by recording the electric field potentials generated by brain electrogenic cells through neuroelectronic interfaces, i.e., devices that transduce ion fluctuations to electronic signals. For long, electrophysiological studies centered in the activity of the brain's basic computational unit, the neuron, which yielded remarkable findings that largely contributed to neuroscience [2]. However, monitoring the activity of a single unit hardly permits gaining insight into the dynamics of a complex neural network. Since complex brain functions such as speech or learning are distributed across the brain, it is widely accepted that gaining insight about brain function is contingent upon simultaneous monitoring of the coordinated activity of neuron populations within and across multiple brain areas.

Technology development efforts have yielded multichannel arrays and systems which are used for simultaneously recording the electrical activity of different neuron populations and have become a standard technology to characterize brain function and assess its physiopathological state [3, 4]. Moving forward, electronic neural interfaces also hold great potential as assistive neuroprosthesis [5]. However, current neural interfaces are not able to transduce with high fidelity the whole range of brain activity that occur over several temporal and spatial scales, from nm to meters and from μs to hours.

Currently, the main limitations of recording neural interfaces can be grouped in three topics. One major line of research is focused on minimizing the foreign body response in invasive neural interfaces, a cause of signal-to-noise ratio (SNR) deterioration or device failure that hampers achieving a long-term interface [6–8]. A second line of research deals with increasing recording site density and coverage of current neural interfaces [9]. Connectivity limitations of passive devices when

moving towards thousands of parallel recording sites require the use of multiplexing technologies [3]. Although high-density multiplexed microelectronic circuits are common nowadays, translating rigid technology to biocompatible, flexible and conformable neural interfaces remains a technological challenge. Finally, another persisting major challenge is the transduction of the broad frequency bandwidth of brain activity with high fidelity. Since sensing materials form the interface between the target signal and acquisition electronics, their properties are of paramount importance for a high-fidelity signal transduction at the interface. Due to present limitations, the exploration of novel materials for neural interfacing is warranted. The discovery of field-effect of two-dimensional material graphene in 2004 [10] and the subsequent determination that graphene presents a set of properties that make it suitable for bioelectronics [11], such as electrochemical stability, biocompatibility and high-charge sensitivity, indicated that graphene, used as channel of a field-effect transistor, could potentially be the basic element of a new technology for neural recording.

Developing a novel neural interface technology based on active transduction requires establishing standardized procedures that allow to fabricate neural interfaces in high enough number to consistently test its performance both in the lab and in relevant *in vivo* conditions. Moreover, since common recording technology is based on passive electrodes, electronic instrumentation as well as recording methodologies have to be adapted to active transducers. Also methodologies to recover the neural signal from the current flowing through the transistor should be investigated, validated and implemented. Importantly, any novel technology should also be compared to state-of-the-art gold standards to assess its performance and identify its benefits, potentialities as well as aspects to improve. The results of this comparison would hopefully allow to identify potential niche applications for the developed technology either for basic neuroscience applications or clinical neurophysiology. Summarizing, the aim of this Dissertation is to study the capabilities of graphene microtransistors as the building block of a new generation of neural interfaces. To that end, the objectives of this PhD Dissertation are:

- To establish procedures for the fabrication of flexible graphene microtransistor arrays.
- To develop methods for the high-fidelity recording of electrical activity using graphene microtransistor arrays.
- To assess the *in vivo* recording performance of graphene microtransistor neural probes compared to state-of-the-art recording technologies.
- To identify potential applications of graphene microtransistor technology in both basic neuroscience and translational research.

Dissertation Outline

This dissertation is organized in six chapters. Chapter 1 introduces the main concepts required to interpret the methods, results and discussions presented in this dissertation. A brief description of cortical structure and physiology of the rodent animal models used for the assessment of the recording performance of gSGFETs is given. Also, a brief description of brain activity is provided and the principles of extracellular field potential recording are outlined. A literature review of the present state-of-the-art of neural recording technologies is included. Then, a thorough description of single-layer chemical vapor deposition grown graphene highlighting its unique set of properties is provided. Finally, this Chapter introduces the concept of field-effect transistor and the operation principles of a graphene field-effect transistor, the basic component of the recording technology presented in this dissertation.

Methods to produce high-performance flexible graphene transistor neural recording interfaces are presented in Chapter 2. Parameters affecting intrinsic performance are described and discussed to provide guidelines for application-specific design of graphene transistor neural probes. A detailed step-by-step microfabrication process is described for two different flexible substrates and descriptive performance indicators of the microfabricated neural probes are provided that characterize current state-of-the-art.

In Chapter 3, the use of graphene transistors for electrophysiological recordings is presented. Particularly, the electronic instrumentation, gSGFET operation and the calibration methodology used to obtain high-fidelity recordings is described. To experimentally determine the feasibility of *in vivo* voltage sensing with graphene transistors, *in vivo* recordings are performed in rodents. Benchmarking against state-of-the-art microelectrode technology and comparisons between *in vivo* and post-mortem recordings are also provided. Moreover, gSGFET stability and recording fidelity during acute hour-long acute recordings is studied. The results of a pilot chronic study are also reported.

The ISA recording capabilities of gSGFETs are explored in Chapter 4. To experimentally determine the feasibility of infraslow *in vivo* voltage sensing, slow propagating depolarization waves are induced in anesthetized rats and the recordings of epicortical graphene transistor arrays and platinum black microelectrode arrays compared against the gold standard in the field, a liquid-filled micropipette.

The possibility to apply graphene transistor recording technology in day-to-day neuroscience research is studied in Chapter 5. Wide-bandwidth recordings of gSGFET epicortical probes in awake head-fixed mice are presented. Cortical spreading depression, a neurophysiological phenomena related with numerous pathologies such as brain injuries, epilepsy or migraine, is studied using an optogenetic

induction method. The waveform characteristics and the neural effects of CSD as also proof-of-concept pharmacological modulation and epicranial CSD monitoring are also presented.

In Chapter 6, the use of gSGFETs for mapping other field potentials of the brain that can be measured using DC-coupled recordings is presented. Moreover, proof-of-concept experiments demonstrating gSFET recording compatibility with brain imaging techniques such as functional ultrasound and calcium imaging are reported.

Finally, the principal conclusions of this dissertation and future potential applications of graphene transistor arrays are described. In addition, remaining challenges for applying graphene microtransistor technology for neuroscience research and to the clinics are also described.

Chapter 1

Background

In order to interpret the methods, results and discussions presented in this Dissertation, concepts from a wide variety of fields ranging from physiology to electrical engineering, electrochemistry or solid-state physics are required. In this chapter several concepts will be presented, including the basics of brain field potential generation and recording. Moreover, a literature review of current state-of-the-art transducers for recording field potentials is provided. Finally, the properties of single-layer graphene will be described and the principles of a graphene solution-gated field-effect transistor, the basic element of the technology presented in this Dissertation introduced.

1.1 Introduction

Brain diseases and disorders are a major public health problem in Europe and all other high-income countries causing a considerable social and economic burden [12]. It is estimated that one third of European citizens suffer from brain diseases or disorders such as depression, dementia, schizophrenia, stroke, migraine, sleep disorders, Parkinson's disease or pain syndromes to name a few, with expectations of this percentage to grow due to aging population [12]. Despite significant advances in treatments, extensive work on brain research is still needed to improve our understanding of brain function at molecular, cellular, and system levels as well as to unravel the pathogenesis of complex brain diseases [1].

Current brain knowledge has been acquired thanks to the advances in many scientific fields. To monitor brain activity, techniques based on different working principles (electrical, optical, and magnetic to cite the most common ones) have been developed, each of them covering a specific range of spatiotemporal brain activity (see Fig. 1.1) [13–15]. Among them, electrical techniques are highly suited to measure brain activity and allow measuring brain activity at different spatial scales and invasiveness. At the microscale, patch-clamp techniques based on glass micropipettes are used to measure currents of single ion channels or single neuron

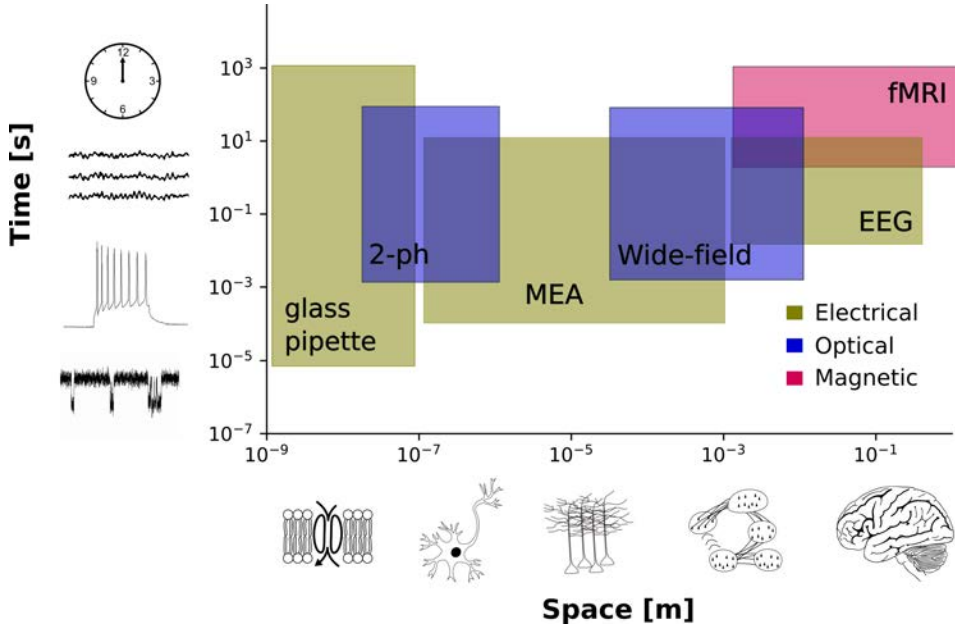


Figure 1.1: Spatiotemporal scales of neural activity monitoring techniques. Electrical techniques: glass micropipette electrode, multielectrode array (MEA), electroencephalography (EEG). Magnetic: functional magnetic resonance imaging (fMRI). Optical: two-photon(2-ph) and wide-field imaging.

activity with excellent temporal resolution ($< \text{ms}$) and signal stability over long periods (hours). However, intracellular electrical activity recording is extremely invasive and technically difficult, with current technologies limited to recordings from single or few neurons [16, 17]. At the macroscale, electroencephalography (EEG) is based on recording spontaneous or evoked electrical activity from the scalp using centimeter-scale electrodes. EEG is consistently used in clinical practice due to its non-invasiveness [4, 18]. Nonetheless, since EEG electrodes are largely separated from current sources in the brain (by cerebrospinal fluid, the skull, and the scalp), EEG has poor spatial resolution, and recorded signals result from superposition of large neural populations and filtering by the mentioned barriers [19–21].

Technologies that measure other aspects of neural activity such as blood flow, calcium signaling or magnetic fields have also been developed. Large areas of the brain can be observed via non-invasive techniques such as functional magnetic resonance imaging (fMRI), or magnetoencephalography (MEG), although their spatial and temporal resolution is limited [14, 15]. Optical techniques have been developed that allow imaging either small areas of the brain ($\approx \mu\text{m}^3$) with high spatial

resolution (2-photon) or larger areas of the brain ($\approx cm^3$) with coarser spatial resolution (wide-field imaging) [22]. The major disadvantage of some optical techniques is that they require the use of genetic modifications or dyes which constraints their use to animal studies. Moreover, their temporal resolution generally does not cover the entire frequency bandwidth of brain signals due to limited time response of the indicators used or their long-term instability. Despite these limitations, optical techniques are highly beneficial for animal studies when specific indicators in combination with targeting strategies, such as genetic approaches, that allow selectively measuring a single cell type, molecule or ion [23] are used.

Technologies that allow to monitor neural activity bridging the gap between biology and technology are often termed neural interfaces. Neural interfaces have applications from fundamental neuroscience to clinical practice [5]. For example, since brain activity contains information about intentions, neural interfaces can be used to control external hardware and when used in this manner, neural interfaces are often termed brain-machine interfaces (BMI). Neural interfaces can also be used to control assistive devices aiming to restore motor or speech disabilities and due to its chronic intended use are referred as neuroprosthesis. Both BMI applications and neuroprosthesis require technologies with fast response times that transduce brain activity with high-fidelity.

However, current technologies do not enable the wide variety of brain signals across its spatial and temporal scales to be quantitatively recorded (Fig. 1.1). Multisite electronic interfaces are nonetheless able to cover the most substantial part of brain spatiotemporal scales and are also compatible with chronic human use. The current clinical solution to obtaining brain recordings where higher spatial resolution than EEG is needed, for example for resection of epileptic foci is electrocorticography (ECoG). ECoG consists in placing arrays of large-diameter electrodes ($> mm$) directly on the cortex or over the dura. ECoG arrays are made by means of precision mechanics with platinum or stainless steel recording sites embedded into silicone rubber that serves as substrate and electrical insulation. The flexibility and elasticity of the silicone rubber ensures that the arrays adapt to the curvature of the brain and that the electrode sites stay close to the surface of the brain. The electrode site diameter typically varies between 1 mm and 10 mm and the pitch, i.e. the distance between the electrode centers, is usually fixed to 10 mm in commercially available electrodes for humans.

Advances in microfabrication have allowed to improve the spatial resolution of ECoG arrays. Microelectrode or microtransistor arrays (MEAs/MTAs) with dimensions ranging from 10 to 100 μm and site-to-site separation of few tens of μm have been developed using flexible polymers, offering high spatial and temporal resolutions. This opened a new field of ECoG called μ -ECoG, which is a very powerful technique to investigate neural network function as also to establish novel diagnos-

tic procedures, and will certainly be a major component for future neural prostheses [24, 25]. Indeed, increasing spatial density has been shown to improve signal decoding performance [24] which is of paramount importance for BMI. Therefore, state-of-the-art in μ -ECoG has been focused on developing a mesoscale technology able to record on large surfaces with an intermediate spatial resolution [26]. More invasive neural interfaces have also been developed and have become a practical route to understand brain function and its physiopathological state. For example, intracortical arrays allow brain potentials to be measured at specific cortical layers or subcortical areas [27, 28].

Overall, multisite recordings coupled with advanced decoding methods and neuromodulation techniques are currently used in the diagnosis, prognosis and treatment of neural diseases and disorders as well as the restoration or rehabilitation of multiple disabilities [5, 4, 12, 29]. However, despite the huge advances in neuroelectronic interfaces over the last decades, some issues remain to be solved. Current challenges of μ -ECoG technology can be classified in three main topics: biocompatibility, high-density mapping and signal fidelity. Biocompatibility research aims to achieve long-term interfacing with the brain [6–8]. Nonetheless, chronic studies of neural signals are still precluded by the electric recording interface; partly because the mismatch of the Young moduli and the chemical nature of the transducing material that induce fast degradation of the quality of recorded signals. The substrate used for the scaffold of the implant also plays an important part in the efficiency of the technology. The substrate must be very flexible, even more than the transducing material, to reach the conformability of the full device to the brain shape, highly biocompatible and highly stable. So far the most commonly used flexible substrates are parylene, polydimethylsiloxane (PDMS), polyimide, and SU8 [6]. μ -ECoG arrays can be placed either over or below the dura and are termed epi or subdural arrays respectively.

Developing high-density neural interfaces that cover large areas [9] is another research topic in neural interfaces. High-density MEA arrays can be fabricated which allow to map single cell activity with micron resolution [30]. Nevertheless, the detection area covered by the MEAs is limited due to fabrication constraints and the spatial arrangement of the connections to the recording system. Covering an important part (few square centimeters) of brain with high density requires hundreds of thousands of channels. Since individual connections to this high number of channels is not practical, alternative array architectures based on different multiplexing concepts are being developed [3]. Finally, another topic focuses on addressing the challenge of signal quality, and aims to develop novel transducers and methods to record with high fidelity and signal-to-noise ratios the whole variety of extracellular brain signals (see Fig. 1.2). State-of-the-art microelectrode recording technology suffers from limitations to record with high-fidelity certain types of

brain extracellular field potentials [31–33]. Therefore, research in novel transducers with improved signal recording quality are required. The material of the recording site has a prominent role in neural technology since it forms the interface between biological tissue and electronic circuitry and is responsible for field potential transduction between ionic and electronic charge carriers. The application requirement on materials is very stringent (biocompatibility, low polarization, high-fidelity field potential transduction and stability in the harsh biological environment) and is difficult to met completely by current materials. This PhD Dissertation can be considered as included in this research topic.

The discovery of field-effect of two-dimensional material graphene in 2004 [10] and the subsequent determination that graphene presents a set of properties that make it suitable for bioelectronics [11], such as electrochemical stability, biocompatibility and high-charge sensitivity, suggested that graphene, used as channel of a field-effect transistor, could potentially be the basic element of a new technology for neural recording. This PhD Dissertation will focus on exploring gSGFET as a novel transducer for μ -EcoG applications.

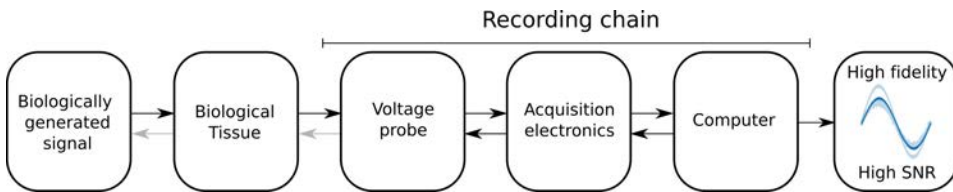


Figure 1.2: Electrophysiological recording chain. From the biological source, signals have to travel within the target tissue to the interface with the voltage probe, be transduced from ion to electron charge carriers, and processed by electronic instrumentation to amplify and digitize the signals making them suitable for display and post-processing using computers. During each of the steps of the recording chain, signals can get distorted and mixed with undesired signals. The objective of an electrophysiological recording technology is to minimize signal distortion and noise incorporation yielding high-fidelity recordings.

Importantly, the objective of any electrophysiological recording technology is to minimize signal distortion and noise incorporation yielding high-fidelity recordings. The process of recording electrophysiological signals can be splitted in several steps (see Fig. 1.2): signal generation, propagation to the transducer interface, signal transduction from electrolyte to solid state, signal amplification and digitization. During each of the steps of the recording chain, signals can get distorted and mixed with undesired signals. In the following sections the different steps and components involved in the recording chain and their potential effects on the signal are described with the aim to discuss the main concepts required to interpret the methods, results and discussions presented in this dissertation.

1.2 Brain field potentials

As a result of their activity, electrogenic brain cells produce transmembrane ion fluxes. Those ion fluxes generate field potentials which can be measured extracellularly. However, the relation between transmembrane ion fluxes and extracellular potentials is extremely complex. In this section, the basics of brain field potential generation by cells, and how they are shaped by cytoarchitecture and connectivity is discussed to provide the background for the interpretation of electrophysiological signals.

1.2.1 Mammalian brain macro- and microstructure

The human brain is composed of billions of interconnected neurons forming neural circuits. Since neurons with shared synaptic efferents will generate similar transmembrane currents, knowledge about the spatial organization and synaptic connections of neurons can aid in the interpretation of the extracellular field potential. While it is largely accepted that the brain is topographically organized into distinct areas that are integrated into networks, the unique contribution of each area to behavior is yet to be elucidated [34]. Luckily, many properties of neurons, from the type of neurotransmitters used to ion channel composition, are maintained across species, allowing scientists to study in much simpler organisms, the processes that occur in complex organisms. To get an idea of the complexity, mice and rats have about 71 and 200 million neurons respectively [35] and similar number ($\sim 1 \cdot 10^{12}$) of synapses, while humans have around 86000 million neurons and $\sim 1.5 \cdot 10^{14}$ synapses [36]. Despite the huge variation in the total number of neurons and synapses, most of the basic structural elements are shared between mammals. Figure 1.3A shows the basic organizational elements of the CNS of all mammals for a rat and human brain. While many similarities exist, the many convolutions on the surface of the human cerebrum is a clear structural difference with a rat brain. The neocortex is the brain structure thought to be involved in higher-order brain functions such as sensory perception, cognition, generation of motor commands, spatial reasoning and language. Experimentally, the cerebral cortex is easily accessible as it spans over most of its surface. Moreover, it has a characteristic cytoarchitecture that distinguishes it from other brain structures.

The cerebral cortex in the brain of all vertebrate animals has several common features as revealed by microscopy (Fig. 1.3B). First, the cell bodies of cortical neurons are arranged in layers that usually lie parallel to the surface of the brain. Second, the most superficial layer (layer I or molecular layer) contains very few neurons and is mainly composed of the apical dendrites of pyramidal cells and the most distal branches of afferent axons projecting to the cortex from the subcortical

areas such as the thalamus. Third, at least one cell layer contains pyramidal cells that emit large dendrites, called apical dendrites, that extend up to layer I, where they form multiple branches, and efferent axons that project to subcortical areas such as the striatum, brainstem, spinal cord or thalamus [37].

The exact layer structure varies in detail from one region to another, permitting the cortex to be mapped into dozens of histologically different ‘areas’. More concretely, experimental data provides arguments supporting the hypothesis that cortical organization, perpendicularly to the layers, is composed of at least three different spatial scales: modular-like structures, micro-, and meso maps [38]. Modular-like structures include columns, which represent different types of repetitive invariant structural and/or functional entities such as mini-columns, as well as other repetitive invariant entities like hypercolumns, blobs, inter-blobs (visual cortex, primate brains), barrels (somatosensory cortex, e.g., rodent brains), etc. Some modules are activated by specific thalamocortical inputs, some by cortico-cortical inputs from the same hemisphere, while others by inputs from the opposite hemisphere. Micro-maps are non-repetitive elements, formed by many repetitive modular-like structures, and represent local specializations within cortical areas (e.g., retinotopy, somatotopy). Meso-maps are non-repetitive entities of cortical areas, which change in their cytoarchitecture, connectivity, and function at the border between areas. Jointly, columnar organization, micro-maps, and the meso-map of a cortical area, define the structural basis of function.

Due to cortical functional importance and ease in accessibility all recordings presented in this PhD Dissertation are performed in the neocortex. The specific structural basis of cortical function is related to the morphological and behavioral specializations of each species [39]. Thankfully some common traits exist between mammals and even more between rats and mice (Fig. 1.3C). The use of rodent models is adopted since they share the laminar organization of cerebral cortex with humans and generate the electrophysiological signals (such as evoked potentials) required to validate the developed technology towards the human use.

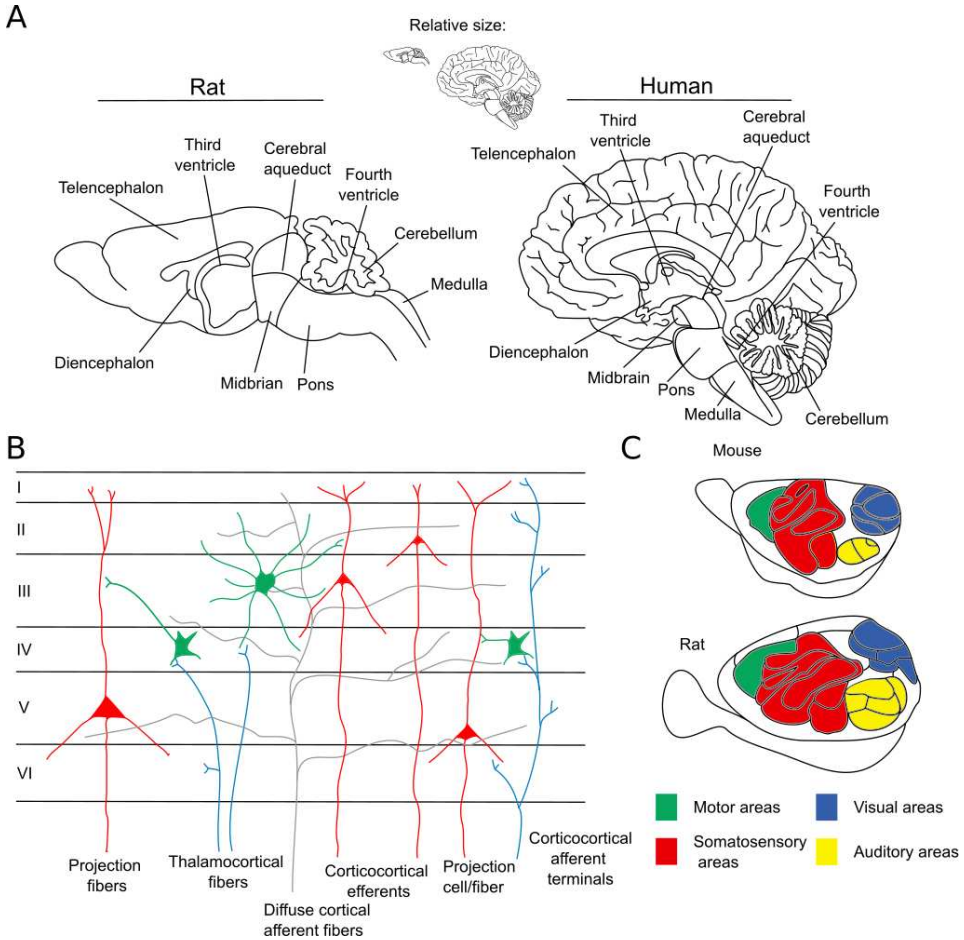


Figure 1.3: Brain macrostructure and cerebral cortex microstructure. A: Schematic of a rat and human brain with their major brain sections labelled. B: Laminar structure and connections in cerebral cortex. Afferent fibers are shown in blue and gray, interneurons in green, and efferent fibers in red. Thalamocortical fibers terminate primarily in layer IV, whereas corticocortical fibers and diffuse cortical afferents synapse in all layers. Pyramidal cells in the outer layers give rise to corticocortical projections, and those in layer V project to a wide range of subcortical targets. C: Topography of mouse and rat functional cortical areas.

1.2.2 Brain activity

At a cellular level, the brain is mostly composed by neurons and glial cells. Glial cells are located between neurons and make contact with neurons and vessels (Fig. 1.4A). All this arrangement results in a cerebral extracellular space consisting of very narrow intercellular clefts. Neurons are electrically excitable cells formed by soma (body), the axon and dendrites (Fig. 1.4B). Most neurons receive signals via the dendrites and soma and send out signals down the axon, which provides contact with other neurons through synapses. Synapses cover the dendrites, the soma, and the axon of neurons in large numbers. At the majority of synapses, signals cross from the axon of one neuron (presynaptic neuron) to a dendrite of another (postsynaptic neuron).

Electrical signalling is mostly based on transmembrane ion fluxes. Ions, being the most important ones sodium, potassium, chloride, and calcium, have different concentrations inside and outside neurons (Fig.1.4B). Cell membranes are made mainly by lipid bilayers, that behave electrically as insulators. Cell membranes also contain protein structures that are electrically active. These include ion channels, that permit ions to flow across the membrane, and ion pumps that chemically transport ions from one side of the membrane to the other. Some ion channels are permeable only to specific types of ions. Other ion channels can be gated either by voltage difference across the cell membrane or chemically gated. The collective interactions between ion channels and ion pumps produce a voltage difference across the membrane. Neurons generally have a resting membrane potential of -60 to -70 mV. If the voltage changes by a large enough amount over a short interval, the neuron generates an all-or-nothing sequence of transmembrane ion fluxes called an action potential. Fig.1.4C shows the Hodgkin–Huxley model of the neuron membrane. Chloride and leak channels contribute to the resting membrane potentials while voltage-gated sodium and potassium channels are required for action potential firing [40].

Action potentials propagate along the axon, and when they reach a synapse, voltage-gated calcium channels open allowing calcium ions to enter the terminal. Calcium causes synaptic vesicles filled with neurotransmitter molecules to fuse with the membrane, releasing their contents into the synaptic cleft (Fig. 1.4D). Then, neurotransmitters diffuse across the synaptic cleft and activate receptors on the postsynaptic neuron. The effect upon the postsynaptic neuron is determined by the type of receptor that is activated. Receptors can be classified broadly as excitatory (causing excitatory post-synaptic potentials (EPSP)), inhibitory (causing inhibitory post-synaptic potentials (IPSP)), or modulatory (causing long-lasting effects). With an elicited EPSP, a net inflow of cations occurs across the post-synaptic membrane and a local potential gradient develops along the neuronal

membrane in the intra- and extracellular spaces. Because of this potential gradient, cations redistribute along the nerve cell membrane through the extracellular space in the direction of the synaptic region while an inversely directed flow takes place in the intracellular space (Fig.1.4E). The inverse phenomena occurs with an IPSP. Importantly, a small percentage of the basal concentrations of ions are needed to change substantially the membrane potential during an action potential. AP firing is determined by the summation of EPSP or lack of IPSP (Fig.1.4 F).

Apart from the main two classes of neurons (excitatory and inhibitory) multiple neuron types exist that have specific membrane excitability and modulatory properties [41–43]. Alternatively to chemical synapses, some neurons also communicate via electrical synapses, which are direct, electrically conductive junctions between cells. Electrical synapses also play a role in neural synchronization of membrane oscillations. Some neurons do not generate all-or-none action potentials, but instead generate a graded electrical signal, which in turn causes graded neurotransmitter release.

Glial cells, the other main type of cell of the brain, have slightly more negative (-80mV) membrane potential than neurons and do not fire action potentials nor synaptic potentials [44]. Importantly, their membrane potential is not constant, and can be depolarized with an increase of the concentration of extracellular potassium. Repetitive firing of neurons locally rises the extracellular potassium concentration and causes glial cell depolarization (Fig.1.4 G).

In summary, neurons are responsible for information transfer in the brain mainly through transmembrane ion fluxes at synapses as also through release of neurotransmitter and neuromodulatory molecules. Glial cells, on the other hand, play a role in supporting neuron function but can also produce transmembrane ion fluxes. The ion fluxes, associated to neuron and glial function, give rise to field potentials at both the intracellular and extracellular space which can be measured using electrical techniques. Neural activity also produces magnetic fields associated to the transmembrane currents or local changes in energy demand and metabolism that are the target of brain activity monitoring techniques such as MEG and fMRI.

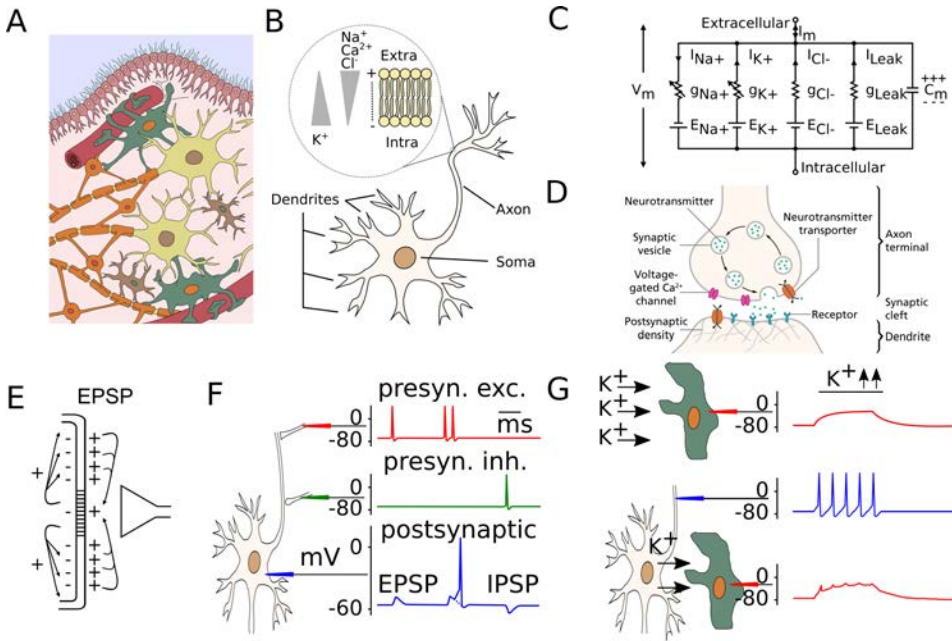


Figure 1.4: Basics of central nervous system (CNS) electrophysiology. A: Schematic of brain tissue, composed of neurons (yellow) and different types of glial cells. In reality, cells are much more packed together and the extracellular space consists of very narrow intercellular clefts. B: Schematic of a neuron with the soma, axon and dendrites labelled. Inset shows the potential and ion gradients across the cell membrane. C: Equivalent electrical circuit for the Hodgkin–Huxley model of the action potential. I_m and V_m represent the current through, and the voltage across, a small patch of membrane, respectively. The C_m represents the capacitance of the membrane patch, whereas the four g 's represent the conductances of four types of ion. The two conductances on the left, for potassium (K) and sodium (Na), are shown with arrows to indicate that they can vary with the applied voltage, corresponding to the voltage-sensitive ion channels. The chloride and leak conductances also contribute to the resting membrane potential. D: Schematic of a chemical synapse showing the different parts and the Ca^{2+} mediated release of neurotransmitters. E: Intra- and extracellular ion flow as a consequence of an excitatory synapse. F: Excitatory and inhibitory synapses modulate postsynaptic excitability and action potential generation. G: Membrane changes of a glial cell due to changes in extracellular potassium concentration (top) and neural activity (bottom). E-G: Adapted from [4].

1.2.3 Extracellular field potentials

After providing a description of how cellular activity generates transmembrane ion fluxes and of cortical laminar organization, in the following, the complex relation between extracellular field potentials and neuron activity is discussed. From an electrical point of view cortical tissue consists of a tightly packed collection of neurons and other cells embedded in a low-resistance extracellular medium filling less than a fifth of the total volume [18]. The extracellular potential (V_E), with respect to a reference potential, at any given position (r_i) is the result of the superposition of all electric currents (I_i) from cell activity (Eq.1.1, Fig. 1.5A):

$$V_{\mathbf{E}}(\mathbf{r}, \mathbf{t}) = \frac{1}{4\pi\sigma} \sum_i \frac{I_i(t)}{|\mathbf{r} - \mathbf{r}_i|}, \quad (1.1)$$

where σ is the extracellular conductivity, assumed to be real, scalar (the same in all directions) and homogeneous (the same at all positions). Although some of the assumptions may not strictly hold, slight modifications can be added to Eq. 1.1 (see section 4.2 from [14]). Importantly, the low resistance of the extracellular medium implies that neighboring cells are typically poorly electrically decoupled and that the difference between the extracellular potential recorded at different positions will be small, typically less than a millivolt (see Fig. 1.5B for an example of extracellular potentials produced by an action potential of a pyramidal neuron).

The low-frequency part (< 500 Hz) of the extracellular potential is generally called the local field potential (LFP). Despite the name, the reach of the LFP may not be "local" [45, 46]. The high-frequency band (> 500 Hz) of the extracellular potential is called multiunit activity (MUA). The interpretation of the LFP is complex as it is a less local measure of neural activity than MUA. Modeling of the extracellular potential is helpful to improve understanding of action potential waveforms, ionic and spectral components and reach of LFPs; as well as for validating data analysis methods for spike sorting or current-source density estimation [47, 48].

Table 1.1 summarizes the events contributing to extracellular currents which arise from many sources, and include synaptic currents, fast action potentials and their afterpotentials, calcium spikes, voltage-dependent intrinsic currents, glial oscillations and ephaptic coupling. Generally, the major contributor to the extracellular signal is the synaptic transmembrane current, but other sources can substantially shape the extracellular field [20]. Fast sodium action potentials are thought to contribute primarily to MUA, afterpolarizations to event-related potentials, glial cells to slow and infraslow oscillations and electrical synapses and ephaptic coupling to have modulatory effects. Moreover, synaptic potentials can be extremely different in amplitude and duration depending on the type of ion channel activation

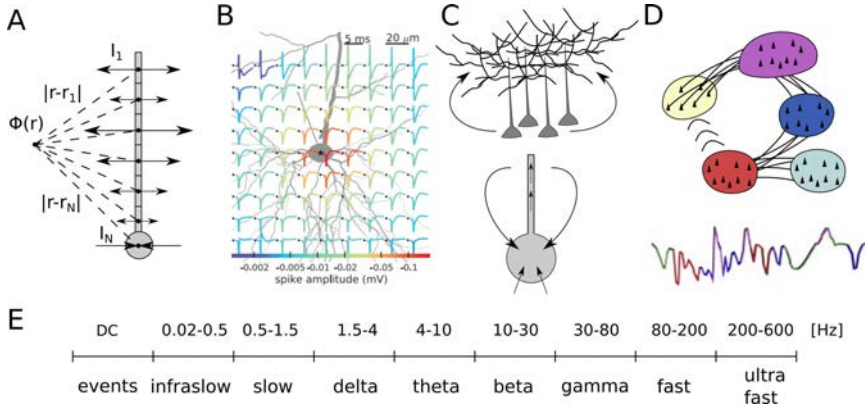


Figure 1.5: Extracellular field potentials. A: Extracellular potential at a given point in space results from the superposition of all currents. B: Extracellular potentials produced by an action potential of a pyramidal neuron. Figure from: [47]. C: Spatially separated and organized population sink/source create dipoles that strongly contribute to LFP. D: Coactivation of aggregates of neural populations that share synaptic afferent are the main contributor to LFPs. Adapted from: [49] E: Logarithmic frequency scaling of brain oscillations.

and due to synaptic plasticity [50]. The excitatory-inhibitory (E-I) balance is also a factor shaping the recorded brain field potentials. An E-I imbalance can produce highly synchronized epileptic activity which is indicative of brain malfunction [51].

The geometry of the cell is also of paramount importance in shaping extracellular potentials [46]. Pyramidal cells have long, thick apical dendrites that can generate strong dipoles along the somatodendritic axis. The considerable spatial separation of the active sink (or the source) from the return currents induce substantial ionic flow in the extracellular medium. Together with the population organization of pyramidal neurons makes their activity a high contributor to LFPs (Fig. 1.5C).

Event	Timescale	Contribution
Synaptic potentials	>100ms	High to LFP (1-100Hz)
Fast action potentials	<2ms	High at $f > 100$ Hz
Long lasting Ca^{2+} spikes	10-100ms	Moderately to LFP
Membrane oscillations	100ms	Moderately to LFP (θ , γ)
Afterhyperpolarizations	0.5-2s	High pre-after event
Electrical synapses	-	Excitability and synchronization
Glia membrane oscillations	>1s	Slow and infraslow
Ephaptic coupling	-	Modulatory effect

Table 1.1: Events contributing to extracellular field potentials.

Apart from spatial orientation the temporal, synchronization of the various current sinks and sources plays a vital role in shaping the extracellular potentials. For example, the voltage gradients generated by highly synchronous activity of neuronal groups can affect the transmembrane potential of the neurons and alter their excitability through ephaptic coupling. Volume conduction can also have a role on the measured extracellular potential. Nevertheless, the two most important factors thought to contribute to the LFP are the cellular-synaptic architectural organization of the network and synchronization of the current sources. Coactivation of aggregates of neural populations that share synaptic afferent (Fig. 1.5D), and synchronized firing are thought to be main contributors respectively of low and high-frequency components of the local field.

Due to the complexity of the signals, some have dismissed extracellular potentials as a so-called epiphenomenon, i.e. a measure peripheral to genuine scientific interest or utility. Yet it is evident that human and animal extracellular potentials vary in frequency and amplitude content during different brain states. Accurate measurement allows identification of distinct sleep stages, consciousness levels and other physiopathological events. That is, mammalian cortical neurons form behavior-dependent oscillating networks of various sizes, which span several orders of magnitude in frequency (Fig. 1.5E). Moreover, these oscillations are phylogenetically preserved, suggesting that they are functionally relevant [52]. Importantly, despite the several-thousand-fold variations in brain volume among mammals, the hierarchy of brain oscillations remains remarkably preserved. All these arguments are in favour of the importance of specific brain oscillations. Despite this, some still argue for a non-rhythmic irregular nature of extracellular field potentials [53].

Extracellular potentials represent information flow across neural networks, and reflect underlying physiological state. The theoretical biophysics underlying transmembrane currents that produce extracellular voltages is well established: quasi-static approximation of Maxwell's equations, cable theory and the electrical properties of the neuron and glial membranes and extracellular medium. However, although the underlying biophysics are the same, the recorded signal can vary significantly depending on the recording position, brain area and depth, or the dimensions of the sensor. High density recordings are thus expected to aid in determining the spatiotemporal occurrence of neural processes, increasing our understanding of the populations contributing to the extracellular signal in different situations.

1.3 Principles of extracellular potential recording

Brain field potential recording technology has evolved substantially over the last decades. Modern electrophysiological recording technology is based on multi-channel voltage probes, differential amplifiers and analog-to-digital conversion. Once digitized, data can be manipulated: resampled, rearranged, filtered and analyzed [54]. However, prior methodological and technological aspects during signal acquisition can affect the fidelity of the raw digitized signal to the “true” electrophysiological signal. Therefore is of utmost importance to take all those aspects into account when recording brain field potentials. In the following sections, the main components of a recording system are detailed and methodological considerations discussed to minimize potential sources of signal distortion and contamination.

1.3.1 Components of a recording system

Recording brain field potentials requires of several components (see Fig. 1.6): the target tissue which generates the signal; the voltage probes that transduce the field-potential fluctuations produced by ions in the tissue to solid-state electrical signals; instrumentation that powers the transducer if needed and amplifies, filters and digitizes the electrical signals; and a computer which stores the data and allows (real-time) visualization and signal processing. Next, the function of the two main components of the recording chain, the voltage probe and the electronic instrumentation will be further detailed and its requirements for high-fidelity signal acquisition discussed.

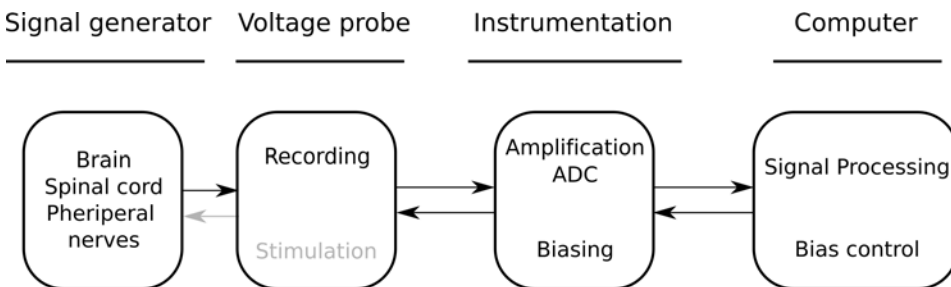


Figure 1.6: Neural interface schematic showing the different steps in a recording system. From left to right: the target tissue generating the signal to be measured, the voltage probe that transduces the ion fluxes into an electronic signal, the instrumentation, that allows signal amplification and ADC as also biasing of the voltage probe and the computer that allows to control the operation of the transducer as also signal visualization and processing. ADC: analog-to-digital conversion.

Voltage probes

Voltage probes form the interface between brain tissue and the recording system and transduce the field-potential fluctuations produced by ions in the tissue to solid-state electrical signals. An electrical double layer capacitance (EDLC) is created at the interface of any charged material positioned in an electrolyte since due to the hydration shell of ions in the electrolyte, or its finite dimensions in case of adsorption, they cannot approach the interface infinitely close and form a charge density separated from the surface [55]. The simplest picture of the EDL is a two-layer physical model in which one layer of the EDL is envisaged as a fixed charge firmly bound to the particle or solid surface, while the other layer is distributed more or less diffusely within the solution in contact with the surface. This diffuse layer contains an excess of counterions (ions opposite in sign to the fixed charge), and has a deficit of co-ions (ions of the same sign as the fixed charge). More complex models are needed to account for chemically affinity interactions such as ions specifically adsorbed to the surface.

The EDLC is the mechanism of signal coupling in an ideal polarizable material. However, most materials react with the electrolyte solution causing either the reduction or oxidation of some chemical substance. Therefore, the ionic/electronic interface is generally electrically modelled as a resistance (R_{ct}) and capacitance in parallel at the interface accounting for faradaic charge transfer processes and the electrical double-layer respectively (Fig. 1.7A). Also a resistance accounting for voltage drop at the electrolyte side (R_s) is generally added. More complex parameters may be introduced such as a voltage source to model polarization and diodes to represent the irreversible pathways of hydrogen and oxygen evolution that occur selectively at negative and positive voltages, respectively, due to electrolysis of water. This latter effect occurs if the electrode specific potential limits of the so-called water window have been exceeded, which is much more likely to happen during stimulation than during recording. Also rugosity of the material can require modelling the interface with more complex electrical components such as the constant phase or distributed elements.

The specific electrical properties of a material in a given electrolyte affecting signal transfer can be characterised by electrochemical techniques such as electrochemical impedance spectroscopy (EIS) [56] or cyclic voltammetry (CV). EIS analyses the response of an electrode to a periodic perturbation (typically a sinusoidal signal). The amplitude of the excitation signal must be low, i.e., between 10 and 100 mV, to prevent undesired irreversible electrochemical changes at the phase boundary. By comparing the amplitude and phase of the applied voltage input signal with the recorded current signal, the impedance (Z) of the system can be deduced. When the measurement is repeated over a range of frequencies this results in a spectrum of impedances, commonly plotted in two separate parts: the

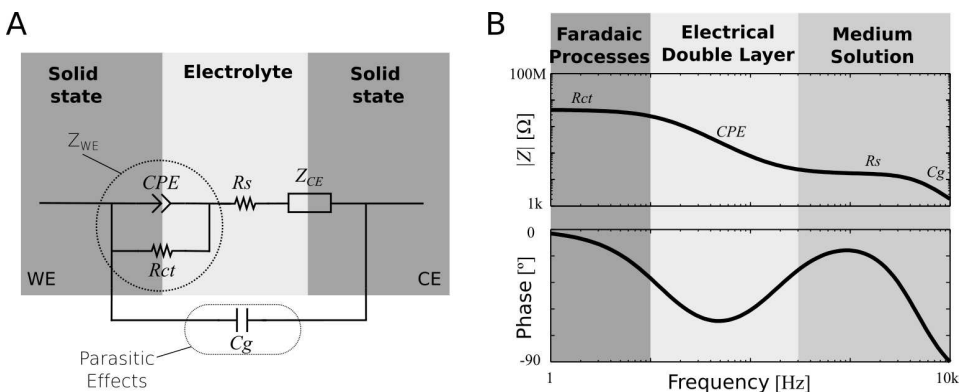


Figure 1.7: Solid/electrolyte interface. A: Electrical schematic which includes the working and counter electrode impedances (Z_{WE} , Z_{CE}) a resistive term contribution from the electrolyte (R_s) and parasitic effects (C_g). Z_{WE} can have faradaic and non-faradaic contributions which are generally modelled as a resistive term (R_{ct}) and a double-layer capacitive term (CPE). To accurately characterise Z_{WE} , the condition $Z_{CE} \ll Z_{WE}$ must be fulfilled. B: Representation of the solid/electrolyte interface impedance magnitude and phase versus frequency. Shaded areas indicate the regions generally dominated by faradaic, double layer and electrolyte contributions.

magnitude of Z in logarithmic scale,

$$|Z| = \sqrt{\text{Re}(Z)^2 + \text{Im}(Z)^2} \quad (1.2)$$

and the phase shift of Z ,

$$\phi = \arctan\left(\frac{\text{Im}(Z)}{\text{Re}(Z)}\right) \quad (1.3)$$

in linear scale, both versus a logarithmic scale frequency x axis. This representation is called the Bode plot, and outlines the transfer function of the interface, i.e. how well various frequency contents (tones) of an input signal are transferred over the solid-liquid boundary. Fig. 1.7B represents a common behaviour of the bode plot of an electrode in an electrolyte which includes regions generally dominated by charge transfer at low frequencies, an intermediate region where the double layer dominates and a region dominated by the electrolyte or parasitic effects at higher frequencies. The exact transition point between these regions depends on the material under test, its area and electrolyte conductivity.

While EIS characterizes the frequency dependent signal transfer, voltage dependent electrochemical processes are better characterized using CV. In CV, the potential of the electrode is driven between oxidising and reducing potentials, at a constant rate (V/s), while the current is monitored. The measured current is influenced by capacitive and faradaic processes in both sweep directions in a characteristic manner. As voltage changing rate is constant (apart from at the respective

vertex potentials), capacitive charging contributes a steady positive or negative current over the anodic and cathodic sweep, respectively. By contrast, any current related to faradaic charge transfer varies with the voltage applied since it is dependent on the activation voltage for a reaction (V_r). If the reaction is mainly kinetically limited, then driving the potential further from the equilibrium will immediately result in an exponentially increased faradaic current. An example of such a reaction is the electrolysis of water in a water-based solution, with a sharp increase in the CV current on either side of the ‘water window’. Commonly, the supply of reactant is not unlimited, and thus, the initial increase in current will rapidly consume the reactants at the surface. Continued reaction is possible only as new reactants become available and the reaction rate, and therefore current, quickly becomes diffusion limited. Consequently, the initial increase in current as the voltage approaches V_r will drop at potentials further from the equilibrium. In the cyclic voltammogram, diffusion limited faradaic surface interactions appear as peaks at characteristic voltages. These peaks outline an electrochemical signature of the surface in the specific electrolyte and by varying composition and concentration of the supporting electrolyte, it is possible to identify key reactants in faradaic charge transfer.

Charge transfer properties at the electrode/electrolyte interface strongly depend on the material characteristics of the surface, the electrolyte composition and the amplitude and frequency of the signal. Moreover, not only the electrochemical processes determine the signal transfer properties (Fig. 1.7A). For example, the placement of the voltage probe, either extracorporeal or invasive, acute or chronic contact and the size of the voltage probe are factors potentially affecting the signal transfer properties. An ideal voltage probe allows signals to be sampled with high-fidelity while minimizing its own influence on the biological signal generators.

Commonly used voltage probes are electrodes, i.e. a passive material that does not require to be actively polarized. Electrode signal coupling is characterized by its impedance. Other types of voltage probes require biasing to work properly, such as transistors, and they are referred as active probes. Many transistor configurations exist such as field-effect transistors and electrochemical transistors, among others [57, 58]. In brief, transistors are three terminal devices that transduce voltage signals at its gate into current fluctuations. To recover the signal at its gate, the transistor transfer function has to be properly characterized in terms of voltage and frequency dependence. A more detailed description of electrode and transistor signal recording mechanisms is provided in Section 1.3.1, after introducing the acquisition instrumentation since it plays an important role in the discussion.

As a general rule, to form a reliable interface with the tissue, voltage probes must be biocompatible, have stable characteristics in a wide bandwidth, have both low thermal and electrochemical noise and low polarization. For chronic applications,

the devices where the transducers are embedded will be in contact with the harsh biological environment and therefore in addition to the aforementioned requirements, they must be resilient to swelling, delamination, dissolution and corrosion. As no material is optimal for all applications, the desired recording application determines the specific requirements and thus influences the voltage probe selection process.

Instrumentation

To allow signal manipulation using computers, signals sensed by voltage probes have to be amplified in order to meet the dynamic range of analog-to-digital converters (ADC). The aim of the electrical recording instrumentation is therefore to amplify electrical signals while minimizing noise contamination and signal distortion. Amplification is performed by a so-called (pre)amplifiers that operates in differential mode, i. e., the signal between two points is amplified by a given factor (gain). Output voltage (V_o) is defined as [4]:

$$V_o = V_{gain}(V_+ - V_-) + 1/2CM_{gain}(V_+ + V_-) \quad (1.4)$$

where V_{gain} is the voltage gain and CM_{gain} is the common-mode gain. Both gains define the common-mode rejection ration (CMRR) that determines how well the shared signal is removed and not amplified.

$$CMRR = 20\log_{10}\left(\frac{V_{gain}}{CM_{gain}}\right) \quad (1.5)$$

Modern amplifiers fulfill the requirements of high gain and high CMRR (>80dB). Another important property of an amplifier is the input impedance which has to be as high as possible. General values of input impedance are in the 100M Ω up to T Ω range and generally have a capacitance of arround 10pF in parallel. In summary, requirements for recording amplifiers are a high and constant gain over a wide bandwidth, linearity, high common-mode rejection ratio, low intrinsic noise and high input impedance.

Signal coupling

The voltage probe (either an electrode or transistor) and the corresponding recording circuitry must be considered together to discuss the effects of recording on the input signal. In electrodes, the recording of electrical signals is based on a voltage divider between the electrode and amplifier impedance (Z_e , Z_a):

$$V_{in} = V_{sig} \frac{Z_a}{Z_a + Z_e} \quad (1.6)$$

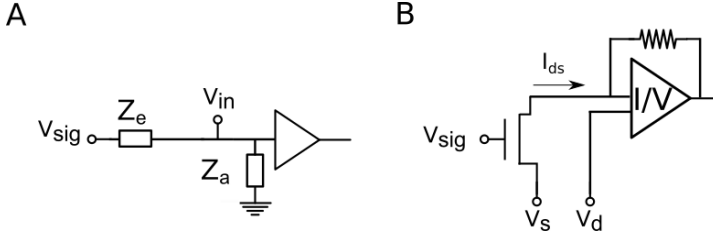


Figure 1.8: Signal recording through electrode and transistor circuits. A: Schematic of the circuit elements of signal recording through electrodes. Recording of electrical signals is based on a voltage divider between the electrode and amplifier impedance (Z_e , Z_a) see Eq. 1.6. B: Schematic of the circuit elements of signal recording through transistors. Transistors require biasing (V_s, V_d) and its current I_{ds} is determined by the transfer function of the device plus the signal $I_{ds}(V_{ds}, V_{gs}, V_{sig})$. In a small signal approximation, the current $I_{ds} \approx I_{ds_{DC}} + g_m V_{sig}$.

where V_{in} is the recorded signal that will be further amplified and V_{sig} is the original signal. The recording principle is based on the assumption that by far, the highest impedance in the circuit is the input impedance of the amplifier (Z_a) and therefore $V_{in} = V_{sig}$. However, when electrode impedance is not negligible relative to amplifier input impedance, this assumption does not hold producing frequency-dependent attenuation and phase shifts [31] (Fig. 1.8A). The signal is sensible to changes in the impedance of electrodes and sudden changes in contact, contributing to misinterpretations. For example, a change in the impedance of just one or few electrodes, can produce distortions that seem local signals [4]. Therefore, the complex electrical model of the electrodes, the biological components and the short circuit pathways has to be taken into account to understand the behavior of the system and account for signal distortion and attenuation.

Active coupling is based on transistors. The main figure of merit of a transistor for signal recording is its gain, also called transconductance (g_m). The transconductance relates the induced current flow variations in the channel with the voltage oscillations at the gate ($g_m = \frac{\partial I_{ds}}{\partial V_{gs}}$). Importantly, the amplitude of the coupling depends on the frequency dependence of the transistor gain, which is generally constant until the so-called cut-off frequency [59]. Therefore, signals recorded by transistors are intrinsically amplified and are not dependent on the input impedance of subsequent amplification stages but determined by the absolute value of the transistor transconductance frequency-dependence.

1.3.2 Considerations for electrophysiological recordings

When designing a recording session different aspects should be considered such as the reference electrode material and location, the different noise and artifacts sources and how to minimize them.

Reference electrode

An ongoing issue for recording electrophysiological potentials concerns the choice of reference electrode placement. The absolute value of the electrical field potential has no physical meaning (electrical potential is defined with respect to another point at infinity, understood as "far" from other sources). In experimental measurements one or multiple electrodes are placed near the sources of potential and another electrode (the so-called "reference") at a much larger distance. However, sometimes because all current is confined to a given volume, there may be no location that qualifies as a genuine reference. One obvious trouble with this procedure in electrophysiological applications is that generally no prior knowledge of source locations is available. If the so-called reference electrode is placed anywhere near the head, it is not known in advance that it is (electrically) far enough from all sources to be considered a so-called quiet reference, since sources of electrophysiological signals are typically distributed throughout large regions of the brain.

Therefore, when analyzing signals, it has to be taken into account that they can be closer to the reference electrode than the recording electrode. The use of multiple recording electrodes generally implies that each electrode is connected to one point of a differential amplifier while the other one (reference) is shared by all electrodes. This helps in identifying reference occurring potentials since they will be shared among the recording electrodes. However, these potentials are impossible to differentiate from a potential occurring in the whole region of the recording electrodes. The so-called "reference free" measurements using averaged values of all recording electrodes are also not a perfect solution and their advantages and limitations have to be known in order to decide if worth applying for a given application [60, 61].

A good test for reference location is that changes in the location of the reference electrode, for example to contralateral side or to more posterior/anterior regions, should not alter substantially the recorded signals. Placement of the reference electrode in muscle is a good approach for recordings under anesthesia. However, under awake conditions, it can be a source of noise contamination by nerve potentials. In conclusion, in electrophysiological recordings the choice of reference electrode positioning is of utmost importance and has to be chosen depending on the experimental conditions and objectives.

Regarding electrical properties, reference electrodes should be non-polarizable and reversible and their electrode potential has to be nearly independent of their exchange current over the phase boundary. Generally, the most used reference electrode in biomedical applications is the silver-silver chloride electrode, although its use for chronic invasive applications is discouraged due to toxicity of the dissolved silver. In human ECoG applications is common to use one of the electrodes of the grid as reference. Research on biocompatible, long-term stable reference electrodes is needed and would allow the use of a proper reference in human ECoG recordings.

Noise and artifact considerations

There are different noise and artifact sources in electrophysiological recordings which include the intrinsic noise contribution from the recording transducer and recording system as well as extrinsic contributions.

Intrinsic noise Intrinsic noise is the noise related to the transducer or recording circuitry. A main contribution to intrinsic noise is thermal noise. Thermal noise depends on temperature (T), the real part of the impedance ($Re(Z)$) and the recording bandwidth:

$$v_{th} = \sqrt{4kT \int_{f_1}^{f_2} Re(Z) df} \quad (1.7)$$

where k is the Boltzmann constant and f_2 and f_1 the upper and lower frequencies of the bandwidth. Thermal noise is white (constant with frequency) and gaussian distributed. Thermal intrinsic noise level of an amplifier generally does not exceed $2\mu\text{V}$ root mean square (RMS) in the electrophysiological bandwidth. Instead, the thermal contribution of the voltage probe is generally the main source of noise in electrophysiological recordings, specially for small electrode sizes due to their high impedance [62]. In the case of low-pass filters such as the one formed by the electrolyte resistance and the double layer-capacitance, voltage noise is dependent on the total capacitance:

$$v_n = \sqrt{kT/C} = \sqrt{\frac{kT}{C_A \cdot A}} \quad (1.8)$$

where A is area and C_A is the capacitance per unit area [63]. Therefore, for a given capacitive electrode material, downscaling increases the intrinsic noise with one over the square root of the area.

In active transducers, intrinsic noise is generally frequency-dependent. The intrinsic noise of a transistor is measured by acquiring the fluctuations of the drain current (I_{ds}) over time at a fixed bias (V_{ds}, V_{gs}). The fluctuations are then analyzed

in the frequency domain and the power spectral density (S_I) of the current is calculated. By integrating the S_I over a frequency bandwidth of interest, the RMS drain-source current noise (I_{ds}^{RMS}) can be extracted [59] ($I_{ds}^{RMS} = \sqrt{\int_{f_L}^{f_H} S_I^2 df}$). A more useful noise figure of merit of the transistor as a voltage sensor is the equivalent effective gate voltage fluctuation (V_{gs}^{RMS}), which is obtained by dividing I_{ds}^{RMS} by the transconductance ($V_{gs}^{RMS} = I_{ds}^{RMS}/g_m$) and provides relevant figure of merit used to evaluate the ultimate recording resolution of the transistor.

Electrochemical reactions are also a source of intrinsic noise [62] and can be minimized by using inert materials and low biasing voltages.

Extrinsic noise Extrinsic noise includes biological and environmental sources. Environmental noise sources are electromagnetic signals such as telecommunication waves and power line noise. Environmental noise tends to be relatively constant over the body surface and the sensing and reference probes. The same applies to biological noise such as the electrical activity of the heart or muscles that produces relatively constant potentials over the head [64]. In those cases, both environmental, biological and power line noise tends to be canceled by differential amplifiers with high CMRR, however, exceptions occur and heart rate signals or power line often manifest in just few channels. Also movement artifacts, even in anesthetized recordings resulting from breathing, can be coupled to the signal.

Strategies for noise reduction The use of an integrated (pre)amplifier can be very useful to minimize noise contamination [64]. Filtering is another strategy used to minimize noise. Filters can be used for reducing the effective noise bandwidth (low pass filter, generally at some kHz), decoupling DC and slow components (high pass filter, generally at $f > 0.5$ Hz), selecting a desired signal bandwidth using a bandpass, or using notch filters to reduce interference of 50/60 Hz from the power supply. Also, low pass filtering limits the signal to prevent non-linear aliasing in the succeeding analog to digital conversion before the data are displayed, stored and further processed. Finally, for reducing noise it is also important to properly ground all instrumentation and specially to avoid ground loops, which are minimized by bringing all the ground wires to the same potential in a ground bus.

1.3.3 Passive and active recording technologies

When critical technical issues are properly addressed, electrical recording techniques can provide robust measures of electrophysiological signals. However, high-fidelity recording of neural activity from the central nervous system is a challenging task with respect to voltage probe selection due to absence of an ideal solution. Each application, with its specific requirements (spatial and temporal resolution, biocompatibility, signal amplitude as well as the desired frequency components) drive the selection process. In the following, a comparison of passive and active recording technologies is provided.

Technology	Pre-amplification type	Noise	Signal coupling
Electrode	Differential Amp.	$\propto Re(Z_e)$	$V_{in} = V_{sig} \frac{Z_a}{Z_a + Z_e}$
Transistor	Transimpedance Amp.	I_{ds}^{RMS}/g_m	$I_{ds} \approx I_{dsDC} + g_m V_{sig}$

Table 1.2: Comparison of electrode and transistor recording technologies. Electrode technology is passive and relies on differential amplifiers, its noise is determined by the real part of the impedance of the electrode (Z_e), and signal coupling is based on a voltage divider between Z_e and Z_a . Transistor recording requires active biasing and relies on current measurement generally through transimpedance amplifiers. Transistor effective noise depends on both the intrinsic noise of the transistor (I_{ds}^{RMS}) and its transconductance (g_m) while the recorded current must be converted to the original signal by applying the inverse of the transfer function or under linear approximation the transconductance at the biasing point. All those variables (Z_e , Z_a , I_{ds}^{RMS} and g_m) can be frequency dependent which could cause signal distortion.

Table 1.2 summarizes the properties of electrode and transistor technology for neural recording. While electrode technology is passive and relies on voltage measurement, microtransistor technology requires active biasing and relies on current measurement. Noise in electrode technology is determined by the real part of the impedance of the electrode (Z_e), while for transistors it depends on both the intrinsic noise of the transistor (I_{ds}^{RMS}) and its transconductance (g_m). The original signal (V_{sig}) is recorded with high fidelity when the Z_e is negligible with respect to the amplifier input impedance (Z_a) for electrode technology while for transistors the recorded current must be converted to the original signal by applying the inverse of the transfer function using g_m at the V_{gs} bias point in a small signal approximation. All those variables (Z_e , Z_a , I_{ds}^{RMS} and g_m) can be frequency dependent which could cause signal distortion. When comparing recording technologies is therefore important to consider the reported performance indicators and their relation to the target signal.

1.3.4 Assessing recording quality

Assessing the recording quality is essential for determining the performance of any recording technology. For a recording system, the objective is to acquire the input signal with no distortion nor added noise. Multiple indicators have been developed that help determine the quality of the recorded signal. Here below they are presented in an order that considers whether they assess signal distortion, noise contamination or both.

First some theoretical aspects of signal processing are provided and discussed. The process of signal recording can be characterised by a transfer function (F) such that:

$$V_{rec}(t) = F(V_{sig}(t)) \quad (1.9)$$

where V_{sig} is the original signal and V_{rec} the recorded signal. In an ideal noise-free system, if the transfer function is constant for both gain and phase in the whole bandwidth of the input signal, the output is said to be distortion-free.

Distortion occurs for more complex transfer functions. There are different types of distortions that can occur. Some distortion effects are dependent on the linearity of the transfer function (amplitude, harmonics) while others are due to the frequency response (limiting bandwidth, attenuation and phase delays). If F is a linear function, for instance a filter whose gain and/or delay varies with frequency, the signal suffers distortions that do not introduce new frequency components to a signal but alters the balance of existing ones and its phase. Instead, non-linear transfer curves cause the introduction of new frequency components as also causing amplitude distortion. Examples of amplitude distortions are clipping of the signal due to amplifier saturation or harmonic distortion.

Using Taylor series allows studying distortion independent of the specific shape of the non-linearity. Mathematically, given a signal $x(t)$, the output signal $y(t)$ can be approximated by a Taylor series:

$$y(t) \approx \alpha_0 + \alpha_1 x(t) + \alpha_2 x^2(t) + \alpha_3 x^3(t) \quad (1.10)$$

where α_j is the n term $\frac{f^{(n)}(a)}{n!}$ with $n!$ being the factorial of n and $f^{(n)}(a)$ the n -th derivative of the transfer function evaluated at point a . In the case of $x(t)$ being a sinusoidal with amplitude A and angular frequency ω , Eq. 1.10 yields:

$$\begin{aligned} y(t) &\approx \alpha_0 + \alpha_1 A \sin(\omega t) + \alpha_2 (A \sin(\omega t))^2 + \alpha_3 (A \sin(\omega t))^3 \\ &= \alpha_0 + DC_{offset} + \alpha_1 A' \sin(\omega t) + \frac{\alpha_2 A^2}{2} \sin(2\omega t) + \frac{\alpha_3 A^3}{4} \sin(3\omega t) \end{aligned} \quad (1.11)$$

where $DC_{offset} = \frac{\alpha_2 A^2}{2}$ and $A' = \alpha_1 A + \frac{3\alpha_3 A^3}{4}$. Eq. 1.11 shows the appearance of harmonics ($2\omega, 3\omega$) due to non-linearity, as well as DC-offsets.

Harmonic distortion is generally quantified in terms of the relative strength of individual components, in decibels, or as the total harmonic distortion (THD). THD is defined as the RMS amplitude of all harmonic components (V_n) to the RMS amplitude of the first harmonic (V_1), or fundamental frequency:

$$THD_F = \frac{\sqrt{V_2^2 + V_3^2 + V_4^2 + \dots}}{V_1} \quad (1.12)$$

Correction of distortion is possible in some circumstances. As the system output is given by the transfer function, if the inverse function F^{-1} can be found, and used intentionally to distort the output of the system, then the distortion is corrected.

In contrast to distortion, noise contamination is generally not possible to correct, although some techniques and methods exist to mitigate its effects. Different quality figures of merit that take into account noise have been developed that are based on absolute noise levels such as noise power spectral density, noise power and methods based on percentiles or on signal-to-noise ratios. A description of the most common methods and its uses is summarized below.

A common manner to assess the noise of a system is by calculating the noise amplitude power spectral density (V/\sqrt{Hz}). It has dimension of power over frequency, whose SI unit is watts per hertz. The rms amplitude can be calculated by integrating in a given bandwidth. Noise can also be measured by statistical methods. The n-percent exceeded level, L_n , determines that for n percent of the time, the fluctuating levels are higher than the L_n level. This value is very useful in discriminating signal from noise with a given false rate. For example for event detection, one can set the threshold at a given L_n to ensure a given percentage of false positives.

Generally one is interested not just on the absolute noise of the system but on the SNR. SNR allows to quantify the size of the applied or controlled signal relative to fluctuations that are outside experimental control. A common use of SNR is to compare the quality of electrophysiological recordings containing events recorded in the presence of noise. Since SNR depends upon the choice of signal, it is a property of the experimental conditions rather than being an intrinsic property of the recording system itself.

SNR can be calculated by different methods. Current approaches for assessing SNR in brain recordings rely mostly on the amplitude of the signal of discrete events. SNR can be calculated by taking the highest peak during a period of evoked or epileptic activity and dividing it by the standard deviation of the background signal during a period of low biological activity ($SNR = A_{peak}/\sigma_N$) [65, 66]. Another method of calculating SNR is based on the voltage amplitude ratio of up and down states of slow oscillations [67]. Since these methods of calculating

SNR are based on the amplitude of the signal, the calculated SNR values only evaluate the performance of the devices at the frequencies of the recorded events. Nonetheless, obtaining information about the SNR at different frequency ranges of the brain signals is a relevant step in the characterization of recording devices. This can be done by an spectral SNR [68]. The signal-to-noise ratio pertaining to each frequency is $SNR(f) = P_S(f)/P_N(f)$ with $P_S(f)$ and $P_N(f)$ are the power spectrum of the signal and noise respectively. The signal-to-noise ratio for a given frequency band can also be obtained as the ratio of the area under the signal and noise power spectral density curves: $SNR = \int P_S(f)df / \int P_N(f)df$.

In the case of event detection, one is generally interested in discriminating the signal from the noise. One indicator of signal discriminability is d' defined as signal mean divided by the standard deviation of the noise, for events with a gaussian distribution. For non-gaussian distributed events, it is useful to establish a discrimination criterion based on percentiles. For example, d' can be defined as the percentile of the signal corresponding to a given percentile of the noise.

Some quality indicators exist that try to summarize both signal distortion and noise. One of such is the total harmonic distortion plus noise (THD+N). This measurement is common and comparable between devices. It is usually measured by inputting a sine wave, notch filtering the output, and comparing the ratio between the output signal with and without the sine wave:

$$THD + N = \frac{\sum_{n=2}^{\infty} \text{harmonics} + \text{noise}}{\text{fundamental}} \quad (1.13)$$

Like the THD measurement, it is a ratio of RMS amplitudes.

In addition to the aforementioned distortion, noise and SNR estimators, the crosstalk is an effect on signal quality that has to be taken into account when measuring multiple channels. Crosstalk is any phenomenon by which a signal transmitted on one channel of a recording system creates an undesired effect in another channel. Crosstalk is usually caused by undesired capacitive, inductive, or conductive coupling from one channel to another.

Different indicators for determining the quality of a recorded signal, both for distortion, such as the transfer curve, the frequency response of the system and THD, as well as for noise such as noise level estimators and SNR have been presented. These methods are adequate in cases where signal and noise can be easily separated and experimental conditions can be replicated.

In electrophysiological recordings where the signal can be separated from noise such as in evoked activities, signal power and SNR has been found to be highly variable. Therefore, the reliability of signal detection in a given set of conditions is hard to be adequately predicted from estimates of noise power alone, or from

SNR estimated under different experimental conditions [69, 70]. Results suggest the need for estimation of SNR for each recording session to ensure adequate signal quality.

In the case of *in vivo* spontaneous activity, the signal is generally not known, and hence, evaluating recording performance is more complex, specially since spontaneous activity has a wide spectral distribution without clear peaks. Assumptions might have to be made of what is signal and what is noise (such as more silent periods). Comparison with post-mortem recordings is another method to assess SNR in a given experimental conditions. Alternatively, signal fidelity can be tested against a gold standard recording technology, for example a glass micropipette, using crosscorrelation techniques.

In general, due to the wide diversity of neural signals in terms of amplitude, duration, occurrence and frequency components, reporting noise estimates based on rms value or percentiles in a frequency bandwidth of interest is better suited for assessing the performance of a recording technology than SNR obtained in a given recording paradigm.

1.4 State-of-the-art voltage probes for mapping brain field potentials

Transduction of biological ionic signals to electronic signals with high-fidelity and low-noise requires of materials and circuits that are biocompatible, have stable characteristics in a wide bandwidth, have both low thermal and electrochemical noise and low polarization. This section provides a brief review of the state-of-the-art of the most common transducers (microelectrodes and microtransistors) for mapping brain field potentials.

1.4.1 Microelectrodes

Decades of research has produced a variety of electrode materials that can perform reasonably well in biological environments. Noble metals such as gold or platinum are commonly used in microelectrodes, due to its superior electrochemical stability compared to other metals. Iridium and titanium nitride are also used for thin films and coatings, while alloys such as Pt/Ir are also established materials. However, electrode miniaturization to achieve high-density arrays causes an increase of electrode impedance. Since electrode impedance is one of the most important factors for signal recording affecting both signal coupling and noise [71, 72], efforts have been put to obtain low-impedance (high capacitance per area) materials. Electrode materials investigated are based on micro- or nano-roughened versions of noble metal surfaces, oxides, carbon or conductive polymers [68, 73–76]. Strategies focused to increase the effective area allow downscaling the recording site while preserving the impedance and hence the intrinsic noise. Despite those efforts, downscaling electrode size can compromise the recording bandwidth, specially at very low frequencies, due to high Z_e (see Eq. 1.6). Moreover, having a stable impedance over time of high-surface area materials can be challenging.

1.4.2 Microtransistors

One commonly used type of transistor is the field-effect transistor (FET). Evidence that field effect is a useful mechanism for field potential transduction is known since the 1950s and indeed, FETs have been at the base of many analog technologies since then. One of the main advantages of transistor technology is an inherent local preamplification of the recorded signals.

The use of FETs in biological environments to measure the tiny oscillations occurring in the extracellular space adds considerable challenges, being arguably the

most important the electrochemical inertness of the transducing material under the stringent conditions of humidity and complex chemical composition of the extracellular space. Most materials that undergo field-effect suffer from electrochemical reactions that even increase when polarized or form a native oxide such as silicon. For this reason most FETs used in aqueous environments are oxide-semiconductor field-effect transistor (OSFET)s [77, 78], it is, they use an oxide layer that separates the semiconductor from the liquid (see Fig. 1.9). The enhanced electrochemical stability gained with the oxide layer comes with a loss in sensitivity due to the larger separation of the electric field sources to the field-sensitive material. Importantly, oxide layers are also generally prone to polarization and indeed electrochemical reactions take place at oxides in complex aqueous environments [78]. To avoid these effects, the concept of extended-gate transistor was conceived [79], which consists of coupling an electrode at the gate of the transistor that is in contact with the tissue.

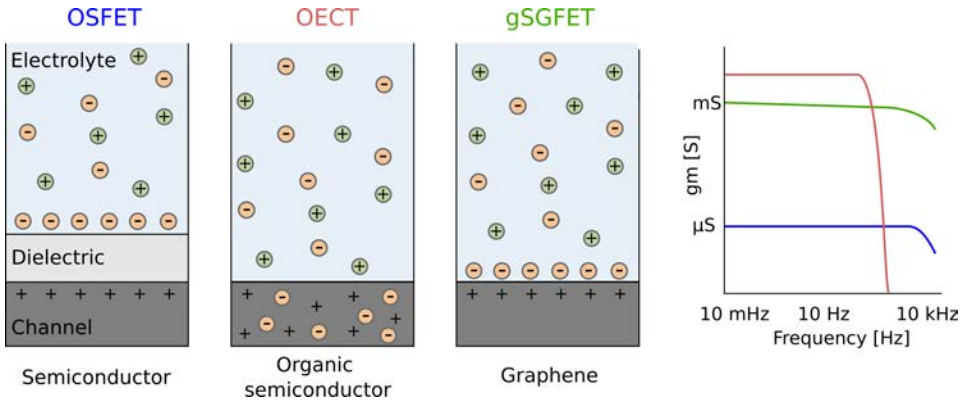


Figure 1.9: Comparison of transistors for recording brain activity. From left to right: Schematics of electrolyte-transistor interface for an oxide-semiconductor FET (OSFET), an organic electrochemical transistor (OECT) and a graphene solution-gated FET(gSGFET). Right: Comparison of the transconductance magnitude and frequency response of OSFETs, OECTs and gSGFETs.

Other types of transistors not based on field-effect have been explored for electro-physiological recordings such as the organic electrochemical transistor (OECT) [80, 81]. In an OECT, ions in the electrolyte penetrate the channel material leading to changes in the doping state (see Fig. 1.9). This configuration is described not by a parallel plate capacitance but by a volumetric capacitance, which can be many orders of magnitude larger [81].

Adequate figures of merit for comparing transistors are their intrinsic noise, transconductance magnitude and frequency response. OECTs have generally a higher transconductance than most FETs but also reduced bandwidth due to at-

tenuation of its gain frequency response above several hundred hertz (Fig. 1.9). Although under specific operation conditions this limit can be surpassed [82]. Transistors with constant g_m up to several tens of kHz are desired for transducing the full bandwidth of electrophysiological signals.

Overall, achieving a long-term, high spatiotemporal bandwidth and high-quality recording interface with neural tissue, remains a challenge in neurotechnology. Thanks to their suitability for flexible technology and their high biocompatibility, as well as electronic properties, graphene-based materials have high potential for neural interfaces [11, 67, 83–85].

1.5 Graphene field-effect solution-gated transistor

Here, the basic component of the recording technology presented in this dissertation, the graphene solution-gated field-effect transistor is described. Special emphasis is put to provide a thorough description of single-layer graphene highlighting its unique set of properties. A section is devoted to electrochemical properties of the graphene-electrolyte interface. Finally, the last part is dedicated to introduce the architecture of a graphene field-effect transistor and its operation principles.

1.5.1 Graphene

Graphene is a two-dimensional material formed by the arrangement of carbon atoms in an honeycomb pattern [86]. It is the basic structural element of other allotropes, including graphite, carbon nanotubes and fullerenes. Graphene can also be considered as an infinitely large aromatic molecule, the ultimate case of the family of flat polycyclic aromatic hydrocarbons [87].

Although few-layer structures of sp^2 -bonded carbon atoms were already known in the early 1960s [88], it was not until 2004 when scientists at Manchester University managed to isolate these layers and characterized them electrically that graphene potential was discovered [10]. The use of a new preparation method (mechanical exfoliation) allowed A. Geim and K. Novoselov to produce graphene layers that clearly showed semimetal behavior and remarkably high charge carrier mobilities. These experiments earned these two researchers the Nobel prize in Physics in 2010 [89].

Structurally, graphene carbon atoms form a triangular Bravais lattice with a two-atom basis (A and B) that has an atomic density of $3.9 \cdot 10^{15} \text{cm}^{-2}$ (Fig. 1.10A). Regarding the electronic structure, in the atomic ground state, the 6 electrons of the carbon atom are in the configuration $1s^2 2s^2 2p^2$. However, in the presence of other atoms, such as H, O, or other C atoms, it is favorable to excite one electron from the 2s to the third 2p orbital, in order to form covalent bonds. In the excited state, there are four quantum-mechanical states, $|2s\rangle$, $|2p_x\rangle$, $|2p_y\rangle$ and $|2p_z\rangle$. A quantum-mechanical superposition of the state $|2s\rangle$ with n $|2p_j\rangle$ states is called sp^n hybridisation, which plays an essential role in covalent carbon bonds. In the case of graphene, the carbon atoms are sp^2 -hybridized (Fig. 1.10A) resulting in three sp^2 orbitals used for bonding with neighbor carbon atoms (σ bonds) and one p orbital. The experimental carbon-carbon distance of 0.142 nm (equal for all atoms) can be explained as the average of the single C-C (0.135nm) and double C=C bonds (0.147nm) (Fig. 1.10B). This rather uncommon bond is one of the strongest bonds that occur in crystals making graphene both chemically

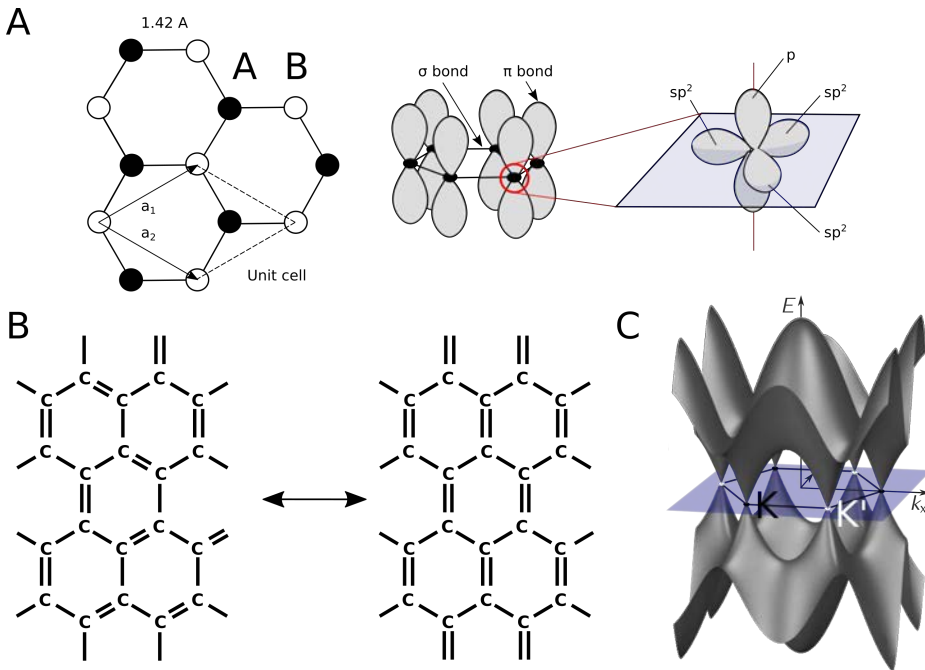


Figure 1.10: Graphene atomic and electronic band structure. A: Atomic structure of graphene showing the two-atom unit cell together with the orbital representation of the carbon atom. B: Resonant structure of graphene. C: Electronic band structure of graphene. Valence and conduction bands meet at the six vertices of the hexagonal Brillouin zone and form linearly dispersing Dirac cones. Adapted from Ponor <https://commons.wikimedia.org/w/index.php?curid=92511752>.

and mechanically stable [90, 91]. Furthermore, the thinness of graphene results in a low optical absorption of only 2.3% [92] in the visible range and together with the aforementioned mechanical stability its thinness confers graphene with flexibility which is very important for electrophysiological applications to surpass the long-lasting problem of poor match between recording devices and the curved and textured surfaces of the brain.

In graphene, only the electron in the p orbital, which is perpendicular to the graphene plane, contributes to electrical conductivity, since due to the overlap with the equivalent orbitals of neighboring atoms, a π orbital parallel to the graphene sheet is formed. Graphene uncommon electronic properties (ambipolar behavior, field-effect and high mobilities) emerge from its bandstructure [93]. Graphene band-structure can be calculated using a next-neighbor tight-binding approach. Valence and conduction bands meet at the six vertices of the hexagonal Brillouin zone and

form linearly dispersing Dirac cones that make graphene a zero-gap semiconductor (Fig. 1.10C). This allows direct shifting of the Fermi level between conduction and valence band, causing a change in the type of the majority charge carriers. In other words, graphene can act as a n or p-type semiconductor depending on the position of the Fermi Level with respect to the Dirac Point (see Fig. 1.11B-C). Moreover, the shape of the bandstructure at the Dirac points is linear (Fig. 1.10C), in contrast with the typical parabolic shape observed in semiconductors. This causes the suppression of many scattering mechanisms resulting in high carrier mobilities [94]. Lastly, it is important to mention that all the graphene used in this dissertation is grown by chemical vapor deposition (CVD) method [95] which provides large-area, high-quality graphene. See Appendix C.1 for a description of graphene production methods. In the remaining of this dissertation the term graphene is adopted referring to a single-layer of CVD grown graphene.

1.5.2 Graphene-electrolyte interface

Electrochemical studies have shown that graphene behaves nearly as an ideal polarizable electrode [83, 96]; i.e. in an electrolyte without any redox species that could react within its electrochemical window, no charge is transferred across the interface [97]. Instead, ions accumulate at the surface of graphene when a potential is applied between a reference electrode and graphene. The graphene-electrolyte interface can be modelled as a series combination of two capacitors. One component is the electrical double-layer capacitance. In addition to EDLC, the quantum capacitance must also be considered to fully model the graphene-electrolyte interface. Due to Pauli exclusion principle, electrons cannot occupy any energy state but only those permitted. This causes that added charge on the material must occupy a higher energy state. For metals or high-density of states systems, the required energy is very low and this justifies neglecting the effect. However, for the appropriate description of the graphene/electrolyte interface the quantum capacitance has to be considered. In the case of graphene, the quantum capacitance is small near the charge neutrality point where the density of states is low [98]. Therefore, at low charge carrier densities, the quantum capacitance becomes lower than the EDLC and thus prevails in the interfacial capacitance.

Graphene-electrolyte interface can be characterized by impedance spectroscopy. Importantly, the frequency response of the graphene/electrolyte interface has to be described considering a distribution of resistive and capacitive elements along the graphene surface related to the graphene sheet resistance and the interfacial capacitance [99]. The effect of the relatively high sheet resistance of single layer graphene must be considered for large-area devices ($> mm^2$) where the impact of sheet resistance is more important, whereas for microdevices this effect is not as

significant since the capacitance dominates the impedance over a wide frequency bandwidth. The voltage dependency of the interfacial capacitance can be obtained from fitting impedance data measured at different voltages against a reference electrode. Experimental results show an interfacial capacitance between $1\text{-}2\ \mu\text{F}/\text{cm}^2$ that is modulated by the voltage applied [99].

The wide electrochemical window in water and slow heterogeneous electron transfer (HET) kinetics of monolayer graphene enable its use for voltage sensing in aqueous environment [100, 101]. Recent evidence points to the primary contribution of edge defects in the charge transfer kinetics [102]. Also, large-area graphene has been demonstrated to be biocompatible [85].

Summarizing, graphene ensemble of properties, more typically found in different materials than in a single one, is the reason why so many scientists have envisioned a large number of potential applications and started carrying graphene research. Specially, the described properties pointed us towards the application of graphene in the bioelectronics field.

1.5.3 gSGFET working principle

Here, the working principles of a solution-gated graphene field-effect transistor for electrical field potential recording are described. The first solution-gated field-effect transistor (SGFET) was developed by Bergveld in 1970 based on a silicon metal-oxide-semiconductor field-effect transistor (MOSFET) [103]. As commented in 1.4.2, the main difference between the working principle of a MOSFET and the working principle of a SGFET is the way in which the current is modulated by the gate electrode. In a SGFET, the gate voltage is applied by a reference electrode immersed in an electrolyte (see Fig. 1.9). The possibility of using graphene in a solution-gated transistor configuration in direct contact with an aqueous medium is due to the aforementioned special interface that is created between graphene and a polarizable electrolyte and its low leakage across the interface. In the remaining of this dissertation the term transistor is adopted referring to a solution-gated field-effect transistor used as a transducer of voltage signals.

A graphene solution-gated field-effect transistor is composed of a graphene sheet, the channel, connected by two metallic contacts, namely the drain and the source terminals, interfaced by an electrolyte in which a reference electrode is immersed to be used as the gate terminal. The current flowing through a graphene SGFET is extremely sensitive to any voltage change in the electrolyte near the interface. A method to characterize this coupling is by performing a transfer curve, sweeping the gate-source voltage (V_{gs}) with a fixed drain-source voltage (V_{ds}) while measuring the drain current (I_{ds}). The ambipolar modulation of the conductivity of

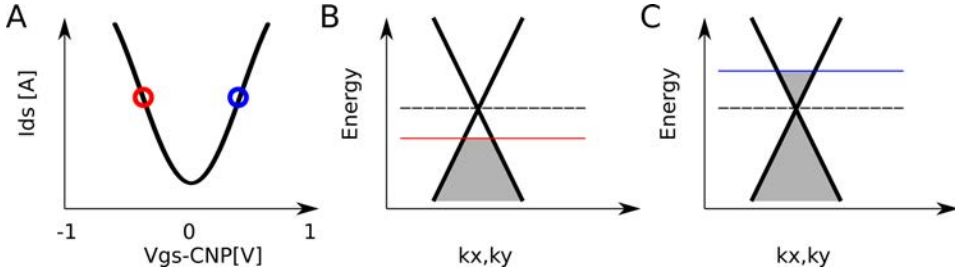


Figure 1.11: A: Graphene field-effect transistor transfer curve (I_{ds} vs V_{gs}). B-C: Simplified energy-momentum diagrams of the graphene bandstructure filling under different bias. The electronic transport is governed by holes or electrons when graphene channel is biased either above or below the charge neutrality point respectively.

the graphene sheet when sweeping the V_{gs} bias is a consequence of its bandstructure. Fig. 1.11 shows that by applying a voltage between the reference electrode and graphene, the Fermi level in graphene is shifted, consequently modulating the number of free carriers in graphene. The minimum of free carriers, and thus the minimum of conductivity, is reached at the gate bias potential at which the Fermi level reaches the Dirac point (energy point where the valence and the conduction band meet). That gate bias potential is called the charge neutrality point (CNP). Depending on the position of the Fermi level with respect to the CNP, the transport in the graphene channel will be dominated by holes or electrons.

Unlike standard field-effect technology, such as MOSFET technology, that uses a dielectric to create a capacitor, solution gating allows achieving higher capacitance, leading to a very strong coupling. Actually, the thickness of the electrical double layer capacitor is extremely thin so the electric field generated at the surface of the material is higher, allowing to tune the number of carriers with lower applied gate bias than with a standard dielectric capacitor [104]. The high chemical stability of graphene [105] allows the operation without a gate dielectric layer, increasing the gate capacitance and therefore the transistor transconductance [99]. In the case of graphene the double layer capacitance is often reported to be about $2 \mu\text{F}/\text{cm}^2$, which is one order of magnitude higher than for solution-gated transistors based on typical semiconductors [94]. Thus, mainly due the high interfacial capacitance and also due to a high charge carrier mobility, SGFET transconductance is higher than most other FETs [94]. Moreover, gSGFET frequency response is constant over a similar or even wider bandwidth than other microtransistors (Fig. 1.9).

Flexible graphene transistors under stress have been explored and experimental measures of the transistor transfer curves when the neural array is bent show that the transistor transfer curves of flexible solution-gated field-effect transis-

tor (SGFET)s are preserved [67]. Some studies have reported the use of graphene kirigami to achieve extremely flexible and stretchable SGFETs, showing that even with a strain of 240% no change in the transconductance can be observed [106]. This structure has never been reported in an array configuration for μ -ECoG recording. However, these results suggests that the graphene SGFET can be extremely folded to fit the shape of the brain gyri and sulci. This would help to have the device very close to the region of interest. Therefore, graphene mechanical properties helps to create a very intimate interface with the tissue. Optical transparency [92] of graphene is also very interesting for the study of neural networks and especially of cortical features where optogenetics and calcium imaging can provide complementary information [107]. Before graphene was tried for neural recording, only few materials such as indium tin oxide [108] or conductive polymers [109] offered the transparency required to combine optogenetics and electrical neural recordings. Making use of graphene transparency, graphene-based neural interfaces using an electrode configuration have already been reported, suggesting that graphene is a suitable material for neural recordings [65, 96]. Previous *in vivo* studies using single layer CVD graphene have used an electrode configuration; nonetheless, in this thesis the use of a transistor configuration is adopted. The main reason for this choice is certainly the local preamplification that is inherent to the transistors configuration [110] that reduces the sensitivity to external noise sources. Prior to graphene transistors, poly(3,4-ethylenedioxythiophene) polystyrene sulfonate (PEDOT:PSS) transistors already proved that this type of active devices can provide very good performance for μ -ECoG [80]. The higher electron mobility and high chemical stability of graphene motivates us to explore this new technology.

1.6 Summary

This background chapter has covered the several elements that form the recording chain of electrophysiological brain signals (Fig. 1.2). Electrophysiological signals are generated by a large number of contributors including synaptic currents, fast action potentials and their afterpotentials, calcium spikes, voltage-dependent intrinsic currents, glial oscillations and ephaptic coupling. Postsynaptic potentials of aggregates of neural populations that share synaptic afferents (specially pyramidal neurons due to its geometry) are considered the main contributor to extracellular field potential (EFP)s measured either at the dura or cortical surface. Moreover, the EFP is shaped by a multitude of factors such as the cellular-synaptic architectural organization of the neural network and their synchronization.

Methodological considerations for recording EFPs relative to the reference electrode and noise and artifact minimization have been discussed as well as considerations for assessing the quality of the recorded signal. The requirements for recording electrophysiological signals have been defined and both passive and active recording technologies have been described and their benefits and pitfalls in recording EFPs discussed. Moreover, it has been determined that both state-of-the-art electrode and transistor recording technologies have limitations to transduce the wide bandwidth of neural signals with high fidelity.

Graphene exhibits properties such as high carrier mobility [10], chemical stability [100, 101], and very good mechanical conformability [91]. Thanks to its unique set of properties, graphene is considered as a transducer with very high potential for the next generation of neural interfaces, particularly as a channel material of a solution-gated field-effect transistor (gSGFET). The following chapters of this PhD dissertation are devoted to gSGFET technology development and to explore the capabilities of gSGFETs neural arrays for providing high-fidelity *in vivo* field potential recordings with high spatial resolution and wide-bandwidth.

Chapter 2

Flexible graphene transistor arrays for neural recording interfaces

Requirements for a voltage probe that can be used in high-density arrays for mapping brain field potentials are very stringent. Voltage probes should be biocompatible, have constant transfer characteristics in a wide bandwidth, exhibit both low thermal and electrochemical noise and be stable over time. Graphene satisfies most of these material requirements. Graphene electronic properties such as field-effect and high charge mobility enable the use of this material as channel of field-effect transistors, a device which current can be modulated by external electric fields. Biocompatibility and chemical inertness properties permit establishing a direct interface of graphene with brain tissue. For these reasons, graphene solution-gated field-effect transistors (gSGFETs) have been suggested as a highly promising transducer for *in vivo* electrophysiological recordings.

In this Chapter, methods to produce and characterize flexible graphene microtransistor arrays are presented. High-quality single-layer graphene is grown by chemical-vapour deposition on copper and transferred to polymer-coated silicon wafers. Microelectronic technology is adapted to allow wafer-scale processing of this two-dimensional material and used to fabricate flexible microtransistor arrays. A 16-channel, common-source, 4x4 gSGFET array design suitable for rodent cortical recordings is presented. Fabrication yield, signal coupling and noise performance are extracted from the electrical characterization of the fabricated devices. A thorough evaluation of the dependence of gSGFET transfer characteristics on pH and ion strength of the electrolyte solution is also performed.

Since extracellular field potentials are signals with amplitudes generally in the range of few hundred μV , a suitable recording device should offer an intrinsic noise level significantly below this value to achieve a high signal-to-noise ratio. In this Chapter, how the intrinsic noise of gSGFETs can be affected by the transistor

geometrical design, graphene combination with the substrate or insulation materials, and the mode it is electrically biased, will be discussed providing design, fabrication and operation guidelines. Finally, descriptive statistics of a set of electrical gSGFET performance indicators are reported to illustrate current state of the developed technology.

Part of the contents of this chapter have been published in:

- C. Hébert, E. Masvidal-Codina, A. Suarez-Perez, A. B. Calia, G. Piret, R. Garcia-Cortadella, X. Illa, E. D. C. Garcia, J. M. D. l. C. Sanchez, D. V. Casals, E. Prats-Alfonso, J. Bousquet, P. Godignon, B. Yvert, R. Villa, M. V. Sanchez-Vives, A. Guimerà-Brunet and J. A. Garrido. Flexible Graphene Solution-Gated Field-Effect Transistors: Efficient Transducers for Micro-Electrocorticography. *Advanced Functional Materials*, 28(12):1703976, 2018. ISSN 1616-3028. doi:10.1002/adfm.201703976.
- E. Masvidal-Codina, X. Illa, M. Dasilva, A. B. Calia, T. Dragojević, E. E. Vidal-Rosas, E. Prats-Alfonso, J. Martínez-Aguilar, J. M. D. l. Cruz, R. Garcia-Cortadella, P. Godignon, G. Rius, A. Camassa, E. D. Corro, J. Bousquet, C. Hébert, T. Durduran, R. Villa, M. V. Sanchez-Vives, J. A. Garrido and A. Guimerà-Brunet. High-resolution mapping of infraslow cortical brain activity enabled by graphene microtransistors. *Nature Materials*, 18(3):280–288, March 2019. ISSN 1476-4660. doi:10.1038/s41563-018-0249-4.

2.1 gSGFET electrical characteristics

A graphene solution-gated field-effect transistor is a three terminal device composed of a graphene sheet, the channel, connected by two metallic contacts, namely the drain and the source terminals. Most of the device is fully insulated, except the graphene channel which is in direct contact with an electrolyte where a reference electrode, generally a Ag/AgCl electrode, is immersed to be used as the gate terminal (see Fig. 2.1A). Under an applied drain-source voltage (V_{ds}), a current (I_{ds}) flows through the graphene channel which is modulated by the gate-source voltage (V_{gs}) due to the field-effect properties of graphene. Any potential fluctuation near the graphene channel, such those produced by electrogenic cells, alters the potential at the interface and modulates the I_{ds} current.

The transfer curve relates the current through the channel with the applied V_{gs} voltage and allows characterizing the current-voltage relation (I_{ds} - V_{gs}) of the transducer. Experimentally, the transfer curve of a gSGFET is obtained by sweeping the V_{gs} voltage for a fixed V_{ds} . Fig. 2.1B shows an example of an experimentally obtained gSGFET I-V curve. As mentioned in Section 1.5.3, graphene has an ambipolar transfer curve owing to its bandstructure. The voltage corresponding to the minimum of the transfer curve is defined as the CNP.

Two important figures of merit for voltage recording are the transconductance (g_m) and the input-referred noise (V_{gs}^{RMS}). From the transfer curve, the transconductance g_m (Fig.2.1B) can be obtained as its derivative with respect to the gate voltage (V_{gs}).

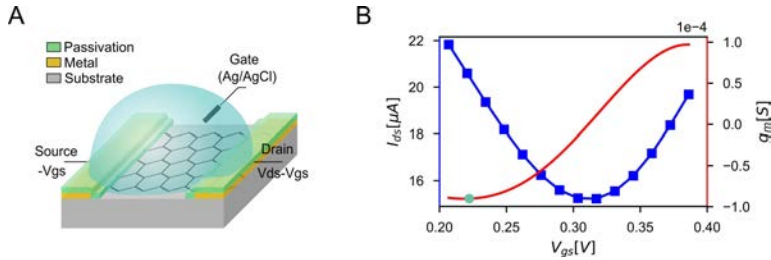


Figure 2.1: Steady-state characteristics of a graphene solution-gated transistor. A: Schematic of a graphene transistor polarized in common gate mode. B: Transfer curve (blue squares and line) and its first derivative (transconductance (g_m), black line) of a gSGFET. Green dot highlights an appropriate operation point.

In order to characterize the electrical intrinsic noise of a gSGFET, the fluctuations of the I_{ds} are measured over time at fixed V_{ds} and V_{gs} (Fig. 2.2A). The fluctuations are then analyzed in the frequency domain and the power spectral

density (PSD) of the current is calculated. Graphene SGFETs, as many other electronic devices, exhibit gate-voltage dependent $1/f$ noise (Fig. 2.2B). By integrating the PSD in a given bandwidth the I_{ds}^{RMS} value can be obtained. Repeating this at each V_{gs} polarization, the I_{ds}^{RMS} gate voltage dependence can be obtained (Fig. 2.2C). The effective rms voltage noise (V_{gs}^{RMS}) can then be calculated for each gate voltage, by dividing the I_{ds}^{RMS} by the transconductance. V_{gs}^{RMS} generally shows a minimum near (± 0.1 V) from the CNP (Fig. 2.2C).

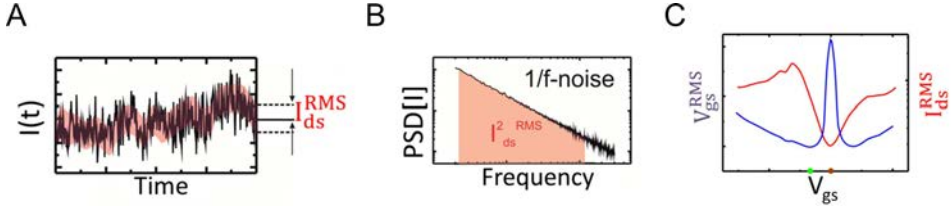


Figure 2.2: Intrinsic noise of gSGFETs. A: Time series of gSGFET current fluctuations. B: Power spectrum density (PSD) of the current fluctuations. Integral of the shaded area yields the root mean square (RMS) current noise. C: RMS current noise (I_{ds}^{RMS} , red) and equivalent RMS gate noise (V_{gs}^{RMS} , blue) for different V_{gs} voltages. Brown and green dots represent the position of the CNP and the optimal biasing point respectively.

gSGFET steady-state current

In this section, theoretical aspects of the electrical characteristics of gSGFETs are discussed. The drain-source current at any position in the channel is determined by the product of the carrier concentration ($n(x)$) and drift velocity ($v(x)$) scaled by the elementary charge (q), and width (W):

$$I_{ds} = -qWn(x)v(x) \quad (2.1)$$

Generally, the voltage used to operate gSGFETs in electrophysiological applications is low in comparison to the velocity saturation voltage; hence, carrier drift velocity can be defined as

$$v(x) = \mu \left(-\frac{\partial V}{\partial x} \right) \quad (2.2)$$

where μ is the carrier mobility. Inserting, Eq. 2.2 into Eq.2.1 yields

$$I_{ds} = q \frac{W}{L} \mu \int_{V(x=0)}^{V(x=L)} n[V(x)] dV \quad (2.3)$$

where $n[V(x)]$, the charge carrier density at a particular location along the channel, can be expressed as [111]:

$$n[V(x)] \approx \sqrt{n_o^2 + [C_{int}(V(x))[V_{gs} - V(x) - Ud_0]/q]^2} \quad (2.4)$$

where n_o is the minimum carrier concentration [112], which is related to substrate impurities and charge traps as well as thermal carrier excitation; while the other term in the summation is the gate-induced charge density that depends on both the gate-source voltage applied (V_{gs}) with respect to the intrinsic CNP (Ud_0) and the interfacial capacitance (C_{int}). Having a detailed model of C_{int} is of utmost importance for understanding gSGFET as voltage probes. As presented in the previous chapter, graphene-electrolyte interfacial capacitance has a V-shape with values around $0.5\text{-}2 \mu\text{F}/\text{cm}^2$ [99]. Graphene-electrolyte interfacial capacitance (C_{int} , see Fig. 2.3) can be modelled as the series combination of an electric double layer (C_{dl}) and graphene quantum capacitance (C_q). C_{dl} is typically modelled as a parallel plate capacitance with no voltage dependence while C_q depends on the applied voltage. More details of the graphene-electrolyte interface model are provided at Appendix A.1.

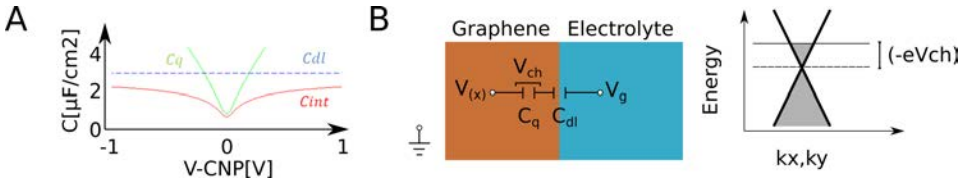


Figure 2.3: Graphene-electrolyte interface model. A: Simulations of the interfacial capacitance resulting from the series combination of the double layer (C_{dl}) and quantum capacitance ($C_q(V_{ch})$), see equations A.2 and A.1. B: Equivalent circuit of the graphene-electrolyte interface and graphene energy dispersion showing the effect of V_{ch} . Since the value of C_q depends on the voltage that falls across it (V_{ch}) the system has to be solved self-consistently.

Using the presented interface model, the total current is obtained by integrating the carrier density along the graphene channel [111]:

$$I_{ds} = q \frac{W}{L} \mu \int_{V_{ds} - I_{ds} R_S}^{I_{ds} R_S} n(V) dV \quad (2.5)$$

In an ideal case the whole V_{ds} applied should drop in the channel; however, in real transistors, the effect of extrinsic resistances (R_S) in series with the channel has to be taken into account (see Fig. 2.5A).

The previously explained physical current-voltage model [111] was implemented in MATLAB (see Appendix A.2 for implementation details and simulation parameters used, code is freely accessible at [113]). Fig. 2.4A shows simulated I_{ds} current vs V_{gs} for a set of V_{ds} values. As seen, the V_{gs} voltage modulates the channel resistance (2.4B) while V_{ds} is a scale factor, although not linear. The CNP shifts linearly with V_{ds} (see 2.4B,C).

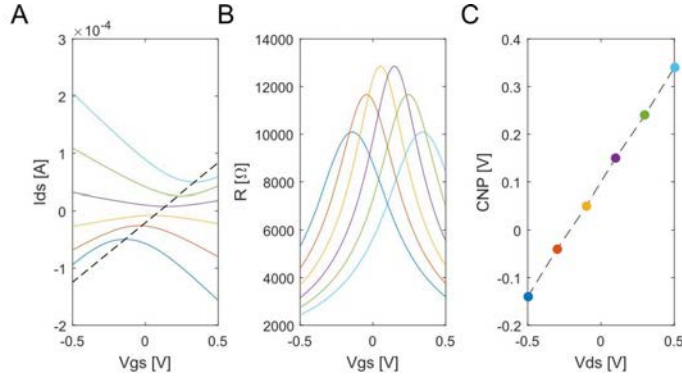


Figure 2.4: Bias dependence of steady-state gSGFET current. A-B: gSGFET Current (A) and resistance (B) versus gate voltage (V_{gs}) for different drain voltages (V_{ds}). Line colors correspond to V_{ds} values in C. A: V_{ds} controls the direction of the current as also its magnitude while V_{gs} modulates the current. Dashed line shows the displacement of the minimum current. B: Channel resistance dependence on V_{ds} . The applied V_{ds} has an effect more complex than just a linear scaling factor which will result in the same resistance for all V_{ds} applied. C: Scatter plot of charge-neutrality point versus drain voltage. CNP displaces as $V_{ds}/2$. From that linear dependence (dashed line), the intrinsic CNP when $V_{ds}=0$, also termed Ud_0 , can be interpolated.

Noise

Several contributions to the intrinsic noise of gSGFETs [114] can be distinguished. Fluctuations in the electrical current, $I_{ds} \propto qN\mu$, can be written as $\partial I_{ds} \propto q(\partial N)\mu + qN(\partial\mu)$, where q is the charge of an electron, N is the number of charge carriers and μ is the mobility. Correspondingly, the mobility-fluctuation and carrier-number-fluctuation mechanisms are generally discussed in noise theory. In graphene, lattice defects generate mobility fluctuations which ultimately cause resistance variations. In addition, charge trap states in the graphene channel or in the surrounding materials such as the substrate or encapsulation layers can cause fluctuations in the number of charge carriers. Due to the 2-dimensional nature of graphene, the contribution of charge-number fluctuation mechanisms is expected to be dominant, as shown for certain transistor configurations [115].

As seen, graphene SGFETs exhibit gate-voltage dependent $1/f$ noise (Fig.2.2B,C). The $1/f$ noise can be described with Equation 2.6 where a , b and c are the fitting parameters. a is a noise offset, b is the exponent of the $1/f$ spectra and c is a frequency-independent noise source.

$$S_I = a/f^b + c \quad (2.6)$$

Frequency response

Another important characteristics of gSGFETs for signal recording is the frequency response of the transconductance. MOSFETs have a g_m frequency response that is frequency-independent over the electrophysiological bandwidth. Also, solid-state graphene FETs have shown a non-attenuated g_m frequency response up to the gigahertz range due to its high mobility [116]. The gSGFET g_m frequency response will be investigated in this chapter.

2.2 Considerations for designing gSGFET arrays

Designing high-performance gSGFETs for neural recording requires considering both geometrical and process-dependent effects on its electrical characteristics such as drain current, transconductance, noise and frequency response. Important geometrical parameters are the width-to-length ratio (W/L), the metal-graphene overlap at the contact (L_{cov}) and the distance between passivation edge and metal (L_{pass}). L_{cov} and L_{pass} affect the contact and access resistance terms and contribute to the total resistance in series with the channel (R_S) (see Fig. 2.5A). Regarding the electrical parameters, the most important ones are the charge carrier mobility (μ) and the total charge carrier density (n), which can be estimated from experimentally obtained transfer curves, see Section 2.5.4. To get an insight about the effects of all those parameters, the previously mentioned physical current-voltage model [113, 111] was implemented in MATLAB (see Appendix A.2). Fig. 2.5B illustrates the effect of different physical parameters such as the charge neutrality point (CNP), carrier mobility(μ), contact resistance (R_c) and minimum charge carrier concentration (n_o) on graphene steady-state transfer curve and transconductance. Coloured areas represent the effect of varying a single parameter (μ , R_c , n_o) between values higher and lower than that represented by the solid line. In the following the effect of each of those parameters will be discussed.

The dotted line in Figure 2.5B represents the I-V curve of a transistor with a CNP more positive than that of the transistor represented by the solid line. The exact value of the CNP is related to the doping of the graphene sheet, the electrochemical potential of the reference electrode and properties of the electrolyte solution where it is immersed such as the pH or ionic strength(these effects are studied in Section 2.6). Graphene doping can arise from post processing residues [117], as well as from charge traps in the substrate or from foreign atoms in the graphene lattice; it's nature is p or n if results in a shift of the CNP towards higher or lower V_{gs} values. Importantly, a change of CNP causes a lateral shift of the curve without altering its shape, which is not the case for the other parameters.

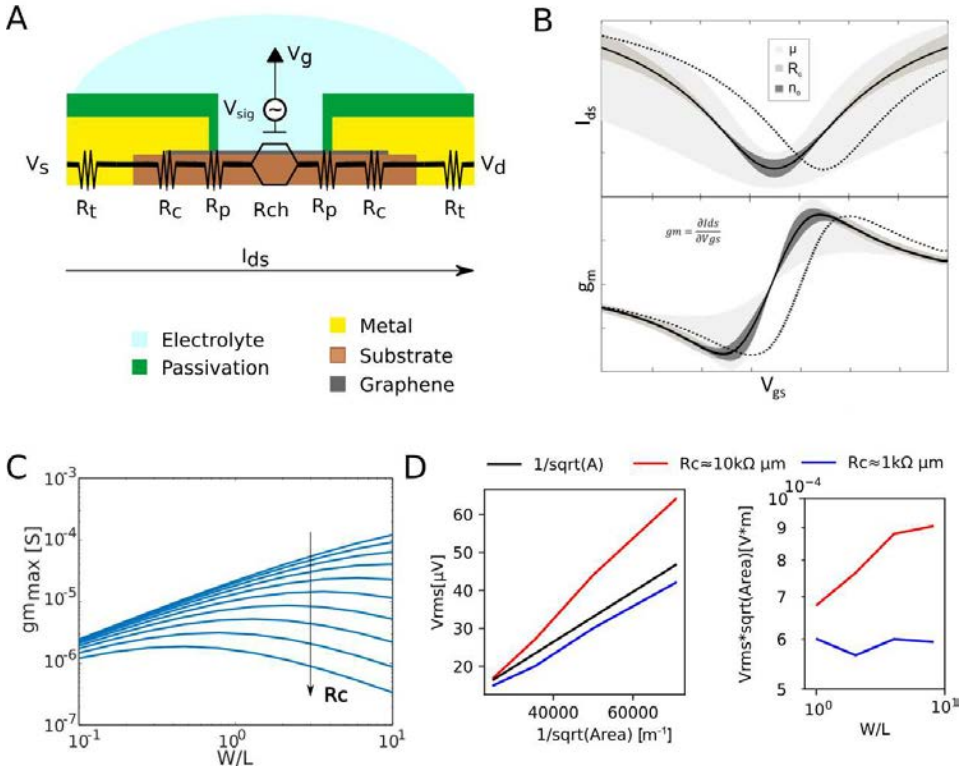


Figure 2.5: Effect of design or process dependent parameters on gSGFET recording performance. A: Schematic of a gSGFET cross-section showing the different materials and electrical schematic showing the biasing points (V_g , V_s , V_d) and the different resistances that determine the measured current (I_{ds}). R_t , R_c , R_p and R_{ch} correspond to track, contact, access and channel resistance respectively. B: Effect of mobility (μ), contact resistance (R_c) and minimum carrier concentration (n_o) on drain-source current (I_{ds}) and transconductance (g_m) for different gate bias (V_{gs}). Dashed line indicates the shift induced by a change in the charge neutrality point (CNP). C: Maximum transconductance versus W/L ratio for different contact resistances. As R_c increases, g_m deviates from the ideal linear dependence with W/L and the W/L that maximizes g_m shifts towards lower values. Simulations performed using a current-voltage model (see A.2, [113]). D: V_{rms} dependence on geometrical parameters for two different contact technologies. Left: V_{rms} noise versus one over the square root of area. Low contact resistance (blue line) shows proportionality to $1/\sqrt{A}$ as indicated by the black line. Instead, a larger contact resistance results in a deviation from this dependence. Right: V_{rms} noise normalized by the square root of the channel area for different width-to-length ratios. For low contact resistance, V_{rms} is independent of the W/L whereas for high contact resistance, increasing W/L is detrimental. Data from [118].

Charge carrier mobility (μ) affects the overall shape of the transfer curve and

has a strong impact on the maximum values of the transconductance. Therefore, the carrier mobility of graphene plays an important role in the performance of graphene SGFETs. Charge carrier mobility depends on graphene quality, thus different graphene production methods yield different mobility ranges. Due to the 2-d nature of graphene, its mobility is also highly dependent on its surroundings such as the substrate where it is attached. A more in depth discussion of how the mobility depends on growth method and substrate is presented in Appendix C.1 and Section 2.4 respectively.

Both n_o and R_c also affect the shape of the transfer curve. n_o has its main effect close to CNP while contact resistance affects the transfer curve away from the CNP. Both parameters affect the range of linear operation and the maximum transconductance ($|g_{m,max}|$). Since a high transconductance is generally desirable for sensing applications to allow for best signal transduction, the influence of the contact resistance has to be considered when designing sensor channel geometry, and charge impurities should be minimized. Importantly, when using a shared biasing of all transistors in the array, having a wider range of high transconductance is beneficial to allow optimal operation of all transistors.

While the minimum carrier concentration (n_o) is difficult to control, the effect of different resistances in series with the graphene channel are highly affected by design and fabrication procedures. Contributors to R_S are the resistance of the metal tracks (R_t), the graphene-metal contact resistance (R_c), and the resistance of non-gated graphene channel section due to excess passivation to avoid metal contact with the tissue (R_p) (see Fig. 2.5A). The resistance of metal tracks commonly used in microelectrodes (few μm wide and hundred of nm thick) results in few hundred Ω . This resistance magnitude is negligible in comparison with the electrode impedance and therefore is not an important design parameter for electrodes. Instead, track resistance can have a significant role for gSGFET performance. Therefore, it is important to minimize its value to less than $\approx 100\Omega$ for squared gSGFETs, for example by designing wider tracks if possible or by increasing the metal thickness. For high-density arrays or narrow probes, multiple layers of metal can be an option to decrease track resistance.

The access resistance (R_p) is the resistance of the graphene area that is covered by the insulation and is determined by the design parameter (L_{pass}), the distance between passivation edge and metal (see Figs. 2.5A and 2.6 D). This so-called access region is required to avoid contact of the metal with the electrolyte or brain tissue in which the array will be immersed, which could produce undesired electrochemical reactions. Electrically, access resistance has a similar effect than the track resistance, since it is in series with the channel resistance and therefore has to be minimized. The exact value of the design parameter (L_{pass}), has to be adapted in each case since it is constrained by the fabrication technique used which sets the

minimum tolerance.

Regarding the graphene-metal contact resistance (R_C), poor metal contact interfaces are one of the main limitations preventing unhampered access to the full potential of two-dimensional materials in electronics [119]. The formation of an ohmic contact, crucial for most electronic devices, can be nontrivial on a 2D material. High contact resistance R_C between the metal contact and underlying graphene can limit device performance [119] as also dope graphene, the type of doping being either p or n, depending on the metal used [120]. High contact resistance, resulting from the work function mismatch between graphene and metals as well as from the low density of states of graphene, has a negative impact on the performance of graphene FETs, resulting in a poor charge transfer and thus in a low conductance of graphene FETs [119, 121, 122]. The detrimental effect of contact resistance in transconductance is illustrated in Fig. 2.5C. While ideally the peak amplification transconductance ($|g_{m,max}|$) is directly proportional to the width-to-length (W/L) ratio, in reality, this relation is non-linear, with higher attenuation for larger R_C values.

L_{cov} , the distance of metal-graphene overlap, is an important design parameter for establishing a low-noise and low-resistance contact (see Figs. 2.5A and 2.6 D). For pristine graphene, the charge transfer to the metal is generally low due to graphene inertness and most charge transfer occurs at the graphene edges where the carbon atoms are not sp^2 -hybridized. Approaches to reduce contact resistance have been explored, showing that minimizing graphene metal overlap is beneficial to reduce the electrical path from the channel to the graphene edge where most of the charge transfer to the metal is produced, this is called edge contact technology. Edge contact technology is not trivial to implement at wafer scale and can suffer from low reproducibility, in particular for devices aimed at flexible electronics. Another approach is to create defects to the graphene lattice at the contact site to improve charge transfer [118]. Defect creation methods are easy to adapt to wafer scale production and can create defects with high homogeneity. Therefore, the value of L_{cov} has to be defined based on the graphene properties at the metal contact in accordance with (if any) the graphene treatment implemented at the contact areas. Further details of strategies to reduce R_C are described in Section 2.4 .

Noise aspects should also be considered when designing gSGFETs. In an ideal gSGFET, V_{gs}^{RMS} is assumed to decrease with the square root of the area (see Appendix B for a theoretical derivation). In non-ideal cases, the total normalized noise S_I/I_{ds}^2 generated in a gSGFET includes the contribution from the contacts (S_{R_c}) and from the channel ($S_{R_{ch}}$). The relative contribution of each term can be identified by evaluating the dependence of noise on L [118]. From a geometrical design perspective, the channel area is therefore the main parameter affecting the

performance of a gSGFET and should be adapted to each application. For example, high SNR for LFP recordings is obtained for a wide range of transducer sizes from tens of μm up to a few hundred μm [123]. Therefore, designs of several tens of μm are preferred in the case of gSGFETs to reduce the noise and increase SNR. However, if action potential recording is desired, lower transistor sizes similar to a neuron soma (few μm of side) will be required. Another aspect to take into account is that the V_{rms} noise is affected by the aspect ratio of the transistor for non-negligible contact resistances due to the aforementioned transconductance attenuation (Fig. 2.5C-D).

Regarding geometric aspects of the frequency response, the W/L ratio is just an scale factor, while the g_m magnitude is not affected by the graphene total area in the micrometer range [124]. However, for large area transistors, it has to be taken into account that there is a threshold frequency above which capacitive leakage current becomes significant, causing the channel to exhibit a non-resistive frequency response [99]. For microtransistors, fabrication residues can significantly attenuate the frequency response [125], and is therefore important to have a clean interface to avoid high-frequency attenuation of signals. Another important parameter to take into account for an adequate frequency response is the thickness of the passivation layer since it determines the parasitic capacitive coupling.

Summarizing, channel area is the main geometrical design parameter driving gSGFET performance due to V_{gs}^{RMS} decrease with the square root of the area [124]. Therefore, for a given application, the amplitude of the minimum desired signal to be detected determines the minimal channel area. Channel areas above $400 \mu m^2$ are needed with the current technology to allow measurement of LFPs with adequate signal-to-noise ratios. Other important design aspects are metal track resistance, the metal-contact overlap depending on contact technology, minimization of access region, and parasitic couplings. All those aspects should be considered to achieve a high performance gSGFET.

2.3 Array design

The gSGFET arrays used in this thesis were designed using CleWin (WieWeb software, The Netherlands). The design involves defining four different masks for each of the following levels: structure, metal, graphene and passivation. Figure 2.6A shows a schematic of the gFET array tip with the different layers. All the devices used in this thesis consist of 16 graphene transistors arranged in a 4x4 squared array of $400\mu\text{m}$ pitch (see layout in Fig. 2.6 B). The probe tip dimensions ($2\times 2\text{mm}^2$) are designed for either mouse or rat cortical recordings, covering a fraction of an hemisphere. Holes in the flexible substrate are included to improve adhesion to brain tissue.

Regarding connections, a common source terminal is introduced to reduce the required number of metal tracks/contacts from 16×2 to $16+1$. Large contact pads are designed to ease connection to a zero insertion force (ZIF) of 20 pins (see Fig. 2.6 C). Apart from the 16 drain contacts (which are located in the middle), there are 4 free contacts (two at each side). A single source track that goes from the two contacts in one side to the other two in the opposite side through the edges of the tip was designed. This design improves the robustness of the probe since the common source terminal, which if broken will not allow to operate the array, is not single fault sensitive, but can be contacted by different points, providing fault tolerance.

As discussed previously, any resistance between the contact pad and the graphene channel results in a smaller voltage gradient at the channel. Therefore, it is important to take into account the resistance of the metal tracks in comparison with the graphene channel resistance when designing gSGFET arrays. Due to the use of a single common source terminal, source track resistance can introduce crosstalk between channels as a local signal in a given channel can lead to voltage fluctuations of the biasing point of the other transistors in the array. Therefore, in order to minimize crosstalk between channels, since more current will flow through the common source, a common source with a wider track ($50\mu\text{m}$) than drain tracks ($35\mu\text{m}$), targeting a track resistance below 100Ω was designed. A narrow tail was designed to provide flexibility to the neural probe and facilitates probe placement. Neural probes with two different tail lengths (T_{length}) were fabricated (see Table 2.1 for details), for acute and chronic applications.

Regarding the design of the graphene transistor, parameters such as its area, W/L ratio, L_{cov} and L_{pas} have to be defined. In the previous section, a general discussion about design guidelines has been presented. Here, a brief rationale of the chosen values is provided. Experimental and computational results show that for recording LFPs, signal-to-noise ratio is high for a wide range of transducer

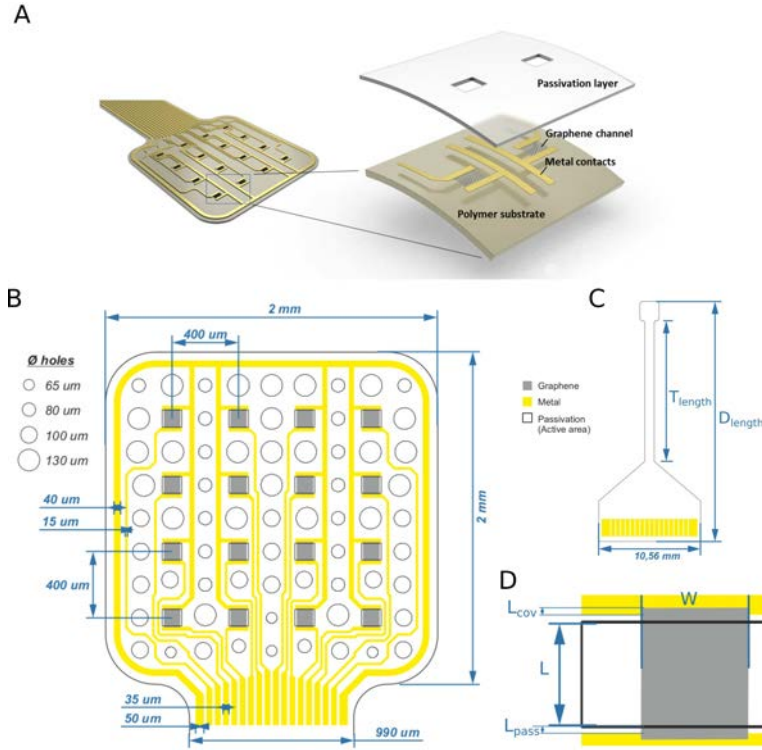


Figure 2.6: gSGFET array design. A: Schematic of the graphene SGFET array with an explosive view showing the different components [126]. B-D: Layout of a 4x4 gFET arrays at different zooms. B: Tip layout showing its dimensions ($2 \times 2 \text{ mm}^2$), intergFET distance of $400 \mu\text{m}$, tail width of 0.99 mm and track widths of $35 \mu\text{m}$ and $50 \mu\text{m}$ for drain terminals and common source terminal respectively. Also holes in the flexible substrate are included in the design for enhanced adhesion to the brain tissue. C: Probe layout indicating its tail length (T_{length}), the device length (D_{length}) and the width of the connector side. D: gSGFET layout showing its width (W), length (L), and metal-graphene overlap (L_{cov}) and passivation-graphene overlap (L_{pass}).

sizes from few μm up to a few hundred μm [123]. A square shape was chosen as an appropriate trade-off between maximizing gain and minimizing intrinsic noise (see Section 2.2). Designed transistors are in the range of $50\text{-}150 \mu\text{m}$ side, values slightly larger than optimal electrode sizes for LFP ($20\text{-}30 \mu\text{m}$ diameter). This larger area was decided in order to reduce the intrinsic noise of the devices, since gSGFET intrinsic noise depends on the inverse of the square-root of the area [124]. See Table 2.1 for details of the different sizes used. Regarding passivation overlap of the graphene channel (L_{pas}), with the photolithographic technique used (UV-photolithography) an access region of at least $1 \mu\text{m}$ of length is needed to ensure

Mask Set	D_{length} [mm]	T_{length} [mm]	L_{pass} [μm]	L_{cov} [μm]	W [μm]	L [μm]	n
CNM946	25	15	3	4	100	100	9
					150	100	4
					150	150	4
CNM985	18	7.5	5	5	50	50	9
					100	100	9

Table 2.1: Design details of the two different mask sets used. D_{length} : Device length, T_{length} : Tail length, L_{pass} : distance between metal and start of the channel, L_{cov} : metal-graphene overlap distance, W,L:width and length of the graphene channel respectively and n: number of arrays of each type per wafer.

metal from contacts is not exposed due to misalignments. Therefore values slightly larger to ensure a proper insulation of the metal contacts were chosen. Details of the two different L_{pass} used are provided in Table 2.1. Regarding graphene-metal overlapping, optimum values of L_{cov} are generally on the range of few μm [118]. Values in this range were chosen (see Table 2.1).

Overall, the presented arrays are designed for surface brain potential recordings. Due to the high number of variables influencing gSGFET performance, the exact design has to be adapted to a given application and fabrication procedure. For example, transistors with smaller areas may be better suited for intracortical applications, while transistors with larger areas may prove better for less-invasive skull recordings.

2.4 Microfabrication considerations

Various technology procedures have been reported for the fabrication of flexible transistors, the majority of which use fabrication techniques developed for semiconductor processing. Although these techniques are mature technologies providing high yield, their use for graphene processing is relatively recent and generally requires some adaptation. Considerations regarding the production of two-dimensional material graphene and its characterization can be found at Appendix C. The microfabrication of flexible gSGFETs neural arrays consists of several steps: substrate deposition, graphene transfer and patterning, metal deposition and patterning of tracks and contacts, passivation deposition and opening of active areas, substrate patterning and finally, device release. Next, the different layers and steps in the microfabrication of flexible gFET arrays are introduced and discussed. Standard lithographic techniques to pattern graphene, together with considerations

when using different photoresists and formation of metal contacts with low contact resistance to graphene are described.

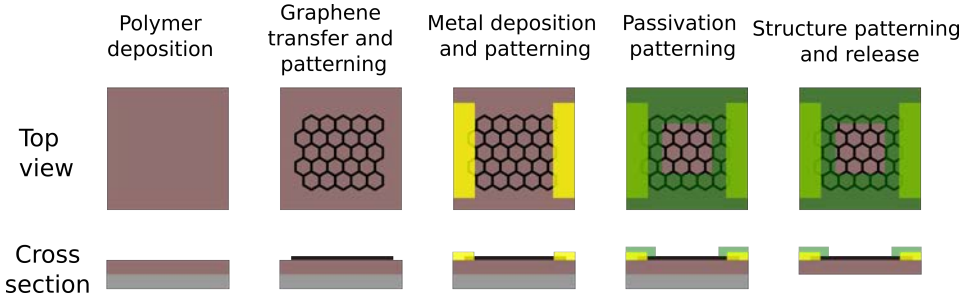


Figure 2.7: Microfabrication schematic of flexible gSGFET arrays. gSGFET microfabrication consists of substrate deposition, graphene transfer and patterning, metal deposition and patterning of tracks and contacts, passivation deposition and opening of active areas, substrate patterning and finally, device release.

Substrate

Since graphene is only one-atom-thick, the underlying substrate can significantly affect its electronic properties. For fabrication of electronic devices, graphene is typically transferred onto Si/SiO_2 substrates. Interaction with the substrate limits the practically obtainable electron mobility to around $15,000 \text{ cm}^2/\text{Vs}$ (compared to theoretical values of over $200,000 \text{ cm}^2/\text{Vs}$) due to surface roughness and oxide charge traps.

Electrophysiological applications add requirements to the substrate such as flexibility, conformability and biocompatibility [6] in addition to microfabrication processing compatibility. Polymer materials used in flexible neural probe fabrication include polyimide, poly(dimethylsiloxane)(PDMS), SU-8 and parylene-C [7, 6, 127–130]. In those cases, the first fabrication step consists in depositing the polymer on a silicon wafer. The polymer needs to be released at the end of the fabrication process, however not all polymers are easier to delaminate. In order to ease the release of the device, a thin sacrificial layer can be deposited previous to the deposition of the polymer [67]. That layer is then chemically etched at the end of the process.

The thickness of the surface arrays is of paramount importance to avoid excess pressure that can deform the cortex and ensure a conformable interface that brings the transducer closer to the signal sources. Thickness between $5\text{-}10\mu\text{m}$ of polyimide are considered optimal [131]. Another important aspect of the substrate is its

surface roughness. Polymer surface roughness is generally higher than for Si/SiO₂ which can potentially deteriorate graphene electronic properties. Reduction of flexible polymer roughness is therefore a potential line of research for improving performance of graphene flexible devices.

Graphene Transfer

Chemical vapor deposition (CVD)-grown graphene needs to be transferred from the growth substrate onto a polymer-covered wafer for further processing. The impact of the transfer process is being discussed in the literature and is considered one of the limiting factors affecting graphene technology [132]. The most common transfer method is by polymer-supported transfer, using polymers such as polymethyl methacrylate (PMMA). The polymer is needed since a large-area graphene layer that is not supported by any substrate (for example, floating in water) is almost invisible and easy to roll. So called “direct transfer” methods exist that do not require polymer and perform the transfer by pressure or temperature assisted transfer [133], or by direct deposition of the flexible substrate on top of the graphene/metal stack [134].

In the more common, polymer-assisted transfer, first, the polymer is spin coated and cured onto the graphene/metal substrate. Different techniques exist for detaching the graphene covered by the polymer from the grown substrate, the main being metal wet etching or electrochemical delamination techniques. In wet etching, the polymer/graphene/metal stack is then transferred to a metal etchant. For copper, this is commonly aqueous iron nitrate or aqueous iron chloride. The stack remains in the etchant until the metal has been completely removed. Alternatively, in electrochemical delamination, no etching is performed but water electrolysis induced H₂ bubbling detaches the graphene/polymer from copper [135]. After the metal has been completely removed or delaminated, the polymer-supported graphene floating in the solution can be cleaned and transferred to the target substrate. The target substrate may be pretreated with oxygen plasma to reduce the folds and wrinkles during transfer. Generally, a post-transfer annealing step is performed to dehydrate the layers and improve graphene planarization. Finally, the supporting polymer is dissolved, leaving the graphene on the new substrate.

Ideally, the transfer process should neither leave any residues or contaminants on the surface nor further introduce defects into the graphene sheet. However, residues from the supporting polymer are common, as the polymers are difficult to remove completely. The etchants used to remove the metal substrate can also leave contaminating particles. Moreover, while direct transfer methods are generally cleaner, they can mechanically damage the graphene layer. Therefore, all transfer methods have their advantages and limitations and the choice of the best transfer

method has to be done depending on the target substrate and application [136].

Lithography

To fabricate graphene devices, the capability of patterning the material efficiently and consistently is a necessity. In microelectronics, ultraviolet lithography is a common processing step towards patterning a given material. For example, lithography is part of the lift-off process to define the metal tracks, or is performed to define etching masks, such as the photoresist pattern that allows to structure the probe layout by rapid ion etching. Similarly, a pattern can be transferred onto graphene using standard lithographic methods [137]. However, since most lithographic methods rely on a polymeric resist to transfer the pattern, care needs to be taken during processing. For example, photoresist layers may not be completely removed during development and even small amounts of residue may adversely affect the performance of graphene devices. Removal of residues is therefore an important processing step for graphene devices. This can be done by annealing in vacuum or inert gas, or by chemical solvents.

Graphene patterning

Graphene is generally etched by oxygen plasma [126, 124]. This process has to be optimized to find the appropriate power since both incomplete etching and overetching have a dramatic effect on electronic device performance producing short-circuits or the absence of graphene channel respectively. Also, problems may arise due to graphitic and polymer residues from the transfer. High power may be required to eliminate both graphitic and polymer residues although care must be taken since high power can also etch the polymer substrate.

Metal contacts

Metal-graphene contacts have been reported to exhibit time-dependent resistance fluctuations [138], thus contributing to low-frequency noise. Therefore, achieving low contact resistance is of paramount importance in gSGFET microfabrication. One strategy to reduce contact resistance includes the use of metals which interact strongly with graphene [139, 140]. In this dissertation, Ni is used as top metal contact as it is one of the metals that forms strong chemical bonds with graphene through orbital hybridization [141, 142].

Another approach to decrease the resistivity of the contacts, is to transfer graphene onto a substrate where the metallic tracks have already been defined, so called ‘bottom contact’ and further process the stack to add another layer of

metal, forming a so called ‘sandwich-like contact’. Also, the creation of defects in the graphene lattice, for instance, by the introduction of dangling bonds, can enhance the graphene-metal interaction. Typical ways to create defects in graphene include, patterning the graphene sheet beneath the metal contacts, increasing the graphene edge length [143–145] and treating the contacted graphene with oxygen plasma [146].

Recently, ultraviolet ozone (UVO) contact treatment before deposition of the contacting metal, has been shown to significantly improve charge injection at the contacts by a combination of surface cleaning and defect creation and has demonstrated to reduce contact resistance [118]. Also, after UVO treatment, CNP and noise homogeneity is significantly enhanced [118].

Summarizing, contact resistance variability is a main contributor to device heterogeneity and a limiting factor for gSGFET recording performance. Strategies such as UVO contact treatment are therefore of paramount importance for achieving homogeneous and high-performance gSGFETs .

Passivation layer

Passivation of the structure is a crucial step to obtain a well-operating SGFET device. It defines graphene active areas and protects metal tracks from contacting with the electrolyte. Cracks and holes in the passivation layer can cause leakage currents and deteriorate transistor performance. Moreover, the thickness of the passivation layer is also a determinant factor as it defines the separation between electrolyte and metal tracks that form the two plates of a parasitic capacitance. SU-8 (MicroChem Corp.,USA) a permanent epoxy-based negative photoresist commonly used in biomedical applications [129, 147] is chosen as passivation layer due to its biocompatibility [148] and long-term chemical and thermal stability.

2.5 Methods

In this section, the fabrication details of flexible gSGFET arrays, its electrical characterization and the processing of the obtained data are described.

2.5.1 Fabrication details

The microfabrication of flexible graphene transistor arrays consists of several steps, as shown in Fig. 2.7. First, the CVD graphene growth and its transfer to a given substrate are described. Then, the fabrication details of flexible gSGFET arrays either in polyimide or parylene-C substrate are provided.

CVD Graphene growth

Graphene layers were grown by CVD using one of the following procedures: a) A lamp-heated rapid thermal CVD equipment from Jipelec and 25 μm thick, 99.8 % metal basis copper foil provided by AlfaAesar have been employed. Prior to graphene CVD growth, copper foils were sequentially cleaned in acetic acid and acetone, and finally rinsed in isopropyl alcohol. Sample dimensions were 6 x 5 cm^2 . Growth processing conditions consisted in 10 minutes at 750 $^\circ\text{C}$, 200 sccm H_2 plus 5 minutes at 800 $^\circ\text{C}$, 25 sccm CH_4 / 200 sccm H_2 . b) Chemical vapour deposition was on a 4.5x7 cm^2 copper foil (Alfa Aesar, annealed, Coated). Prior to the growth, the copper foil was electropolished during 5 min at a fixed current density of 62 mA/cm^2 in a solution containing H_2O (1 L) + H_3PO_4 (0.5 L) + ethanol (0.5 L) + isopropanol (0.1 L) and urea (10 g). Then, the copper foil was loaded in a planar quartz tube (1600x60 mm) and heated by a three zone oven. A first annealing step at 1015 $^\circ\text{C}$ under a 400 sccm argon flow at 100 mbar during 1 h was followed by a 15 min growth step at 12 mbar under a gas mixture of 1000 sccm Ar, 200 sccm H_2 and 2 sccm of CH_4 . The sample was then cooled down under a 400 sccm Ar flow by removing the quartz tube from the oven. For most samples, a complete Raman characterization was performed using a Witec spectrograph (Fig.2.8a-d). Raman maps of 30x30 μm^2 were registered with a spatial resolution lower than 1 μm^2 (using a 50x objective). A 488 nm excitation wavelength was used to minimize the copper substrate luminescence signal. The laser power was kept below 1.5 mW to avoid sample heating and a 600 gr/nm grating was used to provide a pixel to pixel spectral resolution below 3 cm^{-1} .

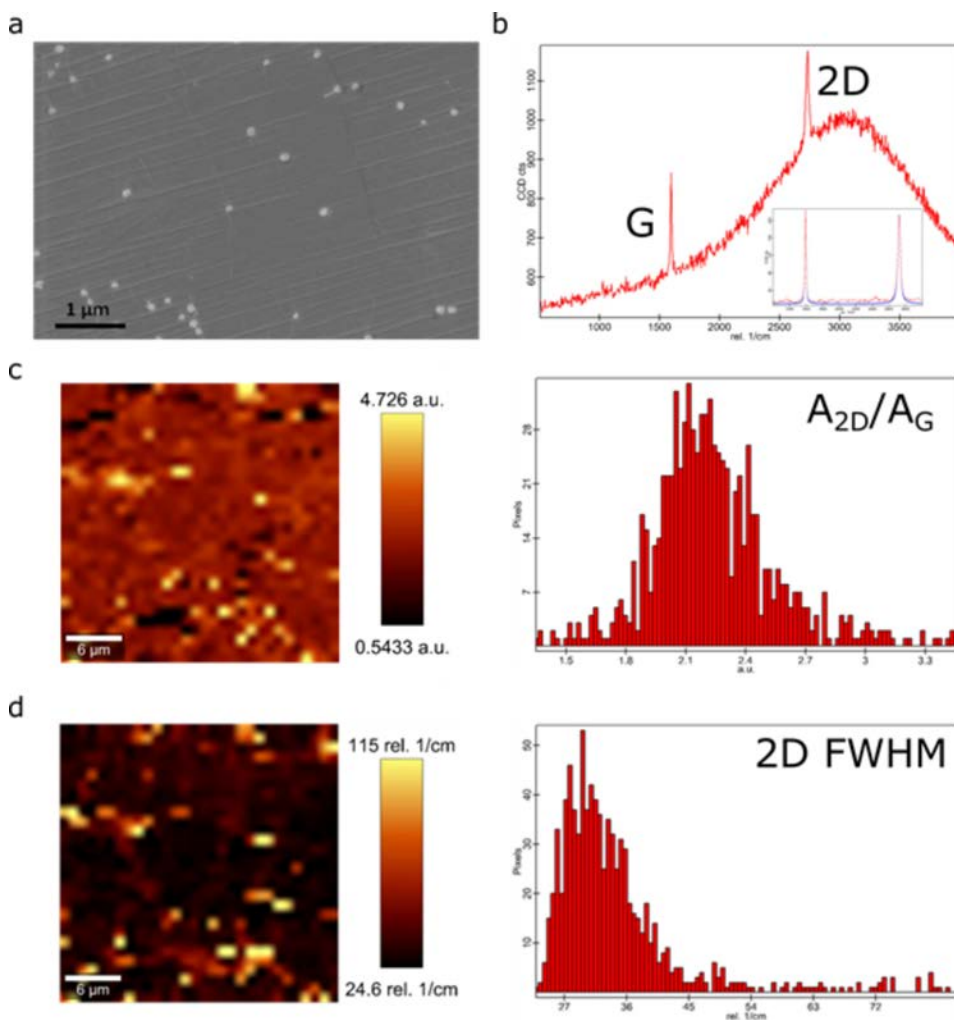


Figure 2.8: SEM and Raman characterization of CVD grown graphene. a, scanning electron microscopy (SEM) image of as-grown CVD graphene on copper foil. b, Raman spectrum of as grown graphene on copper. The absence of the D Raman peak, activated with disorder, indicates the good quality of the as grown samples. Inset shows a Raman spectrum after copper background subtraction where Lorentzian contribution of the G (1592 cm^{-1}) and 2D (2722 cm^{-1}) bands are shown in blue. c, Raman map of the 2D/G peak area intensity ratio and its corresponding histogram. 90% of the scan area presents an intensity ratio of 2.2 characteristic of monolayer graphene. d, Raman map of the 2D band width (full width at half maximum, FWHM) and the corresponding histogram. The average FWHM of the monolayer region is about 32 cm^{-1} . Regions of less than $2\text{ }\mu\text{m}^2$ that show larger 2D FWHM correspond to the thicker (multilayer) nucleation spots.

Graphene transfer

An electrochemical delamination method is used to transfer the graphene from the copper foil to the flexible substrate. First, PMMA 950k A7 (MicroChem Corp., USA) layer (≈ 500 nm) was spincoated at 3000 rpm on top of graphene in order to provide mechanical stability to the graphene layer. Subsequently, graphene with the PMMA layer is detached from the copper film by electrochemical delamination as described in [135] without the use of a frame. This consists in immersing the sample in a 0,25M NaOH solution together with a Pt electrode. When a potential of 5V is applied, bubbles are formed at the interface between graphene and copper due to water hydrolysis detaching graphene from copper. Then the sample is cleaned several times in water and transferred onto the polyimide wafer previously activated by oxygen plasma. The wafer is dried for 30 min at 40°C on a hot plate and then gradually up to 180°C annealed in a vacuum oven. Finally, the PMMA is dissolved in acetone and isopropanol.

gSGFET array fabrication on polyimide substrate

All wafers were fabricated at the clean-room facilities of the Institut de Microelectrònica de Barcelona (IMB-CNM, CSIC). Four-inch silicon wafers are used as a support to build the devices. First, a 10- μm -thick polyimide layer (PI-2611, HD Microsystems) is spin-coated to be used as substrate, soft baked to 120°C at ambient atmosphere and hard-baked during one hour at 350°C under nitrogen atmosphere to complete the imidation process. Graphene transistors are then fabricated in a sandwich-like structure. For that, a first layer of metal (Ti/Au, 10/100 nm) is deposited by electron-beam vapour deposition and defined in a standard lift-off process using the image reversal photoresist AZ5214E (Clariant GmbH, Germany). Graphene is then transferred as described in the Section 2.5.1. After removing the PMMA protection layer, a positive photoresist (HiPR6512) is used to protect graphene active areas. Graphene active areas are defined by means of an oxygen-based reactive ion etching. Photoresist is then removed by 20 min in acetone plus 10 min in isopropanol and 5 min in water. A second metal layer (Ni/Au, 20/200nm) is evaporated and defined in a similar standard lift-off process. In order to avoid damaging the graphene with the ultrasounds of the sonicator, the lift-off is achieved by leaving the wafer 1 h in acetone and by flushing acetone with a syringe. A layer of 1.5-2 μm of SU-8 (SU-8 2005, MicroChemCorp., USA) a permanent epoxy-based negative photoresist is used to passivate the metal leads while defining the graphene channel and metal contacts. The device is then hard baked up to 120°C. Finally, the polyimide substrate is structured in a deep-RIE process using the thick AZ9260 positive photoresist (Clariant GmbH, Germany) as an etching mask. Photoresist is removed by bathing the wafer in acetone for 30 seconds plus 5 minutes in iso-

propanol and 5 min in water. Finally, polyimide probes are carefully peeled off from the wafer.

gSGFET array fabrication on parylene-C substrate

A similar process is used to fabricate flexible graphene transistor array probes on a Parylene-C substrate. Parylene-C has a lower thermal budget than polyimide, a consequence of its thermoplastic nature. In atmosphere Parylene-C is subject to oxidation at temperatures greater than 100 °C, glass transition temperature around 90 °C and a melting temperature at 290 °C [149]. These temperatures are commonly encountered and even surpassed during standard silicon micromachining and electrical packaging which can cause Parylene C to burn, bubble, or crack. Therefore, Parylene C fabrication requires modification of the polyimide process at the following steps: annealing of graphene after transfer which is commonly performed up till 180°C is instead changed to a longer baking time at 100°C. Ultrasounds are avoided at all steps even at the first lif-off before graphene transfer to not damage the parylene layer. All annealing steps, such as the SU-8 hard-bake are reduced since by reducing baking temperature, parylene-C was found to be less attached to the silicon wafer and peeling the neural probes at the end of the process was easier.

2.5.2 Instrumentation for electrical characterization

There are no commercial instruments for characterizing multiple transistors simultaneously. For this aim, an electronic setup consisting of a data acquisition system (National Instruments USB-6353) and a custom electronics was developed (Fig.2.9). The custom electronic circuit used was designed by the GAB research group. A general problem of preamplifier design for active transducers for neural recording is that they require a large dynamic range that allows to measure both the transfer characteristics as also the current fluctuations induced by the neural signals. To solve this issue, signals are split into low-pass filtered (LPF) (frequency < 0.16Hz) and band-pass filtered (BPF) (0.16 Hz < frequency < 7 kHz) components with a lower (10^4) and higher (10^6) gain respectively. To perform the device characterization, the bias control and both LPF and BPF signals are managed by the data acquisition card. Also special effort was devoted to minimize the floor-noise of the system, which was measured to be well below gSGFET noise in all the neural signals bandwidth ($1 \cdot 10^{-23} A^2/Hz$). The total leakage current that flows through the reference electrode is measured with a high gain ($2 \cdot 10^6$) transimpedance amplifier. To connect the fabricated probes to the instrumentation, techniques like soldering or ZIF connectors exist. ZIFs connectors and custom printed circuit board (PCB)

allow flexibility for testing. Therefore, in this PhD dissertation, the flexible neural probes are connected to the electrical instrumentation via a 20-contact ZIF connector and a custom-designed PCB.

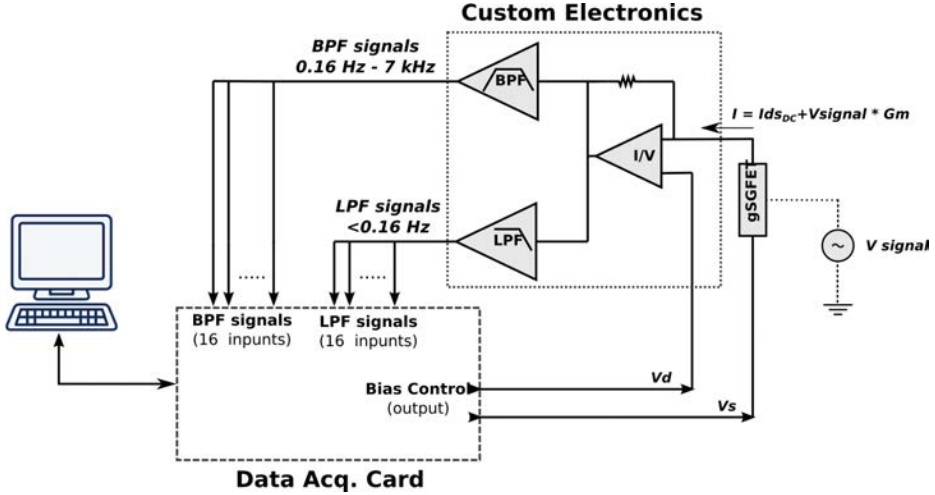


Figure 2.9: Instrumentation for electrical characterization of graphene transistor arrays. Schematic of the setup which consists of a DAQ card which allows programmable control of the polarization of the graphene solution-gated field-effect transistor (gSGFET)s (V_{gs} , V_{ds}) and acquires the current signals as output by the custom electronics. Prior to acquisition, current signals are filtered and amplified differently in two bands: LPF (<0.16 Hz, $gain=10^4$) and BPF (0.16 Hz-7 kHz, $gain=10^6$).

2.5.3 Electrical characterization details

Transfer curve characteristics of graphene transistors are performed in common gate mode with a fixed drain-source voltage (V_{ds} , generally 50 mV) varying the gate-source voltage (V_{gs} , generally between 0 and 400mV with 20mV steps) vs. a Ag/AgCl reference electrode in 10 mM phosphate buffer saline (PBS) solution. PBS is used as electrolyte due to the similar ionic concentrations than extracellular fluid [71] as well as its buffering capacity. Steady-state is ensured by acquiring only after time derivative of 1 s of current is below a given threshold (generally $5 \cdot 10^{-7}$ A/s), as determined online during the characterization. When this condition is met, the I_{ds} for each channel and the total leakage current that flows through the reference electrode is acquired and the next V_{gs} of the sweep is applied. Since the gSGFET arrays used in this dissertation have a shared drain terminal, the leakage current is the same for the whole array and corresponds to the sum of the

individual leakage currents of all transistors in the array.

Also in some cases, the intrinsic noise of the arrays was also measured. For that, once steady-state was achieved at each biasing step of the transfer curve, the fluctuations of the I_{ds} are acquired for a given amount of time depending on the minimum frequency desired.

The frequency response of the transconductance is measured by applying a sum of sinusoidal signals, with different frequencies within the frequency range of study, at the electrolyte solution through the reference electrode. The output acquired drain current signal is demodulated to obtain the transconductance for each evaluated frequency. The acquired signals were splitted into two bands, low frequencies ($\approx 0-10$ Hz) in which drain-source current is simultaneous acquired for all transistors in an array, and higher frequencies (10 Hz-30 kHz) in which each transistor is recorded individually.

2.5.4 Data Analysis

The workflow adopted for the storage and analysis of gSGFET electrical characterization data is based on free open-source software. All data was acquired using Python software. Data was uploaded to a local database for storage as a Python object using the custom library (<https://github.com/aguimera/PyGFETdb>). Further data processing was also performed using Python code. Next, some details of the most important aspects of the data analysis implemented in the PyGFET library are described.

Polynomial fitting of transfer curve

Experimental transfer curve measurements in this thesis have been performed at V_{gs} steps of 20-25 mV for the sake of time. To improve the accuracy of extracted parameters such as transconductance and CNP a 10-order polynomial fitting using `numpy.polyfit` function is performed. The transconductance is then obtained by the derivative of the $I_{ds}(V_{gs})$ polynomial. For the extraction of the CNP, 10000 points over the V_{gs} range (generally 500mV, and therefore providing a voltage resolution of 0.05mV) are evaluated to find the minimum of the $I_{ds}(V_{gs})$ polynomial.

Charge carrier density and mobility

Charge carrier density (n) was estimated by the field-effect method using Eq. 2.7 and considering a voltage independent capacitance ($C_{int} = 2\mu F/cm^2$). Other pa-

rameters used are $n_o=8 \cdot 10^{11}$, and $q=1.602 \cdot 10^{-19}$ C.

$$n = \sqrt{n_o^2 + [C_{int}[V_{gs} - CNP]/q]^2} \quad (2.7)$$

Field-effect carrier mobility was then estimated using Eq.2.8.

$$\mu = \frac{L}{W} \frac{I_{ds}}{V_{ds} n q} \quad (2.8)$$

pH and ionic strength measurements

For the characterization of pH and ion sensitivity of gSGFETs, two sets of solutions were prepared. A first one with a fixed ionic strength (10mM PBS with just additional 100mM NaCl) and varying the pH between 4 and 10 and a second set of solutions with pH of 7.2 and 10mM PBS and varying concentrations of sodium chloride between 25 to 250mM. All measurements were performed using a pHmetre GLP22 (CRISON, Baccelona) and its internal reference electrode was used as gate terminal for the gSGFET array. This allowed determining the pH value of the solution at the same time of the transfer curve acquisition.

2.6 Results and discussion

In this dissertation a total of 15 wafers containing more than 200 neural arrays and 2800 graphene transistors have been fabricated. Next, optical images of the fabricated graphene SGFET arrays and its electrical characterization are presented.

Most fabricated wafers used polyimide as flexible substrate although parylene-C was used in some two wafers. Also, two different CVD graphene sources were used, either graphene grown at CNM and transferred by electrochemical delamination or wet transfer (see Methods 2.5.1) or graphene grown and transferred by an external company, Graphenea (San Sebastian, Spain). In some wafers an UVO treatment of 20 min was applied to the graphene contact area to improve the metal-graphene contact as reported in [118]. Table D.1 includes the fabrication details of all wafers.

Flexible gSGFET arrays

Figure 2.10A shows a fabricated 4-inch wafer which includes 18 neural probes. Graphene layers were succesfully transferred to the polymer substrates with predefined metal tracks. During subsequent processing, in some occasions graphene can

be delaminated, for example see Fig. D.1 for photographs of successfully transferred and a delaminated graphene layer before graphene active area patterning. The fabrication of gSGFETs on polyimide substrate resulted in well defined graphene area, metal tracks, and SU-8 insulation both at the sensor and array levels (see Fig. 2.10C-D). The fabrication of gSGFETs on parylene-C substrate also resulted in well defined graphene area, metal tracks, and SU-8 insulation (see Fig. D.2A). At the end of the fabrication process, gSGFET arrays were peeled off from the wafer and inserted into the connector for interfacing with the electronic instrumentation (Fig. 2.10B).

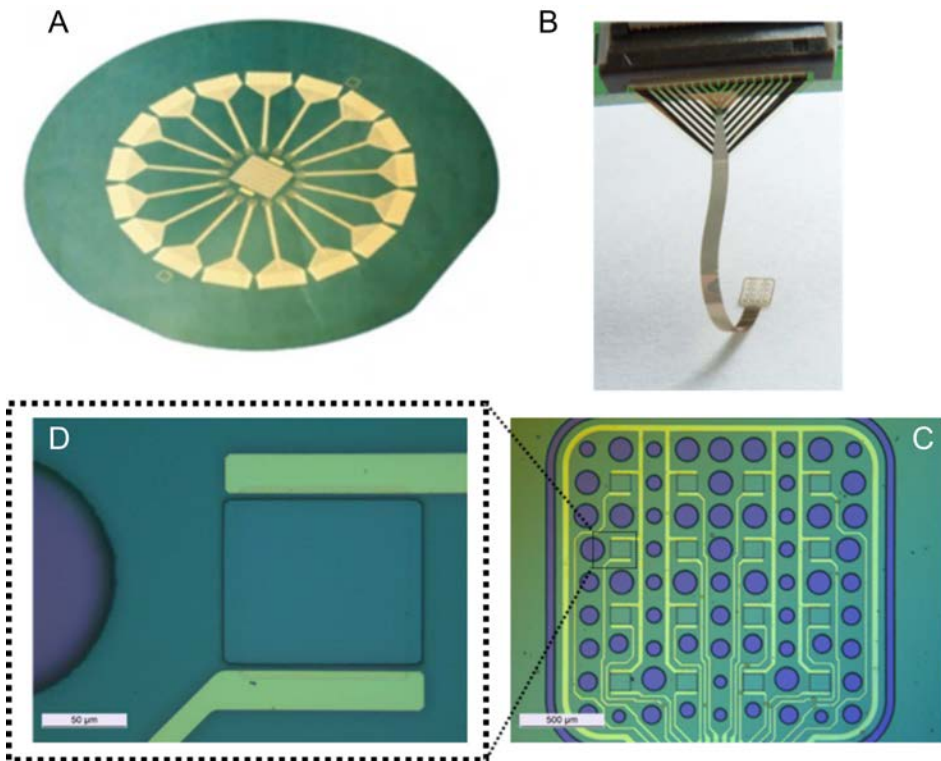


Figure 2.10: Flexible graphene SGFET arrays. A: Photograph of a 4-inch wafer with the fabricated gSGFET neural interfaces. B: Photograph of a flexible gSGFETs array after releasing from the wafer and connecting to a ZIF. C: Optical microscope picture of the active area of a 4x4 graphene SGFET array. D: Tip zoom where a single gFET can be observed as also the tracks and part of a hole.

Steady-state characterization

Fabricated flexible gSGFET arrays were extensively characterized. I_{ds} and I_g were acquired at multiple V_{gs} values and several performance indicators extracted. Fig. 2.11 shows the median and median absolute deviation (MAD) of the V_{gs} dependence of different measured (I_{ds} and I_g) and extracted indicators (GMV, μ , Irms, Vrms) from more than 200 gSGFETs (wafer B12708W2, see TableD.1 for wafer details) grouped by gSGFET channel dimensions (blue, $100 \times 100 \mu^2\text{m}$ and red, $50 \times 50 \mu^2\text{m}$). The fabricated graphene transistors have the ambipolar drain-source current (I_{ds}) characteristic of gSGFETs. The maximum transconductance is located at approximately ± 0.1 V from the CNP. The lower of both voltages, the -0.1 V from CNP value, is used to extract statistics for comparison between wafers. The attenuation of V_{ds} normalized g_m (GMV) far from the CNP is attributed to contact and track resistance contributions. The carrier mobility was also extracted from the measured transfer curves (see Section 2.5.4) as it is a useful parameter for comparing transistor technologies. μ for the fabricated gSGFETs is in the range of 1000 to 10000 $\text{cm}^2/\text{V} \cdot \text{s}$ with higher values near the CNP where carrier density is lower. The obtained values are comparable with those obtained for graphene SGFETs prepared on rigid substrates [94].

The leakage current (I_g) was also measured as it is an essential indicator of the electrochemical processes occurring at the graphene/electrolyte interface and it also has important implications for clinical translation. A leakage current (I_g) below 10 nA throughout the voltage sweep was obtained demonstrating the good insulation of the passivation layer and the negligible electrochemical reactivity of CVD graphene (see Fig.2.11).

The intrinsic noise of the devices was also characterized and analyzed. As expected, current noise decreases near the CNP, where the drain current is lower since it is dependent on $I_{ds}^2 \cdot V_{gs}^{RMS}$, which represents the detection threshold for signals, has its optimal value around ± 0.1 V from the CNP with values in the 20-30 μ V range (RMS integration bandwidth between 5 Hz and 7 kHz). Results show a constant V_{gs}^{RMS} in a large V_{gs} bias range which facilitates operating the transistors at their optimal sensing performance. A large low-Vrms window is also beneficial to ensure optimal performance over long recordings where the transfer characteristics can be shifted laterally due to reference electrode drift. A larger window is achieved thanks to the UVO-treatment of the contacts which reduces the contact noise [118]. Comparing the two transistor sizes in the wafer, a expected reduction of Irms and Vrms when increasing the transistor area is obtained, while the other measured or extracted parameters do not change significantly (since they depend on the aspect ratio and not the total area of the channel), validating the extraction methodology.

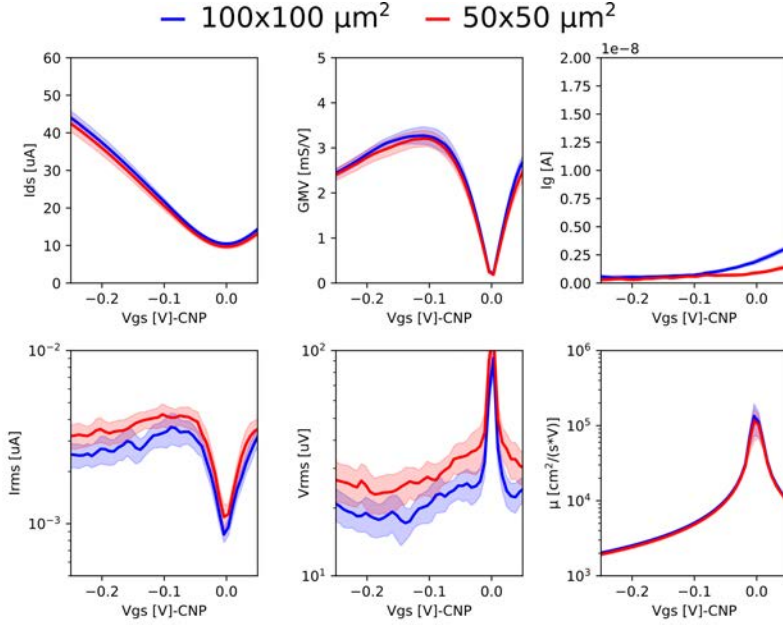


Figure 2.11: Results from electrical characterization of all (more than 200) graphene transistors from wafer B12708W2 normalized to the CNP. $V_{ds}=50$ mV. Bold line represents the median and dispersion is represented by the MAD. Colors represent two different transistor sizes: blue, $100 \times 100 \mu\text{m}^2$ and red, $50 \times 50 \mu\text{m}^2$. From top-left to bottom-right: Measured drain-source current (I_{ds}), absolute transconductance normalized by the V_{ds} voltage (GMV), measured leakage current (I_g), integrated root-mean-squared current (I_{rms}), derived root-mean-square voltage (V_{rms}) and carrier mobility (μ). RMS integration bandwidth between 5 Hz and 7 kHz.

The CNP for the fabricated gSGFETs is a positive value in the hundreds of mV range. Parameters affecting the CNP are the V_{ds} voltage applied, the reference electrode and chemical composition of the solution (pH and ionic strength). Another parameter affecting the position of the CNP is the doping of the graphene layer. Doping can occur due to metallic or photoresist residues introduced during the fabrication.

A stable steady-state response is of utmost importance for recovering the recorded signals at the gate of the transistor. During the first few electrical characterizations after releasing the flexible probes from the wafers, a CNP shift towards less positive values starting generally above 400 mV vs Ag/AgCl was observed. After a few measurements, the CNP stabilized at values lower than 400 mV. This effect is tentatively attributed to the presence of residues that get away with the passage of current. Contaminants can also be removed by immersion of the arrays in ethanol

during a few minutes. After that, CNP shifts to lower values vs Ag/AgCl and the transfer curve remains stable over repetitive characterization.

Voltage dependence of spectral density noise

To gain insight about the noise, the measured current frequency spectrum was fitted with Eq. 2.6 for different V_{gs} values, obtaining the voltage dependence of the fitting parameters (a and b , see Fig. 2.12). The results show a voltage dependence of the a and b parameters with lower values near the CNP. No voltage dependence was found for c that remained at values around $1 \cdot 10^{-23} \text{ A}^2/\text{Hz}$, indicating that thermal noise from the electronic instrumentation does not dominate our noise analysis. As expected, a has a similar shape than the Irms voltage dependence. While the change in b with voltage suggests that a change in the contribution of the different noise sources occurs. The b decrease near the CNP could be attributed to a higher contribution from the channel thermal noise at the CNP due to increased channel resistance. Another possibility is that the electrolyte thermal noise contributions start to dominate at higher frequencies due to the a parameter decrease. More investigations are required to determine the relation between the noise-derived parameters from spectral analysis and their V_{gs} dependence with the graphene and device properties.

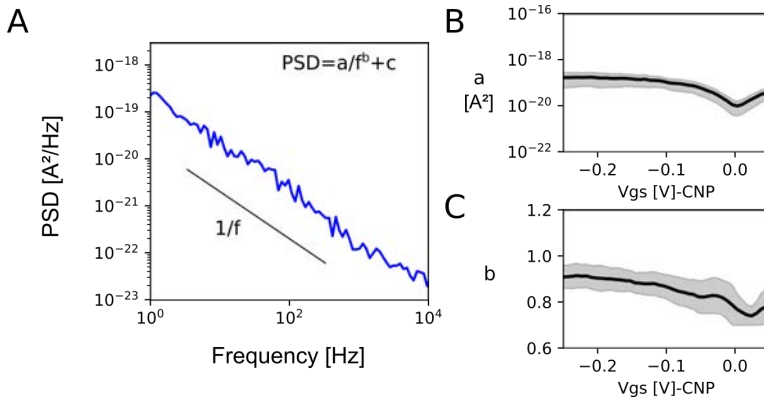


Figure 2.12: Gate voltage dependence of gSGFET spectral noise characteristics. A: Log-log plot of the power spectral density versus frequency for a gSGFET. Black line shows an ideal $1/f$ dependence. $V_{gs}=100$ mV. B-C: Gate voltage dependence of parameters obtained from fitting power spectral density data to Eq. 2.6. Data from electrical characterization of all (more than 200) graphene transistors from wafer B12708W2. Dark line represents the median and dispersion is represented by the MAD. $V_{ds}=50$ mV.

pH and ion sensitivity

Due to its 2D-nature, graphene has the highest surface to volume ratio possible, which makes it very sensitive on the presence of charge at its surface. Since surface charge can vary depending on the chemical composition of the electrolyte such as pH or ionic strength, it is important to characterize its effects on the transfer curve. In the following, the effect of the chemical environment where a gSGFET is immersed in its steady-state electrical characteristics is discussed and the pH and ionic strength sensitivity of the fabricated gSGFETs characterized.

Many works have reported pH and ion sensitivities of graphene transistors with apparently contradicting results [150, 151]. Importantly, in most works, the pH-ion strength interaction and their global effects on the transfer curve of gSGFETs are not described. One notable exception is the work of Zuccaro et. al. [152] where both pH and ion strength effects are modelled. Below, a detailed characterization of the effects of pH and ionic strength of the solution in the transfer characteristics of flexible gSGFETs is provided.

Fig. 2.13A,C shows a series of transfer curves measured for a range of pH (4-10) at a fixed ion strength and for a range of NaCl concentrations (25mM-250mM) at a fixed pH (7.2). It can be seen how increasing the pH shifts the transfer curve towards more positive voltages with respect to a Ag/AgCl reference electrode while increasing NaCl concentration shifts the transfer curves towards more negative values. This is even more clearly seen in Fig. 2.13B,D where the CNP position is tracked. From the experimental results a mean sensitivity to pH of 18 mV/pH with a linear range between (4-8) and a NaCl sensitivity of $-23\text{mV}/\log_{10}([\text{NaCl}])$ can be extracted. These results are in agreement with the values reported by others in rigid substrates (SiO_2 , SiN_3 or sapphire) [153].

A charge-potential model of the graphene-liquid interface based on Zuccaro et. al. [152], was implemented (code available at [154]) and used to fit the experimental data (Fig. A.1a-b). In brief, Gouy-Chapman-Stern theory [56] is used to model the graphene-electrolyte interface while the presence of surface groups is modelled as a (functional) layer of definite thickness and dielectric constant with its charge density determined by a modified Langmuir-Freundlich isotherm (see Appendix A.3 for details). The parameters of the model (see Table 2.2) are next described. m is an heterogeneity parameter in the distribution of ionizable groups, σ_{off} represents the charge density offset, pK_a^μ is the minus logarithm of the acid dissociation constant, and σ_{max}^μ is the maximum surface charge, of a given type of surface group (μ). σ_{min} was estimated from fitting experimental transfer curves of the fabricated transistors using a physics-based current-voltage model [113]. Extracted parameters for a model consisting of two ionizable surface groups are reported in Table 2.2. Results point to surface acidic groups (pKa around 2.4) at graphene surface as

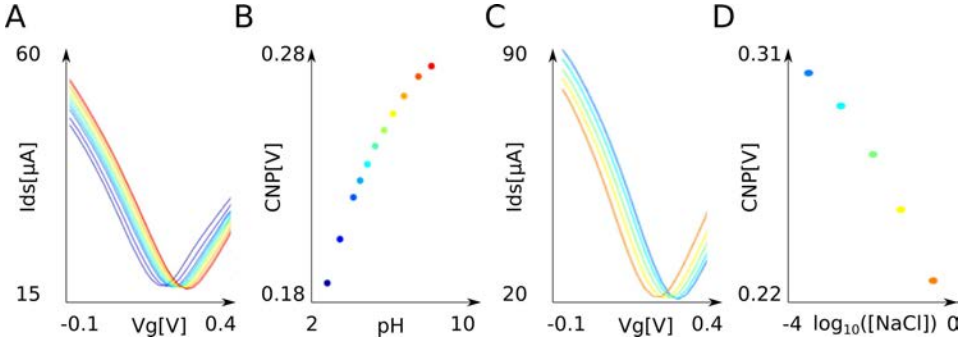


Figure 2.13: pH and ion-strength sensitivity of fabricated gSGFETs. A,C: Current-voltage measurements of a flexible graphene transistor (Width: $80\ \mu\text{m}$, Length: $30\ \mu\text{m}$) with $V_{ds} = 100\text{mV}$ measured vs a Ag/AgCl reference electrode in a) 10mM PBS solution with 100mM NaCl and C) 10mM PBS solution at $\text{pH } 7.2$ for different NaCl concentrations. B,D: CNP variations that correspond to a sensitivity of $18\text{mV}/\text{pH}$ and $23\text{mV}/\log_{10}([\text{NaCl}])$.

the source of pH sensitivity. We tentatively attribute gSGFET sensitivity to pH to acidic surface groups coming from transfer process residues such as PMMA. The extracted parameters (Table 2.2) have been further used to simulate the CNP for a wide range of pH and ion strengths (Fig. 2.14). Importantly, the implemented model could be used to predict the sensitivity of the fabricated gSGFETs in a wide variety of situations, such as under different surface functionalizations targeting biosensing applications.

m	pK_a^1	$\sigma_{max}^1 [C/cm^2]$	$\psi_{off} [V]$	pK_a^2	$\sigma_{max}^2 [C/cm^2]$
0.5	2.4	-0.0018	-0.13	7	0.0003

Table 2.2: Extracted graphene-electrolyte charge-potential model parameters. m : heterogeneity parameter in the distribution of ionizable groups, σ_{off} : charge density offset, pK_a^μ : minus logarithm of the acid dissociation constant and σ_{max}^μ : maximum surface charge, of a given type of surface group (μ). Experimental data used to fit is shown in Fig. 2.13 and fitting in Appendix Fig. A.1b.

Importantly, the shape of the transfer curve does not suffer significant modifications as seen in Fig. 2.15A, presumably due to graphene interfacial capacitance which is weakly dependent on the ionic composition since it is dominated by the quantum capacitance near the Dirac point. The stability of the shape of the transfer characteristics is of pivotal importance for sensing applications as the transconductance is preserved (see Fig. 2.15b).

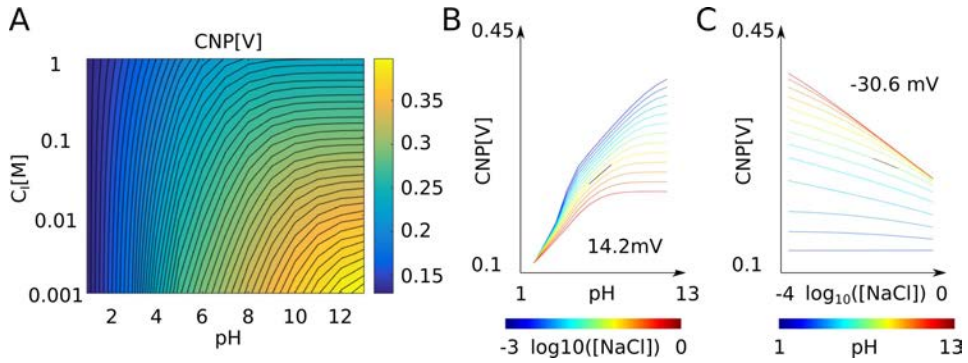


Figure 2.14: Modelling gSGFET CNP dependence on pH and ion strength of electrolyte solution. A-B: CNP simulations using the fitted parameters of Table 2.2. A: Simulated 2d map of the CNP in function of the pH and ionic strength. B: CNP variations while changing the pH for different ion strengths (left) or changing the ionic strength for different pH values (right).

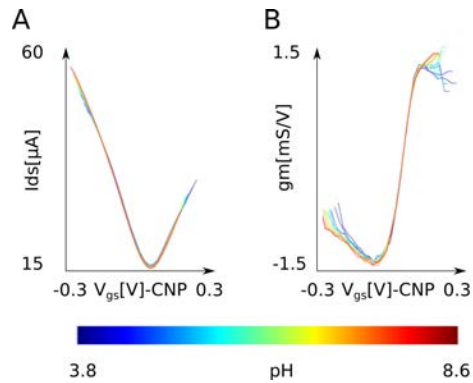


Figure 2.15: gSGFET transfer curve shape is not altered by pH of the electrolyte solution. A,B: Current-voltage measurements and extracted transconductance of a flexible graphene transistor with $V_{ds} = 100\text{mV}$ measured vs a Ag/AgCl reference electrode in 10mM PBS solution with 100 mM KCl for different pH values normalized to the CNP.

Frequency response

Determining how the transconductance depends on the frequency of the input signal is important to assess the transistor behaviour in the frequency range of neural activity and has implications for calculations such as the input-referred noise and for calibrating the recorded signals. To this end, the frequency response of the transconductance (g_m), was measured at a similar ionic strength than in vivo conditions (see Section 2.5.3).

Obtained results are shown in Fig. 2.16 as a Bode plot for two different V_{gs} values, lower and higher than the CNP. Negative g_m magnitude is obtained for V_{gs} values lower than the CNP, resulting in an inversion (180° phase) of the signals measured at such bias. For V_{gs} values higher than the CNP the signal phase is preserved. In both cases, almost constant g_m magnitude values in a wide bandwidth (0.005-800 Hz) with the same value as the steady-state measured transconductance was obtained. Also the phase values remain constant over the frequency range. Other measurements have corroborated a flat magnitude and phase response in a large bandwidth (DC-10kHz) [125] for ion concentrations similar than in vivo conditions.

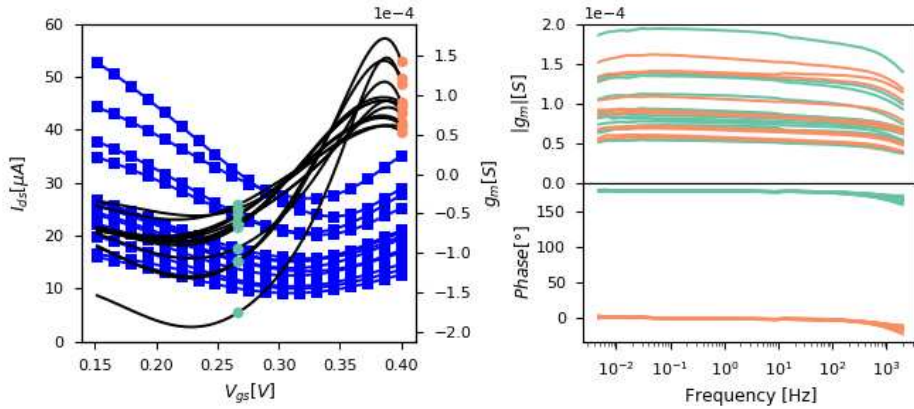


Figure 2.16: gSGFET frequency response characterization. Transistor transfer curves (blue squares and lines) and transconductance (black lines) of a $100 \times 50\text{-}\mu\text{m}^2$ gSGFET array in 10 mM phosphate buffered saline with a drain-source voltage bias of 50 mV. Frequency response of the transconductance is shown at two different points of the transfer curve: V_{gs} lower than the CNP (green dots), where g_m is negative resulting in a signal inversion (180° phase); and V_{gs} higher than the CNP (orange dots), where g_m is positive and thus results in no inversion (0° phase). Independently of the branch of the transfer curve where a gSGFET is biased, the module of g_m is similar to the steady-state value for a wide bandwidth (\approx DC-1kHz).

The obtained transconductance response of gSGFETs allows signals in the frequency range of neural activity to be transduced without distortion nor delay, validates the use of the steady-state obtained transconductance for the estimation of the input-referred noise (V_{gs}^{RMS}) as well as the use of the steady-state I_{ds} - V_{gs} curve for signal calibration. This last aspect will be further explored in the next chapter. The obtained results demonstrate that gSGFETs have a wider transconductance frequency bandwidth than other types of flexible transistors not based on field-effect such as organic electrochemical transistors [81] and a similar transconductance magnitude (see Fig. 1.9).

Yield

An important figure of merit of any technology is the fabrication yield which provides information about the maturity of a given technology. As a general overview, a median of 88% of working transistors for each array (defined as having a channel resistance between 400Ω and $10k\Omega$) has been obtained (first and third quantiles between 75-94%). A more detailed wafer by wafer median yield in terms of percentage of either working or low noise ($< 100 \mu V_{gs}^{RMS}$) channels of the arrays of each wafer is shown in Fig. 2.17. Most arrays in all wafers have a high working yield.

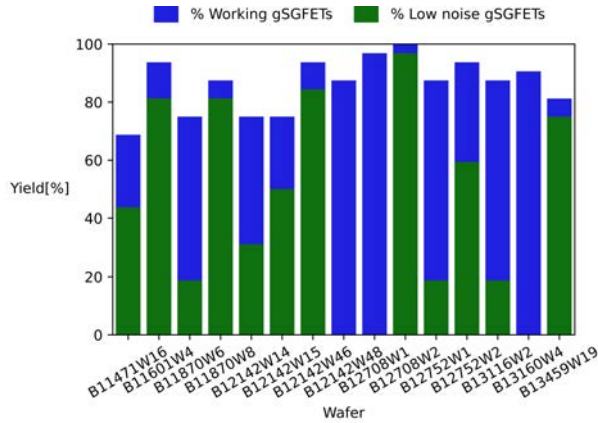


Figure 2.17: Working and noise yield of fabricated gSGFET arrays per wafer. Working refers to transistors with channel resistance between 400 and $10k\Omega$ while low noise refers to transistors with V_{gs}^{RMS} below $100\mu V$. RMS integration bandwidth between 5 Hz and 7kHz.

As can be observed, substantial differences exist between fabrication batches in terms of noise, presumably due to heterogeneity coming from graphene growth,

transfer or metal-graphene contact. Even when processing some wafers in parallel to share graphene source and most processing conditions, heterogeneity between the wafers was found. This suggests that the graphene transfer step, which is a manual process for each wafer, is a main process affecting noise performance. From all processed wafers, best results were obtained using electrochemical delamination transfer method with CNM-grown graphene. Results also show the improvement when UVO treatment at the metal-graphene contact was used.

Summary of gSGFET technological state

Next, the current state of gSGFET technology is summarized and discussed by providing distribution estimates of many electrical parameters that characterize gSGFETs. Fig. 2.18 shows box plot of different parameters for four different fabrication batches, while Table 2.3 provides the 25-75% percentile range of the more than 800 gSGFETs. Parameters have been extracted at $V_{gs} = \text{CNP} - 0.1$ V since it is generally an adequate operating point for recording.

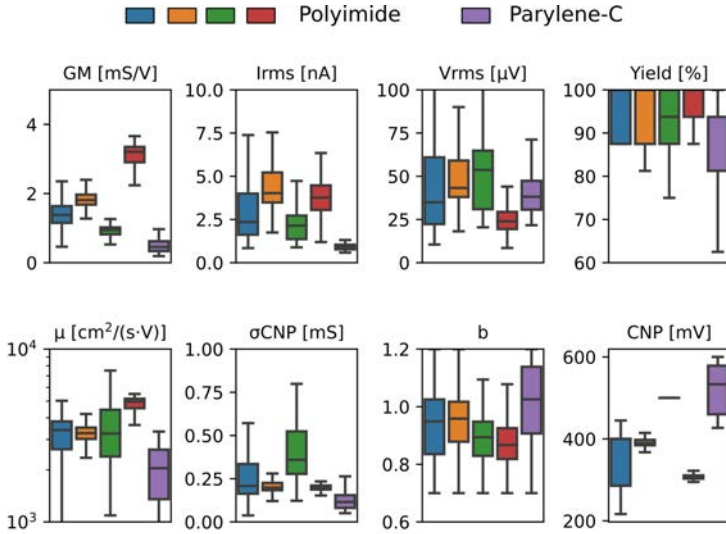


Figure 2.18: Boxplot of steady-state characterization of fabricated devices. Extracted parameters at $V_{gs} = \text{CNP} - 0.1$ V and $V_{ds} = 50$ mV of $n = 874$ gSGFETs from four different fabrication batches (B11601W4 (blue): $n = 202$, B11870W8 (yellow): $n = 159$, B12142W46 (green): $n = 237$ and B12708W2 (red): $n = 276$). From top-left to bottom right: Normalized maximum transconductance (GM), rms current (I_{rms}) and voltage (V_{rms}), intra-array yield of working transistors, extracted charge carrier mobility (μ), conductance at the CNP (σ_{CNP}), b from equation $1/f^b$ and charge neutrality point (CNP). RMS integration bandwidth between 5 Hz and 7 kHz.

Transconductance values around 1-3 mS/V and carrier mobility (μ) values in the few thousand of $cm^2/V \cdot s$ are obtained. μ values are high as compared to other types of EGFET transistors [94] and to organic electrochemical transistors (OECTs) [66]. Regarding the leakage current (I_g), the values remain below 10nA in all fabricated wafers demonstrating the maturity of the fabrication technology to insulate well all the tracks except the active area as well as confirming CVD graphene inertness in electrolyte solution.

g_m [mS/V]	I_{rms} [nA]	V_{rms} [μ V]	$Yield$ [%]	μ [cm^2/sV]	Rds_{CNP} [$k\Omega$]	$1/f^b$ []	I_g [nA]
1-3	2-4	25-55	87.5-100	3000-4800	2.8-5.0	0.82-0.98	< 1

Table 2.3: Summary of steady-state characterization (25-75% percentiles) of fabricated devices (data from Fig. 2.18) at $V_{gs}=CNP-0.1$ V and $V_{ds}=50$ mV of n=874 gSGFETs from four different fabrication batches. From left to right: Normalized maximum transconductance (GM), rms current (I_{rms}) and voltage (V_{rms}), intra-array yield of working transistors, extracted charge carrier mobility (μ), conductance at the CNP (σ_{CNP}), b is the power decay of $1/f^b$ and leakage current (I_g). RMS integration bandwidth between 5 Hz and 7 kHz.

Results show that wafer to wafer variability is generally higher than intra-wafer dispersion for transfer curve related parameters (see for example transconductance from Fig. 2.18), while noise is also disperse intra-wafer. The obtained b parameter around 0.9 indicates that gSGFET noise is almost 1/f noise. Different sources of noise affect gSGFETs [155]. First, graphene quality is one of the parameters affecting noise. Single layer graphene presenting too many defects or second nucleation areas results in electronic devices with large noise due to charge scattering processes [156, 157]. Second, it has been shown that the coupling between the graphene layer and the substrate can influence the electronic noise of the device. Thus, the polyimide or parylene-C substrate might contribute to the electronic noise of our devices. Finally, the contact resistance can be an important source of noise [118]. Indeed, a lower mean overall noise was obtained for wafer B12708W2 which applied UVO to the graphene at the contacts to lower contact resistance.

The gSGFET technology developed in this dissertation has high yield and produces devices with high transconductance, charge carrier mobility and low intrinsic noise. Further technological development can be focused to factors that affect the electronic transport properties such as metal-graphene contact, homogeneity among devices and 1/f noise. Advances on those aspects are required for downscaling transistor size while keeping recording performance.

2.7 Conclusions

In this Chapter, the concepts and methods to design, produce and operate high-performance flexible graphene transistor neural recording interfaces have been discussed. Regarding the design, a common source is adopted to reduce the number of required tracks from $2 \cdot n$ to $n+1$ where n is the number of transistors. This design comes with few drawbacks in terms of gFET performance being the most important the limitation to operate the array at a single V_{gs} voltage, therefore requiring high-homogeneity of the CNP. Regarding fabrication, CVD graphene grown on copper is shown to be a suitable graphene production technology yielding large-area high-quality graphene which results in high mobility transistors. For graphene transfer, the bubbling method has been primarily used yielding low-noise devices, although alternatives to PMMA may be explored since its total elimination from graphene surface is challenging. The adaptation of standard microelectronic processing for fabricating graphene devices is feasible and does not add much complexities which is of paramount importance for industrial translation.

In this dissertation a total of 15 wafers containing more than 200 neural arrays and 2800 graphene transistors have been fabricated and electrically characterized. Measurements of gSGFET transfer curve under different pH and ionic strength of the solution where they are immersed indicate that the chemical composition of the electrolyte solution does not alter gSGFET transfer characteristics, which is pivotal for charge sensing. Further electrical characterization results have shown low-leakage and constant transconductance magnitude and phase over a wide frequency bandwidth (\approx DC-1kHz). Overall, the results presented in this chapter show that gSFETs have outstanding properties for high-fidelity field potential recordings in a wide-bandwidth and that flexible gSGFET arrays can be produced in high yield, low noise and considerable homogeneity using wafer-scale microfabrication methods.

Chapter 3

Recording brain field potentials with graphene transistor arrays

As determined from bench characterizations in Chapter 2, gSGFETs fulfill the material and electronic requirements for the ideal transducer of brain field potentials such as stable and constant characteristics in a wide bandwidth and low intrinsic noise. Nonetheless, since recording brain signals with active transducers is not a common procedure, voltage recordings with gSFETs requires developing and validating an acquisition methodology that includes a specific electronic instrumentation allowing gSGFET biasing, a procedure to characterize the $I_{ds} - V_{gs}$ relation, and a post-processing calibration procedure to translate the recorded current signals into the equivalent voltage signals at the brain-channel interface. In this chapter, the full acquisition methodology of gSGFETs for high-fidelity voltage recording is presented and validated.

The feasibility and adequacy of gSGFETs for brain potential recording is demonstrated by *in vivo* recordings with epicortical graphene transistor arrays of spontaneous and sensory-evoked activity in rodents. Benchmarking against state-of-the-art microelectrodes shows that gSGFETs have similar recording performance than platinum-black microelectrodes in the local field potential bandwidth. Comparison of *in vivo versus post-mortem* recordings allowed to estimate the signal-to-noise ratio of gSGFET recordings in awake spontaneous or epileptiform states, confirming the excellent recording capabilities. In addition, a pilot chronic study was conducted showing stability of the gSGFET array for the whole implant duration, up to five months, suggesting a lower bound of gSGFET chronic recording capabilities.

Finally, the stability of the transfer characteristics of gSGFETs *in vivo* is evaluated and its effects on the acquired signals studied. These results confirm that the *in vivo* observed changes in their transfer characteristics do not produce significant signal distortion. Overall, the results obtained in this Chapter demonstrate that

the graphene SGFET technology is suitable for μ -ECoG recordings either in acute or chronic use and that gSGFETs are able to transduce brain field potentials with high-fidelity.

Part of the contents of this chapter have been published in:

- C. Hébert, E. Masvidal-Codina, A. Suarez-Perez, A. B. Calia, G. Piret, R. Garcia-Cortadella, X. Illa, E. D. C. Garcia, J. M. D. l. C. Sanchez, D. V. Casals, E. Prats-Alfonso, J. Bousquet, P. Godignon, B. Yvert, R. Villa, M. V. Sanchez-Vives, A. Guimerà-Brunet and J. A. Garrido. Flexible Graphene Solution-Gated Field-Effect Transistors: Efficient Transducers for Micro-Electrocorticography. *Advanced Functional Materials*, 28(12):1703976, 2018. ISSN 1616-3028. doi:10.1002/adfm.201703976. URL [https:// onlinelibrary.wiley.com/doi/abs/10.1002/adfm.201703976](https://onlinelibrary.wiley.com/doi/abs/10.1002/adfm.201703976).

3.1 Considerations for electrophysiological recordings with gSGFETs

Due to the novelty of the gSGFET technology for neural recordings and the methodological differences that an active technology requires as compared to passive electrode technology, some methodological considerations are provided as guidelines for the appropriate operation of gSGFETs and post-processing of the acquired signals to ensure recording voltage signals with high fidelity.

3.1.1 Operation of gSGFET arrays for neural recordings

The use of gSGFETs for *in vivo* recordings imposes some methodological restrictions to the operation mode of gSGFETs. For example, it is best to assume that the animal can be grounded, and therefore, to avoid undesired voltage gradients along the tissue it is convenient to set the reference electrode terminal as ground. Another methodological step is to determine an appropriate set of V_{ds} and V_{gs} voltages to ensure high-quality transduction as the operation point determines gSGFET amplification gain and intrinsic noise.

As seen in the previous chapter, the optimal V_{gs} biasing point of a transistor is found at its lower V_{rms} noise point, which is generally -100 mV from the CNP. Since the CNP position is not known a priori, a transfer curve characterization needs to be performed *in vivo*. Importantly, given an array with n transistors with shared source terminal, only one V_{gs} can be applied to the whole array and therefore, selection of an appropriate V_{gs} value has to take into account the CNP dispersion between gSGFETs. The method used in this thesis consists in determining the appropriate V_{gs} value from the *in vivo* measured transfer curve as the voltage where the sum of the absolute value of the transconductance of all gSGFET of an array is maximum. Moreover, whenever possible, V_{gs} is preferred to be situated at more negative voltages than the CNP due to the lower leakage current, as determined from bench characterizations (see Section 2.6).

Regarding the V_{ds} value, the high transconductance of gSGFETs ($\approx 1-2mS/V$) allows to use V_{ds} values below 100 mV. This feature is particularly important for neural interfaces since it demands lower power consumption, which is critical for chronic implants powered by battery. However, since the V_{ds} affects almost linearly the current flowing through the transistor, it has to be set in accordance to the current noise and saturation voltage of the amplifier. Values around 25-200mV are appropriate depending on the amplitude of the neural activities to be measured. In this thesis values of 50-100 mV V_{ds} have been used.

3.1.2 Calibration of gSGFET recordings

As determined from characterizations in saline solutions performed in the previous chapter, the transfer curve of a gSGFET is non-linear, which causes harmonic distortion of input signals. Therefore, in order to recover the original signal, the recorded current fluctuations need to be calibrated. There are different options to perform that calibration. Fig. 3.1 compares two of these methods. A first approximation is to assume linearity of the transfer curve and use the transconductance at the operation point as a conversion factor. This approximation works well when the signals to be measured have a low amplitude and linearity is (almost) satisfied near the operation point. However, if non-linearity near the operation point is considerable, it can lead to significant harmonic distortion and this will not be removed by a simple linear calibration (Fig. 3.1B). Harmonic distortion caused by non-linearity can be compensated by interpolation of the current signals into the inverse of the transfer curve, preserving the signal amplitude and spectrum Fig. 3.1C.

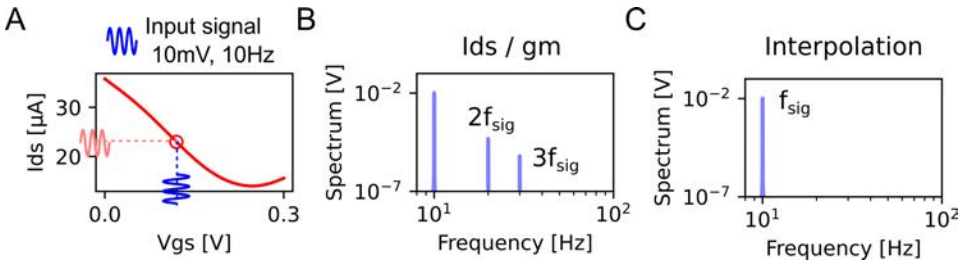


Figure 3.1: Comparison of gSGFET calibration methods. A: *in vivo* measured transfer curve of a gSGFET. Point marks the biasing point (120 mV). An $I_{ds}(t)$ signal is obtained by interpolation of a 10 mV, 10 Hz sinusoidal into the transfer curve. B-C: Frequency spectrum of the resulting signals after calibration by a constant value (I_{ds}/g_m) or by interpolation of I_{ds} into the inverse of the I_{ds} - V_{gs} transfer curve. See Section 3.2 and 3.2 for details.

This interpolation method is chosen as the calibration methodology for all signals presented in this dissertation. An example of the interpolation method for calibration of a test signal recorded by a gSGFET array is shown in Fig. 3.2. Due to the different I_{ds} - V_{gs} relation for each channel, input of a sinusoidal signal results in current modulations with different offsets (Fig. 3.2A). Interpolation into the corresponding transfer curve (Fig. 3.2B) recovers the sinusoidal signal introduced (Fig. 3.2C). Details of the methodology are provided at Sections 3.2 and .

Importantly, both calibration methods (linear and interpolation methods), assume that the steady-state transfer characteristics are time and frequency invariant under the timescales and bandwidth of use. Non-constant frequency response can

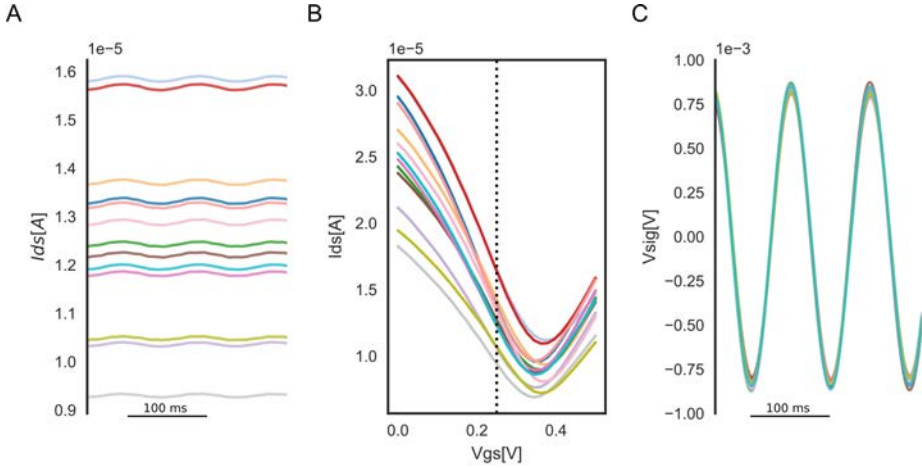


Figure 3.2: Calibration procedure of gSGFET current recordings to recover the voltage signal at the gate. A: gSGFET current recordings of a 10 Hz, 1 mV-peak sinusoidal gate signal applied through a reference electrode. Graphene transistors are biased at $V_{ds}=50$ mV and $V_{gs}=250$ mV. B: Transfer curves of the same graphene transistors at $V_{ds}=50$ mV. Dotted line indicates the V_{gs} bias voltage used in a. C: Voltage signal as obtained by interpolation of the current signal (a) of each transistor into its corresponding transfer curve and removal of the V_{gs} offset.

occur due to residues at graphene surface or low ionic concentration in the solution. To take into account these effects and obtain distortion-free recordings, the frequency dependence of the gain has to be considered [125]. However, due to the complexities of *in vivo* measuring the frequency dependent gain, and that gSGFETs have been demonstrated to have constant characteristics in the frequency bandwidth of the signals analyzed in this dissertation (DC-200Hz), this compensation is not performed.

Regarding the time-variance of the transfer characteristics, lateral shifts of the curve do not cause problems for calibration as those caused by pH or ionic strength sensitivity or charge doping. However, vertical shifts or changes in transconductance can induce distortion. This effects are further studied in Section 3.3.5. As a general advice, multiple transfer curves (or at least a transfer curve at start and end of the recording session) should be measured to ensure stability or advert of any steady-state transfer curve changes. If those practices are followed, gSGFETs allow to obtain wide-bandwidth and high-fidelity recordings of brain field potentials.

3.2 Methods

Instrumentation for *in vivo* recordings with gSGFETs

Commercially available electronic instrumentation for recording electrophysiological signals has been commonly based on low noise voltage amplifiers. However, gSGFETs are active devices, i.e. they require to be biased at certain potential and specialized electronic instrumentation is required that allows obtaining their transfer characteristics and acquire with high-fidelity voltage signals. The used acquisition setup is similar than the one used for gSGFET array characterization (Fig. 2.9) since it uses a data acquisition system (National Instruments USB-6353) to provide biasing of the transistors. Current through the transistors is splitted in two bands as described in the previous chapter by a custom electronic instrumentation. The LPF signals are recorded by the data acquisition system while the band-pass filtered signals can be recorded by commercial recording systems used for electrode recordings (Figure 3.3).

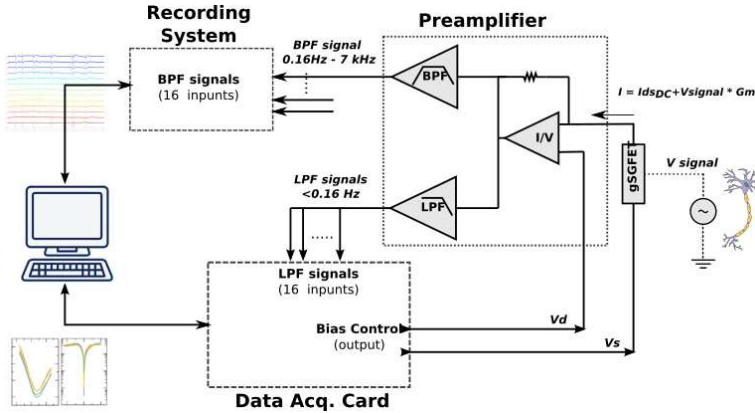


Figure 3.3: Instrumentation for electrophysiological recordings using graphene transistor arrays. Schematic of the setup which consists of a Data Acquisition card which allows programmatic control of the polarization of the gSGFETs (V_{gs} , V_{ds}). Current signals are filtered and amplified differently in two bands: LPF ($<0.1\text{ Hz}$, $\text{gain}=10^4$) and BPF ($0.1\text{ Hz}-5\text{ kHz}$, $\text{gain}=10^6$). LPF signals are managed by the data acquisition system while the BPF signals containing the electrophysiological signals are acquired by a recording system.

Data from section 3.3.2 was acquired using a custom g.HIamp biosignal amplifier, (g.RAPHENE, g.tec medical engineering GmbH Austria) developed in collaboration with the company. This system is based on the same preamplifier architecture presented above, implements off-the-grid, battery-based setting of the polarization and acquires both LPF and BPF signals for each channel.

Modelling gSGFET recording

The recording of a pure tone by a gSGFET is modelled by interpolation into a experimentally obtained gSGFET transfer curve. Due to non-linearities of the transfer curve, the spectral analysis of the recorded signal showed a series of harmonics. The obtained harmonics were compared with the theoretical distortion as assessed by Taylor expansion of the transfer curve:

$$\begin{aligned}
 I_{ds}(t) = & I_{ds}|_{V_{gs}^{bias}} + DC_{offset} + \frac{\partial I_{ds}}{\partial V_{gs}} \Big|_{V_{gs}^{bias}} A'_{sig} \sin(\omega t) \\
 & + \frac{1}{2!} \frac{\partial^2 I_{ds}}{\partial V_{gs}^2} \Big|_{V_{gs}^{bias}} \frac{A_{sig}^2}{2} \sin(2\omega t) + \frac{1}{3!} \frac{\partial^3 I_{ds}}{\partial V_{gs}^3} \Big|_{V_{gs}^{bias}} \frac{A_{sig}^3}{4} \sin(3\omega t)
 \end{aligned} \tag{3.1}$$

where V_{gs}^{bias} is the applied V_{gs} voltage and A and ω are the amplitude and angular frequency of the sinusoidal. See Eq. 1.11 and [158, 159, 125] for the expression of DC_{offset} and A' and the derivation of the whole equation. The agreement between the distortion obtained by interpolation and the predicted by Taylor expansion validates the presented methodology for modelling gSGFET transfer characteristics.

To display the power spectrum of the harmonics, the one-dimensional discrete Fourier Transform for real input is performed using `numpy.fft.rfft` function and the voltage calculated as $\frac{|FFT|}{N/2}$ where N is the product of the signal duration and the sampling frequency.

Calibration by interpolation

Experimentally obtained transfer curve (I_{ds} - V_{gs}) values are splitted in two branches at each side of the CNP and the corresponding branch where biasing is performed, selected. The selected I-V branch is fitted with a 10-order polynomial using `numpy.polyfit` function and re-sampled with 1000 points resulting in voltage steps of ≈ 0.25 mV. Then, calibration is performed by interpolation, with `scipy` function (`interpolate.interpld`), of the recorded signals into the re-sampled I-V relation.

gSGFET arrays

Arrays of transistors of $80 \times 30 \mu m^2$ (equivalent to an electrode of $55 \mu m$ of diameter) and $100 \times 50 \mu m^2$ (equivalent to an electrode of $80 \mu m$ of diameter) were used in for data in Figures 3.3.1 and 3.7. Otherwise, in the other figures of the chapter, $50 \times 50 \mu m^2$ or $100 \times 100 \mu m^2$ sizes were used. The fabrication procedure of the arrays is described in 2.5.1. Devices were electrically characterized as described in Section 2.5.3 prior to *in vivo* use.

Procedures for slow oscillation and visual evoked potential recordings

For the *in vivo* experiments, adult male Wistar (n=15; 225-418g) rats from Charles River Laboratories International, Inc. were used. All experiments were supervised and approved by the university committee and were carried out in accordance with the present laws of animal care, EU guidelines on protection of vertebrates used for experimentation (Strasbourg 3/18/1986) and the local law of animal care established by the Generalitat of Catalonia (Decree 214/97, 20 July). The animals were placed in an anesthesia induction chamber for 5 minutes at 100% of O₂. Next, anesthesia was induced by raising the isoflurane concentration to 5% (0.6 L/min, 1 bar) for 5 more minutes always watching out respiration. The concentration of isoflurane is next set to 3% for one more minute before the rat was placed in the stereotaxic apparatus with mask delivering isoflurane and oxygen. For the rest of the surgery, 1.5-2% of isoflurane was used to maintain deep anesthesia. Heart rate was continuously monitored and maintained at ca. 300 bpm. A subcutaneous injection of atropine (0.05 mg/kg) was given to prevent respiratory secretions. All pressure points and tissues to be incised were sprayed with lidocaine before surgery. Body temperature was maintained at 37°C. A craniotomy of 4 mm ML and 5 mm AP was performed in the left hemisphere revealing different cortical areas such motor (M1), somatosensory (S1) and visual primary (V1) cortices. Electrode recordings were pre-amplified with a multichannel system (Multichannel Systems, Germany) while graphene SGFET recordings were treated and pre-amplified with an electronic system developed by GAB group (see Section 3.2). Pre-amplified signals were sampled at 10 KHz and digitized with a CED 1401 acquisition board using Spike2 software (Cambridge Electronic Design, UK). At the end of the experiments the animals were administered a lethal dose of sodium pentobarbital.

Slow oscillations recordings for SNR analysis

Spontaneous slow oscillations were recorded simultaneously using graphene SGFET probes and black platinum microelectrode array (MEA)s covering different areas of the cerebral cortex (S1, M1, V1). Signal analysis was performed using MATLAB® 2012a (The MathWorks Inc., Natick, MA). From the raw signal, Up and Down state detection was performed by using a reconstruction of the signal based on the principal component analysis (PCA) of three resulting signals obtained from applying different filters to the raw signal: smoothing filter with a 5-ms moving window, bandpass filter from 15 to 100 Hz [160], and MUA bandpass filter from 200 to 1500 Hz [161]. A threshold was set on the reconstructed signal to classify the parts of the recording with more frequency content (Up states) and less frequency content (Down states). For electrodes where the detection did not work, the detection times from the nearest electrode were used.

Once the detection was performed, the PSD with a resolution of 4096 points of the fast Fourier transform (FFT) was calculated for every Up and Down state separately using Welch's method. The mean PSD of the Up states and Down states in the recording fragment were calculated. The Spectral SNR was calculated for every transistor and electrode recording dividing the PSD of Up states by the PSD of Down states and expressed it in decibels (dB).

Visual evoked response in *in vivo* recordings

Graphene SGFET arrays were placed over primary visual cortex (V1; 7.3 mm AP, 3.5 mm ML). To evoke visual responses in the cortex, a white light emitting diode (LED) was placed in front of the right eye (contralateral to the recording site) of the rat and a flash of 100 ms was automatically delivered every 4 to 5 s (random delay).

Implantation of gSGFETs

To assess the chronic performance of the devices, a gSGFET array was implanted epidurally on an adult male Wistar rat. Anesthesia and surgical pressure was done as described in section 3.2. A craniotomy of 4 mm medio-lateral (ML) and 5 mm anterior-posterior (AP) was performed in the left hemisphere revealing different cortical areas such motor (M1), somatosensory (S1) and visual primary (V1) cortices. The array was placed over S1-V1 and the craniotomy sealed with dental cement. To evoke visual responses in the cortex, a white LED was placed in front of the right eye (contralateral to the recording site) of the rat and a flash of 100 ms was automatically delivered every 4 to 5 s with a random delay.

3.3 Results

3.3.1 Recording brain activity under anesthesia

Acute recordings under isoflurane anesthesia were chosen to evaluate the performance of graphene SGFET for recording LFPs. Isoflurane anesthesia generates slow-wave activity, which is a pattern of spontaneous rhythmic activity that alternates between periods of neural firing (Up states) and periods of silence (Down states) at a frequency around 1 Hz [162, 163]. This low frequency signal results from a synchronized state of the cortex and leads to high amplitude activity originating in neural assemblies. This well-studied, spontaneous activity pattern is consequently a convenient scheme to assess the performance of recording devices.

Platinum (Pt) black electrodes with a diameter of 50 μm were used together with the graphene SGFETs as a reference control. The transistor transfer curve (Fig.3.4a) and the transconductance (Fig. 2b) were measured before all the *in vivo* recordings for selecting the optimum gate bias and for calibrating the recorded signals. Typically, the gate voltage is fixed at a value where the value of the transconductance is the highest; in the particular case of the experiment shown in (Fig.3.4), the gate was fixed at 100 mV versus the used reference electrode and the drain-source voltage at 50 mV. The transistor array, together with the Pt electrode array, are placed on the surface of the cortex of the anesthetised rat to record the slow wave activity during anaesthesia.

As shown in Fig.3.4c, graphene SGFETs are able to detect the slow wave activity with a similar amplitude to the one detected by Pt black electrodes. In order to further investigate the performance of the two sensors, the PSD of the Up and Down states recorded with the transistor array of 100x50 μm^2 and with the Pt black electrodes are calculated and plotted in Fig.3.4e. The signal-to-noise ratio over frequency can be extracted (Fig.3.4f) from the PSD using a procedure described in Section 3.2 [68]. In this particular case, graphene transistors exhibit a better performance than Pt black electrodes below 5 Hz. Between 5 Hz and 100 Hz, graphene transistors present a SNR as good as or slightly lower than the electrodes. Above 100 Hz, the SNR of the transistors becomes lower than that of the Pt black electrodes. This frequency analysis also shows that graphene transistors can measure signals up to nearly 1 kHz.

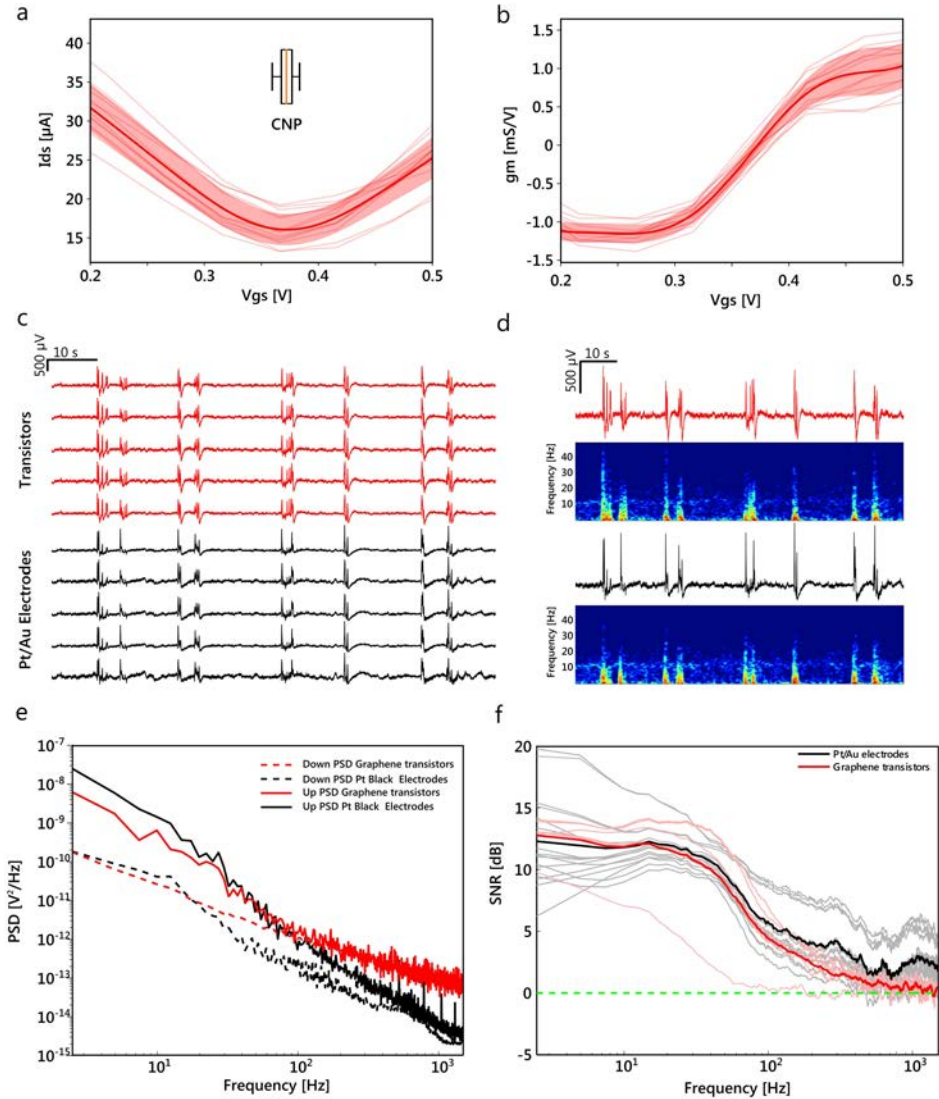


Figure 3.4: Recording of slow wave activity with graphene SGFET and comparison with platinum black electrodes. Recordings were obtained from the cerebral cortex in Wistar rats. a) *in vivo* transistor transfer curves using $V_{ds} = 50\text{mV}$. The insert shows the dispersion of the position of the CNP. b) Normalized transconductance versus gate noise for the devices shown in part a. c-f, recordings with graphene SGFET (red line) and platinum black electrodes (black line). c) Spontaneous oscillatory activity. d) Spectrograms of the spontaneous oscillatory activity. e) Power spectral density of the Up states (solid line) and Down States (dash line). f) Signal-to-noise ratio versus frequency extracted from the PSD for graphene SGFETs (light red lines) and platinum black electrodes (grey lines). The mean values are given by the bold lines.

3.3.2 Recording activity in the awake brain

Previous section details experiments performed under anesthesia. In those cases, activity is widely synchronized through the cortex and the presence of up and down states allows to estimate signal quality. Whether gSGFETs were also able to record awake activity, that is generally more desynchronized and of lower amplitude, remained to be verified. Therefore, to estimate signal quality in awake recordings the acquired signals were compared to post-mortem recordings after intraperitoneal injection of an euthanasic agent (sodium pentobarbital). The data presented in this section comes from experiments using gSGFETs to ask a given scientific question (for example data from Chapter 5 or 6). In those experiments, post-mortem recordings were performed just at the end of the recording session under the same conditions therefore allowing to determine the non-biological contributions, i.e. the noise fraction of the recorded signals.

Post-mortem recordings were performed in two situations: after recording awake physiological activity or after induced epileptiform activity. Figure 3.5 shows the *in vivo* to post-mortem transition for the physiological spontaneous awake activity as recorded by a gSGFET. Recording is shown at full-bandwidth (black line), which shows the appearance of a terminal depolarization (this brain phenomena will be further discussed at Chapter 6), as well as filtered at several well-known frequency bands (slow, delta, theta, alpha, beta and gamma) showing the silencing of neural activity after the injection. The presence of biological activity at different frequency bands was validated by taking the probability density function of the *in vivo* and post-mortem periods (Fig. 3.5B). To further quantify recording quality, the spectral SNR was calculated from the power spectral density of the *in vivo* and post-mortem periods (Fig. 3.4C). Results confirm the ability of gSGFETs to record spontaneous awake activity in a wide frequency bandwidth, from DC up to 100 Hz.

A similar methodology was followed to assess the recording quality of epileptiform activity in an awake mouse. Epileptiform activity is composed of a wide-variety of activity patterns such as interictal spikes, polyspikes, seizures and high-frequency oscillations. Results show that the recorded signals are well-above the noise in a wide bandwidth that extends to ≈ 1 kHz and covers from slow to high-gamma activity (see Fig. 3.6). The extended high-SNR bandwidth range can be attributed to the higher power of epileptiform activity, due to the synchronization of many neural populations as compared to spontaneous physiological activity where activity is largely synchronized and therefore of lower amplitude. Nonetheless, the results demonstrate that gSGFETs are able to transduce a wide-bandwidth of epileptiform activity with high SNR.

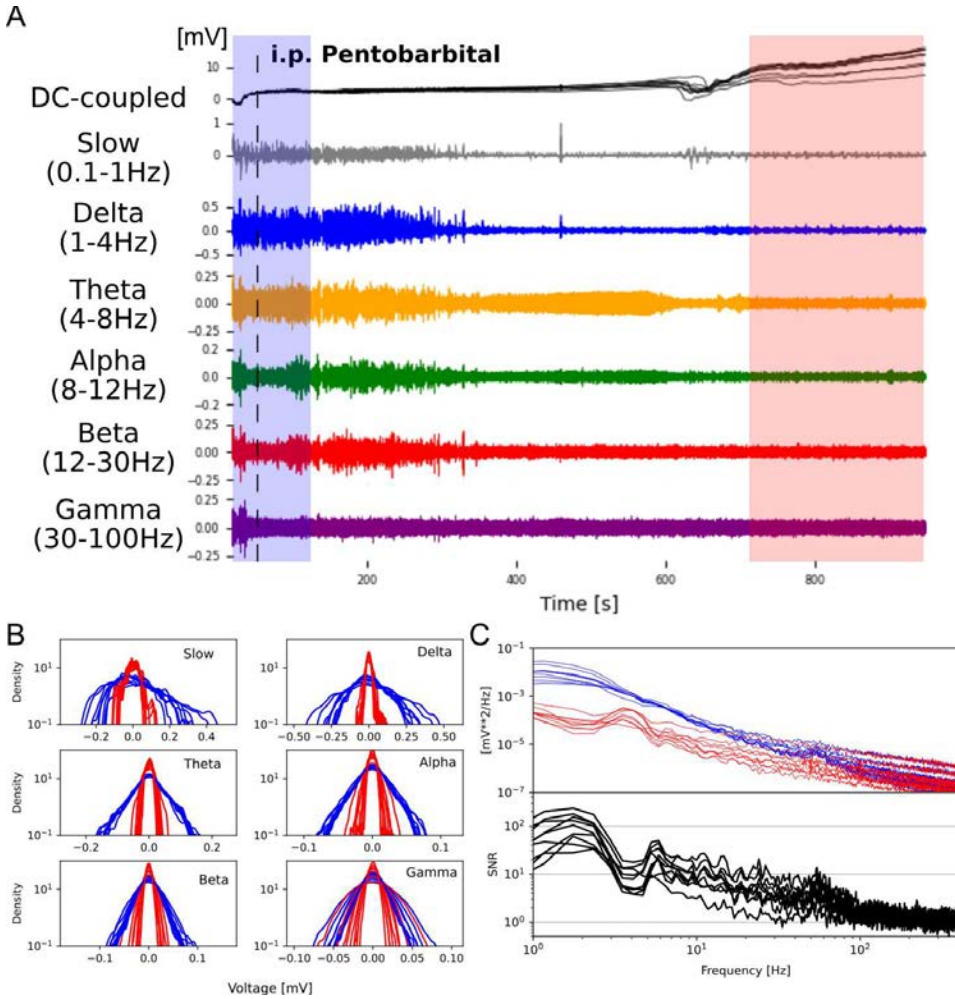


Figure 3.5: Recording of awake activity with graphene SGFETs. Recordings were obtained from the cerebral cortex of a head-fixed mouse. A: Suppression of brain field potentials of an awake mouse after pentobarbital intraperitoneal injection for different frequency bands as also DC-coupled recordings showing a terminal CSD around 10 min after the injection. Blue and red shaded epochs were considered as signal and noise respectively. B: Probability density function of the two epochs for each band as defined in A. Each line represents a gSGFET channel. C: Top, power spectral density of an *in vivo* (blue) and post-mortem (red) period, as marked from the shaded periods in A. Bottom: Spectral signal-to-noise ratio as obtained by the ratio of *in vivo* to post-mortem activity.

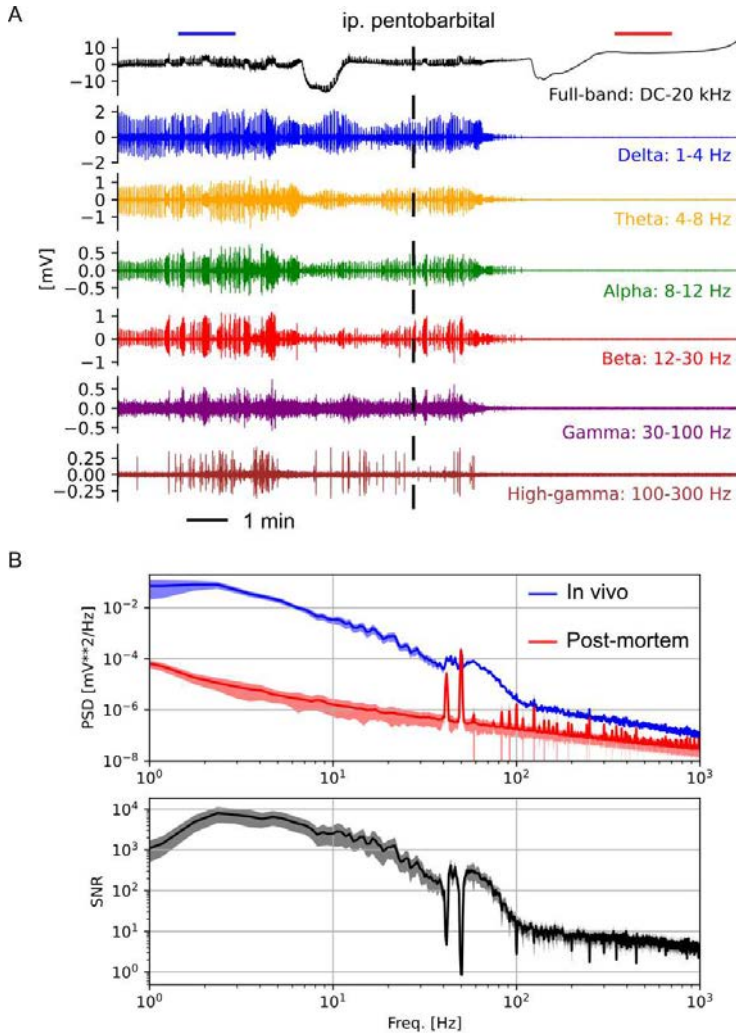


Figure 3.6: Recording quality of awake epileptiform activity. A: Full-band and bandpass filtered timeseries of the *in vivo* to post-mortem transition as recorded with a gSGFET of a parylene-C flexible array over cortex of an awake mice injected with a proconvulsant showing the silencing of activity after sodium pentobarbital intraperitoneal (ip) injection. B: Top, power spectral density of an *in vivo* (blue) and post-mortem period (red) as shown in A. Bottom: Signal-to-noise ratio (SNR) of the recorded signals as estimated by dividing the *in vivo* power spectra by the post-mortem power spectra for each channel. Dark line and shaded areas represent the mean and standard deviation of all channels of the array.

3.3.3 Recording of evoked potentials

Sensory evoked responses were also analysed to explore neural network activity given that they constitute a critical signal for the design of neural prostheses. A good neural interface should be able to detect the evoked activity after one or few trials. To evaluate the potential of graphene transistors for possible applications involving sensory-evoked responses, visual evoked activity was investigated. Visual activity was evoked using a light stimulus provided by a white LED. An On-Off visually evoked-response occurred 40 ms after the stimulus and could be detected already after one single stimulus (Fig.3.7a). The signal shows a main component with a frequency around 20 Hz with maximum amplitude of 250 μV and that lasts 70 ms.

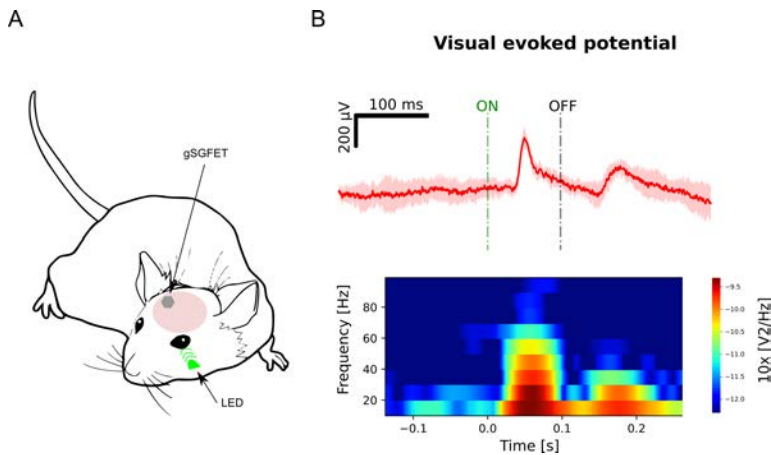


Figure 3.7: Recording of visual evoked potentials using gSGFETs. A: Schematic of the experimental setup. Recordings were obtained from the primary visual cortex of Wistar rats during visual stimulation using an LED. B: Top, visual evoked potential as recorded by a gSGFET. The dark red curve is the mean value of 10 events and the shadow represents the standard deviation. Bottom, spectrogram of the recorded visual evoked potential.

3.3.4 Chronic recordings

The feasibility of long-term use of gSGFET neural probes as chronic implants was studied. An gSGFET was implanted over the visual cortex of an adult male Wistar rat and visual-evoked potentials used to assess recording quality evolution. Evoked potentials are useful experimental paradigms to evaluate chronic performance, since they have a preserved stereotypical pattern and reflect functional integrity of the neural circuitry. Therefore, changes in the recorded evoked potential waveform can be attributed to device or neural deterioration. Our results show that graphene SGFETs are able to record visual evoked potentials during several months with minimal differences with the evoked response at the start of the implantation [164]. The devices' transfer curves obtained *in vivo* (Fig.3.8A) at the start of each recording session were used to select the appropriate biasing point and for the calibration process [124]. A shift in the CNP over the implantation time is observed (Fig.3.8B), which is tentatively attributed to charged molecules adsorbed on graphene surface from the biological environment. This adsorption process could also lead to a decrease in the coupling capacitance and therefore explain the observed decrease of the transconductance. Overall, our results show that implanted graphene transistor neural probes can chronically record evoked potentials over several months of operation *in vivo* remaining functionally operative (Fig.3.8C) and that the current gSGFET technology is suitable for long-term use.

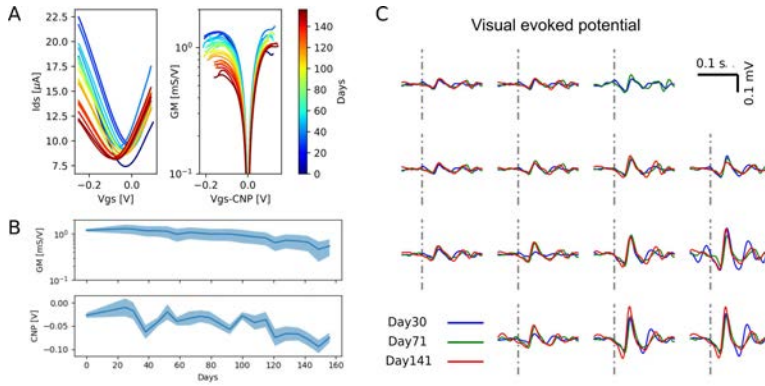


Figure 3.8: Chronic performance of graphene SGFETs. A) Evolution of the electrical characteristics of an implanted 16-channel gSGFET array. Lines represent the mean value of all transistors in the array and colors indicate implanted days. B) Time evolution of the transconductance and CNP after implantation. Solid lines show the mean value of all transistors of the implant and shadows show the standard deviation. C) Evolution of recorded visual evoked response at different days after implantation, plotted in the same spatial mapping as the 4×4 grid. Solid lines are the averaged response for each experiment for a given transistor. Dashed vertical lines indicate the start time of the LED visual stimulus.

3.3.5 Assessing recording fidelity of gSGFETs

The I_{ds} - V_{gs} transfer curve (TC) determines the coupling of signals in gSGFETs. If the transfer characteristics are known, the voltage change that induces a given transistor current change can be determined, yielding distortion-free recordings [124, 125]. Ideally the TC should remain unchanged during the recording session. However, in reality the TC might not be stable over time, either due to extrinsic factors to graphene, such as electrode reference drift or changes in the array to brain tissue adhesion, or due to intrinsic factors such as graphene degradation. Hence, applying a TC obtained at the start of a recording might not represent the real transfer characteristics at a later time, hampering the distortion-free calibration of the recorded signals. To be able to evaluate the consequences of non-stable transfer curve on signal fidelity, we measured the TC at both start and end of the recording session and analyze the stability of the transfer characteristics. A methodology for determining how TC changes affect signal distortion is implemented, validated with theoretical predictions and used to illustrate how different types of changes affect the recording fidelity. Finally, this methodology is used to estimate the distortion produced by the observed *in vivo* TC changes during hours-long *in vivo* recordings.

Evaluation of gSGFET *in vivo* transfer curve stability

The stability of the transfer curve of epidural gSGFETs after more than 2 hours of *in vivo* recording has been studied. In most cases, the TC was stable (Fig. 3.9A left), while in others changes could be observed. To quantify the variations of the transfer curve, three parameters were analyzed: the CNP, the conductivity at the CNP (σ_{CNP}) and the transconductance at -0.1 of the CNP (GM01). Fig. 3.9B displays the density plots of the occurrence of the variation in CNP and the relative percentage change of the σ_{CNP} and GM01 for five different experiments. Results show a small <15 mV shift in CNP and $<5\%$ variation of σ_{CNP} and GM01 for some experiments while for others changes up to 40 mV and 10% can occur. The results indicate that gSGFET transfer curve are mostly stable in *in vivo* conditions and during hours-long recordings. Moving forward, research towards understanding the mechanisms underlying what causes the changes observed in some cases could be beneficial to further improve stability.

Understanding how transfer curve changes affect recording fidelity

During recording, the TC of a gSGFET can suffer transformations such as lateral drift or transconductance attenuation. To assess how a non-stable transfer curve affects recording fidelity, the effect of signal recording is modelled using a similar

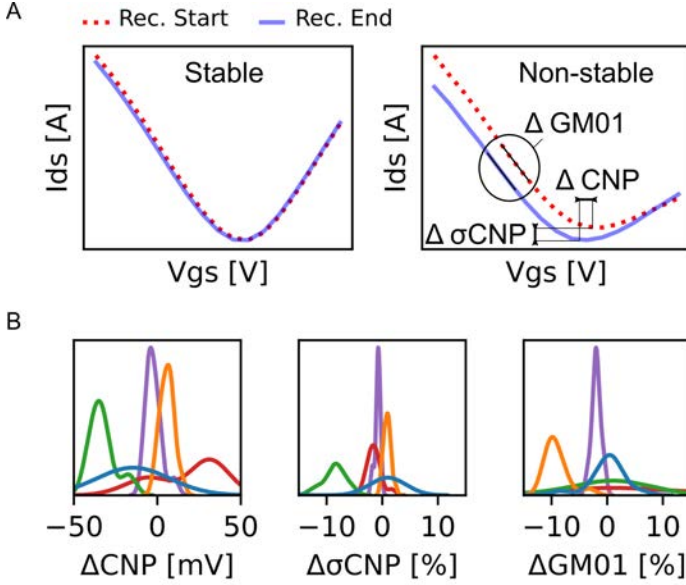


Figure 3.9: gSGFET transfer curve stability after >2h epicortical recording session. A: *in vivo* measured transfer curves at start (red dotted line) and end (blue line) for two different transistors (left: very stable experiment, and right, case where larger changes to the transfer curve occurred). B: Quantification of the changes occurred in the transfer curve of graphene transistors of 16-ch epicortical arrays during a >2h recording session. The density plots show the occurrence of the variation in CNP and the relative percentage change of the minimum conductivity (σ_{CNP}) and transconductance at -0.1 V of the CNP (GM01) for five different experiments (different colors).

procedure that the one used to validate the calibration methodology by interpolation (Sections 3.2 and 3.2). To model a time-varying effect, a different TC is used to transform the input signal (10 mV, 10 Hz sinusoidal) at a given time step ($V_{\text{sig}}(t)$) into current ($I_{\text{ds}}(t)$). The TC at time t is determined by a time-dependent TC using a linear TC transformation between the initial and final TC. Then, to convert back to voltage, the unchanged TC (that of time $t=0$) is used, simulating the calibration with a TC at the start of the recording. This methodology allows to compare the known input signal with the one obtained with a gSGFET in which their transfer characteristics have progressively changed during a recording session. Spectral analysis is used to compare the time-dependent evolution of the signal and the presence or not of harmonic distortion.

The impact of three different TC transformations was studied: lateral voltage shifts, vertical shifts and shape changes. Lateral shifts were observed to cause only an offset of the recorded signal, without introducing signal distortion (Fig. 3.10).

This is true as long as the lateral shift causes the biasing voltage to remain in the range of the measured values of the same TC branch, i.e. to not cross the CNP nor go beyond the maximum current measured at the TC extreme of that branch.

Opposite to the previous discussion, any vertical shift or shape changes in the gSGFET TC distort the recorded signal (see spectrograms from Fig. 3.11 and 3.12). Vertical shifts can even cause the impossibility of interpolation in the TC if the biasing points yields currents that are outside the measured TC. Overall, the analysis shows that shape changes and vertical shifts are the main transformations of TC causing signal distortion, while voltage shifts are distortion-free.

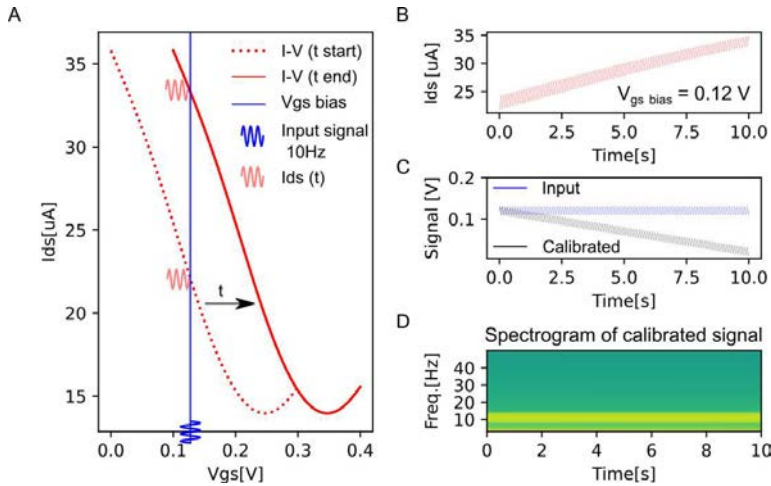


Figure 3.10: Effect of a progressive lateral drift of the transfer curve on the recorded signals. A: Initial transfer curve (red dotted line) and end transfer curve (red line). Red thin line represents the current change caused by a lateral shift of the transfer curve while recording a 10 Hz, 10 mV sinusoidal. B: Current signal resulting from the transfer curve variation and the input signal. C: Input signal (blue) and calibrated signal (black) as obtained from interpolation of the current signal into the transfer curve at $t=0$. D: Spectrogram of the calibrated signal. No distortion is observed due to the lateral shift.

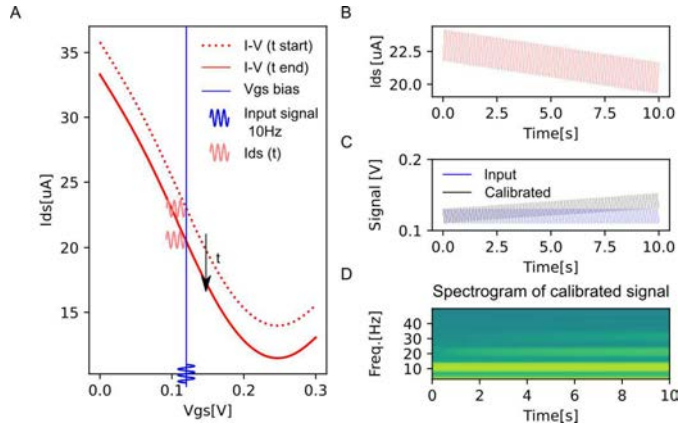


Figure 3.11: Effect of a progressive vertical shift of the transfer curve on the recorded signals. A: Initial transfer curve (red dotted line) and end transfer curve (red line). Red thin line represents the current change caused by a vertical shift of the transfer curve while recording a 10 mV sinusoidal. B: Current signal resulting from the transfer curve variation and the input signal. C: Input signal (blue) and calibrated signal (black) as obtained from interpolation of the current signal into the transfer curve at $t=0$. D: Spectrogram of the calibrated signal. Distortion of the signal increases with time due to the vertical shift.

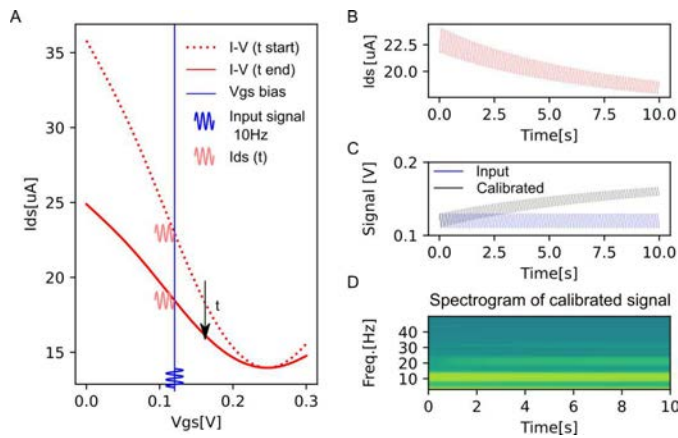


Figure 3.12: Effect of a progressive shape change of the transfer curve on the recorded signals. A: Initial transfer curve (red dotted line) and end transfer curve (red line). Red thin line represents the current change caused by a shape change of the transfer curve while recording a 10 Hz, 10 mV sinusoidal. B: Current signal resulting from the transfer curve variation and the input signal. C: Input signal (blue) and calibrated signal (black) as obtained from interpolation of the current signal into the transfer curve at $t=0$. D: Spectrogram of the calibrated signal. Distortion of the signal increases with time due to the shape change.

Effect of the observed *in vivo* transfer curve changes on recording fidelity

Using the same methodology presented in the previous sections, how the observed TC changes during hour-long *in vivo* recordings (see Fig. 3.9) affect the recorded signal has been studied. For that, the recording of a 10 mV peak, 10 Hz pure sinusoidal is simulated using the TC at the end of the recording and calibrated using the TC obtained at the start of the recording. By comparing the calibrated signal to the known input signal it is possible to assess the amplitude changes and harmonic distortion introduced by the gSGFET which transfer curves has changed during the recording session. As we used the TC at the end of the recording for signal calibration, which represents the maximum change occurred to the TC, the obtained distortion quantifiers represent an upper bound of the real distortion introduced to the recorded signals.

To quantify the distortion, two figures of merit have been used: the relative change in peak amplitude and the total harmonic distortion (THD) (see Section 1.3.4 and Eq. 1.12). The box plots of the THD and amplitude variations for five different experiments are shown in 3.13. Results show that THD in most cases is below 3% while variations in amplitude are generally <10%. Overall, the results indicate that graphene transistors are adequate for high-fidelity hour-long recordings since the observed changes in their transfer characteristics do not produce significant signal distortion.

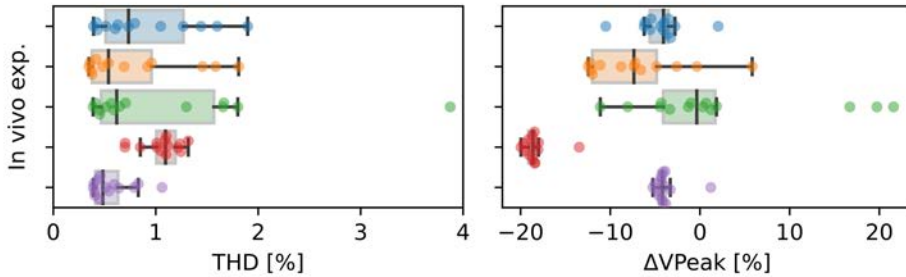


Figure 3.13: Evaluation of signal distortion due to gSGFET transfer curve changes during *in vivo* recordings. Total harmonic distortion (THD) and peak-voltage amplitude (VPeak) changes occurred to a test signal (10 mV, 10 Hz sinusoidal) to quantify the maximum distortion introduced during a >2h recording session. Box plots show the occurrence of the variation in THD and VPeak for five different experiments.

3.4 Discussion

In this Chapter, a full acquisition and post-processing methodology has been developed that allows to record *in vivo* brain activity with high-fidelity. Similar *in vivo* transconductance values ≈ 1 mS/V than those obtained in saline solutions have been obtained *in vivo* when the gSGFETs are placed on the cerebral cortex. This indicates that the conductance of the neural tissue is sufficient to ensure a good modulation of the graphene channel, and validates the experimental setup used. For the *in vivo* experiments described here, the drain-source voltage was fixed at 50 mV, leading to typical drain-source currents of few tens of μ A. Given that the channel resistance is around 1 k Ω , this results in a local heating power of less than 1 μ W. In comparison, other active technologies such as PEDOT:PSS OECTs are reported to be biased with -400 mV for the drain-source voltage and have drain-source currents of few hundreds of μ A [80]. The input power of the PEDOT:PSS transistors is thus around 80 μ W, almost two orders of magnitude higher than that of the graphene SGFETs reported here. A low input power is of utmost importance, in terms of thermal dissipation and power consumption, facilitating the scalability towards transistor arrays in which hundreds of recording transistors will be operating simultaneously.

Due to the non-linearity of gSFETs a calibration post-processing methodology has been implemented and validated that allows to record brain activity with high-fidelity. During the recording of neural activity flexible graphene SGFETs have been shown appropriate for the detection of local field potentials, attested by the clear recordings of slow wave activity (see Fig.3.4) and in awake conditions (Section 3.3.2). Importantly, the signal-to-noise ratio of graphene SGFETs is similar to the SNR of a state-of-the-art technology, platinum black microelectrodes, in particular for frequencies under 100 Hz. In the high frequency side, graphene SGFETs present a limit of detection at around 1 kHz. This limit is sufficient for the recording of local field potential.

Furthermore, it has been shown that graphene transistors can potentially be used for recording physiological and pathological activity, which has clinical applications. Moreover, a single stimulus was observed as sufficient to detect the evoked potentials thus allowing on-line treatment of the information using recognition pattern algorithms for neural prostheses [165–167]. An additional characteristic of the transistor configuration of graphene SGFETs is that they could potentially pave the way for arrays with a large number of recording sites. The current state-of-the-art technology for clinical recording of the pathological activity is based on 30 to 256 electrodes [168–170]. This implies that up to 256 wires have to go from the brain to the recording systems. One of the solutions to overcome this issue is to use multiplexed electrode arrays, which would allow to reduce the number of connec-

tions from n^2 (non multiplexed $n \times n$ array) to $2n+1$ (multiplexed $n \times n$ array). Being three-terminal active devices, transistors offer advantages over electrodes for the design and implementation of multiplexed arrays. Indeed, the design of a multiplexed array of electrodes implies a higher level of complexity because it typically requires a buffer transistor connected to the electrode [26], which is not necessary in the case of the transistor configuration. Multiplexed technology is expected to be necessary for the development of recordings over large surfaces with a high density of recording sites. Recent reports have indeed demonstrated the feasibility of multiplexing with graphene transistors [171, 172].

The achievement of a long-term neural interface is an objective of all neural interface development since chronic recordings are of paramount importance for the advance of neuroscience. The results presented in this Chapter indicate that graphene electrical properties are not degraded in contact with brain tissue. It also indicates that long-term operation of graphene transistors does not degrade its performance. To date this is the longest report of chronic use of graphene transistors *in vivo* and set a lower bound for their long-term operation at five months. Therefore, the reported results are of paramount importance and state graphene as a material for long-term neural interfacing applications.

Also in this chapter, how changes in TC affect the recording fidelity; how stable are *in vivo* measured TC and the amount of distortion that this TC changes introduce to hour-long *in vivo* recordings has been studied. Importantly, gSGFET transfer curves have been found to be highly stable in *in vivo* conditions and during hours-long recordings with generally only small $<15\text{mV}$ shifts in CNP and $<5\%$ variation of minimum conductance or transconductance. A methodology to assess recording fidelity has been developed, validated and used to estimate introduced distortion. The effect of the observed *in vivo* TC changes to signal fidelity was determined to be $<2\%$ for harmonic distortion and $<10\%$ for peak amplitude. Moving forward, research towards understanding the mechanisms underlying the causes underlying the observed changes could be beneficial to further improve gSGFET stability and recording fidelity.

3.5 Conclusions

In this Chapter, the feasibility of recording local field potentials using graphene transistors has been studied. *In vivo*, when placed on the surface of cortex for the recording of neural activity, graphene transistors exhibited signal-to-noise ratio similar to platinum black electrodes below 100 Hz. Recordings of epileptiform activity in awake mice suggest that their high SNR recording capabilities further extend into 1 kHz as determined from comparison with postmortem recordings. Moreover, the analysis of the stability of the transfer curve in acute recordings indicates that graphene transistors are adequate for high-fidelity hours-long *in vivo* recordings. Compared to microelectrode technology used for μ -ECoG, gSGFETs provide a local signal amplification and offer the possibility to develop multiplexing technology with a lower level of complexity. Moreover, the presented results show that implanted graphene transistor neural probes can chronically record evoked potentials over five months of operation *in vivo* remaining functionally operative, opening the possibility to use gSGFETs in chronic implants. Considering that graphene SGFETs combine flexibility, biocompatibility and excellent neural recording performance, gSGFET could constitute the building block of a new generation of neural interfaces that can help to advance the current knowledge and technology boundaries of *in vivo* electrophysiology.

Chapter 4

Mapping infraslow cortical field potentials enabled by graphene transistor arrays

Recording infraslow brain signals (<0.1 Hz) with microelectrodes is severely hampered by current microelectrode materials, primarily due to limitations resulting from voltage drift and high electrode impedance. Hence, most recording systems include high-pass filters that solve saturation issues but come hand in hand with loss of physiological and pathological information. In this Chapter the *in vivo* voltage stability of graphene transistors and wide frequency recording bandwidth is explored. To experimentally determine the feasibility of infraslow *in vivo* voltage sensing, slow propagating depolarization waves are induced in anesthetized rats and the recordings of epicortical graphene transistor arrays and gold or platinum black microelectrode arrays compared against the gold standard in the field, a liquid-filled micropipette. The obtained results show that graphene transistors, thanks to the direct field-effect coupling of the active transistor as well as from the electrochemical inertness of graphene, are able to map infraslow signals together with signals in the typical local field potential bandwidth, surpassing state-of-the-art microelectrode grids in terms of signal fidelity and overcoming micropipette electrode spatial mapping limitations.

Most of the contents of this chapter have been published in:

- E. Masvidal-Codina, X. Illa, M. Dasilva, A. B. Calia, T. Dragojević, E. Vidal-Rosas, E. Prats-Alfonso, J. Martínez-Aguilar, J. M. D. l. Cruz, R. Garcia-Cortadella, P. Godignon, G. Rius, A. Camassa, E. D. Corro, J. Bousquet, C. Hébert, T. Durduran, R. Villa, M. V. Sanchez-Vives, J. A. Garrido and A. Guimerà-Brunet. High-resolution mapping of infraslow cortical brain activity enabled by graphene microtransistors. *Nature Materials*, 18(3):280–288, March 2019. ISSN 1476-4660. doi:10.1038/s41563-018-0249-4. URL <https://www.nature.com/articles/s41563-018-0249-4>.

4.1 Introduction

Recently, there has been a particular resurgence of interest in fluctuations of brain activity occurring at < 0.1 Hz, commonly referred to as very slow, ultraslow or ISA [173]. ISA is suggested to have a unique neurophysiological basis [174], and to be indicative of brain states (e.g. sleep, anesthesia, coma, wakefulness) [174–176]. ISA is also correlated with resting-state networks in functional magnetic resonance imaging [177] and may significantly contribute to the high variability observed in the time course of physiological signals [178, 179]. Interestingly, cortical spreading depression (CSD) [180, 181], a slowly propagating wave of near-complete depolarization of neurons and astrocytes followed by a period of electrical activity suppression, occurs at infralow frequencies. CSD is often triggered in individuals suffering stroke or brain injury as well as migraines and recent research has shown that CSD plays a significant role in brain pathophysiology [182–184]. For this reason, monitoring electrophysiological signals below 0.1 Hz can be very valuable for clinical diagnosis, prognosis and therapy in neurocritical care [185–187].

Non-invasive techniques such as EEG and MEG have been used to study ISA [188, 189]. However, their limited spatial resolution, and averaged signal impose serious limitations, e.g. scalp EEG alone is not sufficient for CSD detection [186, 21]. Hence, invasive electrophysiological techniques are the most widely used to record infralow brainwaves. The proper recording of ISA requires the use of direct-coupled amplifiers and extremely stable and low-impedance invasive electrodes. Traditionally, liquid-filled glass micropipettes are used, which allow only one or few-point measurements [190] and therefore impose serious mapping limitations. For higher spatial resolution and mapping, non-polarizable silver/silver chloride (Ag/AgCl) electrodes could be used, which prevent charge accumulation at the interface and therefore voltage drift. However, due to the toxicity of silver, the use of such electrodes for human or chronic animal *in vivo* monitoring is not an option [191]. This has fostered the search for alternative microelectrode materials with low impedance and drift, although none has yet been found capable of offering performance comparable to Ag/AgCl electrodes [33]. Current ISA recordings in humans are performed with platinum electrodes, which challenge CSD detection due to artefacts and transients [185]. Moreover, miniaturization of electrode size to achieve higher spatial resolution may cause intrinsic high-pass filtering of ISA due to the associated electrode impedance increase [31, 32]. Other invasive optical techniques, such as calcium imaging are also used to monitor ISA, but still nowadays they present serious challenges in resolving high-frequency activity for a large number of neurons [65, 192] and their intrinsic need of indicators limits the translation to clinical use. Consequently, there is a pressing need for a technique that allows measuring large-scale, high-spatiotemporal resolution electrophysiological

signals including infralow frequencies in a potentially fully implantable, nontoxic, clinical-scale system 4.1.

As an alternative to the commonly used microelectrode technology, recording electrophysiological signals with FETs offers several advantages: they are less sensitive to environmental noise thanks to their intrinsic voltage-to-current amplification, and they can be easily multiplexed [193]. Nonetheless, the difficulties in combining high gate capacitance and carrier mobility silicon FETs with flexible materials has historically hampered their use for *in vivo* recordings [194]. gSGFETs have been proposed to potentially overcome most previous drawbacks [11]. Graphene flexibility allows gSGFETs to be embedded in ultra-soft and flexible substrates without loss of performance [195], while its wide electrochemical window and biocompatibility allows direct contact with biological fluids and tissues and ensures a safe operation in *in vivo* conditions [85]. In addition, the two-dimensional nature of graphene provides the highest surface-to-volume ratio possible, making graphene very sensitive to charges at its surface. Taking advantage of the above-mentioned properties, in Chapter 3, it has been demonstrated that gSGFETs are able to record local field potentials.

In this chapter, the potential of graphene microtransistors to record infralow brain activity by performing *in vivo* recordings where we use, gSGFETs for both epicortical and intracortical mapping of cortical spreading depression is investigated. We found that graphene microtransistors are excellent devices for recording infralow signals, performing similarly to solution-filled glass micropipettes while additionally offering the possibility of performing spatially-resolved mapping. Importantly, gSGFETs do not compromise the acquisition of signals in the conventional local field potential bandwidth, therefore allowing recording in a wide frequency bandwidth. Furthermore, we also demonstrate that gSGFET technology can be used in combination with optical techniques, such as laser speckle contrast imaging, to obtain 2-D maps of neurovascular coupling.

Technique	Infralow frequency issues	Spatial scale	Clinically trans-ferable	Chronic recordings	Ref.
Liquid-filled pipettes	-	<neuron - column	No	No	[196]
Fluor. imaging	-	neuron area	No	No	[65, 192, 197]
EEG	Artifacts Drift	area whole brain	Yes	Yes	[187, 188, 21]
ECoG	Artifacts Drift	hypercolumn - area	Yes	Yes	[198]
MEG	-	area whole brain	Yes	No	[199, 200]
MEA	Artifacts Drift Intrinsic filtering	column area	Yes	Yes	[33, 124]
gSGFET	-	column area	Potentially Yes	Potentially Yes	[124]

Table 4.1: Comparison of techniques for the measurement of infralow brain activity.

4.2 Methods

Microelectrode array fabrication and characterization

The flexible microelectrode array was fabricated in polyimide in a very similar process. Here, a Ti/Au (20/200 nm) metal layer was evaporated on a 10 μm -thick polyimide-covered four-inch silicon wafer to define the metal tracks and the microelectrodes, while a second polyimide layer (2 μm thick) was used as the passivation layer. Two subsequent etching steps were used to open, firstly, the microelectrode active areas and, secondly, to structure the polyimide in order to define the probe geometry which is the same as in [201]. Platinum black was deposited in some electrodes (Fig.4.6 a) by constant polarization amperometry. A voltage of -0.2V against a Ag/AgCl reference electrode was applied during 15 s. Impedance spectra were measured against a Ag/AgCl reference electrode using a Solartron SI 1260 equipment (Solartron analytical, UK) with 20 mV signal amplitude (Fig.4.6b).

Ethical approval and animal handling

All experimental procedures were conducted in accordance with the European Union guidelines on protection of vertebrates used for experimentation (Directive 2010/63/EU of the European Parliament and of the Council of 22 September 2010) and all experiments were approved by the ethics committee of the Hospital Clinic de Barcelona. Rats were kept under standard conditions (room temperature $23\pm 1^\circ\text{C}$, 12:12-h light-dark cycle, lights on at 08:00), with food (A04, Harlan, Spain) and water available ad libitum.

In vivo recordings

Eleven adult male Wistar rats (225-375 g) were used in this study. Animals were deeply anaesthetized with isoflurane (4% induction, 1-3% maintenance) and all pressure and incision points were infiltrated with local anesthetic lidocaine. Once under the surgical plane of anesthesia, animals were transferred to a stereotaxic frame with body temperature constantly monitored and maintained at 37°C by means of a thermal blanket. A craniotomy and durotomy were performed on the left or right hemisphere in order to record with epicortical or intracortical arrays, respectively. Additionally, a craniotomy and durotomy were performed over the prefrontal cortex to topically administer 5 mM KCl to induce cortical spreading depression. The large craniotomy was centred at 43 mm AP and 42.5 mm ML and was 6 mm AP by 4.5 mm ML in size while the smaller craniotomy, located at 50 mm AP and 42 ML, was 2.5 mm AP by 1.25 mm ML. A Ag/AgCl electrode pellet

was inserted in temporal muscle and used as reference both for recordings and for the measurement of the transistors transfer curve. All recording probes, either gSGFETs or microelectrodes, were placed directly on the cortical surface and kept in place by adherence to the tissue (Fig.4.1 a-b).

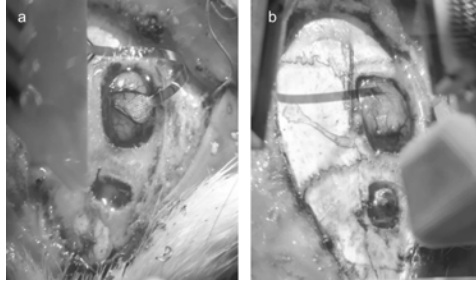


Figure 4.1: In vivo positioning of the gSGFET arrays. a-b, Photographs of the craniotomies and transistor and electrode positioning for the results shown in Fig. 4.7 and for Fig. 4.8c

A custom electronic instrumentation was used (Fig.2.9), which provides the current-to-voltage conversion and the bias control for each channel. The instrumentation splits the recorded signals into two bands with different gains: low-pass filtered (< 0.16 Hz, 104 gain) and band-pass filtered (0.16 Hz $< f < 160$ kHz, 106 gain). In the experiments where only the gSGFET array was measured the low-pass filtered signals and bias control was managed by a data acquisition system (National Instruments USB-6353), while the band-pass filtered signals were directly acquired by a commercial electrophysiological recording system consisting of a programmable gain amplifier (Multichannel Systems, GmbH) and digitizer interface (CED 1401 and Spike2 software, Cambridge Electronic Design, UK). The LPF and BPF bands were sampled at 1 Hz and 5 kHz respectively. Prior to the beginning of the recordings, the transfer curve of the gSGFET was measured in situ to determine the optimum bias point, generally around -0.1 V of the CNP.

For gSGFETs comparison experiments with microelectrodes and the glass micropipettes with Ag/AgCl wire (≈ 0.15 M Ω) a total of four subjects was used: two subjects were measured with gSGFETs, microelectrodes and a micropipette, one with gSGFETs and microelectrodes (data from Fig.4.7) and another one with gSGFETs and a micropipette (data from Fig.4.4e, and Fig.4.5). A custom Simulink model was used to simultaneously measure graphene transistors through an adapted g.HIamp biosignal amplifier (g.tec medical engineering GmbH, Austria) while microelectrodes and the solution-filled glass micropipette were recorded using an g.USBamp (g.tec medical engineering GmbH, Austria). The same reference electrode was used by both amplifiers and signals were sampled at 4.8 kHz.

Laser speckle contrast imaging

For the measurement of the regional cerebral blood flow (rCBF), a laser speckle contrast imaging (LSCI) system was used which consists of a continuous-wave temperature-controlled laser diode (785 nm, Thorlabs, Germany) for homogenous full-field illumination and a charge-coupled device camera (sc640-120fm, Basler, Germany), with an exposure time of 5 ms, which captures the diffused light scattered from the imaging area. The speckle contrast was calculated for the predefined region of interest (ROI) at each pixel in temporal domain over 100 frames, to ensure good signal-to-noise ratio. The statistics of different noise sources [202] was accounted for when calculating the speckle contrast. Speckle contrast was then related to a rCBF index (BF) as reported in [203, 204]. Finally, the relative blood flow ($\Delta rCBF$) was calculated as:

$$\Delta rCBF = \frac{(BF - BF_B)}{(BF_B)} \cdot 100[\%] \quad (4.1)$$

where BF_B corresponds to the basal regional blood flow. Fig.4.2 shows the area where LSCI was measured in Fig. 4.11c.

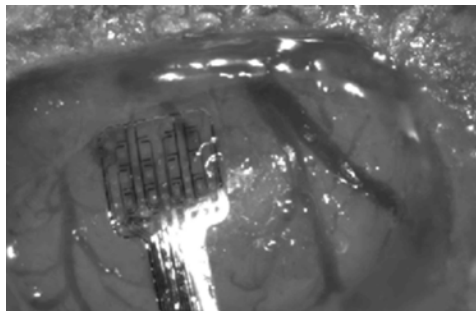


Figure 4.2: Craniotomy image of the right hemisphere of a Wistar rat for the gSGFET and laser speckle contrast imaging experiment of Fig. 4.11c.

Data Analysis

The workflow adopted for the storage and analysis of gSGFET is based on free open-source software [205]. All data were analyzed using Python 2.7 packages (Matplotlib, Numpy and Neo) and the custom library PhyREC <https://github.com/aguimera/PhyREC>. The conversion of the recorded current signals (LPF and BPF) to a voltage signal was performed by summation of both signals and interpolation in the in vivo measured transfer curve of the corresponding gSGFET.

The transfer curve was always measured, at least, at the beginning and end of every acute experiment, and generally some more transfer curves measurements were performed along the duration of the experiment. Comparison of the evolution of the in vivo measured transfer curves was systematically performed during data analysis to ensure that no significant variations are present and to detect (if there are) any misbehaving transistor. Moreover, all recordings presented in the manuscript have been calibrated with the nearest transfer curve measured (following the procedure described in Section 3.1.2) to ensure high fidelity in the voltage-converted signals.

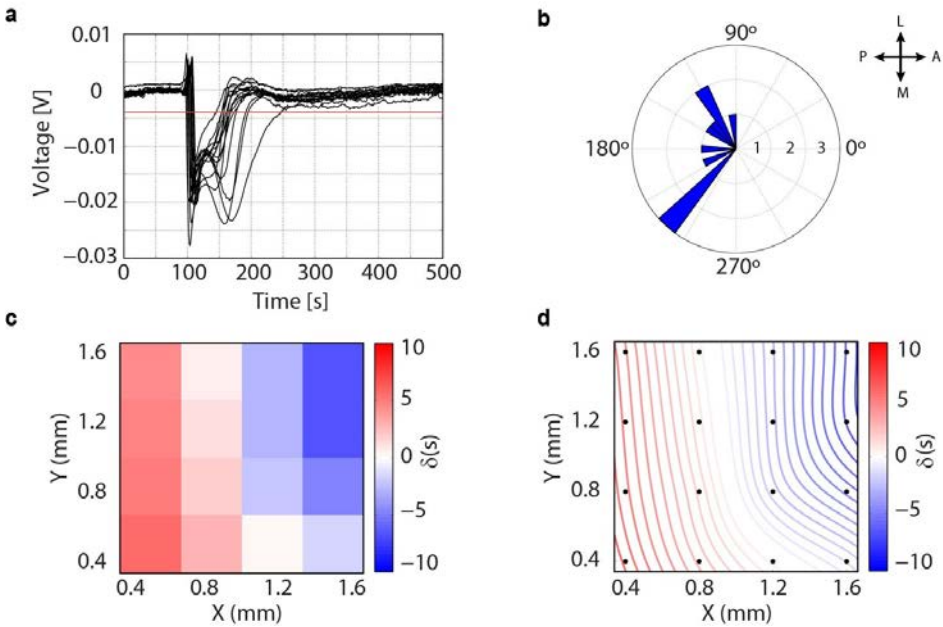


Figure 4.3: Cortical spreading depression propagation analysis. a, example of a CSD event as it is recorded by the 16-channel gSGFET array, the red line indicates the threshold voltage used for the onset detection. b, Polar histogram of the direction of the propagation of ten CSD waves recorded in two subjects; reference frame related to the orientation of the array on the cortex (A=anterior, P=posterior, M=medial, L=lateral). c, Representation of the time lags of each transistor with respect to the mean wave time of the CSD in a; color scale hints the time delay in seconds. d, Contour plot of the spatiotemporal course of the CSD in a in the range of time indicated by the colour bar.

For visualization purposes microelectrode recordings were filtered (band-stop, 48-52 Hz) and down sampled at 300Hz. For the propagation analysis, the baseline of the signal was estimated as the mean value of the signal until the positive deflection. We defined the onset of the CSD as the onset of the negative shift and detected it using a threshold (Fig. 4.3a). We defined the WaveTime of each wave

as the mean time of the triggers detected in the 16 transistors and constructed a TimeLagMatrix containing time lags for each channel computed with respect to the WaveTime (Fig. 4.3c). We interpolated the known time lags with a thin-plate smoothing spline technique (Fig. 4.11a). The velocity of the propagation has been estimated computing the gradient of the TimeLagMatrix on the grid [206]. To determine the direction of the waves, a vector starting at the point with higher negative delay (leader of the propagation) and pointing to the one with the highest positive delay (follower of the propagation) was transformed into polar coordinates to obtain the angle (Fig. 4.3b). For the colormaps of Fig. 4.11b,c and Fig. 4.12b a bicubic interpolation was performed for visualization purposes.

Reference electrode

Voltages at drain and source terminals used to operate graphene transistors are referred to the reference electrode. The reference electrode is generally grounded in anaesthetized subjects to ensure stable recordings, since the subject is grounded at many points. However, the requirement of the reference electrode to be grounded is not necessary; provided that the reference electrode is properly positioned in a non-active location and does not have drifts and oscillations that interfere with the recording, a proper operation of the graphene transistor is achieved. Importantly, gSGFETs are less sensitive than microelectrode technology to the baseline drift associated with the reference electrode. Commonly, baseline drift can lead to saturation of the amplifiers used for microelectrode DC-coupled recordings, while the operation principle of graphene transistors does not lead to saturation. The drift of the reference electrode shifts the biasing point which could lead to non-optimal performance of gSGFETs. However, this can be easily solved by changing the transistor bias to the new optimal value, which can be obtained from measuring an in vivo transfer curve.

4.3 Results and discussion

4.3.1 In vivo wide-band recordings with gSGFETs

Cortical spreading depression [182, 184, 190] was chosen to illustrate the capabilities of graphene transistors to record electrophysiological signals in a wide bandwidth. Experimentally, two craniotomies were performed over the left hemisphere of isoflurane-anaesthetized Wistar rats: a larger craniotomy over the primary somatosensory cortex, where the epicortical probe was placed, and a smaller one in the frontal cortex, where 5 mM KCl was applied locally to induce CSD (Fig. 4.4b). A custom electronic circuit allowed us to simultaneously record at two frequency bands: low-pass filtered band (LPF, $\approx 0-0.16$ Hz) and band-pass filtered band (BPF, 0.16 Hz-10 kHz) with different gains (104, and 106 respectively) to avoid amplifier saturation due to the high-amplitude CSD signal. In a first set of experiments, we recorded the LPF and BPF signals with an epicortical gSGFET array during the induction of CSD events (Fig. 4.4c). The graphene transistors were polarized in the hole conduction regime, i.e. $V_{gs} < \text{CNP}$ (negative g_m) resulting in an inversion of the recorded LPF and BPF current signals with respect to the voltage signal occurring at the gate. The LPF signal shows the very slow CSD event whereas the BPF signal corresponds to the local field potential, revealing the silencing of activity characteristic of cortical spreading depression. It is important to note that the high frequency content of the steep depolarization seen in the BPF signal at the beginning of each CSD event is generally the unique information of the CSD seen in AC-coupled recordings. After calibration the wide-band electrophysiological signal can be obtained (see Fig. 4.4a, c and Data Analysis section in Methods). The calibration procedure eliminates both the variations associated with the different current levels and the transconductance differences at the bias point between the transistors (Fig. 3.2). In each CSD event a small positive shift of 1-2 mV generally precedes the depression, immediately after which a steep negative change (≈ -20 mV) can be observed, which slowly recovers during the next minute or so. The CSD-associated silencing of high-frequency activity and its progressive recovery is shown in the voltage wave and spectrogram of Fig. 4.4d. In order to confirm the fidelity of the CSD recordings of the gSGFET technology, simultaneous recordings with a solution-filled glass micropipette with a Ag/AgCl wire were conducted. The infraslow deflection associated with CSD as measured by gSGFETs has a very similar shape, magnitude and temporal duration than the signal recorded by a micropipette (see Fig. 4.4e and Fig. 4.5: cross-correlation = 0.85 ± 0.1 for the recording of two CSD events).

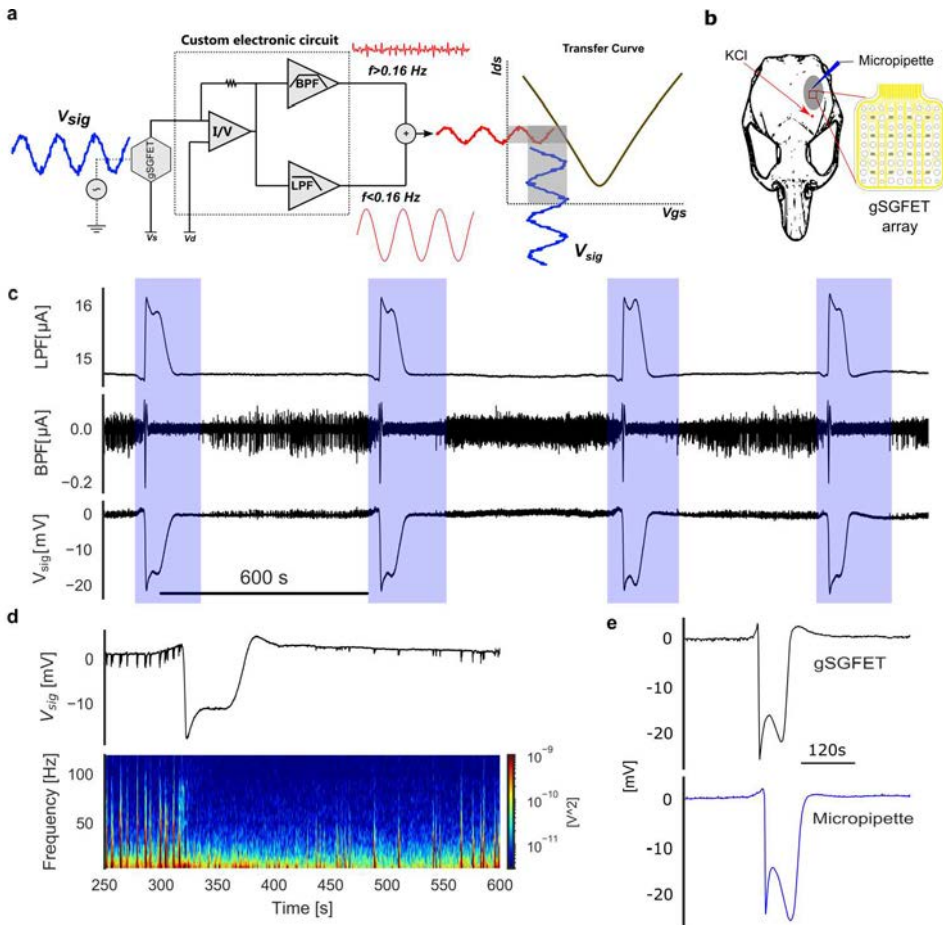


Figure 4.4: Infralow, local field potential, and wide-band in vivo gSGFET recordings of cortical spreading depression (CSD). a, Schematic of the gSGFET recording setup and signal post processing methodology. The custom electronic circuit is used to perform the in vivo characterization (transfer curve) and record the transistor current in the low-pass-filtered (LPF) and the band-pass-filtered (BPF) bands. From the combination of both signals and taking into account the current-to-voltage conversion, the calibrated wide-band signal (V_{sig}) is obtained. b, Schematic of a rat skull depicting the craniotomy (grey area), the location of the gSGFET array and micropipette as also the frontal craniotomy where 5mM KCl was applied to induce CSDs. c, Electrophysiological recordings obtained with a gSGFET epicortical array during the induction of four CSD events (blue shade). From top to bottom: LPF signal, BPF and voltage-converted wide-band signal. d, Voltage-converted wide-band signal of a CSD event recorded by a gSGFET and spectrogram showing the characteristic silencing of activity. e, Comparison of a CSD signal recorded by a graphene transistor and a solution-filled glass micropipette with a Ag/AgCl wire demonstrating the excellent similarity in shape, magnitude and time span.

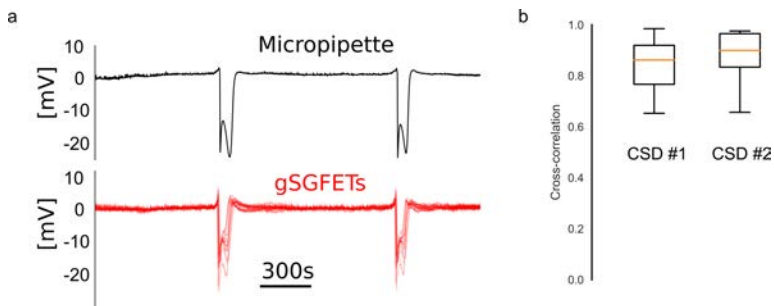


Figure 4.5: Comparison of CSD recordings by gSGFETs and a solution-filled glass micropipette with a Ag/AgCl wire. a, In vivo recordings of a 16 channel epicortical array (red lines) and micropipette (black line) for comparison. b, Boxplots of the maximum cross-correlation (center line, median; box limits, upper and lower quartiles) of the 16 gSGFETs recordings and the micropipette CSD recordings for the two CSDs in a, showing the high similarity of gSGFETs and micropipette CSD recordings. Cross-correlations were calculated using `matplotlib.pyplot.xcorr` function, matplotlib version 2.1.0, for 400 s long signals sampled at 5 Hz and centred at the corresponding CSD.

4.3.2 ISA recording capabilities with gSGFETs and microelectrodes

A second set of experiments was designed to compare the performance of gSGFETs with microelectrodes in in-vivo direct-coupled recordings. CSD was induced and simultaneously recorded with an gSGFET epicortical array located more posterior to a neural probe containing groups of triodes of 50 μm diameter gold microelectrodes 200 μm apart in which one microelectrode of each triode was modified by deposition of platinum black to lower its impedance (Fig. 4.6).

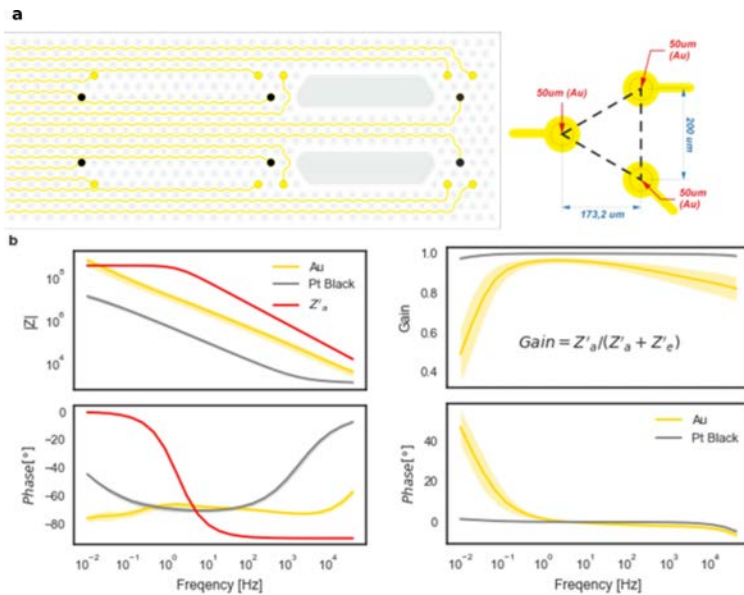


Figure 4.6: Microelectrode array layout, impedance measurements and calculated voltage gain. a, Layout of the microelectrode array used for the comparison of ultraslow frequency recordings with an gSGFET array (left), and dimensions and separation of the electrodes in each triode (right). The central electrodes that were deposited with platinum black are depicted in grey. b, Bode plot of the mean and standard deviation impedance of 9 gold and 6 platinum black microelectrodes and simulated amplifier impedance ($Z'a$, red). c, Mean and standard deviation of the voltage gain and phase calculated from the voltage divisor formed by the electrode impedance ($Z'e$) from c and preamplifier impedance.

Data shown in Fig. 4.7 corresponds to a representative experiment of $n=3$ independent subjects. Fig. 4.7a shows that gold and platinum black recordings exhibit very large and diverse baseline offsets as well as oscillations and drifts (-7.9 ± 3.3 mV/h, $n=10$ and -3.6 ± 1.6 mV/h, $n=6$), while the gSGFET signals are very stable (1.1 ± 1.0 mV/h, $n=15$). Importantly, gSGFETs record significantly higher

amplitudes for the CSD events (-13.3 ± 1.8 mV) in comparison with gold (-4.7 ± 1.6 mV) and platinum black (-3.0 ± 0.7 mV) microelectrodes. Figure 4.7b highlights one of the intrinsic limitations of microelectrode technology for the measurement of ISA: polarization-induced drift. The drift of the baseline potential superimposed over the huge voltage offsets is problematic as it can lead to saturation of the amplifiers used to record the signal. More importantly, baseline oscillations in the infralow frequencies, will potentially hamper the determination of the exact characteristics of CSD, such as amplitude or waveform, as the required high-pass filter used to remove such effects will alter the signal shape (see Fig.4.7c and Fig. 4.9).

Another intrinsic limitation of microelectrode technology is based on the relation between the microelectrode impedance and the input impedance of the recording equipment (Z'_e and Z'_a , respectively) [33, 32]. The recorded signal (V_{in}) is determined by the voltage divider formed by both impedances:

$$V_{in} = I(f)Z'_a = \frac{V_{sig}Z'_a}{Z'_a + Z'_e} \quad (4.2)$$

Eq. 4.2 implies that when Z'_a is not substantially larger than Z'_e , the recorded signals will be attenuated and shifted with respect to V_{sig} [31]. It is important to highlight that the $Z'_a \gg Z'_e$ requirement to achieve a voltage gain equal to 1 could be compromised, especially at very-low frequencies, when the electrode area is scaled down, due to the inverse relation between electrode impedance and its area, leading to high-pass filtering of the recorded signals. By measuring the impedance of both electrode types and modelling the preamplifier impedance with the values reported by the manufacturer, we obtained the voltage gain (V_{in}/V_{sig}) of the equivalent circuit formed by the recording electrode and the amplifier, see Fig. 4.8a-b.

Fig. 4.8c shows a representative CSD recorded by a gSGFET and gold and platinum black microelectrodes and the mean amplitude of the first peak for each type. For the $50 \mu\text{m}$ diameter gold microelectrodes, an attenuation lower than 50% is expected from Fig. 4.8b, which is in agreement with the experimental results. For the platinum black electrodes we tentatively attribute the higher than predicted attenuation to in vivo electrochemical processes that impact the electrode response at very low frequencies [207]. We assign the superior performance of gSGFETs to the following main reasons. First, graphene exhibits an excellent DC stability, as demonstrated by low in vivo drift. We attribute this to the low density of states of pristine graphene near the Fermi level, which decreases the overall electronic overlap with redox species [208], and to the low density of extrinsic electron transfer sites, i.e. defects and edges, all contributing to the excellent electrochemical inertness of CVD graphene [65, 90, 209]. The low leakage current measured also supports the electrochemical inertness.

The second reason why graphene microtransistors can record infraslow signals is related to their working mechanism, which is significantly different from that of electrodes. In gSGFETs, voltage oscillations near the active graphene channel modulate the current flow along it (see schematic and small-signal model in Fig. 4.8a). Eq. 4.3 shows the relation between the recorded current (I_{ds-rec}) and the signal (V_{sig}):

$$I_{ds-rec}(V_{gs}, V_{sig}) = I_{ds}(V_{gs}) + i_{ds}(V_{gs}, V_{sig}) = I_{ds}(V_{gs}) + g_m(V_{gs} + V_{sig})V_{sig}, \quad (4.3)$$

where I_{ds} is the current at the bias point V_{gs} and i_{ds} the current variation induced by the gate signal. This equation is valid and frequency-independent as long as g_m is also frequency-independent. In this work, we provide evidence that the transconductance of gSGFETs remains constant in a wide bandwidth and that this behaviour is preserved with further downscaling of gSGFETs (Fig. 4.10).

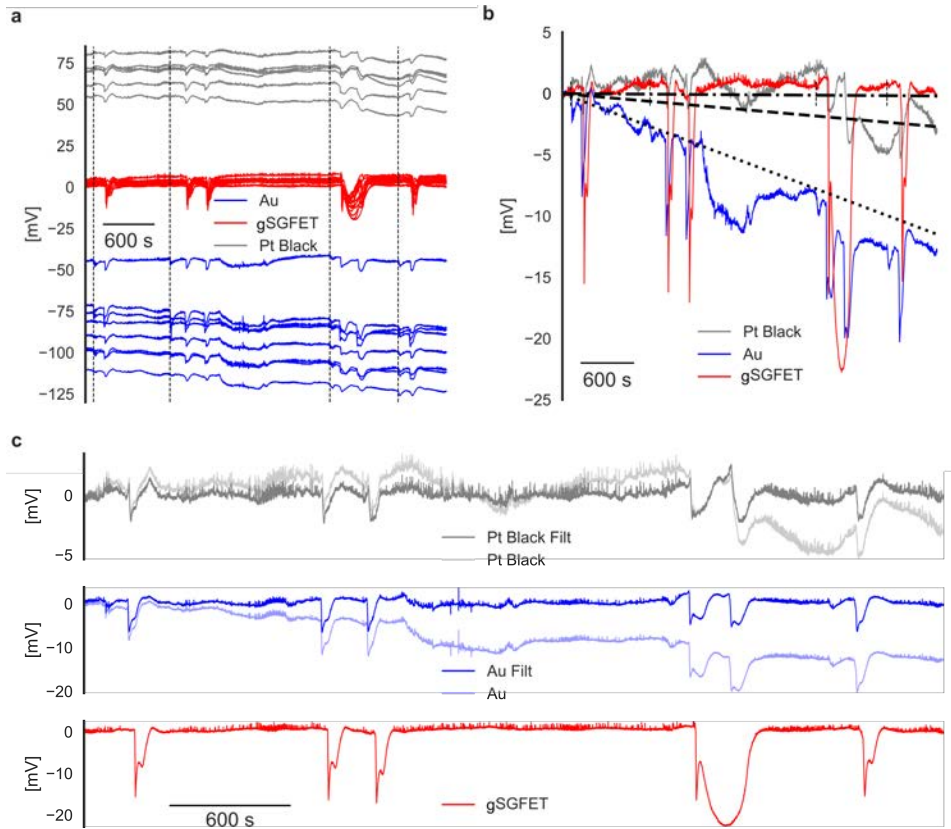


Figure 4.7: Comparison of DC-coupled gSGFET and microelectrode recordings of cortical spreading depression. a-c, Representative data of one of a total of three independent experiments. a, Direct-coupled recordings of $100 \times 50 \mu\text{m}^2$ gSGFET transistors and gold and platinum black $50 \mu\text{m}$ diameter microelectrodes. The vertical dashed lines show the time when KCl (5 mM) was applied to induce a CSD. b, DC-offset removed recordings of a representative channel of each type. Black lines illustrate the mean drift: dotted and dashed correspond to gold and platinum black microelectrodes, respectively, and the dash-dotted line corresponds to gSGFETs. c, DC-offset removed recordings of a representative channel of each type and the same signal filtered at 0.002 Hz to remove oscillations and drift; the gSGFET signal does not require any filtering and is therefore not distorted.

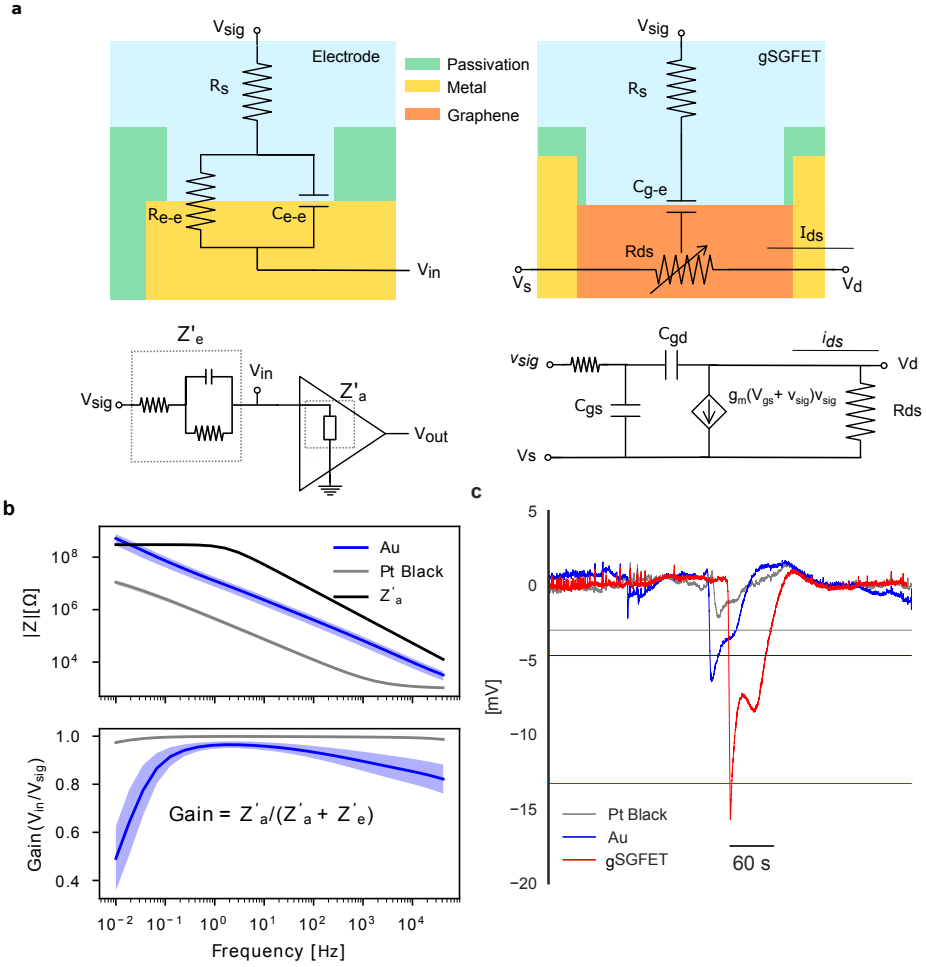


Figure 4.8: Microelectrode and gSGFET recording modes: considerations for infraslow recordings. a, Cross-sectional view and superimposed electric equivalent circuit models of a recording electrode and a gSGFET. For an electrode, the electrode-electrolyte interface, is modelled simply as a capacitor and a resistor in parallel (R_{e-e} , C_{e-e}). V_{in} , the voltage at the input of the amplifier is determined by the voltage divider formed by Z_{e}^{\wedge} and Z_{a}^{\wedge} , the effective electrode and amplifier impedance, respectively. R_s represents the electrolyte resistance. In the case of a gSGFET, V_{sig} modulates the graphene channel resistance (R_{ds}) by field-effect through the gate capacitance (C_{g-e}), which results in current variations (i_{ds}) proportional to the transconductance value at the bias point, plus the voltage signal (which is mostly negligible for small amplitude electrophysiological signals), as seen in the small signal model. b, Mean and standard deviation of the impedance module (experimental data) of nine $50 \mu\text{m}$ diameter gold (blue) and six platinum black (grey) microelectrodes together with Z_{a}^{\wedge} and calculated voltage gain (V_{in}/V_{sig}) for each microelectrode type. c, Recordings of a CSD event for each type of microelectrodes and a gSGFET. Horizontal lines represent the mean value of CSD amplitude.

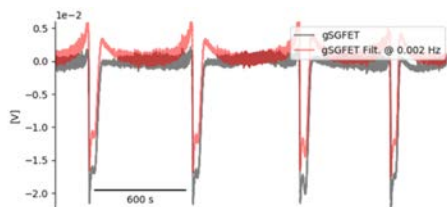


Figure 4.9: Effect of the high-pass filter needed for baseline oscillations removal in microelectrode recordings in the determination of CSD characteristics. Wide-band gSGFET recordings (grey) in which CSD are induced by 5 mM KCl and same signal high-pass filtered at 0.002 Hz (red). Signal distortion (smaller amplitude and overpeaks at the beginning and end of CSD) already occurs at such low cutoff frequency.

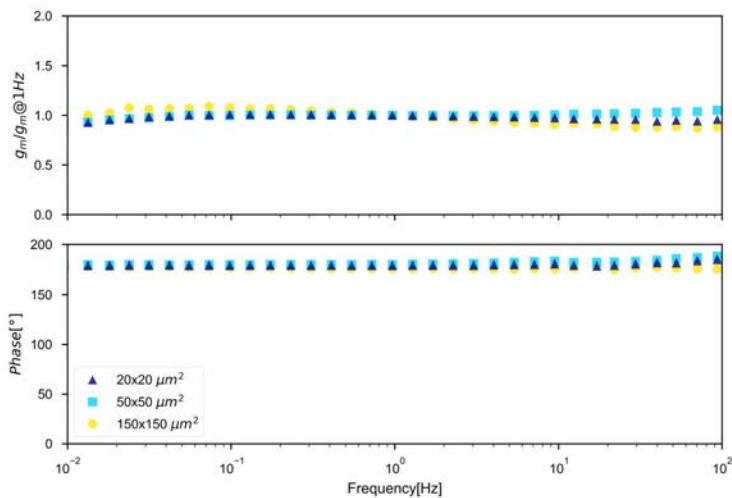


Figure 4.10: The wide bandwidth gain of gSGFETs is preserved when scaling transistor size. Transconductance normalized by its value at 1Hz for gSGFETs of different areas biased at 200 mV V_{gs} versus a Ag/AgCl reference electrode and 50 mV V_{ds} in 0.1 M PBS solution.

4.3.3 Mapping cortical spreading depression with gSGFETs

As an example of the potential of gSGFET technology, we mapped the propagation of CSD events using a 4x4 epicortical gSGFET array and compared the signals with what is observed in conventional high-pass filtered recordings (Fig. 4.11)a-b). The recording of the CSD event with the gSGFET array reveals that while the onset of the negative shift is similar for all gSGFETs, there is much more variety in the subsequent recovery, with some transistors exhibiting a second negative shift with higher amplitude than the first one. This effect can also be observed in the last two frames (corresponding to 80 s and 90 s) of the spatial maps of gSGFET recordings (Fig. 4.11b) where recovered and still depressed brain areas coexist. Importantly, this information is lost in conventional microelectrode recordings, where only the CSD onset is observed due to the high pass filter in the recording electronics. We found that the mean duration of CSD events is 47 ± 8 s and a speed of propagation of 8 ± 1 mm/min (n=10 CSD collected from two different subjects).

Under physiological conditions, there is a neurovascular response, vasodilatation and increased regional cerebral blood flow (rCBF) due to spreading depolarization that causes spreading hyperemia [182]. However, most studies on CSD neurovascular coupling have been performed with mapping techniques for the rCBF while electrical activity is measured only at two sites with glass micropipettes [177]. Here, taking advantage of the gSGFET technology, we designed an experiment in which we could simultaneously map both variables. Fig. 4.11c provides further evidence of the spreading depolarization and hyperemia neurovascular coupling. We used a non-contact, wide-field technique, laser speckle contrast imaging (LSCI) [202], that allows imaging variations of rCBF [203]. Experimentally, a craniotomy was performed in a Wistar rat and a continuous-wave temperature controlled laser diode and a camera were mounted to image a wide area inside in which an epicortical 16-channel gSGFET array was placed. After 5mM KCl administration, CSD was induced, which was followed by an increase in rCBF that slowly returned (4-5minutes) to basal values (Fig. 4.11c).

We also performed in vivo experiments with intracortical probes consisting of a linear array of 15 gSGFETs spanning the entire depth of a rat cortex (Fig. 4.12a). From both the ordered recording and the spatiotemporal voltage map (Fig. 4.12b), it can be seen how CSD occurs in the whole cortex depth. A transition from a superficial long depolarization to a shorter one preceded and followed by a hyperpolarization in the deeper layers can be clearly observed.

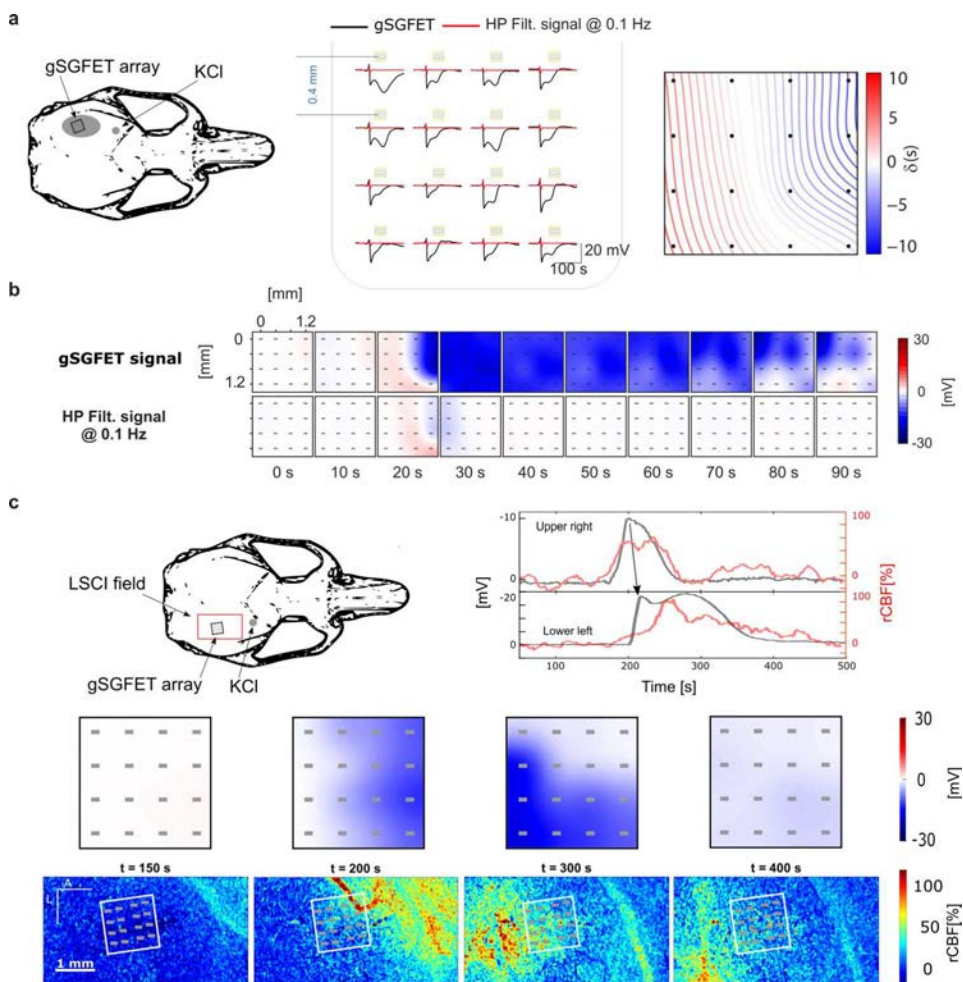


Figure 4.11: Mapping cortical spreading depression with graphene transistors. a, Infralow frequency signals recorded by a 4x4, 400 μm grid spacing, gSGFET array (black lines) during the occurrence of a CSD event as illustrated in the top left schematic. The contour plot shows the time delays of the onset of CSD with respect to the mean time illustrating the spatiotemporal course of the CSD. b, Interpolated spatial voltage maps showing the propagation of the same CSD event as measured by the gSGFET array. a,b High pass filtered recordings at 0.1Hz (red lines in a and bottom spatial voltage maps in b) are included to illustrate the loss of signal information in conventional microelectrode recordings. c, Schematic of a rat skull depicting the laser speckle contrast imaging field-of-view and the position of the gSGFET array. Electrical recordings and optical imaging were performed directly on the cortical surface. Time evolution of the upper right and lower left graphene microtransistors as well as the regional cerebral blood flow (rCBF) measured at the same position showing their co-occurrence. Colour maps represent the spatial value of the extracellular voltage as measured by the gSGFET array (top) and the rCBF (bottom) at a given set of times after the induction of a CSD event. Representative data of one of a total of two independent experiments.

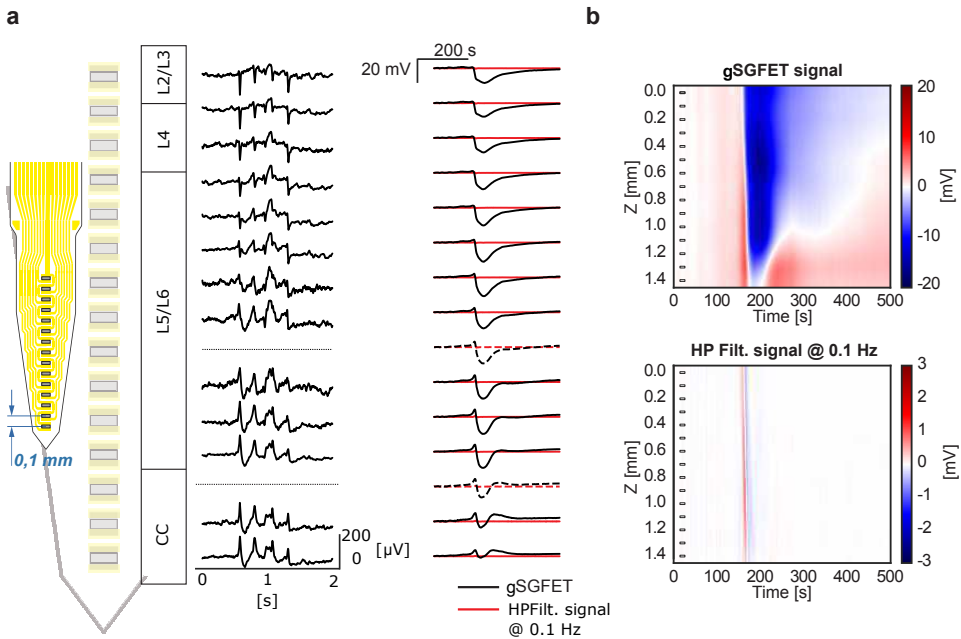


Figure 4.12: Depth profile of the infralow-frequency voltage variations induced by cortical spreading depression in a rat cortex. a, Layout of the fabricated 15-channel graphene intracortical probe and ordered local field potential recordings. Infralow-frequency recordings (black lines) during the occurrence of a CSD event. Dashed lines, have been interpolated from nearby transistors. Depth position is indicated by the layer number and corpus callosum (CC). b, Colour maps of the temporal course of the infralow changes during a CSD event across the depth of a rat cortex. a-b, Same signal high-pass filtered at 0.1 Hz (red lines) and their spatio-temporal colour map are included to illustrate the loss of information in conventional microelectrode recordings.

4.4 Conclusions

In this Chapter we have shown that gSGFETs can record neural signals in a wide electrophysiological bandwidth, from infralow (<0.1 Hz) frequencies to the typical local field potential bandwidth, similar to solution-filled glass micropipettes but with the capability of overcoming their spatial sampling limitations. Importantly, this capability does not depend on a given transistor size but is preserved among a wide range of device sizes, which brings freedom when designing an array for a given application. There are two main reasons that explain this unique recording capability: the direct DC-coupling of transistors, in contrast to standard passive electrodes; and the excellent electrochemical stability of graphene. Making use of these features, gSGFET technology opens the possibility of mapping infralow oscillations with high fidelity and spatial resolution (epicortically and intracortically). This can lead to a better understanding of the brain regions where ISA is initiated, its propagation to other areas and a clarification of the interplay of different cellular types, which are still poorly understood [173, 174, 210]. Additionally, the wide recording bandwidth of gSGFETs can help in determining the relation between ISA and higher frequency signals [189, 211] and contribute to a better understanding of the genesis of local field potentials [46] and of cortical wave propagation features [212, 206].

Since 2014, work exploiting both the transparency and electrical conductivity of graphene has allowed simultaneous local field potential recordings using graphene microelectrodes, and imaging or optical stimulation at the same position, which has profound implications in neuroscience [65, 107]. Our work demonstrates that graphene transistors can be used together with imaging techniques, such as LSCI to map infralow electrophysiological signals and regional cerebral blood flow. This combination of techniques holds great potential and can contribute to a better understanding of neurovascular coupling phenomena.

In the particular case of CSD, where no non-invasive electrophysiological technique has been demonstrated capable of its monitoring, the adoption of invasive DC-coupled electrode recordings has been proposed to provide further diagnostic information and easy and direct detection of CSDs [185]. gSGFET technology emerges as a potential preclinical as well as clinically relevant tool to help determine the relation of CSDs to neural disorders such as migraine, malignant stroke, subarachnoid and intracranial haemorrhage, and traumatic brain injury. If the challenges of translating gSGFET technology to the clinics, such as chronic and safe operation and human compatibility are surpassed, gSGFETs could be applied in neurointensive care monitoring [184, 186] or for CSD intraoperative monitoring since there is evidence that CSD can occur during neurosurgical procedures [213]. Importantly, in contrast to electrodes where a signal is needed to measure elec-

trode impedance, the possibility to measure the characteristic transfer curve of a gSGFET in vivo at any time, allows assessing the stability as well as the signal coupling magnitude (transconductance) during an implant lifetime, therefore easing the evaluation of its chronic performance. In summary, our work demonstrates that gSGFET arrays are ideal candidates to fill the gap of a large-scale, high-spatiotemporal recording technology that covers a wide electrophysiological bandwidth in a potentially fully implantable, nontoxic, clinical-scale device. By measuring the full bandwidth of brain activity with high spatiotemporal resolution we will be able to improve our understanding of brain function in health and disease status, and develop better diagnostic and therapeutic procedures for those affected.

Chapter 5

Graphene transistor arrays for CSD research

Cortical spreading depression (CSD) is a neurophysiological phenomenon that is associated with worsening outcomes in multiple neurological pathologies including epilepsy, migraine and stroke. Current gold-standard electrophysiological CSD monitoring methodology relies on single-point measurements, which prevents thorough examination of the spatiotemporal properties of CSD propagation and correlated neuronal activity changes in various regions of the brain. Anaesthesia additionally complicates preventative pharmacological screening approaches. In this chapter an *in vivo* assay that permits repetitive rounds of optogenetically-induced CSD in awake mice allowing pharmacological intervention assessment is reported. Using graphene transistor arrays enabled full bandwidth electrographic recordings and high-fidelity mapping of CSD initiation and propagation. CSDs waveform have been categorised during repeated rounds of induction. Moreover, proof-of-concept pharmacological modulation of CSD by NMDA receptor antagonists has been demonstrated. Through skull CSD detection is demonstrated allowing both to induce and record CSDs non-invasively in mice. Overall, the results presented in this chapter demonstrate the usefulness of grids of graphene transistor arrays as an experimental methodology to study CSD, setting gSGFETs as a useful tool for neuroscience research.

Most of the contents of this chapter have been published in:

- E. M. Codina, M. Smith, D. Rathore, Y. Gao, X. Illa, E. Prats-Alfonso, E. D. Corro, A. Bonaccini, G. Rius, I. Martin-Fernandez, C. Guger, P. Reitner, R. Villa, J. A. Garrido, A. Guimera and R. C. Wykes. Characterization of optogenetically-induced cortical spreading depression in awake mice using graphene micro-transistor arrays. *Journal of Neural Engineering*, 2021. ISSN 1741-2552. doi:10.1088/1741-2552/abecf3

5.1 Introduction

Spreading depolarization is the largest disruption of brain homeostasis possible in living neural tissue. It is characterized by an abrupt, near-complete breakdown of the transmembrane ion gradients and high-amplitude (tens of mV) negative extracellular potential shift that persists for tens of seconds [182]. Cortical spreading depolarization is usually accompanied by temporary suppression of brain activity, although in some severe conditions, where tissue is compromised, spreading depolarizations can trigger epileptiform activity [214]. We use the term cortical spreading depression (CSD) in this manuscript to describe a propagating wave of cortical depolarization that is accompanied by transient suppression of neuronal activity. CSDs contribute to the pathophysiology of several neurological diseases, including stroke [215], epilepsy [216] and migraine with aura [217, 218] where the characteristics of the propagating wave, the duration of neuronal suppression and the degree of neural injury are determined by the local conditions of the tissue [219].

Given the importance of CSDs to various neurological diseases, development of novel technology that permits electrophysiological detection of CSDs, (both the spreading depolarization and the subsequent depression of neural activity), with high spatiotemporal resolution and its application to study these events in awake brain is warranted. Experimentally, CSD is traditionally electrographically recorded using solution-filled glass micropipettes with Ag/AgCl wires which limits the spatial resolution to just a few-point measurements. Microelectrode grids improve spatial resolution but suffer from polarization-induced drift and signal attenuation causing distortion of the measured signal [31]. As an alternative to the commonly used passive electrode technology, active transducers based on transistors can offer significant advantages in electrophysiology [66]. In particular, graphene solution-gated field-effect transistors (gSGFETs), demonstrate comparable signal-to-noise ratio to platinum black electrodes in typical local field potential frequencies [220, 126]. Additionally, due to excellent stability in aqueous solutions, gSGFETs offer the possibility of wide-bandwidth electrographic recordings including DC-shifts and infraslow oscillations that are superior to those recorded by passive grids of electrodes and comparable to those obtained using glass micropipettes with silver/silver-chloride electrodes [124].

Existing experimental models to induce CSD often rely upon direct chemical (potassium chloride), mechanical (pinprick), or electrical stimulation of the cortex. CSD threshold is difficult to determine using mechanical stimulation and the above methods can all result in tissue damage and injury [221]. Repeated trials may result in cumulative tissue damage affecting reproducibility and reliability, as well as altering thresholds required for CSD induction. Non-invasive optogenetic induction

of CSD has recently been reported using transgenic expression of channelrhodopsin [222, 223](Chung et al., 2019, Houben et al., 2017). We have adapted this approach using viral vectors to target opsin expression unilaterally to neurons of the motor cortex, and establish that this approach can be used to reliably and repeatedly trigger CSD on demand in awake mice.

Therapies targeting CSD may potentially treat a range of neurological conditions. However, many drugs identified from preclinical studies result in translational failure [224]. In vivo drug discovery approaches have often been performed under anesthesia. As general anesthesia may impact on spreading depolarization frequency, propagation speed and sensitivity to pharmacological suppression [225], an in vivo, anesthesia-free assay, which permits repeated, reproducible rounds of CSD, will greatly improve the translatability of pre-clinical findings. Current evidence points to the essential role of NMDA receptors in CSD generation and propagation [226]. Therefore, to determine the feasibility of our model as a drug screening platform we investigated the efficacy and modulation of CSD by NMDA antagonists.

To avoid confounds associated with a craniotomy required for epidural array placement, we investigated a minimally invasive approach to measure CSDs electrophysiologically in awake rodents. We report the practicability of recording CSD through mouse skull using gSGFET transistor arrays.

Overall, this study establishes the feasibility and advantages of applying graphene micro-transistor technology to characterize CSD induced in awake brain as well as the repetitiveness and reliability of optogenetic CSD induction. Application of this in vivo approach in disease-relevant models, including familial hemiplegic migraine and ischemic stroke, will allow characterization of CSDs induced by the underlying pathology, the ability to trigger additional CSDs on demand, evaluate pharmacological interventions, and record localized CSD waveforms and propagation patterns in awake brain.

5.2 Materials and methods

Animal preparation

Animal experiments were conducted in accordance with the United Kingdom Animal (Scientific Procedures) Act 1986, and approved by the Home Office (license PPL70-13691). C57Bl/ mice (38 males and 6 females) were bred and the majority ($n = 33$) were used at ages of ≈ 3 -6 months (140.6 ± 4.65 days), while a subset ($n = 11$) were used at an age of ≈ 7 -9 months (250.0 ± 7.259 days), due to lab closure resulting from the Coronavirus pandemic ($p = <0.001$, ***; Unpaired

T-Test). Animals were housed on 12 h/12 h dark/light cycle, and food and water were given ad libitum. Animals were group housed until their headbar attachment surgery and were then subsequently individually housed. For all procedures, animals were weighed before being anaesthetized in a chamber using isoflurane (100% w/w; 988-3245, Henry Schein, U.S.A.) and placed in a stereotaxic frame (David Kopf Instruments Ltd., U.S.A.). Viscotears (Bausch + Lomb, U.S.A.) were applied to each eye and both pain relief, consisting of Buprenorphine (0.5 mg / Kg; Subcutaneous; Ceva, France) and Metacam (15 mg / Kg; Sub-cutaneous; Boehringer Ingelheim, Germany and 0.5 mL of saline, and dexamethasone (1 mg / Kg; Subcutaneous; MSD Animal Health, U.S.A.) were given. All surgical procedures were performed using sterilized tools and aseptic techniques. At the end of the surgical procedure, warmed saline (0.15 mL / 10 grams) was administered sub-cutaneous. Mice were checked daily and recovered for at least a week before experiments commenced, with the exception of the craniotomy surgery, where recording occurred on the same day, 2-4 hours post-surgery.

Surgeries for Viral Injection and Headbar Attachment

The skin on top of the skull was cut away. The skull was cleaned using a delicate bone scraper (10075-16; Fine Science Tools, Germany) and brief topical application of hydrogen peroxide (6%). Small bur-holes were drilled in the following two positions from bregma: 1) Antero-Posterior: +2.2 mm; Lateral: +1.0 mm and 2) Antero-Posterior: +0.75 mm; Lateral: +1.6 mm. To express channelrodopsin 2 (ChR2), high titer ($1 \cdot 10^{13}$ vg/mL) AAV9-hSyn-ChR2-EYFP virus (*AAV9_hSyn_hCHR2(H134R) – EYFP*; 26973, Addgene, U.S.A.) was diluted 1:1 in 0.9% NaCl and delivered using a 5 μ L syringe (Model 95 Hamilton Company, Switzerland) with a 35-gauge needle. At both sites, the needle tip was lowered from pia until 500 μ m deep. Using a microinjection pump (WPI Ltd., U.S.A.), 500 nL was injected at 100 nL / min to achieve expression in both layer 5 and layer 2/3 pyramidal neurons. To apply the headbars for the Neurotar system a small hole in the skull over the left visual cortex was drilled for a metal support screw (00-96X3-32, Plastics One, U.S.A.). Using vetbond (1469SB, 3M, U.S.A.), the headplate (Model 9, Neurotar, Finland) was firmly attached and strengthened using dental cement before Kwik-cast (W.P.I., U.K.) covered the exposed skull. Mice were checked daily to ensure recovery. Habituation was performed by placing the mouse in the Neurotar mobile-home cage for increasing periods of time (15-60 mins) over several days the week prior to craniotomy surgery.

Surgeries for craniotomy

Due to lab closure as a result of Covid19 the amount of time cortical neurons

expressed Chr2 prior to optogenetic experiments varied. Pre-Covid the average length of time from viral injection to experiment was 59.61 ± 3.142 days, $n = 33$ animals, and post-Covid this was extended to 175.9 ± 2.959 days, $n = 11$ animals ($p = < 0.001$, ***; Unpaired T-Test). There was no difference in the intensity of light required to induce a CSD (threshold) between the two groups, 34.26 ± 7.971 mJ, $n = 33$ animals pre-Covid versus 33.15 ± 15.76 mJ, $n = 11$ animals post-Covid, ($p = 0.255$; Mann-Whitney Unpaired T-Test).

On the day of recording, craniotomies were performed. Three areas were exposed: 1) a large (2x2 mm) craniotomy over somatosensory and visual cortex on the right-hand side, 2) the skull was thinned or removed over the motor cortex ipsilateral to the main craniotomy, and 3) a small drill hole over the motor cortex on the left-hand side (contralateral to main craniotomy) [Fig. 5.1. B]. After completion, exposed dura was covered with cortex buffered saline, sterilized sylgard 184 ($\approx 200 \mu\text{m}$ thickness), and a kwik-cast layer. After ≈ 2 -4-hours post-recovery, the animal was moved to the Neurotar frame and the craniotomies were exposed by removal of the kwikcast and sylgard.

Electrophysiological recordings

Electrophysiological recordings were performed using flexible gSGFETs arrays. The transistor arrays were carefully connected to a PCB and lowered onto the dura or skull using a micromanipulator. Whereas most currently available electrodes are passive, gSGFETs are active devices that transduce local voltage changes to current and permit a wide recording bandwidth [124]. A custom g.HIamp biosignal amplifier, (g.RAPHENE, g.tec medical engineering GmbH Austria) was used for signal acquisition at 9600 kHz and 24 Bit. The system enables simultaneous recording in two frequency bands with different gains preventing amplifier saturation. Prior to recording, $I_{\text{ds}}\text{-}V_{\text{gs}}$ curves were obtained at the start and end of each experiment to allow determination of the performance of the gSGFET and custom code was used to calculate the optimal bias point (average across the arrays of the maximum of the mean absolute transconductance left from charge neutrality point). Subsequent interpolation of acquired current signals into the transfer curve results in DC- coupled voltage signals.

A reference wire (Ag/AgCl2) was placed in the contralateral motor cortex. An LED cannula (400 μm diameter, CFM14L20, Thor Labs, New Jersey, U.S.A.) was lowered via a manipulator over right-hand side motor cortex. For some experiments ($n = 8$), two transistor arrays were used (Methods - Assays using Dual gSGFETs, Figs. 8-9) and larger craniotomies were performed as required for the protocol.

Determination of light threshold for optogenetically-induced CSD and array calibration.

Prior to experimentation the LED current-to-power relationship was calibrated using a power meter (PM16-130, Thor Labs, New Jersey, U.S.A.), and mW values were multiplied by the duration (seconds) of stimulation to obtain a measurement of light power in mJ. After 10-minutes of baseline recording, the light-threshold required to induce a CSD was determined using continuous 5 or 10s stimulations of blue light (470 nm; M470F3, Thors Labs, New Jersey, U.S.A.). Controls were performed using the same power intensity and duration with a green LED (595 nm; M595F2, Thors Labs, New Jersey, U.S.A.) or by using pulse blue light (20 Hz, 50% duty cycle) with a combined light-on duration identical to the square pulsed light duration (5 or 10s), (Fig. 5.1G).

Inclusion criteria

63 mice were prepared for this study. 44 mice (38 male, 6 female) showed reproducible induction of CSD from light stimulation and were included in this manuscript. The remaining 19 mice were excluded for the following reasons: 8 animals because the initial light-evoked CSD was followed by at least one spontaneous CSD. Post-mortem analysis of these animals revealed lesions through sub-cortical (motor) white matter tracts, indicative of accidental damage during surgery (data not shown). 4 animals were excluded as it was not possible to evoke a light induced CSD and 3 animals were excluded due to an inability to trigger a repeatable CSD every trial. Post-hoc analysis of these brains revealed a marked reduction in transduction volume (Fig. 5.2). No data was obtained from 4 mice due to hardware or software problems during experimentation.

Comparison of CSD induction methods

CSD was induced in the motor cortex by the following three methods: 1) Optogenetic 2) pinprick of a 35-gauge Nanofil injection needle (NV33BV-2, World Precision Instruments, U.S.A.) attached to a Nanofil Injection system (UMP3T-1, SMARTtouch Microinjection System, World Precision Instruments, U.S.A.) or 3) injection of 1000 nL, at a rate of 100 nL / second, of 1 M KCl into the superficial layers of the cortex ($\approx 500 \mu\text{m}$ deep from pia; using aforementioned injection system). For this protocol, the order above was used each time, due to the trauma caused from pinprick, which was required for local injection of KCL.

Pharmacological screen assay

The lowest LED current found to induce a CSD twice was multiplied by 1.5 to ensure that optogenetic induction was supra-threshold throughout the experiment. Inter-induction interval was set to 10 minutes to allow full recovery of neuronal activity (Fig. 5.3D). Two baseline light-induced CSDs were followed by a randomized I.P. administration of a substance, either: vehicle (Saline; 0.5 mL), MK801 (3 mg/Kg; 10009019, Cayman Chemical, Michigan, U.S.A.), or Ketamine (15 mg/Kg, Dechra, U.K.). A minimum of 6 post-injection light stimulus were delivered. Analysis of neural activity was conducted post injection of NMDA antagonists. One animal injected with ketamine showed no change post-injection in power (theta), similar to saline injected animals, and in contrast to all other animals injected with either MK801 (n=5) and ketamine (n=3), and was excluded from the study due to concerns that the i.p injection failed, and drug did not reach the brain. To check for a difference in the stimulation thresholds between treatment groups we compared the OptoThreshold and this was not significantly different between treatment groups (Vehicle, 13.18 ± 4.99 mJ; MK-801, 18.00 ± 4.99 mJ; Ketamine, 4.55 ± 2.17 mJ), ($p = 0.0591$, Kruskal-Wallis ANOVA).

Assays using Dual gSGFETs

To explore the neurophysiology at the site of induction of the CSD, experiments were performed with arrays over both the motor cortex and somatosensory/visual cortex (n = 3; Fig. 5.8). Here, a larger craniotomy was completed over the motor cortex to facilitate the placement of the gSGFET. Some experiments were conducted to compare recording CSD through the skull with subdural recordings (n = 5; Fig. 5.9). Here, the craniotomy for on dura placement was narrower and over the precise neuroanatomical area of interest.

Transduction volume calculations

The experiment was terminated using a sodium pentobarbital overdose (i.p. injection). Brains were removed and placed into 4% PFA (J19943.K2; Alfa Aesar, U.K.) chilled at 4 degrees overnight. Coronal sections at 50 μ m thickness were cut using a vibrating microtome (Leica, Wetzlar, Germany). Sections were mounted using Vectashied (2B Scientific Ltd). Tiling images were acquired using a Zeiss Axio Observer inverted widefield microscope and Zen microscope software (ZEISS), with 10x objective at 1024 x 1024 pixels resolution. All images were acquired using the same microscope parameters for analysis purposes. Cortical fluorescence distribution in coronal slices was quantified using ImageJ. The cortex was manually selected as the region of interest and an intensity threshold, consis-

tent across animals applied. Pixels above this value were counted with total area in mm² calculated based on pixel dimensions and magnification. Using the Allen Mouse Brain Atlas, each slice was binned based on distance from bregma. The transduced area within each slice was taken as a representation of the surrounding posterior 250 μ m of tissue. The total transduction volume (mm^3) was calculated as the summation of each 250 μ m volume.

gSGFET arrays

Flexible epidural neural probes (10 μ m in thickness) containing an array of 16 graphene micro-transistors (4x4 array, 400 μ m separation) with active areas of either 150 x 100 μm^2 , 100x100 μm^2 or 50x50 μm^2 were used in this study. gSGFET arrays were fabricated at the clean room facilities of IMB-CNM as reported in [124]. In brief, single-layer graphene was grown by chemical vapour deposition and transferred to a silicon wafer previously coated with a polyimide layer and patterned metal traces. After defining the graphene channels and before evaporating a second metal layer, UVO treatment was applied to improve the graphene-metal interface and reduce its contact resistance [118]. Finally, SU-8 was used as passivation layer and the polyimide layer was etched to define the geometry of the neural probes. Devices were gently peeled off from the wafer and inserted to zero insertion force connectors for electronic interfacing.

Data Analysis

Recorded signals were analyzed using Python 3.7 packages (Matplotlib 3.2.0, Numpy 1.17.4, Pandas 0.25.3, seaborn 0.9.0, Neo 0.8.0) and the custom library PhyREC (PhyREC4, <https://github.com/aguimera/PhyREC>). Transistor recordings were calibrated by interpolating the current signals into the corresponding branch of the in vivo measured transfer curve as reported in [124]. For 2 experiments the signal interpolation to the transfer curve was not possible due to insufficient measured voltage range or presence of artefacts, for these experiments the gain at the V_{gs} bias point of the transfer curve for each transistor was used. No high pass filtering is applied to the recorded extracellular potentials for the analysis of CSD waveforms, extraction of CSD parameters or plotting to avoid any signal distortion. Error bars in all plots represent standard error.

CSD Parameter extraction

For each CSD extracellular voltage shift the following parameters were extracted: latency, peak amplitude, duration and Area under the curve (AUC). Raw signals were down sampled to 3 Hz and zero voltage was set to the average value of the

5s before the light stimulus. We defined the onset of the CSD as the onset of the negative shift with a threshold at -4 mV. Latency was calculated as the difference between the starting stimulation time and CSD onset. Peak amplitude was defined as the minimum value of the wave and reported as an absolute value. CSD duration was defined as the time that the extracellular voltage remained below -4 mV; it was determined using below and above thresholds. AUC was defined as the area below zero voltage during the duration of the depolarization determined. CSD propagation speed was estimated as the distance between the LED induction site and the middle of the transistor array (4mm) divided by the mean latency CSD onset. Code available upon request.

CSD Wave Propagation direction

To determine the direction of propagation, a vector pointing from the lowest to highest latency values in the transistor array matrix was used. A threshold of 2.5 standard deviations from the mean of the latencies was set to remove outliers that could distort the direction of propagation. The angles between the propagation vector of the first induced CSD and the subsequent ones was determined by $\angle(x, y) = \arccos(\langle x, y \rangle / \|x\| \cdot \|y\|)$, where x and y are the two vectors.

CSD band analysis

For each CSD extracellular voltage shift, the calibrated raw signals were either not filtered for full-band or bandpass filtered for the different bands (Delta: 1-4 Hz, Theta: 4-8 Hz, Alpha: 8-12 Hz, Beta: 12-30 Hz and Gamma: 30-100 Hz). Then, root mean squared (RMS) was calculated using a sliding window (window size: 0.5 s, steptime= (window size)/10) and resulting traces were passed through a median filtering (`scipy.signal.medfilt`) to remove artefacts. RMS values for each band were averaged at given epochs with respect to the LED stimulation (referred as 0s), the depolarization onset (t_{onset} , defined as the time extracellular voltage goes below -4 mV of the raw signal) and the depolarization end (t_{end} , defined as the time the extracellular voltage crossed again the -4 mV). The epochs are: before the LED stimulus (bf.: -100s to -10s), few seconds after (aft.: 0s to $t_{onset}-10$ s), depolarization onset (onset: $t_{onset}-10$ s to $t_{onset}+10$ s), depolarization (dep.: $t_{onset}+10$ s to t_{end}) and recovery 1 to 7 being every minute after the end of the depolarization (r1: t_{end} to $t_{end}+60$ s; r2: $t_{end}+60$ s to $t_{end}+120$ s, etc.). To evaluate the neural effects of CSD, RMS power values were normalized with respect to the bf. timepoint. Values for each transistor in the array over multiple CSD events were averaged to yield a single value for each experiment.

CSD shape clustering

To classify the different shapes of the depolarization waves, raw signals were resampled at 10 Hz. Signals from -30 to 400 s around each light-stimulus were extracted and zero voltage was set to the average value of the 30s before the light stimulus. A threshold of -4 mV was used for CSD detection. Then, all detected waves were time aligned to the minimum of the (first) depolarization peak (0 s) and epochs from -50 to 140 s extracted. Depolarization voltage is defined as the mean voltage value between -1 to 1 s. Then, three features were selected to perform the clustering: integral of the prehyperpolarization (area >0 mV in the -15s to 0s), integral of recovery hyperpolarization (area >0 mV in the 0s to 75s) and the second to first peak amplitude ratio. The second peak was detected during the 100 s after the first peak by finding the valley (with the minimum of the first derivative) and then searching from the minimum of voltage after the valley. Based on these three features waveforms were clustered by defining a threshold for each group: first they were classified as DP (second to first peak amplitude ratio >0) or SP. Then DPh (PreHyper >1); DP (PreHyper <1); SPh (RecHyper >1) and others were classified as SP, LV if amplitude was lower than -6mV or ND if a depolarization was not detected at that channel.

Statistical Analysis and Experimental Design

In these studies, the variable of interest was isolated and statistically examined. In general, for comparisons between groups of two, unpaired or paired T-tests were used, while for three or more groups, ANOVA with post-hoc corrections were utilized. To examine the frequency of evoked CSDs for different optogenetic stimulations [Fig. 5.1], since the same animals were used in a non-randomized fashion for each modality, Fisher's exact test was used to compare between groups. For comparing the parameters of CSDs to different modalities [Fig. 5.4], each animal, either male or female, was given the same sequential treatment (due to the nature of induction methods), with at least a single CSD being evoked to each modality. With this data collected, a 1-way ANOVA was run to compare between 1) genders, and 2) groups. As genders showed no differences between induction using either Optogenetics, Pin-prick from a needle, or injection of KCl, the data from each gender was combined to allow for a more informed comparison between modality types. Examining the change in normalized frequency bands between the different CSD shapes [Fig. 5.5] utilized the 2-way repeated measures ANOVA with Sidak's post-hoc comparisons for both 1) Sub-types and 2) Combined sub-types. For the pharmacological study [Fig. 5.7] parameters (Amplitude), a 2-WAY repeated measures ANOVA was used with Sidak post-hoc comparisons. Examining the time response profile for recording at the site of induction also utilized a 2-WAY repeated measures ANOVA with Sidak's post-hoc test to examine the differences

between responses over the 10-seconds of optogenetic stimulation and up until recovery of the voltage. To examine electrophysiological recordings between epidural and skull positioning of the gSGFET, the two arrays were placed and optogenetic stimulation was applied in the motor cortex [Fig. 5.9]. As the CSD propagated across the brain, it was recorded at both sites. Signal-to-noise-ratio (SNR) was calculated as the ratio of the peak CSD amplitude to the standard deviation of the 30 seconds prior to CSD induction. To compare the SNR, an artificial SNR level was set to 3, with slight variation around this, and then a 1-way ANOVA with Tukey's post-hoc test was used to compare this regularly used artificial SNR level to the SNR from epidural and skull gGFET recordings. Next, for other parameters such as amplitude, AUC, and propagation velocity (pro. Vel.), Welch's, unpaired, T tests were used to examine whether there were differences between recording sites. Finally, 2-way ANOVA was used to compare normalized frequency band activity at the two recording sites. Throughout the manuscript standard significance classifications were used (* = $p < 0.05$; ** = $p < 0.01$; *** = $p < 0.001$).

5.3 Results

5.3.1 Optogenetic CSD model in awake head-fixed mice

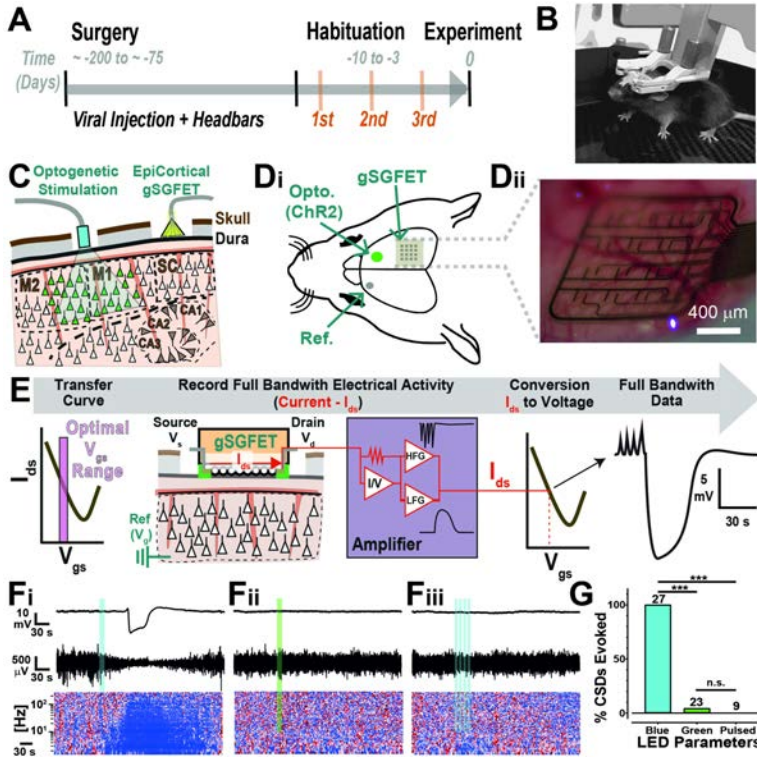
The experimental paradigm for triggering light-induced CSDs in awake mice is illustrated in Fig. 5.1A. Surgery was performed to inject viral vector to transduce neurons in the motor cortex and express light-sensitive channelrhodopsin (ChR2) (see methods, Fig. 5.2). Head bars were attached and in the week prior to experimentation mice were habituated to the head-fixation apparatus over several days (Fig. 5.1. B). To detect CSD, a 16-channel gSGFET was placed on the dura over somatosensory and visual cortex posterior to the ChR2-injected area (illustrated in Fig. 5.1. C-D). Before recording, a transfer curve is obtained that is used to determine the optimal recording settings and also for post-recording current-to-voltage conversion (Fig. 5.1. E and methods).

Continuous 488nm blue light illumination (5-10s) reliably induced CSD (Fig. 5.1. Fi), note the correlated activity suppression shown in the high-pass filtered signal and in the corresponding z-scored spectrogram. To examine the specificity to light wavelength and stimulation parameters we used a green LED 594nm (Fig. 5.1. Fii) with the same light duration and power intensity that successfully evoked a CSD with blue light, or used pulsed blue light (20 Hz) with a total light-on duration identical to the square pulsed light duration (Fig. 5.1. Fiii). Whereas constant blue light illumination always evoked a CSD, pulsed blue light or continuous green light rarely evoked a CSD (Fig. 5.1. G). This indicates that a sustained neuronal depolarization, caused by a single, seconds long square pulse stimulation with blue light in ChR2-expressing areas is an effective and robust mechanism of CSD induction.

Examination of viral transduction volume post hoc revealed that expression of cortical tissue, greater than 1 mm³, was required to express ChR2 to reliably induce CSD optogenetically (Fig. 5.2). Viral injections were variable in the total volume of tissue transduced (5.46 ± 1.7 mm³ n=5 animals) but consistently transduced the area of motor cortex from +0.5 to +2.5 mm (anteroposterior coordinates relative to bregma) where the optic fiber light was positioned during experiments. Light intensity required to trigger a CSD ranged 5.89 to 147.6 mJ, with mean of 33.98 ± 7.065 mJ (n = 44 animals).

CSD parameters were extracted from individual micro-transistors (Fig. 5.3. A). High amplitude (14 ± 0.3 mV) negative shifts in the recorded extracellular voltage lasting tens of seconds (46.0 ± 1.2 s) in duration were recorded. Data corresponding to 633 CSD waveforms recorded from a total of 54 CSDs (2 CSDs evoked in each of 27 animals). However, as the histograms indicate (Fig. 5.3. B)

there was a large degree of variability in these parameters, the 25-75% range for amplitude and duration were 9.8 to 16.4 mV, and 28.9 to 50.2 s respectively. This variability reflects the heterogeneity in CSD waveforms recorded (see Fig. 5.5). In contrast, propagation speed was more consistent, 3.0 ± 0.1 mm/min, (2.8 – 3.3 mm/min, 25-75% range). Light-evoked CSDs in the motor cortex also induced transient changes in local field potential (LFP) activity. For these experiments we recorded CSDs in areas of propagation, somatosensory and visual cortex (Fig. 5.1. C-D). Within seconds of light stimulation, a gradual decrease in 1-30Hz RMS power could be detected, minutes before the actual CSD invaded the area of the brain underneath the transistors. In contrast, gamma RMS power (30-100Hz) increased just prior to CSD invasion, indicative of intense neuronal firing preceding the massive depolarization and subsequent neuronal silencing (Fig. 5.3. C-D) similar to an increase in multi-unit activity previously reported [223]. The rate of recovery of neuronal activity post CSD were similar for frequencies 1-30 Hz with full recovery evident 4 mins after the end of the DC-shift. In some recordings there was a prominent increase in gamma RMS power 30-100 Hz upon recovery indicative of rebound excitation (Fig. 5.3. D, Fig. 5.5. D).



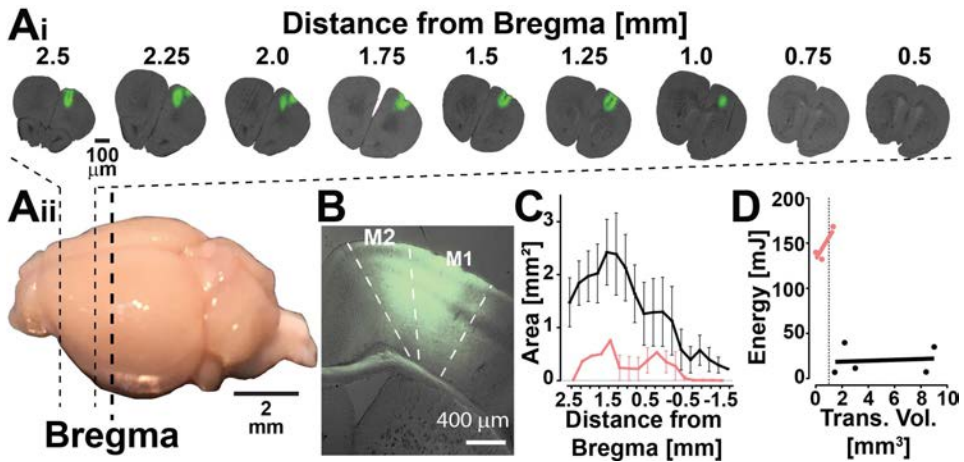


Figure 5.2: Representative example and quantification of AAV9-ChR2 transduction volume. Ai-ii: (Ai) Representative example of cross-sections through a mouse brain expressing AAV9-hSyn-ChR2-EYFP with the distance (mm) from bregma. A(ii) Image of a mouse brain showing the approximate neuroanatomical location of the slices used for analysis in Ai. B: Higher magnification fluorescent image showing expression of AAV9-hSyn-ChR2-EYFP in M2 and M1. C: Quantification of area of viral transduction plotted as the average area calculated per 250 μ m blocks of tissue from the front of the brain until expression decreases beyond bregma. Black line illustrates the transduction volume extracted from animals where optogenetically induced CSDs could be repeatedly and reliably evoked using low light power, $n = 5$ mice. The red line illustrates the transduction volume from mice where an optogenetically induced CSD was not possible $n=2$, or not consistently evoked $n = 1$. D: Plot between transduction volume [mm^3] and energy [mJ] required (black), or tested (red) for optogenetic induction of CSDs, $n = 8$ mice. The dashed line indicates 1 mm^3 . The 2 filled red dots represent animals with a transduction volume calculated to be less than 1 mm^3 and it was not possible to induce a light-induced CSD. The open red circle represents data from an animal where an optogenetically induced CSD could be evoked but not consistently, even at maximum light power.

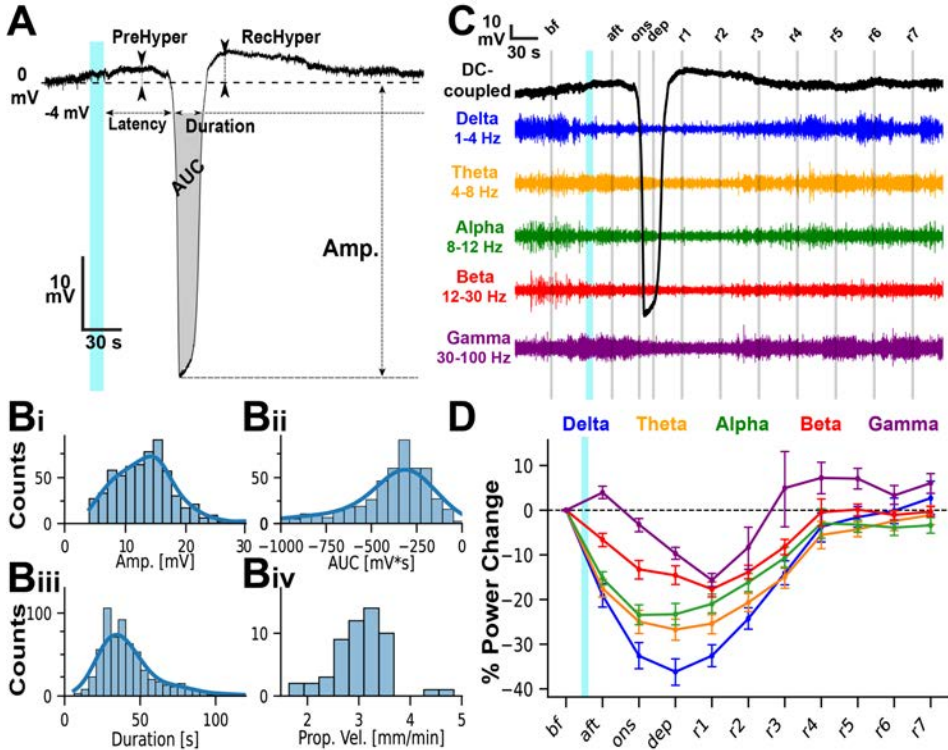


Figure 5.3: Waveform properties and frequency band analysis of optogenetically-induced spreading depression in awake mice. A: Example of a CSD waveform recorded by an individual graphene transistor, highlighting the parameters extracted including duration, amplitude, latency from delivery of LED light, area under the curve (AUC), prehyperpolarization (PreHyper) and recovery hyperpolarization (RecHyper). Bi-iv: Histograms, with a line showing the population estimate, of CSD parameters for amplitude (Bi), Area Under the Curve (Bii), duration (Biii) and propagation velocity (Biv). Bi-Biii includes a total of 633 CSD waveforms recorded from 54 CSDs events (2 CSD events induced in $n = 27$ mice), while Biv is derived from the same 54 CSD events. C: Extracellular voltage depolarization (black line) and filtered voltage of different neural frequency bands (Delta 1-4 Hz, Theta 4-8 Hz, Alpha 8-12 Hz, Beta 12-30 Hz, Gamma 30-100 Hz) during a CSD event recorded by a gSGFET. Vertical grey lines indicate middle point of the epochs: before light stimulus (bf), immediately after (aft), at onset (ons), at maximum depolarization (dep), and every minute after the end of the depolarization (r1-r7). The vertical scale bar y axis is 3mV for the DC coupled trace (black); for the other frequency bands is as follows: Delta: 0.6mV, Theta: 0.4 mV, Alpha: 0.2 mV; Beta: 0.3 mV; Gamma: 0.15 mV. D: Average change in the frequency band root mean square (rms) voltage normalized with respect to the bf. timepoint. There is an immediate and progressive silencing for delta-theta band and an immediate increase in gamma band rms after light stimulus. Data from the same CSD events shown in panel B, grouped by mice ($n = 27$).

5.3.2 Comparison with more invasive CSD induction methodologies

The electrophysiological features of optogenetically-induced CSDs in virally-injected mice were compared to standard induction methodologies including direct application of KCl to the brain and pinprick in the same animal (Fig. 5.4. A-C). CSD waveform parameters (i.e., peak amplitude, duration and area under the curve (AUC) values were not statistically different between CSD induction types, nor between male and female mice. These values (Fig. 5.4. D) are within previously reported ranges for KCl-induced CSDs in non-virally-injected, wild-type mice [227]. However, although there is no difference in the duration or AUC of CSDs between groups, we did observe a difference in the time taken for activity suppression in frequencies above 1Hz to fully recover (Fig. 5.4. E). Compared to optogenetic and pinprick induced CSDs, recovery from KCl-mediated CSD was significantly slower (Fig. 5.4. E).

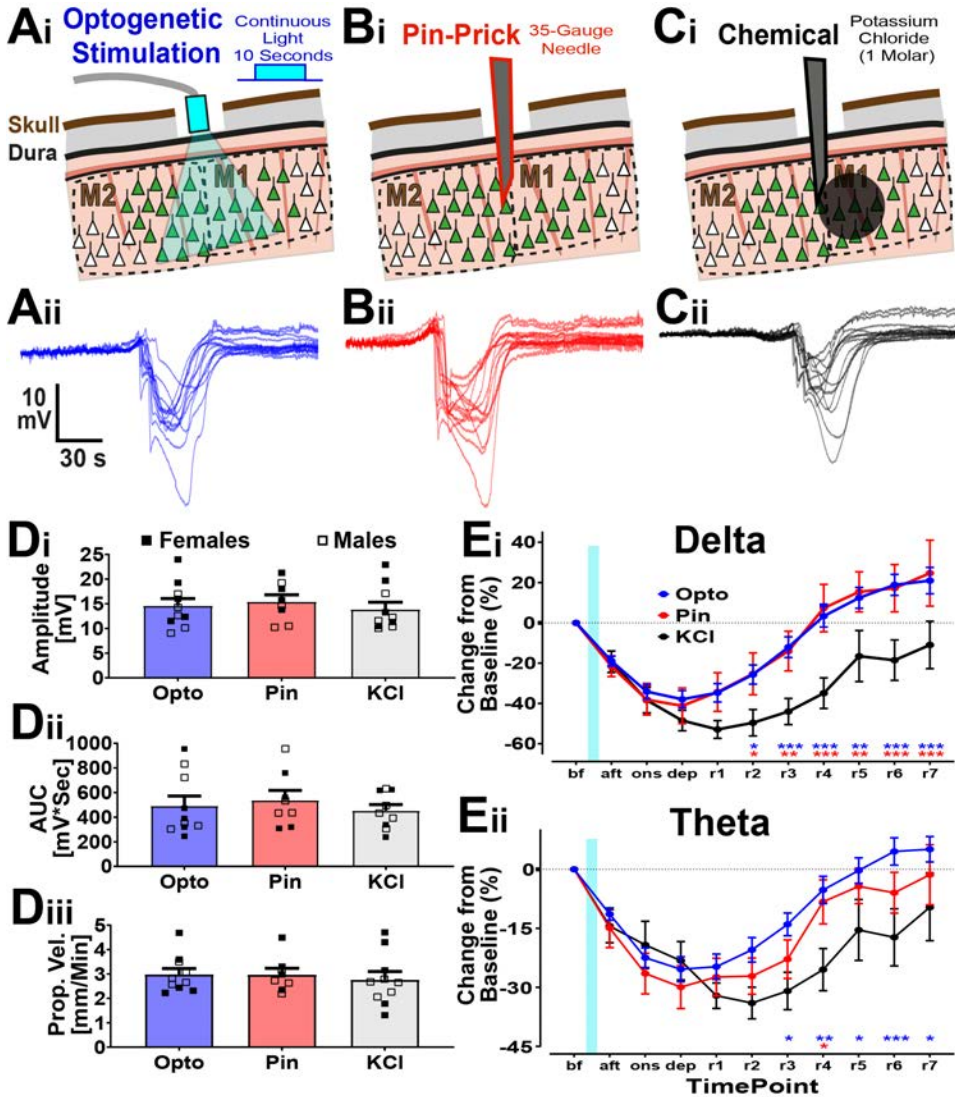


Figure 5.4: Electrophysiological comparison of gender and method of induction for cortical spreading depression in awake mice. A-C: Schematics (i) and raw traces (ii) showing CSDs induced using different modalities: optogenetic (A), pinprick (B), or potassium chloride ($1\mu\text{L}$ at 1M) injection (C). The traces come from the same animal. D: Comparison of the Amplitude (Di), AUC (Dii), and Propagation velocity (Diii) of CSD from induction by Opto (blue), Pinprick (red) and KCl (grey) and, also, gender with females (closed squares) and males (open squares). No statistical difference was found between genders, or between waveform characteristics of CSDs induced by different methods. E: Normalized, to the before CSD timepoint, rms band changes during CSD for the Delta (Ei) and Theta (Eii) frequency bands displayed. $n = 5$ male and 5 females for Opto and KCl, and 4 male and 4 females for Pinprick. For E, statistics used a mixed-model effects analysis with Sidak's post-hoc tests. Asterisk are color-coded depending on the CSD-induction type that is compared against KCl.

5.3.3 CSD waveform analysis

Due to the mapping capabilities of the gSGFET arrays, we observed variability in CSD amplitudes and duration (Fig. 5.3. B), resulting from distinct waveform patterns. Fig. 5.5. A displays the CSD waveform captured by 14 individual transistors as a CSD propagated over the array. Some waveforms have a single peak, whereas others present a double peak. An additional feature is the presence of either a pre- or post- CSD hyperpolarization. We obtained a database of 2323 CSDs waveforms recorded from 224 optogenetically-induced CSD events from 26 mice. We analyzed three waveform features pre-hyperpolarization (F1), recovery post-hyperpolarization (F2) and second-to -first peak amplitude ratio (F3) to classify the recorded waveforms into 4 different clusters: DP (double-peak), DPh (double-peak hyperpolarization), SPh (single-peak), SPh (single-peak hyperpolarization) and a 5th category where the CSD was of low amplitude (<6 mV peak), (Fig. 5.5. B-E and methods). The high channel number and low-invasive induction methodology of our preparation allowed us to study the occurrence and spatial distribution of each waveform. Under our recording conditions, using ‘normal’, non-disease model mice, single peak accounted for 84% of waveforms split similarly between SP and SPh (42% each). DP and DPh were less common (10%), 5% each. Double peak waveforms (DP and DPh) had a higher duration and amplitude than single peak waveforms (SP, SPh) (Fig. 5.5. E) and interestingly, also a faster rate of depolarization (data not shown). DPh was the cluster with the highest values in all parameters tested. We performed frequency band analysis on the waveform types and observed that double peak waveforms caused a higher percentage of activity suppression compared to single peak waveforms (Fig. 5.5. F-G). The arrays were predominately placed in areas of propagation. In these locations no spatial distributional trends across the grid for specific waveforms were identified.

We examined the reproducibility of repeated optogenetic stimulation (Fig. 5.6. A). Separation between light stimulations was set to ten minutes to allow recovery from transient silencing of neural activity (Fig. 5.3. D). Fig. 5.6. A displays 14 transistor recordings from one animal in response to 8 optogenetic stimulations. In contrast to AC-coupled, or DC-Coupled passive electrodes which encounter baseline drift and require either high-pass filtering or electronic off-set readjustments [228, 31], gSGFETs are able to record repeated rounds of CSD over several hours with minimal baseline drift (0.16 ± 0.9 mV/10 minutes, $n=6$ animals), highlighting the superiority of this methodology for long (hours) continuous recordings (Fig. 5.6. A). We analyzed the propagation patterns of CSD across the transistor array (Fig. 5.6. B), and categorized the CSD waveform recorded from each transistor for repeated trials. Overall CSD waveform remained stable with roughly the same percentage of events classified as single peak and double peak, although SPh waveforms decreased and SP waveforms increased during repeated stimulations (Fig.

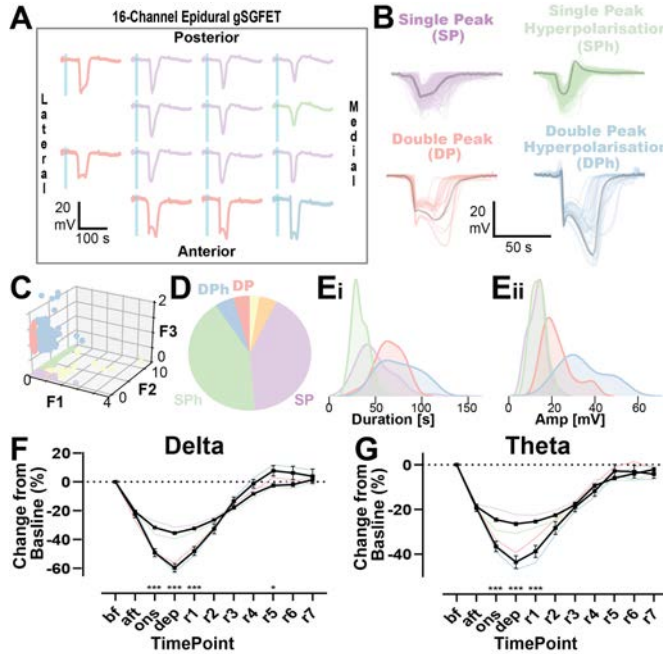


Figure 5.5: Classification of distinct CSD Waveforms recorded using 16-Channel gSGFETs as a CSD propagates through cortex. A: 14-channels from a gSGFET array recording an optogenetically induced CSD. Different waveforms can be observed across the grid. These can be categorized into 4 clusters (panel B) and color-coded. B: CSD Waveforms for each of the four clusters DP (red), DPh (blue), SPH (green), SP (purple). DP=double-peak; SP: single-peak, h=hyperpolarization. Bold lines in black highlight an example case for each group. C: 3D scatterplot of the three features used for clustering (F1: Prehyperpolarization, F2: recovery posthyperpolarization and F3: Second to first peak ratio. Dots are colored to indicate the clusters, as described in B, with orange showing low voltage (< -6 mV). D: Pie chart showing the frequency of the four different clusters, with colors the same as in B and C. Orange indicates the percentage of non-detectable waveforms. E_i-ii: Density plots of the distribution of Duration (i) and Amplitude (ii) extracted from the waveforms for each cluster. F-G: Rms changes, normalized to baseline, during CSD in the Delta (F) and Theta (G) frequency bands. All 4 CSD types are graphed, with grey lines showing combined single and black line combined double peaks. ANOVA with Sidak's post-hoc tests were performed.

5.6. C_{ii}), and there was a trend towards more double peaks by stimulation 7 and 8. Fig. 5.6. D shows an angular histogram of the difference between the propagation direction of any CSD and the direction of the first induced CSD of that experiment. Results indicate very small changes in the propagation angle over repeated optogenetic stimulations.

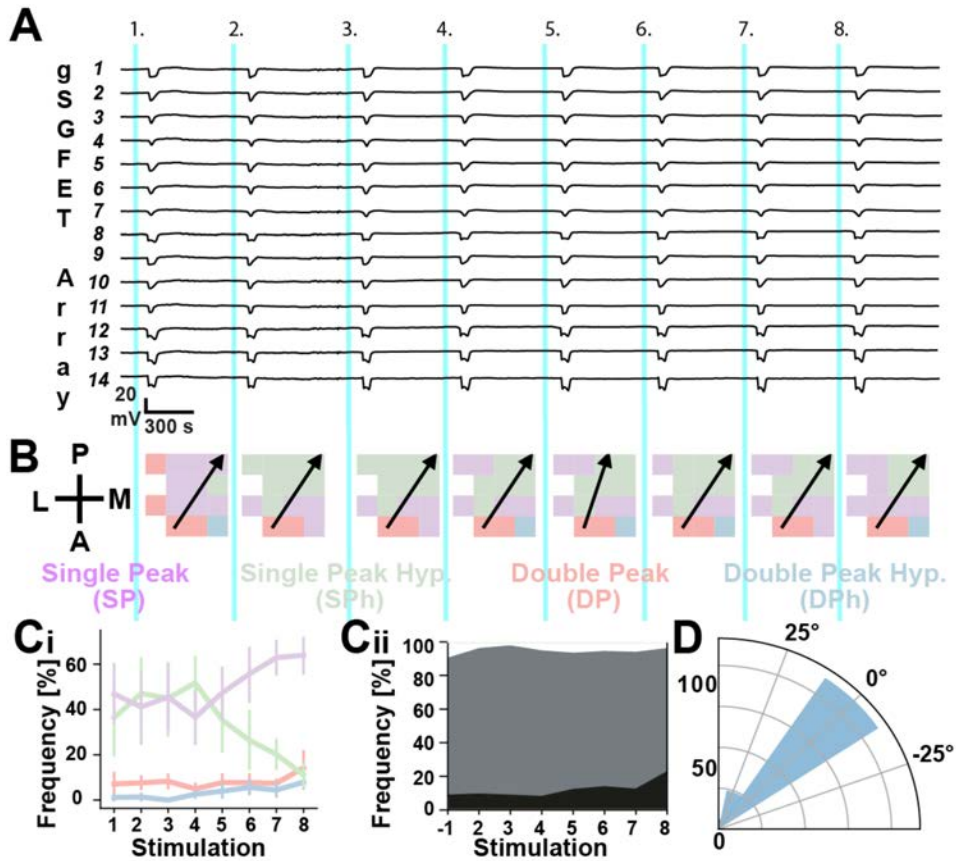


Figure 5.6: Reproducible and stable CSDs recorded using 16-Channel gSGFETs in response to repetitive optogenetic induction. **A:** DC-coupled recordings of 14 individual transistors in an array showing reliable, repetitive induction of CSDs triggered by blue light illumination over a 100 min recording session, with 8 CSD inductions, indicated by the light blue bars. **B:** Left: Schematic indicating the array and fibre optic canula location. CSDs propagated from the motor cortex towards the visual cortex. Color-coded spatial map of the 16-channel gSGFET array based on CSD waveform at each transistor location. Arrow indicates CSD propagation direction. The angular variability of propagation varied little between repetitive induction of CSD. **C:** Polar histogram of CSD wave propagation direction, $n=48$ CSDs, from 6 mice. **D:** (i) Mean frequency of CSD shapes recorded by individual channels. Although there was an increase in SP and a decrease in SPH (purple and green lines respectively), the ratio of single to double peak CSDs varied little during 8 repetitions. (ii) Combining the single (grey) and double (black) peaks. White area indicates the percentage of channels that did not record CSD waveforms.

5.3.4 Pharmacological suppression of CSD in awake mice

To test the effect of drugs capable of suppressing or modulating CSDs we increased the light stimulus to 1.5 times the threshold, *OptoThreshold*, to ensure supra-threshold stimulation across the experiment duration. The protocol consists of two CSD inductions prior to intraperitoneal systemic injection of vehicle or drug followed by an additional 6 supra-threshold stimulations post-drug (Fig. 5.7. A). In this study, we evaluated the efficacy of two NMDA receptor antagonists. A representative trace of the recorded signal corresponding to one transistor of the 16-channel array is shown for an animal in the saline, MK-801 and Ketamine groups (Fig. 5.7. A). To validate the methodology for testing drug effects we used MK-801, a well reported CSD-inhibitor [222]. Intraperitoneal (i.p.) injection of 3mg/Kg MK-801 produced rapid (< 10 min) suppression of CSDs that did not appear in any of the subsequent light stimulations (n=5). MK-801 cannot be used therapeutically due to a number of serious adverse side-effects, so we next turned our attention to a potentially more clinically relevant NMDA antagonist, ketamine. Rodent studies indicate that ketamine can reduce the amplitude of CSDs [229], or block CSD induction completely [230, 231]. The effects are however transient, lasting 20-45 mins after a single injection. An effect we also observed in our studies (Fig. 5.7); complete inhibition only lasted 15-25 mins post injection, although CSD amplitude and AUC was smaller (Fig. 5.7. B and D) and propagation was slower (Fig. 5.7. E) for the remaining trials compared to pre-drug values.

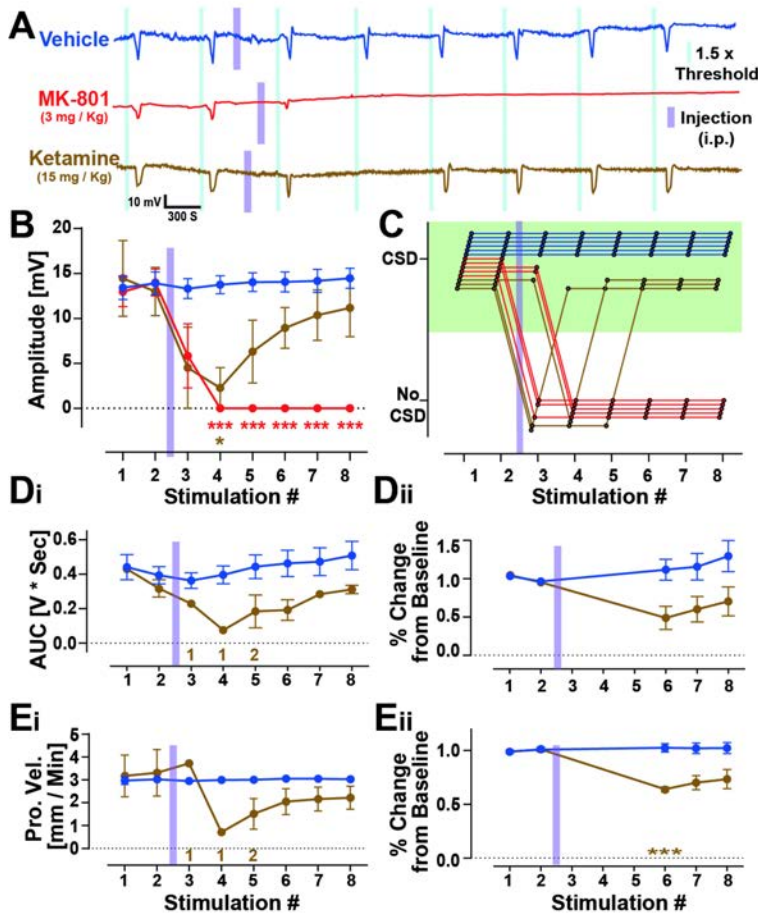


Figure 5.7: Pharmacological sensitivity of optogenetically induced CSD to NMDA antagonists. A: Representative DC-coupled recordings from a single transistor from an animal injected with either saline (blue), MK-801 (red) or Ketamine (Brown). The blue and magenta bars indicate the time of light stimulus and i.p. injection respectively. B: Peak amplitude of CSDs from repetitive induction of CSDs in the presence of vehicle, MK-801 and Ketamine. n (mice) = 6 Vehicle, 5 MK-801, and 3 Ketamine. Absence of CSD was considered as 0 mV amplitude. C: Binary visualization of the presence or absence of CSDs at each experimental timepoint showing the variability in the time and duration of the effects. Each line indicates an experiment and is color-coded by treatment. D and E: (i). Using only datapoints and treatment groups where a CSD was present, a graphical representation of Area Under the Curve (D) and Propagation Velocity (E) for vehicle and Ketamine. For Ketamine, stimulations 3, 4 and 5 did not induce CSDs in all animals in this group and so the n numbers for successful CSD induction are indicated underneath the data, in brown. (ii). Datapoints for AUC and Propagation Velocity when CSD could be detected in all animals (timepoints 6 to 8) were analyzed by normalization to the average of pre-drug tests (stimulations 1 and 2) to illustrate that although CSDs had returned, they propagated slower and did not recover pre-injection parameters within the time course of this experiment (55 mins post drug injection). Statistics. 2-Way Repeated Measures ANOVA with Sidak's post-hoc tests to examine differences between specific stimulations.

5.3.5 Investigation of CSD induction

To examine whether MK-801 and ketamine prevented induction, as well as propagation of CSDs, we modified the experimental protocol and used two epidural arrays; one at the site of LED illumination (gFET#1), motor cortex, and the other, (gFET#2), over somatosensory/visual cortex (Fig. 5.8. A). LED illumination of the ChR2 expressing area resulted in an immediate depolarization, most prominent on the top-left corner of transistor array (gFET#1). This immediate depolarization is not seen in gFET#2, 3mm away from the illumination site (Fig. 5.8. B-C). CSDs induced in the motor cortex propagated and were detected later by the second transistor array gFET#2. After administration of MK-801 (3mg/kg, n=2), or ketamine (15mg/kg, n=1), no CSD was detected at gFET#2 in accordance with the single-transistor array experiments (Fig. 5.7); while at the induction site (Motor cortex, MC) a neuronal depolarization can still be observed (Fig. 5.8. D). Light stimulation results in a time-locked depolarization of 5mV, which then transitions into a larger amplitude depolarization and full CSD (Fig. 5.8. D). In contrast, after administration of MK-801 or ketamine the initial light-induced depolarization returns quickly post-light stimulus to baseline values without induction of a CSD (Fig. 5.8. E).

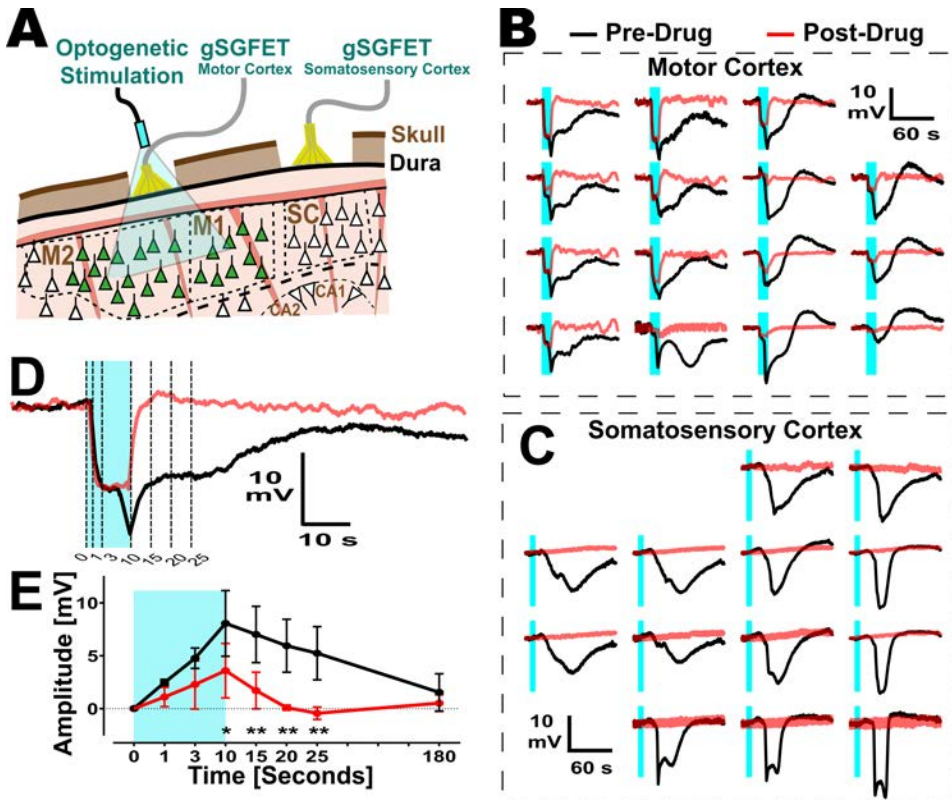


Figure 5.8: NMDA receptor antagonism blocks CSD induction and propagation. **A:** Cross-sectional schematic showing the positioning of both epidural gSGFETs, over either the motor or somatosensory cortex, and the LED fiber optic for optogenetic activation of ChR2-expressing neurons (green). **B-C:** Waveforms recorded by the 2 epidural arrays for an example CSD event with electrophysiological traces both before (black) and after (red) i.p. injection with MK-801 (3 mg / Kg; NMDA receptor antagonist). In this example, the LED stimulus was located top-left of motor cortex array. **D:** The top-left channel of the gSGFET over the motor cortex, showing the light-induced neuronal depolarization before and after administration of MK-801 with dashed lines indicating the timepoints (0, 1, 3, 10, 15, 20, 25 seconds from LED onset) used for analysis. **E:** Absolute amplitudes taken from the listed timepoints from the onset of LED stimulation (0, 1, 3, 10, 15, 20, 25 seconds) and grouped by before and after drug. n numbers consisted of combined data from NMDA receptor antagonists that inhibited CSDs in the somatosensory cortex (MK-801 at 3 mg/Kg ($n = 2$ mice) and Ketamine at 15 mg/Kg ($n = 1$ mouse)). Statistics. 2-Way Repeated Measures ANOVA with Sidak's post-hoc tests to examine differences at specific time points.

5.3.6 Through skull detection of CSD

Finally, we investigated the possibility of recording CSDs electrographically through intact skull. To do this and to quantify our results with epidural placement of arrays, we utilized two gSGFET arrays in a single experiment, one placed over motor/somatosensory cortex, and the other over ipsilateral somatosensory/visual cortex and optogenetically-induced CSDs (Fig. 5.9. A). One of the arrays was placed epidurally and the other on top of the skull. There is a reduction in spatiotemporal properties of recorded CSDs across the array (Fig. 5.9. Eii). The resolution in propagation and CSD waveform across and between individual transistors achieved by subdural placement of the gSGFET is lost. There is also a reduction in amplitude of detected CSDs when recording through bone (epidural was 17.14 ± 2.66 mV, through skull was 9.75 ± 1.57 mV; $n = 6$ animals; $p = 0.0436$, Welch's unpaired T-Test) (Fig. 5.9. Cii). However, CSDs can be detected through the skull travelling at a propagation velocity of 3.198 ± 0.265 mm/min, (Fig. 5.9. Civ). Additionally, we could detect suppression of higher frequency (1-30 Hz) rms amplitude correlated with the CSD, although this suppression recovered faster compared to epidural recordings (Fig. 5.9. D). In order to exclude potential electrical paths through burr holes and craniotomies, we performed additional non-invasive optogenetic induction and recording of CSD (data not shown). Overall, these experiments demonstrate that CSDs can be electrographically recorded through a completely intact mouse skull using gSGFETs.

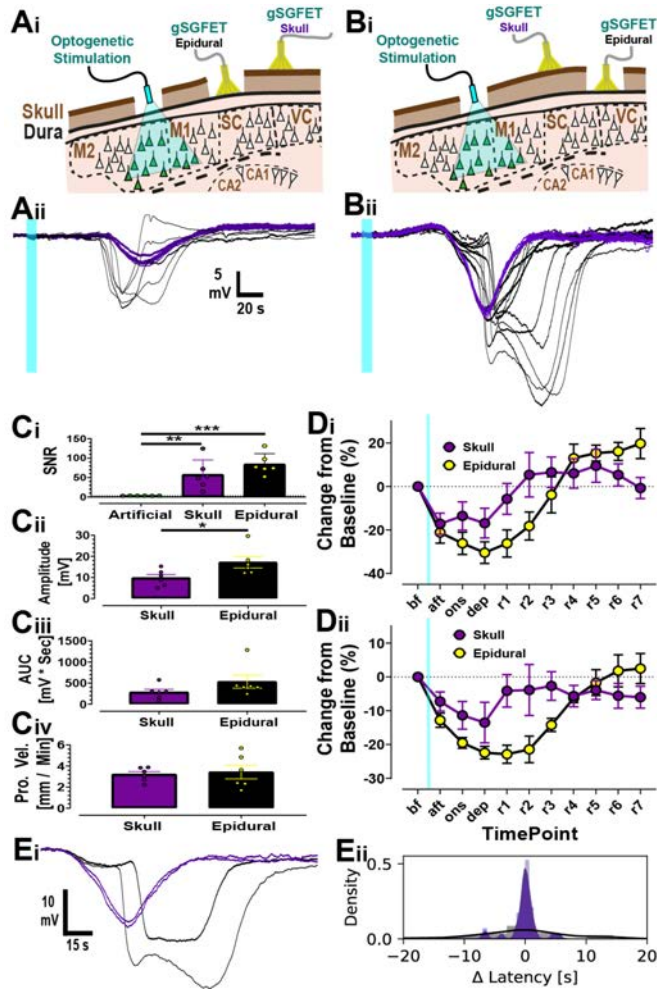


Figure 5.9: Comparing recordings of Opto-CSD through the dura and the skull. A-B: Cross-sectional schematics showing the positioning of two gSGFETs, either over the dura and skull (Ai) or skull and then dura (Bi). Beneath each are representative recordings over the dura and skull (Aii) or skull and dura (Bii), with colours to indicate recording position: skull (purple) and epidural (black). C: Quantification of SNR (Ci), Amplitude (Cii), AUC (Ciii) and propagation velocity (Civ) for data recorded through skull and dura. For SNR (i), the artificial level was set to 3, with s.d. of ± 0.1871 , and then statistics (1-Way ANOVA, with Tukey's post-hoc tests). For Amplitude, AUC, and propagation velocity (ii-iv), statistics were performed using unpaired T-Tests. n (mice) = 6. D: Quantification of normalized rms of delta (Di) and theta (Dii) frequency bands for both skull (purple) and dura (black) recordings. E: Select channels, positioned furthest apart on the gSGFET array showing electrophysiological full bandwidth traces (i) for skull (purple) and dura (black). Note the loss of spatiotemporal resolution in skull recordings compared to epidural recordings depicted as the histogram and population estimate (line) of the latency dispersion around the mean latency in an array (ii), data from 6 optogenetic CSDs (1 CSD from 6 different mice).

5.4 Discussion

A difficulty studying CSDs, either independently or concurrently with higher frequency activity is the lack of appropriate tools to record them *in vivo* with high spatiotemporal fidelity, and to reliably, on-demand, induce CSDs in a minimally invasive manner. Although cerebral blood flow techniques can be a useful complementary method capable of recording the downstream effects of CSD on blood flow; the gold standard for CSD detection requires electrophysiological methods (Ayata, 2013), usually recorded using solution-filled glass pipettes with Ag/AgCl wires. These are not practical for chronic recordings, nor for high-density mapping of CSDs. Using passive electrodes, even with the use of DC-coupled amplifiers is sub-optimal [232]. In contrast, gSGFETs are active devices that dynamically transduce local field potential changes into current [220, 126] allowing multisite DC-coupled electrophysiological recordings with negligible baseline drift [124] and Fig. 5.6. A. Experimental models of CSD often employ highly invasive mechanisms to induce a CSD resulting in tissue damage, problems with reproducibility, and therefore limited translational value. Recently transgenic mice expressing Chr2 under the Thy-1 promoter have been used to non-invasively induce CSD optogenetically via depolarization of predominately layer 5 excitatory neurons in the cortex [222, 223, 233], and have been used to evaluate CSD threshold in ischemic stroke [234]. We have built on this approach by using a viral vector-mediated method. We used the human Synapsin (hSyn) promoter to drive expression in excitatory and inhibitory neurons in all cortical layers [235], using a modified version of channelrhodopsin with a point mutation (H134R) which generates larger photocurrents [236] to maximize neuronal depolarization. By combining these methodologies, we have developed an awake head-fixed mouse preparation that facilitates preclinical CSD research. The reproducibility of optogenetic induction and the enhanced fidelity of micro-transistor recordings permits high density mapping of CSD induction and propagation, examination and categorization of CSD waveform, and the ability to monitor neuronal activity responses across physiologically relevant frequencies.

We used a fiber optic cannula to deliver diffused blue (488nm) light and determined that a volume of tissue expressing Chr2 greater than 1mm³ (Fig. 5.2) was required to reliably induce a CSD. A single continuous (5-10s) light stimulation was more effective than trains of brief depolarizations with matched total light duration (Fig. 5.1), presumably as a result of efficient inter-pulse extracellular potassium buffering mechanisms and relaxation of neuronal depolarization block. As modelling studies indicate that a rise of extracellular potassium above 10-12mM within a restricted area of cortex (>1mm³) in rodents is required for CSD induction [237], we hypothesize that a single continuous (5-10s) light stimulation increases extracel-

lular potassium sufficiently to trigger a CSD. Future experiments using potassium sensitive electrodes can be used to investigate this hypothesis.

Spreading depolarization-induced spreading depression is mechanistically explained by the fact that the sustained depolarization exceeds the inactivation threshold for the action potential generating channels [238]. The depression of activity typically outlasts the neuronal depolarization suggesting that it is maintained by other mechanisms that affect synaptic function. We have quantified that depression outlasts depolarization by around 4 minutes in epidural recordings in normoxic awake brain (Fig. 5.3. D). We recorded >2000 CSD waveforms and categorized these into distinct clusters based on certain parameters including single or double peak and the presence or absence of a pre-event hyperpolarization. Despite individual transistors being close to each other (400 μm), we were able to detect local changes in CSD waveform across the cortex. These waveforms were stable during repeated rounds of induction (Fig. 5.6). The ability to record specific CSD waveforms from localized areas of cortex highlights the advantage of spatial mapping using DC-coupled micro-transistors. The shape of a CSD is thought to reflect a number of ionic processes including activation of persistent sodium channels, NMDA receptors and extracellular potassium diffusion [238, 239]. Double peaks are thought to represent enhanced NMDA receptor activation [229]. In our study, using naïve mice, double peaks were rare, (10%) (Fig. 5.5). The ability to record multiple CSD waveforms with high-fidelity using gSGFETs could be used in collaboration with modelling approaches to investigate predominate ionic contributions to CSD waveform under certain disease states. This technology could also allow real-time evaluation of underlying brain health. Spreading depolarisation properties, ie waveform shape and duration, could be used to infer the boundaries between metabolically challenged and/or dying tissue from uncompromised areas. A change from single to double peak CSD waveform with a concurrent increased duration of neuronal depression, or indeed a switch to post-SD hyperexcitability, could be used to tract infarct or lesion progression.

In contrast to results reported in transgenic Thy-1-ChR2 mice [223], we did not observe a large change in the threshold required to illicit CSDs during repetitive rounds of induction. Although there could be heterogeneity in waveform shape across the array, CSD waveform parameters were stable, and changed little during repeated CSD inductions (Fig. 5.6). In contrast to metabolically compromised brain where SDs are believed to spiral around the edge of an ischemic core [240, 241], CSDs in non-ischemic tissue are thought to propagate radially across the brain (Shibata and Bures 1972). Our results confirm that in normoxic awake mice, optogenetic-induced CSDs behave as non-recurrent propagating waves with a preferred direction that is preserved for repeated stimulations (Fig. 5.6. D). These results are in accordance with the small CSD propagation variability measured by

imaging methods in anesthetized mice [242].

The majority of published pharmacological studies have investigated whether a compound reduces CSD frequency, typically in response to topical application of KCl. Few studies report an effect on CSD threshold, amplitude or waveform characteristics as these can only reliably be investigated *in vivo* when CSD is induced electrically or optogenetically and detected using electrophysiological methods. The stability, reproducibility and consistent CSD threshold during repeated trials in a single recording session, and the ability to conduct experiments in awake rodents, extenuating any confounders due to anesthesia [243] make optogenetic-induction coupled with gSGFET array recording an advantageous model to conduct pharmacological perturbation studies. We performed experiments in awake brain and focused on NMDA receptor antagonists as a proof-of-principle to evaluate the *in vivo* drug-screening platform. Our results confirm previous reports that MK-801 and ketamine can reliably inhibit the induction of CSD [244]. Extrapolation of the pharmacological results obtained in healthy animals has to be taken cautiously, particularly in regard to severe diseases such as traumatic brain injury or stroke where energy failure plays an important role in CSD pathogenesis. Although ketamine can be used to inhibit spreading depolarizations in severe brain injury [245], studies indicate that NMDA receptor antagonists effective under normoxic brain conditions are considerably less effective in tissue modelled to reflect brain trauma by artificially raising baseline potassium concentration [246]. The precise relationship between CSD and the extent of the pathology in ischemic stroke, migraine, and epilepsy, is still poorly understood. Future studies will benefit from the versatility that this *in vivo* assay offers, including viral delivery of opsins to discreet brain regions and awake recordings. Implementation of this methodological approach in disease relevant preclinical models, including transgenic migraine mice [247] or ischemic stroke [241] will permit selection of agents with enhanced translational value. While patients with severe brain trauma require sedation, the vast majority of CSDs will occur in awake, un-anaesthetised brains, and result in lower quality of life for patients suffering migraines and epilepsy. Therefore results obtained in awake brain will have enhanced mechanistic and clinical relevance. Indeed, studies inducing ischemic stroke in awake brain demonstrate how anesthesia reduces not only the extent of ischemic damage after stroke, but also masks the protective effects of a stroke therapy [248].

In this study we demonstrate the usefulness of our methodological approach to investigate mechanisms of CSD induction by directly confirming the importance of NMDA receptor activation for CSD initiation (Fig. 5.8). Similar approaches could be employed to investigate the roles of persistent sodium channels and extracellular potassium to CSD initiation in normoxic brain, as well as in specific disease states. Although we focused in this study on short (5-10s) continuous light stimulation

to evoke CSDs, as this was most efficient (Fig. 5.1); our approach could be used to investigate how more physiological/pathophysiological firing patterns in distinct sets of neurons could result in CSD induction. The flexibility of a viral vector approach permits cell-type specific promoters to be used in future studies, as well as the ability to optogenetically induce CSD in mouse models of neurological disease while mitigating expenses resulting from maintaining and/or crossing multiple transgenic lines, and thus reducing overall animal numbers used in research [249]. Application of optogenetic approaches could be used to gain a better understanding of how spreading depolarisations may promote epileptiform field potentials rather than neuronal depression in damaged brain tissue. Minimally invasive optogenetic stimulation was restricted to cortical brain regions, however recent advances in opsin engineering now permit transcranial activation of any region of the mouse brain expressing ultrasensitive opsins [250] opening the possibility of inducing spreading depolarisations in subcortical areas in awake rodents.

Although we take care to keep the dura intact and record epidurally, therefore minimizing tissue damage and swelling, the ability to record electrographically through intact skull will be a major advance. To explore the possibility of through skull detection of CSD electrographically we placed two gSGFET arrays, one epidurally and the other on intact skull and compared the recorded signals in response to an optogenetically induced CSD. Although some of the spatiotemporal properties are lost with subdermal recordings, including waveform shape due to volume conduction through the bone; 5-10mV amplitude waves of depolarization travelling across the cortex at 3mm/min could clearly be detected (Fig. 5.9). Our data demonstrates that subdermal recordings detect both the depolarization wave and neuronal activity suppression in mice. Through skull graphene micro-transistor recordings, coupled with non-invasive optogenetic induction of CSDs will facilitate longitudinal studies examining inflammatory responses post-CSD where invasive methodology complicates interpretation of results [233]. Additionally, some relevant rodent models, such as the mouse model of familial hemiplegic migraine type 1 expressing the human mutation S218L in the CaV2.1 (P/Q-type) calcium channel subunit, usually die within a few hours/days following invasive brain procedures as a result of uncontrolled brain swelling and edema [247]. Recording non-invasively from these mice will allow recording of spontaneous CSDs associated with migraine, without perturbation of the brain, and for extended periods of time.

5.5 Conclusion

In this chapter, the advantages of combining gSGFET arrays with optogenetic CSD induction to map electrographically with high spatiotemporal fidelity both infraslow activity concurrently with correlated activity suppression and recovery in specified frequency bands have been explored. The multisite recordings allow detailed analysis of CSD waveform characteristics and propagation. This *in vivo* platform is stable, allowing reliable, repetitive rounds of CSDs to be induced on-demand. This experimental methodology offers many advantages over traditional approaches to study CSD *in vivo* in awake brain, and can be utilized in future studies to gain mechanistic insight into disease pathology, and as a pharmacological screening platform for evaluating potential CSD modulating drugs in several distinct neurological disorders.

Chapter 6

Applications of gSGFETs for neuroscience research

The brain generates activity in a wide range of frequencies, from quasi-stable extracellular potentials to high frequency oscillations (\approx DC-kHz) that are modulated by behaviour and pathophysiological states. However, most research has focused on activity above 0.1 Hz due to technical difficulties associated with recording below that frequency range hampering the understanding of baseline potential shifts (BPS) and infraslow activity. In this Chapter, a general overview of the diversity of baseline potential shifts of the brain in both physiological and pathological conditions is provided and proof-of-concept recordings of some of those events performed by gSGFETs are presented.

Moreover, since there is no single technology that can monitor the full complexity of brain function, multimodal approaches where electrophysiological information is complemented with blood flow or ion dynamics, in addition to methods to modulate neural activity, are promising strategies for untangling complex brain phenomena. However, multimodal recordings are generally not straightforward to perform, as strict requirements might be fulfilled depending on the techniques combined. Benefiting from graphene transparency and using a low-autofluorescent substrate polymer, parylene-C, we show that DC-coupled recordings and fluorescence imaging of neuronal activity can be simultaneously obtained from the same spatial location. We demonstrate this multimodal approach by recording extracellular depolarization waves and intracellular calcium dynamics in an awake mouse. We also provide evidence that the level of ultrasounds used for *in vivo* functional ultrasound imaging do not damage graphene field-effect transistors allowing mapping of infraslow activity concurrently with cerebral blood flow changes in both cortical and subcortical areas.

Overall, the results presented in this chapter highlight the usefulness of gSGFET technology for studying a wide-range of brain phenomena, with special benefits for translational preclinical research, as well as prove gSGFET compatibility with state-of-the-art neuroimaging techniques.

6.1 Baseline potential shifts of the brain

Whole-cell recordings allow measuring rapid changes in the membrane potential of individual cells such as the rapid tens of millivolt changes in few milliseconds occurring during an action potential firing in individual neurons (tens of millivolts within a few milliseconds) (see 1.4D,F). Importantly, even in the absence of an action potential, experimental results show that most neuron types undergo millivolt-scale oscillations in their transmembrane potential, and these oscillations can be highly synchronous in large populations of neurons and modulated by behavior [42]. However, intracellular recordings are difficult to perform in more than a few neurons at the same time, particularly *in vivo*. Therefore, extracellular recordings are the standard approach taken to study brain oscillations, with high density multisite arrays allowing mapping of brain activity.

At a given point in space, the extracellular field potential is determined by the superposition of multiple contributing signal sources (see Fig. 1.5A-B) but also depends on technological aspects such as the reference electrode and sensing probe materials, and on the charge distribution near the reference and sensing probes. Most available recording instrumentation works in AC-coupled mode due technical advantages such as decreased likelihood of amplifier saturation causing signal loss. Generally, AC-coupled recordings are acquired using high-pass filters ($f > \approx 0.1$ Hz) which not only avoids amplifier saturation but removes all slower potential fluctuations below the cut off frequency. However, when using HPF, the scaling of dipolar currents to field potentials is distorted by AC coupling (see [46] for a thorough discussion). For example, rapid baseline changes such as those occurring during a cortical spreading depolarization, can induce voltage transients in the AC-coupled signal which are prone to being misinterpreted (see BPF signal in 4.4c, where a huge transient spike is seen at the onset of CSD due to the fast change of the extracellular potential which in reality remains sustained for a few seconds).

Undesired effects of AC-coupling are artificial zeroing which makes it impossible to identify slowly varying levels of baseline potentials [46]. This has implications for current source density analysis [251], as net positive charge can be recorded as positive or negative values at different times distorting the analysis. Also, the signal distortion effect is particularly relevant for extracellular recordings using miniaturized electrodes at cellular scale, due to the aforementioned millivolt-scale oscillations of transmembrane potentials which can be misinterpreted. Attempts have been done to recover the DC-coupled signal from AC-coupled recordings showing that it is non-trivial and that is only possible when the potential shift is mainly contributed by a single source [252]. Therefore, generally only by measuring in DC-coupled mode can misinterpretations be avoided.

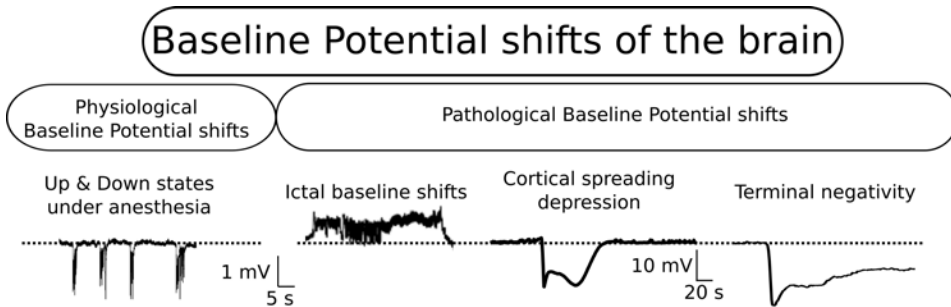


Figure 6.1: Overview of baseline potentials shifts of the brain. Baseline potentials shifts can be divided into physiological and pathological potentials. Example cases are shown to illustrate the diversity of potentials in terms of polarity, amplitude and duration.

Different terms in the literature have been used to refer to the potential changes observed with DC-coupled recordings: DC, slow, infraslow, standing, sustained or steady potentials as well as baseline potential shifts [187]. Here this last term is adopted since in the view of the author, this term does not differentiate signals depending on its rate of variation (slow, infraslow or permanent nature such as sustained or steady) but puts the focus on the very nature of DC-coupled recordings, i.e. the baseline. Under physiological conditions the extracellular space ionic composition is maintained through active homeostatic mechanisms. Therefore, large-scale extracellular baseline potentials are thought to reflect changes in the state of activity of large populations of CNS cells, for example alterations in the excitation level [187, 4]. However, the precise electrogenesis of DC potentials is a highly complex phenomena since in addition to the wealth of elements (ion gradients, active channels and pumps) that contribute to transmembrane currents of both neurons and glia, and their constant neuromodulation, the electrical properties of the extracellular also shape the potentials, causing volume conduction. As a general rule, negative surface potentials are related to superficial excitatory or deep layer inhibitory activity while positive surface potentials are related with superficial inhibitory or deep layer excitatory activity, although other factors such as changes in gas tension (O_2 or CO_2) among others also contribute to DC potentials [4].

Despite the lack of a thorough understanding of its generation, baseline potential shifts have been correlated with a wealth of brain functions and processes. BPS have been correlated with states of high alertness, transitions between wakefulness and sleep as well as between different stages of sleep, awareness of muscle movements, consciousness during decision making, task demand and performance, consummatory behaviours, attention, blood-brain barrier disruption, and several other complex functions in the healthy brain [187]. Importantly, brain BPS may

arise from physiological processes but also from pathological phenomena Fig.6.1. BPS are therefore fundamental electro-clinical signatures of some neurological and psychological disorders and may serve as diagnostic, prognostic, and treatment monitoring tools. Potential applications explored in the literature are in epilepsy for seizure onset zone detection and for determining prognosis in intensive care after brain injury [253, 186].

6.2 Recording baseline potential shifts

Graphene transistor arrays, due to its high fidelity recording of DC-coupled activity such as cortical spreading depression (see Chapter 4) have a high potential to be used to record other types of BPS. In this section, recordings of different types of baseline potential shifts are presented to demonstrate the capabilities of gSGFETs for mapping brain BPS induced in mechanistically different ways.

6.2.1 Infralow activity

Infraslow activity (ISA) was first described in the neocortex of rabbits [254]. Recent studies based on blood-oxygen-level-dependent (BOLD) signals and full-band electroencephalography (EEG) recordings in animals and humans have reported ISA to be a characteristic and consistent signal present during resting states [178, 188, 255, 256]. Moreover, ISA has been shown to synchronize higher-frequency EEG modulating the level of performance of behavioural tasks and influencing sleep [189, 257]. Importantly, ISA has been described as a general phenomenon not only present in the neocortex, but also in other brain structures such as the hippocampus and particularly the thalamus [173, 258]. Thus, ISA can be seen as an integral component of brain function.

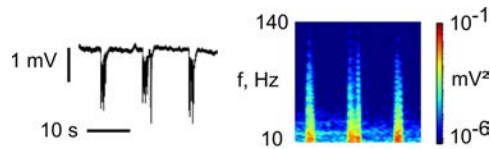


Figure 6.2: Temporal and spectral features of slow-wave activity in a rat under isoflurane anesthesia as recorded by an epicortical gSGFET. DC-coupled extracellular potential (left) and corresponding power spectrogram for a gSGFET channel.

The mechanisms underlying the generation and propagation of ISA are mostly unknown and the dynamics of the interaction between ISA and higher-frequency

cortical activity are far from well understood. Indeed, ISA has been described as a different brain process that follows specific spatiotemporal trajectories, different from that of higher frequency signals and not just the result of the low-pass filtering of high-frequency brain activity [174]. However, most studies on the organization of ISA at the system level have been undertaken by measuring functional magnetic resonance imaging (fMRI) blood oxygen signals during resting state conditions [255], while the exact link between measured fMRI blood oxygen signals and its neurophysiological base remain poorly understood, particularly at the level of ISA [177, 259, 174, 260].

By performing DC-coupled recordings using gSGFETs in isoflurane anesthetized rats (see Section 3.2) we observed few millivolt baseline shifts coupled with the rhythmic slow-wave [261] (see Fig. 6.2). These results show a correlation between baseline-shifts with higher frequency activities (as observed in the spectrogram). Similar correlations have been observed in the literature under more physiological states such as sleep [189]. Importantly, this observation confirms the ability of gSGFETs to record not only large amplitude BPS like CSD but smaller signals. Further experiments with penetrating arrays of gSGFETs may help to elucidate the neurogenesis of the observed baseline shifts.

6.2.2 Seizure-related baseline potential shifts

Epilepsy is a group of neurological disorders characterized by recurrent seizures, a period of symptoms such as convulsions or absence due to abnormal brain activity. Seizures appear to occur randomly and therefore unpredictable seizure episodes can result in physical injuries and limit the quality of life of those who suffer from epilepsy [262]. Seizures can develop as the result of brain injury, stroke, brain tumors, infections of the brain, or birth defects through a process known as epileptogenesis. Seizures are controllable with medication in some but not all cases. Epilepsy surgery may be an option for people with focal seizures that are drug-resistant. Surgery success depends upon resection of the seizure onset focus. Hence, improved methods for seizure onset zone localization are thus expected to increase the number of seizure-free patients after resection surgery.

Both focal and generalized epileptiform activities have been shown to be associated with characteristic fluctuations of the baseline potential in various experimental epilepsy models [263, 4, 264] as well as in the human epileptic brain [265]. It is thought that the basic mechanisms underlying the generation of epileptiform activity and the initiation of baseline potential fluctuations are closely interlinked. The initial burst of single or grouped epileptiform potentials is generally accompanied by a large negative fluctuation of the extracellular potential baseline [266]

with maximum amplitude presumably occurring in the center of the epileptic focus. This has been explored clinically and some reports have shown that seizure freedom is improved when the ictal baseline shift area is resected [253].

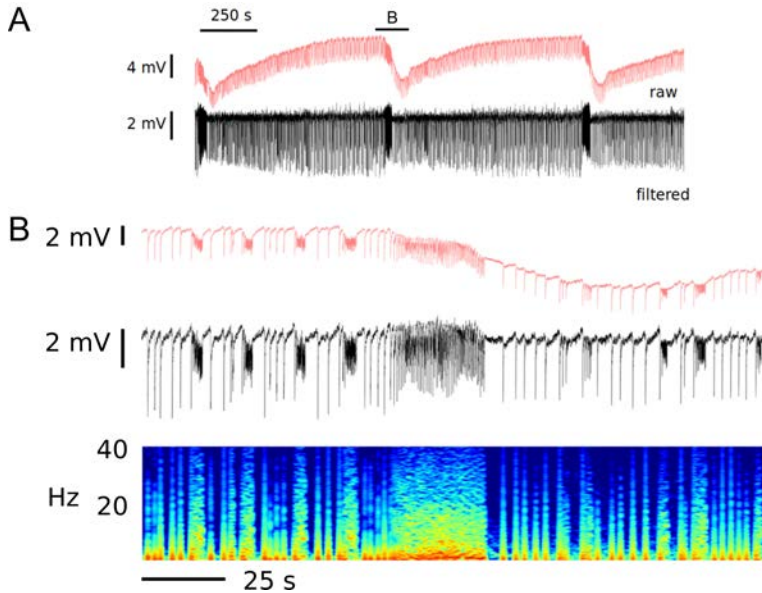


Figure 6.3: Baseline potential changes and epileptiform activity as recorded by an epidural gSGFET in an awake mice injected with a proconvulsant. A-B: Raw (red) and filtered (black, > 0.5 Hz) extracellular potential of epileptiform activity induced by picrotoxin (PTX) locally injected into the cortex proximal to the array. Following injection of PTX, normal activity transitions into patterns of epileptiform and seizure-like activity consisting of high-amplitude spikes synchronized over large areas (interictal spikes), short trains of polyspikes lasting 5-10s and longer duration, tens of seconds, higher-frequency (ictal periods). A: A cyclical baseline shift consisting of a slow increase of the extracellular potential followed by a faster negative shift after the initiation of ictal (seizure) activity. B: Zoom showing interictal spikes, polyspikes, a seizure and a negative baseline shift starting during the pre-ictal to ictal transition.

An open question in epilepsy is how the albeit normal brain activity transitions into seizure or ictal state. Some researchers have proposed that slow variables may direct the transitions between physiological, interictal and ictal states [267]. To investigate if DC-changes were observed in relation to seizures we performed epicortical recordings using a gSGFET array in awake head-fixed mouse injected with a chemoconvulsant (picrotoxin (PTX), a $GABA_A$ ion channel blocker). PTX blocks inhibitory activity and causes network over-excitability. After injection of PTX, normal activity transitions into large spikes synchronized over large areas, so called, interictal spikes, as also few-second higher frequency activity also called, polyspikes, and longer duration (tens of seconds) higher-frequency ictal periods.

We observed interictal, polyspikes and ictal periods as well as cyclic changes in the baseline potential (see Fig.6.3). The cyclic period consisted of a slow increase of the extracellular potential (Fig.6.3A) followed by a faster negative shift after the initiation of the ictal activity (Fig.6.3B).

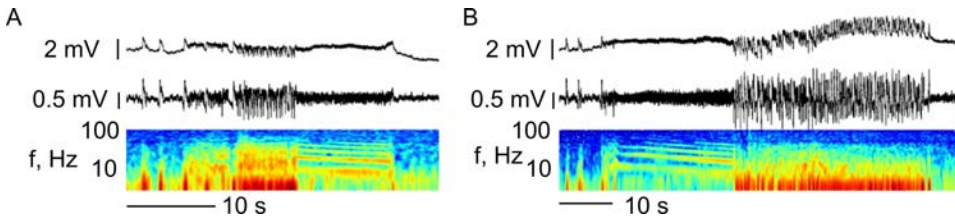


Figure 6.4: Ictal baseline potential changes recorded in an awake rat chronically implanted with an epicortical gSGFET after injection of picrotoxin. A-B: Two different examples of an ictal event. Top: DC-coupled traces showing a pre-ictal shift that is sustained for the whole ictal period and evolves with transitions between well-known seizure phases such as high-amplitude low-frequency activity and low-amplitude high-frequency activity periods as better seen in the high-pass filtered traces (middle) and power spectrograms (bottom).

We next investigated seizures recorded in awake rats chronically implanted with an epidural gSGFET array. Seizures were induced by injection of PTX through a pre-implanted cannula. Pre-ictal BPS were observed which were sustained during the whole ictal period consisting of stereotypical patterns of high-amplitude low-frequency spiking and low-amplitude high-frequency spiking periods.

The presented results confirm the concurrence of BPS and epileptiform activity and demonstrate the ability of gSGFET to monitor those events. They can be used in the future to study systematically the occurrence and spatial location of BPS in a wide variety of epilepsy types, hopefully providing clues about their underlying causes and improving their treatment.

6.2.3 Seizures and spreading depolarization waves

Epileptiform activity such as seizures and spreading depolarization (SD) waves have been observed to occur in combination in many experimental models. However, the relation between seizures and SD is complex [214]. Seizures can precede and presumably trigger an SD, what is called post-ictal SD, presumably due to local increases of extracellular potassium. On the other hand, SD has been suggested to facilitate the development of epileptiform activity, particularly in compromised tissue, presumably by lowering seizure threshold by an increased network synchronization [268].

In rats under isoflurane anesthesia, we used 4-Aminopyridine (4-AP), a potassium channel blocker, as a convulsant. By recording with two epicortical arrays we were able to observe a localized seizure near the injection site in the visual cortex which started a CSD wave that propagated through the ipsilateral somatosensory cortex (see Fig.6.5).

Importantly, not all seizures triggered a CSD. Fig. 6.6 shows two seizures of that recording session. Despite both seizures appearing very similar after high-pass filtering (as routinely performed by AC-coupled recordings), DC-coupled recordings show a post-ictal depolarization for only one of the seizures. Also note the baseline shift prior to seizure onset in both cases. Overall these examples show the diversity and complexity of the relation between CSDs and epileptiform activity in the brain and the ability of gSGFET arrays to map both of them providing qualitative and quantitative improvements over current recording methods.

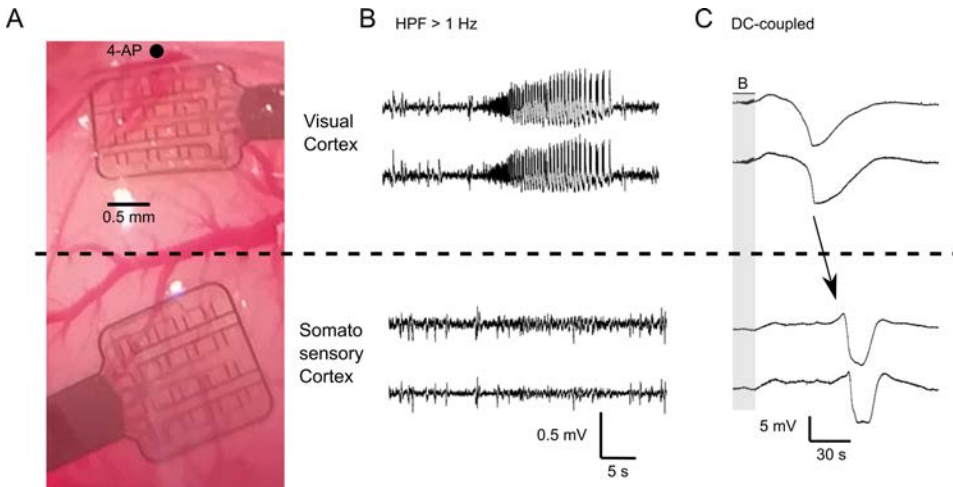


Figure 6.5: *In vivomapping* of cortical spreading depression and seizures in rat cortex. A: Photograph of two epidural gSGFET arrays placed over visual (top) and somatosensory cortex (bottom). Black circle indicates the injection site of a proconvulsant (4-AP). B: High-pass filtered ($f > 1$ Hz) exemplary traces of two channels of each array shown in A where a seizure remains focal to the area of the brain near the injection site and is only detected by transistors in the visual cortex. C: DC-coupled traces of the same channels showing a post-seizure induced cortical depolarization that propagates to somatosensory cortex.

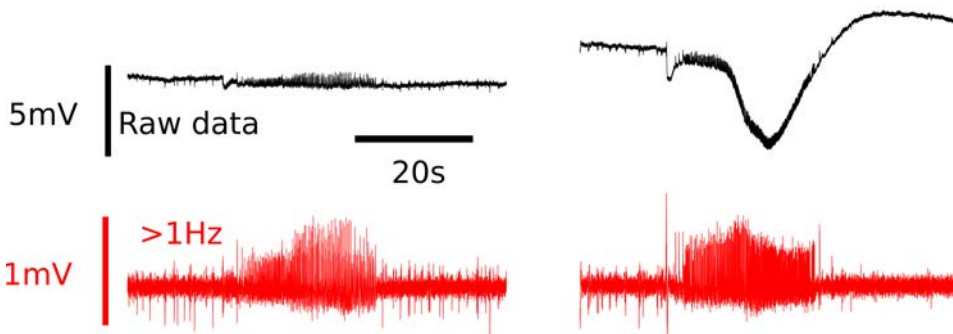


Figure 6.6: Epileptic seizures induced by 4-Aminopyridine (4-AP) in anesthetized Wistar rats. DC-coupled extracellular potential signal (black) and high pass filtered (red, >1 Hz) of two seizures as recorded by an epidural gSGFET.

6.2.4 Pharmacological baseline potential shifts

Correct dosing of drugs is of paramount importance for obtaining the desired function while minimizing side-effects. Dosing is particularly relevant for anesthetics as the consciousness state has to be tuned based on clinical needs. Several markers of anesthetics exist that are based on brain activity, however their prediction of consciousness state is limited. We therefore explored the use of baseline potential shifts for anesthetics monitoring.

To determine how baseline extracellular potential changes with anesthesia level, we implanted a gSGFET array and a Ag/AgCl intracortical reference electrode into a Wistar rat (see Methods Section 3.2) and varied isoflurane levels. Recordings started at isoflurane level set to 2% and were progressively reduced in steps (interval 5-10 minutes), until the animal awakes. After 5-10 minutes awake, anesthesia was reinduced by setting the isoflurane level to 2%. Fig.6.7 shows the DC-coupled signal (top) and high-pass filtered signal ($>0.5\text{Hz}$, bottom) of a gSGFET channel. Red lines indicate the changes in isoflurane concentration. Changes in both baseline level and LFPs are observed. LFPs change from high-amplitude, infrequent up-states to lower amplitude continuous awake activity as described in the literature [269]. Interestingly, the baseline value becomes progressively more positive with reducing isoflurane concentration and recovers to the initial value after reinduction. The transition from awake to 2% isoflurane resulted in a shift of up to 50 mV. Similar large, tens of millivolt results, have been obtained for multiple animals and in multiple experimental days (data not shown). Next, the possible origins of these large baseline shifts is discussed.

BPS due to isoflurane anesthesia have been observed previously from scalp recordings in cats using DC-EEG [270] and were associated to blood-brain barrier disruption. However, the origin of such high amplitude changes in the extracellular voltage is as yet uncertain as multiple origins have been hypothesized. Membrane hyperpolarization together with a conductance increase have been suggested as a common mechanism of anesthetic action. However, reported values indicate much smaller, only 1-2 millivolt changes in membrane potential. Application of isoflurane has also been shown to cause a significant and reversible hyperpolarization in the neuromuscular junction of *Drosophila* larval motoneurons [271]. Responses to application and removal of the drug occurred rapidly (5-10 min) upon exchange of solutions in the chamber which is in accordance with the observed results. The activation of leak conductance channels by isoflurane may partially contribute to the observed results. Other than neurons and glia, a series of other parenchymal elements (blood flow and capillary epithelial cells) may participate in the genesis of potentials that translate into EEG signals [4]. Membrane resting potential of non-neuronal cells such as vascular smooth muscle also get hyperpolarized by

anesthesia and may contribute to the results [272]. Last but not least, the large BPS observed can also arise from indirect effects of isoflurane on oxygenation or extracellular concentrations of ions, therefore more experiments are needed to confirm the origin of the observed DC shifts and its potential as an indicator of the anesthetic level.

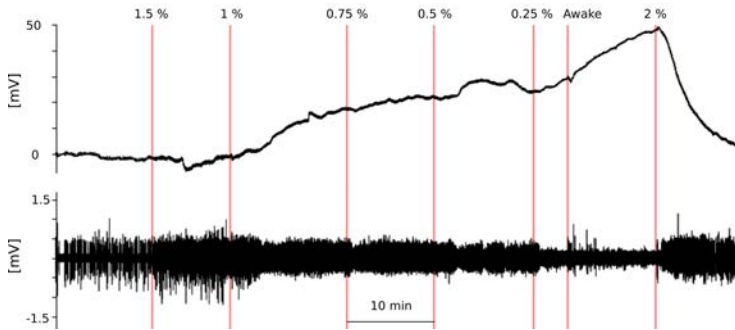


Figure 6.7: Changes in neural activity for the transition from deep isoflurane anesthesia to awake and reinduction. Top: Wide-band signal (DC-100Hz); bottom: High-pass filtered signal (0.5-100Hz). Red lines indicate the isoflurane level change at a given timpoint. Staring isoflurane level was 2%.

A substantial contribution of the reference electrode on the observed extracellular baseline shifts cannot be discarded due to the general effects of isoflurane (see discussion about the reference electrode on signal recording 1.3.2). Therefore, the reference electrode could also be affected by isoflurane-related effects or even be the source of the changes. To further advance in the exploration of BPS by global drugs the field will benefit from improvements in the development of *in vivo* long-term stable reference electrodes as well as methodological guidelines of reference positioning depending on the experimental paradigm. Further experiments could benefit form the capabilities of gSGFET to map local changes in BPS such as those induced by local administration of drug or by selective (photo-)stimulation (see for example Fig.5.8).

6.2.5 Terminal depolarization

SDs that are terminal (understood as inducing persistent isoelectricity of the cerebral cortex) have only been documented in a few instances in the literature in rodents and cats in the context of delayed lesion growth after focal cerebral ischemia [273, 274], in a swine with a declining mean arterial pressure at approximately 40 mm Hg [275], in a patient with a large intracerebral hematoma [276], and in early and delayed cortical infarcts following aSAH [277]. Terminal CSDs have also been recorded in the dorsal brainstem which is a brain area linked to cardiorespiratory function [216]. In the human cerebral cortex of patients with devastating brain injury which triggered a Do Not Resuscitate-Comfort Care order [278] terminal spreading depolarization were also observed. Silencing of spontaneous electrical activity (nonspreading depression) developed simultaneously across regional electrode arrays followed by a terminal CSD starting 13 to 266 seconds after severe ischemia. Computational models have been developed that propose a physiological mechanism for terminal CSD [279]. They suggest that the wave is caused by membrane potential oscillations that occur after the cessation of activity of the sodium-potassium pump, which leads to an excess of extracellular potassium resulting in a sudden change in mean membrane voltage. Simulations also suggest that this process is not necessarily irreversible offering hope for treatment.

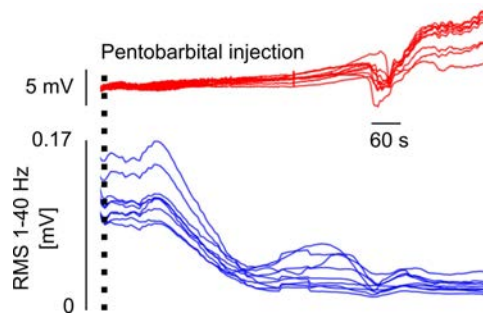


Figure 6.8: Extracellular potential changes after injection of a terminal sodium pentobarbital dose to an awake head-fixed mouse. DC-coupled extracellular voltage and RMS of 1-40Hz signal recorded by an epicortical gSGFET in an awake head-fixed mouse.

Benefitting from the DC-coupling capabilities of gSGFETs, we studied the appearance of terminal CSD in awake head-fixed mice injected with sodium pentobarbital an euthanasic drug. Terminal CSD was observed in 10 out of 13 experiments. Fig.6.8 shows a terminal CSD recorded by an epidural gSGFET array. Red trace corresponds to the DC-coupled extracellular field potentials recorded while blue traces are the the RMS of the LFP activity from 1 to 40 Hz (sliding window of 60 s). After an i.p. injection of 0.3 mL of sodium pentobarbital, LFPs are pro-

gressively reduced in a nonspreading manner in the next 5 min while a shift in extracellular voltage is observed after 10 min. In that case, after the negative shift, the previous extracellular voltage is not recovered and a positive shift is observed.

In summary, we observed nonspreading depression and terminal SD in mice after the injection of sodium pentobarbital. These results provide fundamental insight into the neurobiology of brain death in mice and are in agreement with results observed in humans. Further studies targeting terminal CSD reversibility could have translational implications for survivable after brain insults.

6.3 Combination of gSGFETs with brain imaging techniques

Electrophysiology is an extremely powerful technique to monitor brain function, with both clinical and research applications. However, current electrophysiological techniques suffer from certain limitations such as restricted spatial coverage and difficulty to relate extracellular potentials to a given neuron type or population. Therefore, multimodal approaches where electrophysiological information is complemented with blood flow or ion dynamics imaging, in addition to methods to modulate neural activity, are promising strategies for untangling complex brain phenomena. However, multimodal recordings are generally not straightforward to perform, as one technique could compromise the recording of the other. Research to compatibilize electrophysiology with other techniques is therefore warranted. Next, proof-of-concept experiments showing compatibilization of gSGFET wide-bandwidth mapping technology with two cutting edge imaging techniques are explored: namely functional ultrasound (fUS) and calcium imaging.

6.3.1 gSGFETs and functional ultrasound

An important limitation of current electrophysiological techniques is its limited spatial resolution. Despite advances in neuroelectronic interfaces towards high channel counts and large coverage areas, current designs are based on either flexible surface arrays or local penetrating probes, both insufficient to cover the whole brain with high spatial resolution. Several imaging technologies exist such as functional magnetic resonance or positron emission tomography. Recently, novel methodological developments in the field of ultrasounds have resulted in what is named functional ultrasound (fUS). This technology has the benefits of doppler technology in terms of tissue penetration, spatial resolution and temporal resolution but also has a much higher sensitivity, thus allowing to map several mm in depth into brain tissue with sub-second and sub-millimeter spatiotemporal resolution [280]. An important caveat is that this technique, as with many imaging techniques, does not image brain electrical activity, but changes in cerebral blood flow which can result as a consequence of neural activity. fUS has multiple applications in mapping vascularization, in delineating potential areas involved in a given behavior and for the study of the alterations of cerebral blood flow by different diseases.

Combination of electrophysiology with fUS will allow to benefit from the higher temporal resolution of electrical methods while having a bigger picture of brain activation. Since ultrasound are known to exfoliate graphene, it was not known if the gSGFET will be destroyed by fUS or if the flexible array would be acous-

6.3. COMBINATION OF GSGFETS WITH BRAIN IMAGING TECHNIQUES

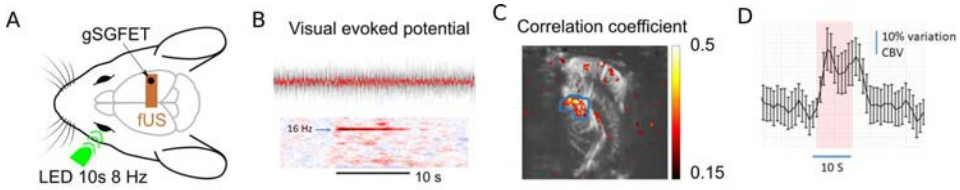


Figure 6.9: Combined fUS imaging and gSGFET recordings of visual evoked activity and CSD. A: Schematic a rat showing the fUS imaging window and the location of an gSGFET over visual cortex. Visual stimulus where applied through an LED during 10s at 8Hz, 50% duty cycle. B: Visual evoked potentials and average (red) and corresponding power spectrogram of the average signal showing the doubling of the stimulation frequency as recorded by a gSGFET during visual stimulation. C: 2D coronal section with superimposed fUS correlation coefficient with the visual stimulus showing increases in both cortical and subcortical areas related to visual processing. D: Evolution of cerebral blood volume at the region of interested delimited by the blue line in B showing an increase of CBV during visual stimulation.

tically transparent. We therefore performed a feasibility study of combining both techniques. We combined fUS with gSGFETs to measure simultaneously extracellular potentials and cerebral blood flow in anesthetized rats. Fig. 6.9A shows an schematic of the experimental setup. A craniotomy was performed and a gSGFET array placed over the dura and covered with gel to ensure a proper acoustic coupling of an ultrasound probe positioned directly above the cranial window surface and connected to an ultrafast ultrasound scanner. To validate the combination of both techniques we used an LED and applied a 10s, 8Hz 50% duty cycle stimulus. As expected a visual evoked response at double the frequency was observed as illustrated by the temporal and power spectrogram of a gSGFET (Fig. 6.9B). Then, maps of ‘activated’ pixels were built using the Pearson correlation coefficient between the local power Doppler temporal signal computed from each spatial pixel of the fUS acquisition and the stimulus pattern [280]. Fig. 6.9C shows a 2D coronal section image obtained with fUS with superimposed fUS correlation coefficient with the applied visual stimulus showing increases in both cortical and subcortical areas related to visual processing. The temporal evolution of cerebral blood volume at the region of interest delimited by the blue line in B shows an increase of cerebral blood flow during visual stimulation. These results demonstrate that no significant interference between both techniques occurred: neither the electrophysiological signal was contaminated by the fUS signal or the gel required to ensure a correct acoustic coupling; nor the fUS imaging of the brain was hampered by the presence of the thin flexible array.

Moving forward, we benefitted from the succesful fUS-ephys multimodal monitoring to test if cortical spreading depression neurovascular coupling could be monitored with this combination of techniques. Multiple evidence shows that SD

occurs in cerebrovascular disease, such as aneurismal subarachnoid haemorrhage, ischemic stroke, subarachnoid haemorrhage, and spontaneous intracerebral haemorrhage as well as traumatic brain injury [182, 190]. Moreover, SD is associated with increased energy metabolism and changes in cerebral blood flow and terms like spreading hyperaemia, spreading oligaemia, and spreading ischemia have been coined to describe the effects of SD on brain perfusion [182].

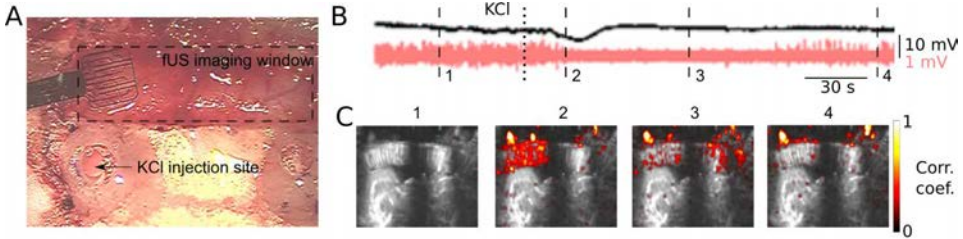


Figure 6.10: Combined fUS imaging and gSGFET recordings of cortical spreading depression. A: Optical image of the experiment showing a gSGFET array over the cortex, the fUS imaging window, and the 1M potassium chloride (KCl) injection site. B: DC-coupled (black) and HPF (>0.1 Hz, red) electrical signal as recorded by a gSGFET. Dashed lines mark the time of each frame of the fUS image shown in E. Dotted line shows the time KCl was injected to induce a CSD. C: 2D coronal section with superimposed fUS correlation coefficient at different times as depicted by the dashed lines in D.

CSD was induced by potassium chloride (KCl) intracortical injection (see Fig. 6.10A) and monitored by both techniques. After 1M KCl injection, a transient depolarization and silencing of neural activity was recorded by a gSGFET (see Fig. 6.10B). Fig. 6.10C shows the mapping of the vascular effects of the induced depolarization wave, which started near the injection, visual cortex (timeframe 2) and propagated through the ipsilateral cortex, invading the motor cortical area (timeframe 3).

The results obtained with this feasibility study are positive and demonstrate the practicability of combining gSGFET DC-coupled extracellular potential mapping and frequency ultrasound imaging of vascular effects, holding great potential to study neurovascular coupling during CSD and other neural events.

6.3.2 gSGFETs and Ca^{2+} imaging

Another limitation of extracellular potential recording by electrical means is the difficulty to separate contributions of different neuronal sources due to the inherent summation nature of the electric field at a given position, what is called the superposition problem, in that only a few regions, neuronal populations or synap-

tic inputs may significantly contribute to the local field recorded. This means that pinpointing the exact location where neurons are active is difficult to determine using electrophysiological approaches with activity recorded in the LFP range [46]. Instead, current fluorescence imaging approaches allow to map the brain with high spatial resolution, and by using genetically encoded indicators, contributions performed by selective neuronal types or ions can be determined. However, the temporal resolution of fluorescence imaging is limited by the dynamics of the indicator which is in the tens to hundred of milliseconds timescale. Therefore, combination of fluorescence imaging and extracellular potential monitoring by neuroelectronic interfaces could benefit from the advantages of both techniques. Due to graphene transparency, gSGFETs an advantageous option to use when combining both techniques.

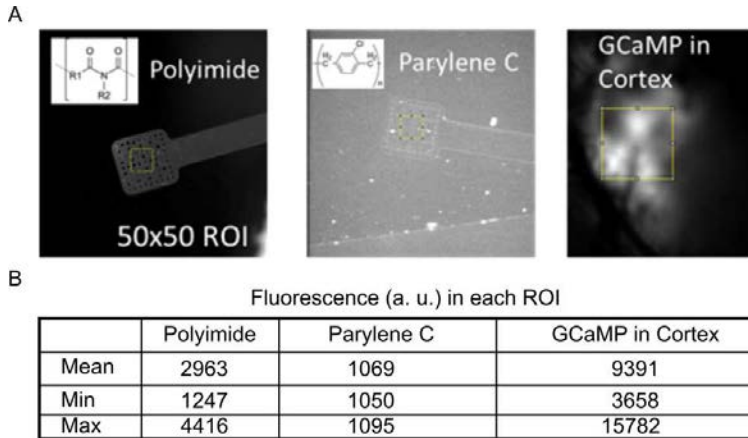


Figure 6.11: Intrinsic autofluorescence of polyimide and parylene-C arrays in comparison with GCaMP6 expression *in vivo*. A: Fluorescence image of a polyimide (left) and a parylene-C gSGFET array (middle) as well as an image of GCaMP6 expression in a mouse cortex. Insets show the respective chemical structure. B: Mean, minimum and maximum fluorescence intensity of a polyimide or parylene C gSGFET arrays as well as common values of GCaMP6 *in vivo* fluorescence extracted from a 50 x 50 pixel region of interest (yellow squares in A). While polyimide arrays have a high level of intrinsic autofluorescence that could contribute significantly to *in vivo* signals and therefore impair measurements, parylene-C has much lower autofluorescence which allows imaging through the array without signal contamination.

We therefore performed a feasibility study of combining gSGFETs DC-coupled recordings and fluorescence imaging using a commonly used genetically encoded calcium indicator, GCaMP6, as proof of concept. Since neural activity is associated with calcium influx into cells, calcium imaging can be used to monitor brain activity. In a first step, as most of the fabricated flexible arrays are not covered by graphene but by the flexible polymeric substrate, we tested the autofluorescence

of the fabricated devices as the main requirement for through-array fluorescent imaging is low autofluorescence of the flexible substrate. We found that polyimide has a high autofluorescence with impedes proper imaging through the array (see Fig. 6.11). We therefore adapted the fabrication process to parylene-C (see Methods 2.5.1), a much more adequate substrate due to its low autofluorescence [281]. The intrinsic autofluorescence of the fabricated polyimide and parylene-C arrays in comparison with GCaMP expression *in vivo* was determined experimentally (Fig. 6.11) and shows that while polyimide arrays have a high level of intrinsic autofluorescence that could contribute significantly to *in vivo* signals and therefore impair measurements, parylene-C has much lower autofluorescence which allows imaging through the array without signal contamination.

Having evaluated the low-autofluorescence and the high-quality signal recording capabilities of the fabricated gSGFETs, we performed combined calcium imaging and DC-coupled recordings using a parylene-C gSGFET array in an awake mouse expressing GCaMP (Fig. 6.12A). Graphene transparency allowed obtaining the extracellular potential and the intracellular calcium imaging at the same spatial location. An example trace for a CSD event after injection of a pro-convulsant is shown in Fig. 6.12B, while different timeframes of the fluorescence signal recorded through the array as the wave propagates over the cortex is shown in Fig. 6.12C.

Overall, the obtained results give a firm indication that highly transparent graphene transistor arrays made of Parylene C are suited for combined recording of fluorescent signals and DC-coupled mapping of field potentials *in vivo*. This combined methodology can be further used to investigate correlations between field potentials and dynamic intracellular calcium responses in all cell types, or in specific neuronal or glial populations. The technical approach is not specific for calcium imaging and can be applied to a growing number of genetically encoded fluorescent indicators of brain activity, including those developed for neurotransmitter detection [282].

6.3. COMBINATION OF GSGFETS WITH BRAIN IMAGING TECHNIQUES

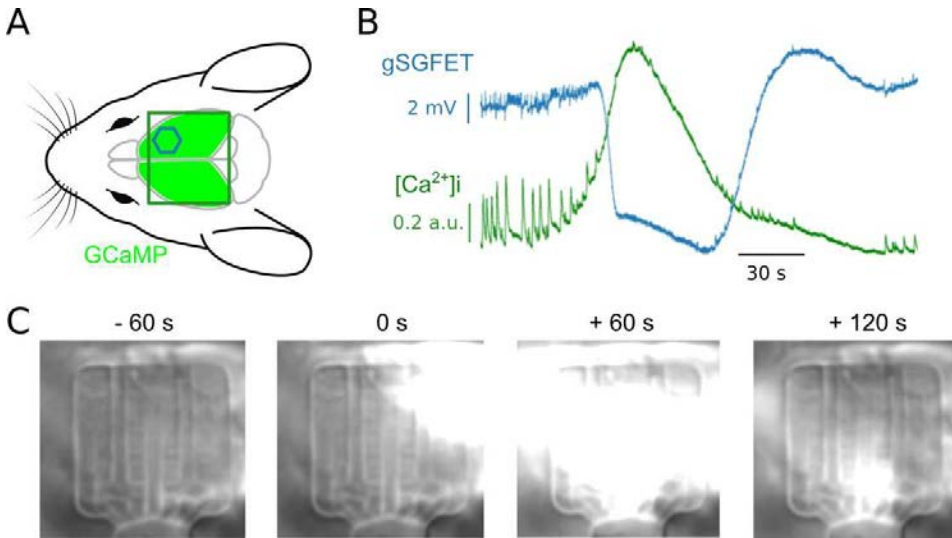


Figure 6.12: Combined calcium imaging and electrophysiological recording of cortical spreading depression in an awake mouse. A: Schematic of the experimental setup. Simultaneous calcium imaging of an awake head-fixed mouse expressing gCaMP (green square represents imaging window) and electrophysiology as recorded by an epidural parylene-C gSGFET array. Hexagon shows the location of the array. B: Concurrent calcium fluorescence signal (green line) and electrophysiology (blue line) during a spontaneous cortical spreading depression event after injection of a chemoconvulsant. Fluorescence has been extracted from a region of interest over the represented gSGFET channel. C: Timeframes of GCaMP fluorescence intensity as imaged through a graphene transistor array during the propagation of a cortical spreading depression through mouse cortex. A high fluorescence intensity (compared to baseline fluorescence levels, -60 s) is seen first at top right corner. After 60 s the wave has propagated through most of imaging area under the array and 120 s after fluorescence is just observed at a bottom-middle region of the imaging window.

6.4 Conclusion

The understanding of the electrogenesis of BPS is far from complete, mainly due to the limited research on BPS in the last decades as a consequence of the generalized use of high-pass filters in multisite electrophysiological recordings. Indeed, despite the pathological consequences, many of the cellular processes underlying the presented BPS in this Chapter are unknown. An improved understanding of BPS will be facilitated by high-fidelity DC-coupled multisite neural interfaces in combination with state-of-the-art neurotechnologies. In this Chapter we demonstrate that gSGFET can monitor a wide variety of BPS such as large amplitude depolarization waves, ictal baseline shifts and baseline shifts in slow-wave activity. Moreover, benefiting from graphene transparency and using a low-autofluorescent substrate polymer, parylene-C, we showed that DC-coupled recordings can be simultaneously obtained at the same spatial location than fluorescence imaging of genetically encoded indicators. We also provide evidence that the level of ultrasounds used for functional ultrasound imaging do not damage graphene field-effect transistors allowing the ability to map infraslow activity at the same time as cerebral blood flow changes of cortical and subcortical areas.

Overall, the results presented in this Chapter demonstrate the capabilities of gSGFET technology for studying a wide-range of brain events, with special usefulness for translational preclinical research, as well as proven graphene compatibility with cutting edge complimentary brain imaging techniques. We believe that the current state of gSGFET technology can both qualitatively and quantitatively improve research on BPS. This will ultimately result in a better understanding of infraslow activity in the brain and in the development of medical treatments for diseases where this type of activity is prominent.

Conclusions

Recordings of extracellular electrical field potentials of the brain are a crucial methodology to assess brain physiology. However, current recording technologies are limited in their ability to map with high precision and accuracy the electrical activity of the brain across its wide spatiotemporal scales. Both theoretical and experimental evidence suggested that graphene, used as channel of a field-effect transistor, could potentially be the basic element of a novel technology for neural recording. Thus, this PhD dissertation has focused on developing a wafer-scale microfabrication of flexible neural interfaces based on graphene microtransistors, establishing a methodology for recording of neural signals using gSGFETs, determining its sensing capabilities in terms of SNR and benchmarking against state-of-the-art techniques, and exploring potential applications in the neuroelectronics field. In the following, the main conclusions of the work presented in this PhD dissertation are detailed:

- The physical basis of graphene solution-gated transistors voltage sensing has been studied and the main aspects affecting their performance have been discussed. Two models describing the current-voltage characteristics of gSGFETs and the interfacial pH and ion strength sensitivity have been implemented and published in open-source online repositories (see Outcomes section). They can be used for guiding the design of gSGFET voltage sensors and biosensors.
- Procedures for a reliable clean-room microfabrication of flexible graphene transistor arrays on polyimide or parylene-C substrates have been established. Importantly, the developed fabrication methodology is based on standard microelectronic processes, except for the graphene transfer, which remains as a manual step in the workflow. The reported methodology allows large-scale production. A total of 15 wafers containing more than 200 neural arrays and 2800 graphene transistors have been fabricated with an average yield of functional transistors higher than 80%.
- The overall interaction of parameters affecting gSGFET voltage sensing performance at a single transistor and array level, such as contact and track resistance, graphene minimum carrier concentration, charge carrier mobility and doping heterogeneity, have been taken into account for designing gSGFET neural interfaces. A square graphene channel has been used in almost all designs with different overall area of the individual transistors (50x050,

100x100 or 150x150), while preserving a $400\mu\text{m}$ pitch, 4x4 array arrangement which is adequate for rodent electrophysiology. At the array level, a common source was adopted to reduce the number of required tracks from $2 \cdot n$ to $n + 1$ where n is the number of transistors. This design comes with almost no drawbacks in terms of gFET performance if the common track resistance is low in comparison with the graphene channel resistance; at the same time, this design eases the scalability of the devices. The adoption of this design was possible thanks to a high homogeneity of the CNP between transistors obtained in the fabrication process, allowing an almost-optimal polarization.

- An extensive electrical characterization of the fabricated arrays has been performed. Results show that the fabricated arrays have low intrinsic noise (few tens of μV in the LFP range), low-leakage (few nA) and almost constant transconductance over a wide frequency bandwidth ($\approx\text{DC-1kHz}$). Importantly for extracellular voltage sensing, the shape of the steady-state gSGFET transfer curve was found to not be significantly modified by pH or ionic strength variations.
- Strategies for optimal gSGFET array biasing as also for calibrating the acquired current signals were proposed. Interpolation into the transistor transfer curve was found to be an adequate calibration procedure to solve signal distortion introduced by non-linearity of the transfer characteristics. Calibration using interpolation into the transfer curve yields distortion-free signals.
- The feasibility of in vivo recordings using gSGFETs has been demonstrated by performing recordings in anesthetized and awake rodents. Benchmarking of recording performance of gSGFET neural probes against state-of-the-art recording technologies showed similar SNR of gSGFETs than platinum black electrodes in the frequency range below 100 Hz. Moreover, successful recordings of slow wave activity and visual-evoked potentials have been demonstrated. Comparing in vivo versus post-mortem recordings further demonstrate the high SNR recording capabilities of gSGFETs over a wide-bandwidth.
- A methodology to assess the effect of transfer curve changes to recording fidelity has been developed. A high stability of the transfer curve during acute hours-long in vivo recording experiments was found and demonstrated to allow high-fidelity recordings.
- A pilot experiment showed that gSGFET arrays remain functionally operative over up to five months, setting a lower bound for gSGFET chronic use.
- The feasibility of gSGFETs to record neural signals in a wide electrophysiological bandwidth, from infralow (<0.1 Hz) frequencies to the typical local

field potential bandwidth was demonstrated by monitoring a physiological event known as cortical spreading depression. gSGFETs were shown to outperform microelectrode arrays of gold or black platinum which suffered from polarization-induced drift or voltage-attenuation. Importantly, gSGFET performed similarly than solution-filled glass micropipettes, the gold-standard for extracellular recordings, while overcoming their spatial sampling limitations.

- The combined use of gSGFET recordings and optogenetics to study electrophysiological effects of cortical spreading depression on an awake brain is demonstrated. Differences in the electrophysiological effects of CSD were found and varied depending on the CSD waveform. Optogenetic CSD induction was compared with more standard (and invasive) methods such as 1M KCl injection or pinprick. No significant differences in the induced depolarization shift were observed between the three induction modalities while a faster recovery of local field potentials in optogenetic-induced CSD than KCl-induced but not pinprick-induced CSD was observed.
- A methodology using gSGFETs and optogenetics was developed allowing to evaluate the effects of pharmacological treatment against CSD, with applications for preclinical translational studies.
- Graphene transistors were shown capable to monitor brain activity while perturbed with through array LED illumination. This allowed investigating the extracellular voltage shifts associated with the induction of cortical spreading depression in an awake mouse brain.
- The feasibility of less-invasive recordings was studied by through intact-skull CSD monitoring in mice. Results showed that is possible to detect CSD through intact mouse skull with high SNR, although significant amplitude attenuation and loss of spatial resolution was obtained compared to epidural recordings.
- gSGFETs have been demonstrated compatible with brain imaging technologies that measure regional cerebral blood flow such as intrinsic optical signal imaging or functional ultrasound allowing to study the neurovascular coupling, as also wide-field imaging of genetically encoded indicators such as GCaMP6.
- gSGFETs are able to measure a wealth of brain baseline potentials shifts such as cortical spreading depolarizations, terminal spreading depolarizations and slow-wave-related and seizure-related baseline shifts.

Together, the results provided demonstrate that graphene is an optimal transducer of in vivo extracellular field potentials since it fulfills all requirements of

an ideal electrophysiological recording probe (biocompatibility, low thermal and electrochemical noise, low polarization and stable characteristics in a wide bandwidth) setting it as the basic unit of a novel generation of neural interfaces. Importantly, the obtained results point graphene microtransistor technology as a superior alternative to the commonly used microelectrode technology for mapping wide-bandwidth brain activity (see Fig. 6.13). The ability to accurately map infraslow and baseline potentials of the brain will facilitate and accelerate investigations in these relatively less explored brain phenomena. Examples of applications of this technology have been discussed in Chapter 6. Briefly, gSGFET arrays allow high-fidelity mapping monitoring of brain physiology, specifically of pathology biomarkers such as cortical spreading depolarizations and ictal baseline shifts. It is also noticeable the gSGFETs compatibility with through array optical illumination which allows to study the spatial response of baseline potential shifts during optogenetic neuromodulation. Moreover, the demonstration of gSGFET capabilities for combination with other neural monitoring techniques such as OISI, fUS or calcium imaging to obtain a wider glimpse of brain activity also opens many and exciting new research avenues. Opportunities and challenges for gSGFET technology are further discussed in the Outlook section.

Outcomes

The work presented in this PhD Dissertation has resulted in three published journal research papers:

- C. Hébert, E. Masvidal-Codina, A. Suarez-Perez, A. B. Calia, G. Piret, R. Garcia-Cortadella, X. Illa, E. D. C. Garcia, J. M. D. l. C. Sanchez, D. V. Casals, E. Prats-Alfonso, J. Bousquet, P. Godignon, B. Yvert, R. Villa, M. V. Sanchez-Vives, A. Guimerà-Brunet and J. A. Garrido. Flexible Graphene Solution-Gated Field-Effect Transistors: Efficient Transducers for Micro-Electrocorticography. *Advanced Functional Materials*, 28(12):1703976, 2018. ISSN 1616-3028. doi:10.1002/adfm.201703976.
- E. Masvidal-Codina, X. Illa, M. Dasilva, A. B. Calia, T. Dragojević, E. Vidal-Rosas, E. Prats-Alfonso, J. Martínez-Aguilar, J. M. D. l. Cruz, R. Garcia-Cortadella, P. Godignon, G. Rius, A. Camassa, E. D. Corro, J. Bousquet, C. Hébert, T. Durduran, R. Villa, M. V. Sanchez-Vives, J. A. Garrido and A. Guimerà-Brunet. High-resolution mapping of infraslow cortical brain activity enabled by graphene microtransistors. *Nature Materials*, 18(3):280–288, March 2019. ISSN 1476-4660. doi:10.1038/s41563-018-0249-4.
- E. M. Codina, M. Smith, D. Rathore, Y. Gao, X. Illa, E. Prats-Alfonso, E. D. Corro, A. Bonaccini, G. Rius, I. Martin-Fernandez, C. Guger, P. Reitner, R. Villa, J. A. Garrido, A. Guimera and R. C. Wykes. Characterization of optogenetically-induced cortical spreading depression in awake mice using graphene micro-transistor arrays. *Journal of Neural Engineering*, 2021. ISSN 1741-2552. doi:10.1088/1741-2552/abecf3

One conference paper:

- A. Guimerà-Brunet, E. Masvidal-Codina, X. Illa, M. Dasilva, A. Bonaccini-Calia, E. Prats-Alfonso, J. Martínez-Aguilar, J. De la Cruz, R. Garcia-Cortadella, N. Schaefer, A. Barbero, P. Godignon, G. Rius, E. Del Corro, J. Bousquet, C. Hébert, R. Wykes, M. V. Sanchez-Vives, R. Villa and J. A. Garrido. Neural interfaces based on flexible graphene transistors: A new tool for electrophysiology. In *2019 IEEE International Electron Devices Meeting (IEDM)*, pages 18.3.1–18.3.4. December 2019 doi:10.1109/IEDM19573.2019.8993433. ISSN: 2156-017X.

As also two software procedures for the current-voltage simulation of graphene transistors and its pH and ionic strength sensitivity:

- E. Masvidal Codina. Current–Voltage Model for Graphene Solution-Gated Field-Effect Transistors, July 2020. doi:10.5281/zenodo.3938679.
- E. Masvidal Codina. pH and ionic strength graphene charge neutrality point model, July 2020. doi:10.5281/zenodo.3938518.

In addition, during this PhD dissertation I have contributed to the following additional research papers:

- R. Garcia-Cortadella, E. Masvidal-Codina, J. M. D. l. Cruz, N. Schäfer, G. Schwesig, C. Jeschke, J. Martinez-Aguilar, M. V. Sanchez-Vives, R. Villa, X. Illa, A. Sirota, A. Guimerà and J. A. Garrido. Distortion-Free Sensing of Neural Activity Using Graphene Transistors. *Small*, 16(16):1906640, 2020. ISSN 1613-6829. doi:10.1002/sml.201906640.
- N. Schaefer, R. Garcia-Cortadella, A. B. Calia, N. Mavredakis, X. Illa, E. Masvidal-Codina, J. d. l. Cruz, E. d. Corro, L. Rodríguez, E. Prats-Alfonso, J. Bousquet, J. Martínez-Aguilar, A. P. Pérez-Marín, C. Hébert, R. Villa, D. Jiménez, A. Guimerà-Brunet and J. A. Garrido. Improved metal-graphene contacts for low-noise, high-density microtransistor arrays for neural sensing. *Carbon*, 161:647–655, May 2020. ISSN 0008-6223. doi:10.1016/j.carbon.2020.01.066.

Also during the development of the PhD several poster and oral contributions to national and international congresses have been performed.

The intellectual property behind the fabrication methodology has been protected under an industrial secret while the operation and calibration methodology for obtaining wide-band high-quality recordings has been patented:

- A. Guimera Brunet, E. Masvidal Codina, J. A. Garrido Ariza, X. Illa Vila, R. Villa Sanz and M. V. Sanchez Vives. WO2020094898A1 System of Graphene Transistors for Measuring Electrophysiological Signals, November 2018.

The developed gSGFET technology has been licensed for commercialization to a private company specialized in the neurotechnology sector (Multichannel Systems) which can ease the adoption of gSGFET-based neural probes for neuroscience research in the near future.

Outlook

To finalize, an outlook of graphene SGFET technology is provided. Neurotechnology is a multidisciplinary field where the cooperation between biologists—to state current challenges and best proof-of-concept scenarios—and engineers—to address the technical challenges—is crucial for advancing the understanding of the brain. Therefore, the use of gSGFETs as a tool for clinical neurophysiology or for basic studies about the neurobiology of physiological and pathological states will benefit from sustained cooperation and collaboration between engineers and neuroscientists.

Interpretation of LFPs has proven to be difficult due to the complex relation between neural activity and extracellular potentials [46]. One of the factors contributing to this complexity is the lack of a true baseline since the vast majority of recordings are AC-coupled or DC-coupled without high-spatial resolution. We envision that interpretation of LFPs will benefit from the capabilities of gSGFET arrays to provide high-density DC-coupled recordings.

From the wide-range of baseline and infraslow brain potentials, the work presented in this dissertation only explores in depth cortical spreading depression, while other pathological baseline potentials (seizure-related shifts, terminal CSD, pharmacological baseline shifts) have only been shown possible to be measured; an exhaustive characterization is out of the scope of this PhD dissertation. Further work could use gSGFETs to gain a deeper insight about those pathological brain potentials. Importantly, as described in Fig. 6.1 there are also physiological baseline potential shifts that are interested to be explored. They exhibit a much lower amplitude than the pathological ones, but with proper methodological procedures, gSGFETs should be appropriate to characterize the spatial distribution of such potentials. Also physiological event-related baseline potentials may probe beneficial for brain-computer interfaces.

Importantly, since only few regions, populations and pathways may significantly contribute to LFPs [283], neglecting the role of neural populations not contributing to LFPs is an oversimplified interpretation [46]. Instead, concurrent electrophysiology recordings with alternative techniques may be needed to get a better understanding of brain function. For example imaging approaches with high-spatial and temporal selectivity can be a good complimentary aid to LFPs interpretation. Combination of recording with neuromodulation techniques is also needed for improving the understanding of brain function. Optogenetics to perturb neural

activity is an excellent way to further study the electrogenesis of baseline potentials, as results presented in Chapter 5 show. Similar approaches can be used to explore baseline potential shifts associated to other neural events.

Less-invasive recording modalities are also interesting to explore. The ability of gSGFET arrays to detect CSD through intact mouse skull can be used to perform long-term studies on CSD susceptibility in a wide variety of disease mice models such as traumatic brain injury or migraine; and explore treatments. Unfortunately, these results are hardly translatable to bigger mammals or humans due to an increased skull thickness, which inevitably results in a significant signal attenuation.

This PhD dissertation has been limited to the study of brain potentials; however, there are other areas where gSGFET may find applications in the electrophysiology field for example in areas such as the retina [284, 285], the heart or intestine where baseline shifts have been reported; not to mention applications other than electrophysiology such as biosensing [286].

From an engineering point, transition from proof-of-concept devices to commercial exploitation in neurotechnology has proven challenging [287]. In this PhD Dissertation, the developed fabrication methodology is based on standard micro-electronic processes, except for the graphene transfer, which remains as a manual step in the workflow. Further research focused on the automatization of graphene transfer to (polymer-coated) silicon wafers would be highly beneficial for standardization and would ease up-scaling. Some recent works towards this aim are described in Section 2.4. Also, improvements on the growth of large area CVD graphene and advances on graphene surface cleaning procedures during the fabrication process will further increase homogeneity and improve performance of gSGFETs. To ease adoption of graphene microtransistor technology, we have made an effort in testing the manufacturing process with first chronic experiments, therefore demonstrating its robustness. Also to facilitate the usability of the technology we have provide guidelines for optimal gSGFET operation and signal post-processing. Nonetheless, future efforts would be needed to further develop material robustness and device usability, improve its homogeneity and recording performance and to take into account regulatory aspects. One important aspect is that of the reference electrode. Research on long-term implantable stable reference electrodes, as well as on optimal reference positioning, would be highly beneficial for the study of low-amplitude slow baseline changes.

It is also important to mention that the high freedom of design of microelectronic technology allows to make not only surface gSGFET probes but arrays that can be inserted to the depth of the brain. Intracortical probes will allow to explore infraslow and baseline potential changes of cortical and subcortical areas. Moreover, if properly downscaled, high-density gSGFET arrays should be able to

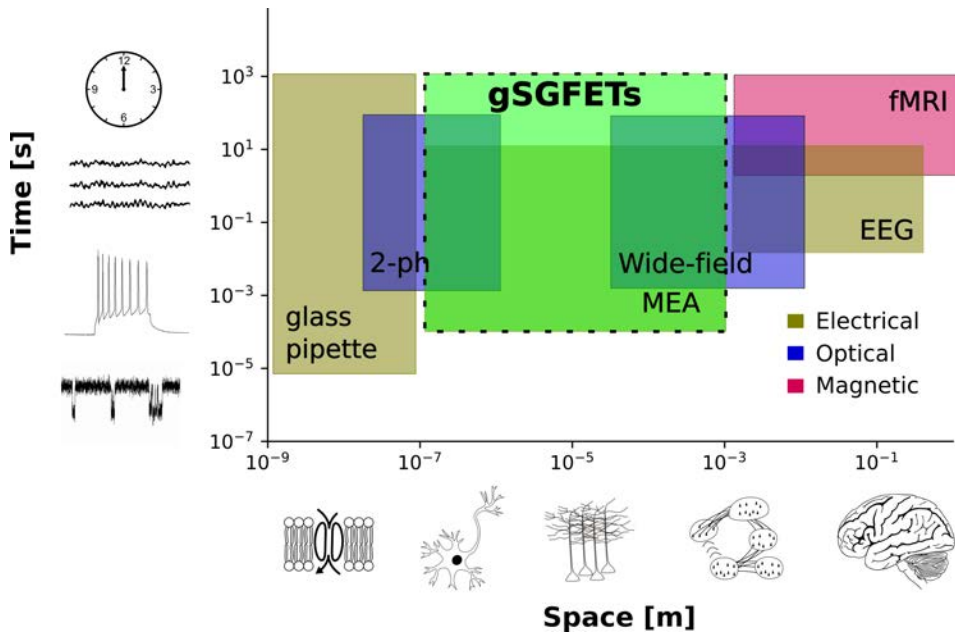


Figure 6.13: gSGFET recording technology in the context of brain monitoring techniques. EEG: electroencephalography; MEA: Multielectrode array; fMRI: functional magnetic resonance imaging; 2-ph: two-photon imaging; wide-field: wide-field imaging. gSGFET future possibilities (dashed box).

map the membrane potential changes associated to individual neurons and even subsections of a neuron. Using the observed dependence of noise on the inverse of the square root of the area, we suggest that transistors of $2\ \mu\text{m}$ by $2\ \mu\text{m}$ would be sufficient with the current state of technology to map large extracellular potential changes in the mV scale. Taking advantage of the multiplexing capabilities of graphene transistors [171, 172] could allow fundamental research on the distribution and modulation of the membrane potential changes in neurons of a variety of phenomena.

To fulfill the clinical applications of gSGFET technology, such as pathophysiology monitoring after traumatic brain injury or stroke in patients [288] as well as for seizure onset zone detection, safety aspects should be carefully considered. gSGFET electronics compatibility with current clinical practice, specific requirements must be fulfilled and human-approved materials should be used.

Advances towards noise reduction, long-term stability and multiplexing could state gSGFET-based neural interfaces as the gold-standard wide-bandwidth, high

spatiotemporal recording technology and accelerate adoption of gSGFET recording technology by both neuroscience and medical communities.

Appendices

Appendix A

Modelling gSGFETs

A.1 Modelling the graphene-electrolyte interface

The total interfacial capacitance is considered as the series combination of the double layer (C_{dl}) and quantum capacitance($C_q(V_{ch})$):

$$C_{int} = \left(\frac{1}{C_q(V_{ch})} + \frac{1}{C_{dl}} \right)^{-1} \quad (\text{A.1})$$

where C_{dl} is modelled with as a parallel plate capacitance with no voltage dependence and C_q is defined as:

$$C_q = \frac{2q^2}{\hbar v_F \sqrt{\pi}} \sqrt{\left(\frac{qV_{ch}}{\hbar v_F \sqrt{\pi}} \right)^2 + |n_{imp}|} \quad (\text{A.2})$$

where \hbar is the reduced Planck constant, v_F the Fermi velocity and n_{imp} is a parameter that represents the effective charged impurity concentration and V_{ch} is the Fermi potential level. See [289] for a derivation of the quantum capacitance based on graphene bandstructure. The equivalent circuit of Fig.2.3B is used to model the interface. By applying Kirchoff's laws to the equivalent circuit, an expression for V_{ch} can be obtained [111]:

$$V_{ch} = \frac{C_{dl}[V_{gs} - CNP - V(x)]}{C_{dl} + 0.5C_q(V_{ch})} \quad (\text{A.3})$$

Due to the V_{ch} dependence of the quantum capacitance, Eq. A.3 needs to be solved self-consistently. Once V_{ch} and C_q are known, the interfacial capacitance can be calculated using Eq. A.1.

A.2 Modelling current in gSGFETs

A current-voltage model of graphene solution-gated transistors was implemented in MATLAB based on Mackin et. al. [111]. The model allows to simulate the current of a gFET of a wide variety of sizes and V_{ds} and V_{gs} voltages. It also allows to simulate the effect of different parameters on the transfer curve (see, Fig. 2.5B). The model properly describes the effects of extrinsic resistance and takes into account the variation of the Fermi Level, interface capacitance, charge carrier density and voltage along the channel. Regarding the limitations, the model does not differentiate between hole and electron charge carriers and uses a constant carrier concentration-independent mobility. Moreover, contact resistance is considered symmetric and voltage-independent. The code of the model is available at [113].

Regarding to implementation, combining Eq.2.5 and 2.4 yields an equation which cannot be integrated. Therefore the resulting equation is rearranged into a numerically-solvable equation that describes the channel potential profile:

$$V(x+h) = V(x) + \frac{hI_d}{q\mu W \sqrt{n_o^2 + [C_{int}(V)[V_{gs} - V(x) - CNP]/q]^2}} \quad (\text{A.4})$$

where h is equal to the step length defined as the channel length divided by the number of channel divisions (n_L): $h = \frac{L}{n_L}$. For a certain current, the implemented algorithm starts at $x=0$ and iteratively calculates the voltage profile (Eq.A.4) solving the interfacial equations (A.3, A.2,A.1) at n_L points along the channel. The correct I_d is obtained when $V(x=L) = IdsRc$ is satisfied.

Next a table is provided with the parameters used for simulations in this PhD Dissertation.

$n_{imp}[cm^{-2}]$	$\mu[cm^2/Vs]$	$C_{dl}[\mu F/cm^2]$	$n_o[cm^{-2}]$	n_L
5.1e12	150	2	1.6e12	20

Table A.1: Parameters used to simulate gSGFET current. n_{imp} : effective charged impurity concentration, μ charge carrier mobility, C_{dl} : double layer capacitance, n_o : minimum carrier concentration and n_L : number of channel divisions.

A.3 Modelling pH and ion strength sensitivity of gSGFETs

The modelling work of Zuccaro et.al. is detailed next and used to gain insights about the surface groups in the fabricated gSGFET devices as also to model their pH and ion sensitivity.

The graphene-electrolyte interface can be described with a charge density at the graphene surface (σ_{gra}), a charge density due to functional groups at the graphene-electrolyte interface (σ_0) and a charge density at the solution side (σ_{EDL}). Gouy-Chapman-Stern theory [56] is used here to model the electric double layer defining a Stern and a diffusive layer connected by the outer Hemholtz plane (OHP) which determines the nearest approach of ions from the solution. The charge density in the solution (σ_{EDL}) can be estimated as:

$$\sigma_{EDL}(\psi_{OHP}) = -2 \frac{\kappa \epsilon_r \epsilon_o k_B T}{q} \sinh\left(\frac{z_i q \psi_{OHP}}{2 k_B T}\right) \quad (\text{A.5})$$

$$\kappa = \sqrt{\frac{2q^2 C_I}{\epsilon_r \epsilon_o k_B T}} \quad (\text{A.6})$$

where ψ_{OHP} is the potential at the OHP, ϵ_r and ϵ_o are the relative permittivity and the permittivity of free space, q is the electronic charge, k_B is the Boltzmann constant, T is the temperature, z_i is the ion valence and κ is the Debye screening length given by equation A.6, where C_I is the total ionic strength of the solution. The Debye screening length is an important parameter for biosensing applications since it provides an approximate distance from the surface within which the system is sensitive to charge variations.

The presence of surface groups is modelled as a (functional) layer of definite thickness (t_{FL}) with a dielectric constant (ϵ_{r-FL}) while the charge density of surface groups is determined by a modified Langmuir-Freundlich isotherm:

$$\sigma_0(\psi_{OHP}) = \sigma_{off} + \sum_{\mu} \frac{\sigma_{max}^{\mu}}{1 + 10^{m(pH - pK_a^{\mu} \text{sign}[\sigma_{max}^{\mu}] e^{q\psi_0(\psi_{OHP}) \text{sign}[\sigma_{max}^{\mu}]/k_B T})}} \quad (\text{A.7})$$

where m is the heterogeneity parameter in the distribution of ionizable groups, σ_{off} is a charge density offset, $\text{sign}[\sigma_{max}^{\mu}]$ is either +1 or -1 for positively or negatively charged groups, pK_a^{μ} is the minus logarithm of the acid dissociation constant, and σ_{max}^{μ} is the maximum surface charge, of a given type of surface group (μ). The charge density at the graphene surface is then defined as:

$$\sigma_{gr} = C_{int}(\psi_{gr} - \psi_0) = C_{int}((V - \psi_{off}) - \psi_0) \quad (\text{A.8})$$

where C_{int} includes both the quantum capacitance and the capacitance of the functional layer, although for the fittings presented in this thesis, we restrict ourselves to the CNP and the quantum capacitance is not explicitly incorporated into the model as in [152]. ψ_{off} accounts for components CNP is dependent on, such as the drain-source voltage (V_{ds}) or the reference electrode used while V is the applied potential. ψ_0 is then obtained as(see Fig. A.1):

$$\psi_0 = \psi_{OHP} - \sigma_{OHP}/C_{stern} \quad (\text{A.9})$$

By ensuring charge neutrality $\sigma_0 + \sigma_{EDL} + \sigma_{gra} = 0$ we can use equations A.5, A.7 and A.8 to self-consistently solve for ψ_{OHP} given that $\sigma_{gra} = \sigma_{min}$ at the CNP for a pH- C_I couple.

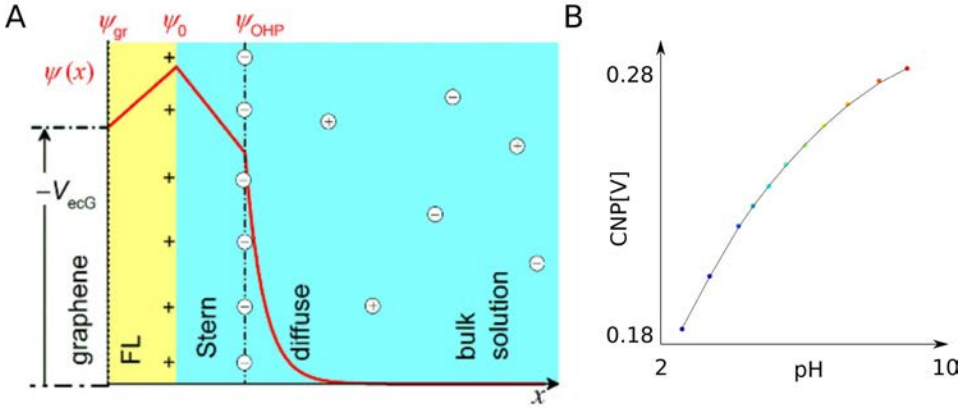


Figure A.1: Graphe-electrolyte interface model schematic and pH-sensitivity experimental results. A: Schematic of the model of the graphene-liquid interface from Zuccaro et. al. [152]. B: Experimental data points and fitting. Extracted parameters are reported in 2.2.

Appendix B

Noise geometrical dependence

For an ideal case, no R_T , the geometrical dependence of V_{rms} can be derived as follow. We start with a relation between current fluctuations(S_I) and resistance fluctuations($S_{R_{ch}}$).

$$\frac{S_I}{I_{ds}^2} = \frac{S_{R_{ch}}}{R_T^2} \quad (\text{B.1})$$

Using ohms law, and that I_{ds}^{RMS} is proportional to the square root of the spectral density ($I_{ds}^{RMS} \propto \sqrt{S_I}$) we obtain:

$$I_{ds}^{RMS} = \frac{I_{ds}^2 \sqrt{S_{R_{ch}}}}{V_{ds}} \quad (\text{B.2})$$

We can then obtain the geometrical dependence of I_{ds}^{RMS} since in an ideal case $I_{ds} \propto W/L$ and assuming a $S_{R_C} \propto L/W^3$ this leads to $I_{ds}^{RMS} \propto \sqrt{W/L^3}$. The geometrical dependence of the effective intrinsic noise in an ideal gSGFET can be derived as:

$$V_{gs}^{RMS} = \frac{I_{ds}^{RMS}}{g_m} \propto \frac{\sqrt{W/L^3}}{W/L} \propto 1/\sqrt{WL} \quad (\text{B.3})$$

B.3 is in accordance with experimental results showing that V_{rms} decreases with the square root of the area [124].

In non-ideal cases, the total normalized noise S_I/I_{ds}^2 generated in a gSGFET includes the contribution from the contacts (S_{R_c}) and from the channel ($S_{R_{ch}}$). The contributions of these terms to the measured current noise can be added linearly with the proper normalization:

$$\frac{S_I}{I_{ds}^2} = \frac{S_{R_c} + S_{R_{ch}}}{R_T^2} \quad (\text{B.4})$$

where R_T is the total resistance of the transistor. The dependence of each of these terms on the channel width (W) and length (L) will determine their relative

contribution to the total noise for different geometries and sizes. The dependence on geometry of S_{R_c} and $S_{R_{ch}}$ can be expressed explicitly:

$$\frac{S_I}{I_{ds}^4} = \frac{k_{R_c}/W^3 + k_{R_{ch}}L/W^3}{V_{ds}^2} \quad (\text{B.5})$$

where k_{R_c} and $k_{R_{ch}}$ include all the constants which are independent of the channel dimensions for S_{R_c} and $S_{R_{ch}}$ respectively.

Appendix C

Graphene production and characterization

C.1 Graphene production

The fabrication of exfoliated graphene in 2004, by the so-called “Scotch-tape” technique, i. e. repetitive cleavage of highly ordered pyrolytic graphite (HOPG) using adhesive tape and then transfer to a substrate, was the beginning of extensive research into the use of the material [10]. Nowadays graphene can be produced by multiple techniques, which vary in cost and quality of the material produced [290]. When considering graphene for a given application, it is vital to choose a production technique that is appropriate for the final device. In the case of electronic devices, appropriate methods are exfoliated graphene, CVD on transition metals, and epitaxial graphene on SiC. Exfoliated graphene will produce devices with the highest carrier mobilities but the exfoliation process is limited in terms of the sizes of the layers that can be obtained. Epitaxial growth on SiC can yield high quality material, and does not require to be transferred to fabricate electronic devices since it is grown on an insulating substrate. However, substrate interactions between the epitaxial graphene layer and the SiC substrate can affect the electronic structure and modify its properties. Importantly, the resulting devices are not flexible.

CVD is one of the most used methods of producing high-quality graphene. Growth is performed at temperatures of 1000°C with a hydrocarbon gas acting as a source of carbon. Metals such as copper, nickel, ruthenium, iridium, palladium, cobalt, and rhenium have been reported to be suitable substrates. The metal substrate catalytically decomposes the hydrocarbon gas and carbon is adsorbed into the substrate. The carbon then precipitates out of the metal, nucleates, grows, and finally merges to form a continuous graphene film. Tuning the growth parameters allows to grow single-layer, bilayer or multiple layer graphene. Moreover, CVD graphene growth is scalable. One caveat of CVD graphene growth is that it requires the resulting film to be transferred to an insulating substrate adequate for electronic devices. Direct growth of CVD graphene on dielectric substrates is a

research line that has reported some success [291, 292], however, direct growth on flexible substrates remains a challenge due to the low-temperature melting point of most flexible materials. Regarding the metal catalyst, copper is one of the best candidates substrates for graphene growth due to the advantages of good control over the graphene number of layers, the growth of high-quality graphene, and the ease for graphene transfer [95, 293].

Theoretically, the values of carrier mobilities in graphene can reach up to 200 000 cm^2/Vs [294]. Experimentally, graphene mobilities up to 140 000 cm^2/Vs at room temperature have been reported [295]. These values are far larger than in any other materials typically used for solution-gated field-effect transistors such as silicon, diamond or III/V semiconductors, which can hardly reach 3000 cm^2/Vs [296, 297]. Since the mobility is strongly affected by the crystal quality of the graphene, its quality and preparation method is crucial to obtain very sensitive devices. The best performance of graphene is obtained using exfoliated graphene flakes. However, as commented, exfoliated graphene cannot be seriously considered a source for commercial production of transistor arrays due to the poor up-scaling offered by this preparation technique. Since CVD allows to obtain graphene with a fairly good quality over a large area, in the last decade big efforts have been done to develop high quality CVD graphene on a large scale. It is now possible, thanks to this technique, to produce and transfer graphene at a rather low cost over large silicon wafers wafers [298], or even squared meters [299] and mobilities superior to 2 000 cm^2/Vs can be regularly obtained on silicon dioxide substrates [300].

Importantly, the quality of the graphene obtained on the growth substrate should not be affected by the technology process. For instance, it is very important to minimize any contamination of the graphene surface, such as the resist residues that are likely to remain after each photolithography step or after the transfer process of graphene.

C.2 CVD Graphene characterization

C.2.1 Optical Microscopy

One could say that the optical identification of individual monolayers is what has made graphene science possible by easing its manipulation. Using Si/SiO_2 substrates with the appropriate thickness produces a visible difference in contrast, enabling location of graphene layers on the substrate [301]. Working with flexible substrates is however more complicated in terms of optical detection. Thankfully some optical contrast is still observed in flexible substrates, specially when graphene is covered by a polymer. Once the polymer is removed, the graphene film is hardly seen, although generally, remaining polymer residues at the edges after transfer allow graphene location to be identified. Also, graphene can be identified due to substrate changes in the region where graphene is not present, for example after graphene patterning by oxygen plasma. In cases of delamination, clear traces of rolled graphene can be seen under the microscope. Care has to be taken in these cases, specially after etching since the layer can be already removed but a pattern image that has been transferred to the polymeric substrate is seen and can be misleading. In summary, although graphene is one-atom-thick and almost transparent, optical microscopy can be considered as the most important tool for graphene localization through all the microfabrication process and provides information about the presence of residues and delamination or rolling of the layer.

C.2.2 Scanning electron microscopy

Despite being almost transparent to the secondary electron (SE) generated in the underneath material, monolayer graphene can be imaged by SEM. That is thanks to several image formation mechanisms. Charging state difference of graphene on an insulator surface causes it to appear brighter. On an air-exposed metal surface, oxidized and non-oxidized surfaces are responsible for the SE contrast generally brighter on the oxidized metal surface. Graphene edges can also exhibit prominent topographic contrast. With a primary electron energy of 1.5–2 keV, it is possible to discriminate the number of layers due to SE intensity decrease with an increase in the number of layers. All this makes SEM a useful technique to image graphene as also both insulating and conducting residues on graphene and also to determine the number of layers.

C.2.3 Raman Spectroscopy

Raman spectroscopy is a spectroscopic technique typically used to determine vibrational modes and relies upon inelastic scattering of photons [302, 303]. Raman shifts are typically reported in wavenumbers, which have units of inverse length, as this value is directly related to energy. Graphene Raman spectrum has three peaks of interest: the D ($\approx 1285 \text{ cm}^{-1}$), G ($\approx 1580 \text{ cm}^{-1}$) and 2D ($\approx 2680 \text{ cm}^{-1}$) peaks [304]. The D peak height gives insight into the number of defects in the graphene lattice, increasing height with defect concentration, whereas the 2D/G peak height ratio illustrates the number of layers. Good-quality monolayer graphene is considered when small or no D peak is present in the Raman spectrum and 2D/G peak height ratio is higher than 3. A typical spectrum of graphene on copper is shown in Fig. 2.8b. The Raman spectrum is affected by the presence of defects in the graphene structure, its stacking in case of multilayer graphene and even its strain. Modern equipment allows mapping a sample with micrometer resolution [305] allowing to assess graphene homogeneity (see Fig. 2.8c-d). Therefore, Raman spectroscopy is an important technique for nondestructively characterizing the lattice structure and electronic, optical and phonon properties of graphene with high spatial resolution.

C.2.4 Atomic Force Microscopy

Atomic force microscopy (AFM) plays a key role in exploring the basic principles underlying the functionality of 2-D materials. It can routinely achieve atomic resolution to identify monoatomic steps and ripples in the z-direction and resolve lattice orientation and surface defects in the xy-plane [306]. Also, surface roughness of the graphene layers can be measured by AFM. The root-mean-square roughness values before/after processing have proven a valuable indicator of the presence and extent of surface residues [118].

Appendix D

Fabrication details

Wafer	Mask	Subst.	Thick.	Graphene	Transfer	UVO
11471-16	CNM946	PI	10um	Aixtron-CNM	Bubbling	
11601-4	CNM946	PI	10um	Aixtron-CNM	Bubbling	
11870-6	CNM946	PI	10um	Aixtron-CNM	Bubbling	
11870-8	CNM946	PI	10um	Aixtron-CNM	Bubbling	
12142-14	CNM946	PI	10um	Graphenea	Graphenea	
12142-15	CNM946	PI	10um	Graphenea	Graphenea	
12142-46	CNM946	PI	10um	Aixtron-CNM	Bubbling	
12142-48	CNM946	PI	10um	Graphenea	Graphenea	
12708-1	CNM985	PI	10um	Aixtron-CNM	Bubbling	
12708-2	CNM985	PI	10um	Aixtron-CNM	Bubbling	20min
12752-1	CNM985	PI	10um	Aixtron-CNM	Wet	20min
12752-2	CNM985	PI	10um	Aixtron-CNM	Wet	20min
13116-2	CNM985	PI	7,5 um	Aixtron-CNM	Wet	20min
13160-4	CNM985	PC	10 um	Aixtron-CNM	Bubbling	
13459-19	CNM985	PC	10 um	Aixtron-CNM	Bubbling	20min

Table D.1: Fabrication details of each wafer. Subst: Substrate, Thick: Thickness, PI: polyimide, PC: parylene-C. Graphenea refers to wafers that were sent to Graphenea (San Sebastian, Spain) for graphene transfer.

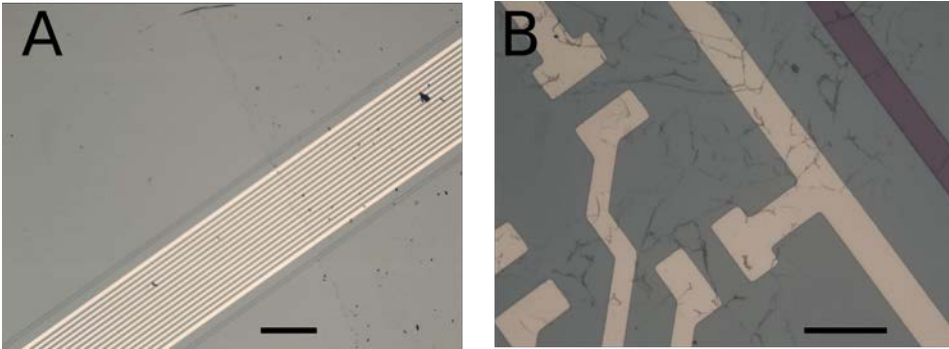


Figure D.1: Photographs of CVD graphene transferred to polyimide covered silicon wafers with predefined metal layer. Scalebars: $500\ \mu\text{m}$ and $100\ \mu\text{m}$ respectively. a) Successful transfer, graphene covers the top right corner of the image. The graphene edge can be seen due to higher contamination. b) Graphene delamination before patterning.

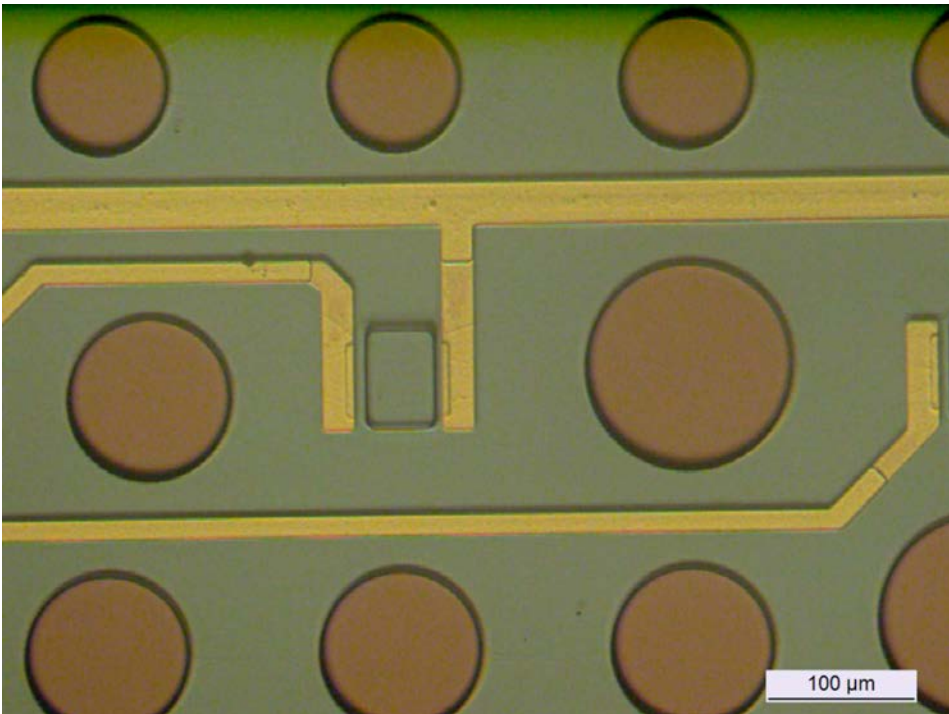


Figure D.2: Photograph of fabricated graphene SGFET arrays on parylene-C substrate. Tip zoom where a gFET can be observed as also the tracks and some holes in the structure.

List of Figures

1.1	Spatiotemporal scales of neural activity monitoring techniques.	6
1.2	Electrophysiological recording chain.	9
1.3	Brain macrostructure and cerebral cortex microstructure.	12
1.4	Basics of CNS electrophysiology.	15
1.5	Extracellular field potentials.	17
1.6	Neural interface schematic.	19
1.7	Solid/electrolyte interface.	21
1.8	Signal recording through electrode and transistor circuits.	24
1.9	Comparison of transistors for recording brain activity.	34
1.10	Graphene atomic and electronic band structure.	37
1.11	Concept of graphene field-effect transistor.	40
2.1	Steady-state characteristics of a graphene solution-gated transistor.	45
2.2	Intrinsic noise of gSGFETs.	46
2.3	Graphene-electrolyte interface model.	47
2.4	Bias dependence of steady-state gSGFET current	48
2.5	Effect of design or process dependent parameters on gSGFET recording performance.	50
2.6	gSGFET array design.	55
2.7	Microfabrication schematic of flexible gSGFET arrays.	57
2.8	SEM and Raman characterization of CVD grown graphene.	62
2.9	Instrumentation for electrical characterization of graphene transistor arrays.	65
2.10	Flexible graphene SGFET arrays.	68

2.11	Results from electrical characterization of all (more than 200) graphene transistors from wafer B12708W2 normalized to the CNP.	70
2.12	Gate voltage dependence of gSGFET spectral noise characteristics.	71
2.13	pH and ion-strength sensitivity of fabricated gSGFETs.	73
2.14	Modelling gSGFET CNP dependence on pH and ion strength of electrolyte solution.	74
2.15	gSGFET transfer curve shape is not altered by pH of the electrolyte solution.	74
2.16	gSGFET frequency response characterization.	75
2.17	Working and noise yield of fabricated gSGFET arrays per wafer.	76
2.18	Boxplot of steady-state characterization of fabricated devices.	77
3.1	Comparison of gSGFET calibration methods.	84
3.2	Calibration procedure of gSGFET current recordings to recover the voltage signal at the gate.	85
3.3	Instrumentation for electrophysiological recordings using graphene transistor arrays.	86
3.4	Recording of slow wave activity with graphene SGFET and comparison with platinum black electrodes.	91
3.5	Recording of awake activity with graphene SGFETs	93
3.6	Recording quality of awake epileptiform activity.	94
3.7	Recording of visual evoked potentials using gSGFETs.	95
3.8	Chronic performance of graphene SGFETs.	97
3.9	gSGFET transfer curve stability after >2h epicortical recording session	99
3.10	Effect of a progressive lateral drift of the transfer curve on the recorded signals.	100
3.11	Effect of a progressive vertical shift of the transfer curve on the recorded signals.	101
3.12	Effect of a progressive shape change of the transfer curve on the recorded signals.	101

3.13	Evaluation of signal distortion due to gSGFET transfer curve changes during in vivo recordings.	102
4.1	In vivo positioning of the gSGFET arrays.	112
4.2	Craniotomy image of the right hemisphere of a Wistar rat for the gSGFET and laser speckle contrast imaging experiment of Fig. 4.11c.	113
4.3	Cortical spreading depression propagation analysis.	114
4.4	Infraslow, local field potential, and wide-band in vivo gSGFET recordings of cortical spreading depression (CSD).	117
4.5	Comparison of CSD recordings by gSGFETs and a solution-filled glass micropipette with a Ag/AgCl wire.	118
4.6	Microelectrode array layout, impedance measurements and calculated voltage gain.	119
4.7	Comparison of DC-coupled gSGFET and microelectrode recordings of cortical spreading depression.	122
4.8	Microelectrode and gSGFET recording modes: considerations for infraslow recordings.	123
4.9	Effect of the high-pass filter needed for baseline oscillations removal in microelectrode recordings in the determination of CSD characteristics.	124
4.10	The wide bandwidth gain of gSGFETs is preserved when scaling transistor size.	124
4.11	Mapping cortical spreading depression with graphene transistors. . .	126
4.12	Depth profile of the infralow-frequency voltage variations induced by cortical spreading depression in a rat cortex.	127
5.1	Experimental paradigm for triggering light-induced cortical spreading depolarizations in awake mice.	144
5.2	Quantification of AAV9-ChR2 transduction volume.	145
5.3	Waveform properties and frequency band analysis of optogenetically-induced spreading depression in awake mice.	146
5.4	Electrophysiological comparison of gender and method of induction for cortical spreading depression in awake mice.	148

5.5	Classification of distinct CSD Waveforms recorded using 16-Channel gSGFETs as a CSD propagates through cortex.	150
5.6	Reproducible and stable CSDs recorded using 16-Channel gSGFETs in response to repetitive optogenetic induction.	151
5.7	Pharmacological sensitivity of optogenetically induced CSD to NMDA antagonists.	153
5.8	NMDA receptor antagonism blocks CSD induction and propagation.	155
5.9	Comparing recordings of Optogenetically induced CSD through the mice dura and the skull.	157
6.1	Overview of baseline potentials shifts of the brain.	165
6.2	Temporal and spectral features of slow-wave activity in a rat under isoflurane anesthesia as recorded by an epicortical gSGFET.	166
6.3	Baseline potential changes and epileptiform activity as recorded by an epidural gSGFET in an awake mouse injected with a proconvulsant.	168
6.4	Ictal baseline potential changes recorded in an awake rat chronically implanted with an epicortical gSGFET after injection of picrotoxin.	169
6.5	<i>In vivomapping</i> of cortical spreading depression and seizures in rat cortex.	171
6.6	Epileptic seizures induced by 4-Aminopyridine (4-AP) in anesthetized Wistar rats.	171
6.7	Changes in neural activity for the transition from deep isoflurane anesthesia to awake and reinduction.	173
6.8	Extracellular potential changes after injection of a terminal sodium pentobarbital dose to an awake head-fixed mice.	174
6.9	Combined fUS imaging and gSGFET recordings of visual evoked activity and CSD.	177
6.10	Combined fUS imaging and gSGFET recordings of cortical spreading depression.	178
6.11	Intrinsic autofluorescence of polyimide and parylene-C arrays in comparison with GCaMP expression <i>in vivo</i>	179
6.12	Combined calcium imaging and electrophysiological recording of cortical spreading depression in an awake mouse.	181

6.13 gSGFET recording technology in the context of brain monitoring techniques.	191
A.1 Graphe-electrolyte interface model schematic and pH-sensitivity experimental results.	198
D.1 Photographs of CVD graphene transferred to polyimide covered silicon wafers with predefined metal layer.	206
D.2 Photographs of fabricated graphene SGFET arrays on parylene-C substrate.	206

List of Tables

1.1	Events contributing to extracellular field potentials.	17
1.2	Comparison of electrode and transistor recording technologies.	28
2.1	Design details of the two different mask sets used.	56
2.2	Extracted graphene-electrolyte charge-potential model parameters.	73
2.3	Summary of electrical characteristics of flexible gSGFETs.	78
4.1	Comparison of techniques for the measurement of infraslow brain activity.	110
A.1	Parameters used to simulate gSGFET current.	196
D.1	Fabrication details of each wafer.	205

References

- [1] R. G. M. Morris, W. Oertel, W. Gaebel, G. M. Goodwin, A. Little, P. Montelano, M. Westphal, D. J. Nutt and M. D. Luca. *Consensus Statement on European Brain Research: the need to expand brain research in Europe – 2015*. European Journal of Neuroscience, 44(3):1919–1926, 2016. ISSN 1460-9568. doi:10.1111/ejn.13236. URL <https://onlinelibrary.wiley.com/doi/abs/10.1111/ejn.13236>, _eprint: <https://onlinelibrary.wiley.com/doi/pdf/10.1111/ejn.13236>.
- [2] K. Christof. *Biophysics of Computation: Information Processing in Single Neurons*. Oxford University Press New York, 1999.
- [3] M. E. J. Obien, K. Deligkaris, T. Bullmann, D. J. Bakkum and U. Frey. *Revealing neuronal function through microelectrode array recordings*. Frontiers in Neuroscience, 8:423, 2014. ISSN 1662-4548 1662-453X. doi:10.3389/fnins.2014.00423. URL <http://www.ncbi.nlm.nih.gov/pmc/articles/PMC4285113/>, type: Journal Article.
- [4] D. L. Schomer and F. L. Da Silva. *Niedermeyer’s electroencephalography: basic principles, clinical applications, and related fields*. Lippincott Williams & Wilkins, 2012. ISBN 1-4511-5315-5.
- [5] U. Chaudhary, N. Birbaumer and A. Ramos-Murguialday. *Brain–computer interfaces for communication and rehabilitation*. Nature Reviews Neurology, 12(9):513–525, September 2016. ISSN 1759-4766. doi:10.1038/nrneuro.2016.113. URL <https://www.nature.com/articles/nrneuro.2016.113>, number: 9 Publisher: Nature Publishing Group.
- [6] J.-W. Jeong, G. Shin, S. I. Park, K. J. Yu, L. Xu and J. A. Rogers. *Soft Materials in Neuroengineering for Hard Problems in Neuroscience*. Neuron, 86(1):175–186, April 2015. ISSN 0896-6273. doi:10.1016/j.neuron.2014.12.035. URL [https://www.cell.com/neuron/abstract/S0896-6273\(14\)01144-1](https://www.cell.com/neuron/abstract/S0896-6273(14)01144-1), publisher: Elsevier.
- [7] K. Scholten and E. Meng. *Materials for microfabricated implantable devices: a review*. Lab on a Chip, 15(22):4256–4272, October 2015. ISSN 1473-0189. doi:10.1039/C5LC00809C. URL <https://pubs.rsc.org/en/content/articlelanding/2015/1c/c51c00809c>, publisher: The Royal Society of Chemistry.
- [8] Y. Fang, L. Meng, A. Prominski, E. N. Schaumann, M. Seebald and B. Tian. *Recent advances in bioelectronics chemistry*. Chemical Society Reviews, July 2020. ISSN 1460-4744. doi:10.1039/D0CS00333F. URL <https://pubs.rsc.org/en/content/articlelanding/2020/cs/d0cs00333f>, publisher: The Royal Society of Chemistry.
- [9] C.-H. Chiang, S. M. Won, A. L. Orsborn, K. J. Yu, M. Trumpis, B. Bent, C. Wang, Y. Xue, S. Min, V. Woods, C. Yu, B. H. Kim, S. B. Kim, R. Huq, J. Li, K. J. Seo, F. Vitale, A. Richardson, H. Fang, Y. Huang, K. Shepard, B. Pesaran, J. A. Rogers and J. Vimenti. *Development of a neural interface for high-definition, long-term recording in rodents and nonhuman primates*. Science Translational Medicine, 12(538), April 2020. ISSN 1946-6234, 1946-6242. doi:10.1126/scitranslmed.aay4682. URL <https://stm.sciencemag.org/content/12/538/eaay4682>, publisher: American Association for the Advancement of Science Section: Research Article.

- [10] K. S. Novoselov, A. K. Geim, S. V. Morozov, D. Jiang, Y. Zhang, S. V. Dubonos, I. V. Grigorieva and A. A. Firsov. *Electric Field Effect in Atomically Thin Carbon Films*. Science, 306(5696):666–669, October 2004. ISSN 0036-8075, 1095-9203. doi:10.1126/science.1102896. URL <https://science.sciencemag.org/content/306/5696/666>, publisher: American Association for the Advancement of Science Section: Report.
- [11] L. H. Hess, M. Seifert and J. A. Garrido. *Graphene Transistors for Bioelectronics*. Proceedings of the IEEE, 101(7):1780–1792, July 2013. ISSN 1558-2256. doi:10.1109/JPROC.2013.2261031. Conference Name: Proceedings of the IEEE.
- [12] M. DiLuca and J. Olesen. *The Cost of Brain Diseases: A Burden or a Challenge?* Neuron, 82(6):1205–1208, June 2014. ISSN 0896-6273. doi:10.1016/j.neuron.2014.05.044. URL [https://www.cell.com/neuron/abstract/S0896-6273\(14\)00488-7](https://www.cell.com/neuron/abstract/S0896-6273(14)00488-7), publisher: Elsevier.
- [13] T. J. Sejnowski, P. S. Churchland and J. A. Movshon. *Putting big data to good use in neuroscience*. Nature Neuroscience, 17(11):1440–1441, November 2014. ISSN 1546-1726. doi:10.1038/nn.3839. URL <https://www.nature.com/articles/nn.3839>, number: 11 Publisher: Nature Publishing Group.
- [14] R. Brette and A. Destexhe. *Handbook of neural activity measurement*. Cambridge University Press, 2012. ISBN 0-521-51622-6.
- [15] Y. G. Maguire, M. G. Shapiro, T. R. Cybulski, J. I. Glaser, D. Amodei, P. B. Stranges, R. Kalhor, D. A. Dalrymple, D. Seo and E. Alon. *Physical principles for scalable neural recording*. Frontiers in computational neuroscience, 7:137, 2013. ISSN 1662-5188. Type: Journal Article.
- [16] T. W. Margrie, M. Brecht and B. Sakmann. *In vivo, low-resistance, whole-cell recordings from neurons in the anaesthetized and awake mammalian brain*. Pflügers Archiv, 444(4):491–498, July 2002. ISSN 1432-2013. doi:10.1007/s00424-002-0831-z. URL <https://doi.org/10.1007/s00424-002-0831-z>.
- [17] S. B. Kodandaramaiah, F. J. Flores, G. L. Holst, A. C. Singer, X. Han, E. N. Brown, E. S. Boyden and C. R. Forest. *Multi-neuron intracellular recording in vivo via interacting autopathing robots*. eLife, 7:e24656, January 2018. ISSN 2050-084X. doi:10.7554/eLife.24656. URL <https://doi.org/10.7554/eLife.24656>, publisher: eLife Sciences Publications, Ltd.
- [18] P. L. Nunez and R. Srinivasan. *Electric fields of the brain: the neurophysics of EEG*. Oxford University Press, USA, 2006. ISBN 0-19-505038-X.
- [19] R. Elul. *The Genesis of the Eeg*. In C. C. Pfeiffer and J. R. Smythies, editors, *International Review of Neurobiology*, volume 15, pages 227–272. Academic Press, January 1972. doi:10.1016/S0074-7742(08)60333-5. URL <http://www.sciencedirect.com/science/article/pii/S0074774208603335>.
- [20] G. Buzsáki, C. A. Anastassiou and C. Koch. *The origin of extracellular fields and currents—EEG, ECoG, LFP and spikes*. Nature reviews neuroscience, 13(6):407–420, 2012. ISBN: 1471-0048 Publisher: Nature Publishing Group.
- [21] J. Hofmeijer, C. R. van Kaam, B. van de Werff, S. E. Vermeer, M. C. Tjepkema-Cloostermans and M. J. A. M. van Putten. *Detecting Cortical Spreading Depolarization with Full Band Scalp Electroencephalography: An Illusion?* Frontiers in Neurology, 9(17), 2018. ISSN 1664-2295. doi:10.3389/fneur.2018.00017. URL <https://www.frontiersin.org/article/10.3389/fneur.2018.00017>, type: Journal Article.

- [22] N. Ji, J. Freeman and S. L. Smith. *Technologies for imaging neural activity in large volumes*. Nature Neuroscience, 19(9):1154–1164, September 2016. ISSN 1546-1726. doi: 10.1038/nn.4358. URL <https://www.nature.com/articles/nn.4358>, number: 9 Publisher: Nature Publishing Group.
- [23] M. Z. Lin and M. J. Schnitzer. *Genetically encoded indicators of neuronal activity*. Nature Neuroscience, 19(9):1142–1153, September 2016. ISSN 1097-6256, 1546-1726. doi:10.1038/nn.4359. URL <http://www.nature.com/articles/nn.4359>.
- [24] J. Hermiz, N. Rogers, E. Kaestner, M. Ganji, D. R. Cleary, B. Carter, D. Barba, S. Dayeh, E. Halgren and V. Gilja. *Sub-millimeter ECoG pitch in human enables higher fidelity cognitive neural state estimation*. NeuroImage, 2018. ISSN 1053-8119. doi: <https://doi.org/10.1016/j.neuroimage.2018.04.027>. URL <http://www.sciencedirect.com/science/article/pii/S105381191830332X>, type: Journal Article.
- [25] D. Khodagholy, J. N. Gelinas, Z. Zhao, M. Yeh, M. Long, J. D. Greenlee, W. Doyle, O. Devinsky and G. Buzsáki. *Organic electronics for high-resolution electrocorticography of the human brain*. Science Advances, 2(11):e1601027, November 2016. ISSN 2375-2548. doi:10.1126/sciadv.1601027. URL <https://advances.sciencemag.org/content/2/11/e1601027>, publisher: American Association for the Advancement of Science Section: Research Article.
- [26] J. Viveri, D.-h. Kim, L. Vigeland, E. S. Frechette, J. A. Blanco, Y.-s. Kim, A. E. Avrin, V. R. Tiruvadi, S.-w. Hwang, A. C. Vanleer, D. F. Wulsin, K. Davis, C. E. Gelber, L. Palmer, J. Spiegel, J. Wu, J. Xiao, Y. Huang, D. Contreras, J. A. Rogers and B. Litt. *Flexible, foldable, actively multiplexed, high density electrode array for mapping brain activity in vivo*. Nature Neuroscience, 14(12):1599–1605, 2011. ISSN 1097-6256. doi:10.1038/nn.2973.
- [27] P. A. House, J. D. MacDonald, P. A. Tresco and R. A. Normann. *Acute microelectrode array implantation into human neocortex: preliminary technique and histological considerations*. Neurosurgical Focus, 20(5):1–4, May 2006. ISSN 1092-0684. doi:10.3171/foc.2006.20.5.5. URL <https://thejns.org/focus/view/journals/neurosurg-focus/20/5/foc.2006.20.5.5.xml>, publisher: American Association of Neurological Surgeons Section: Neurosurgical Focus.
- [28] J. J. Jun, N. A. Steinmetz, J. H. Siegle, D. J. Denman, M. Bauza, B. Barbarits, A. K. Lee, C. A. Anastassiou, A. Andrei, c. Aydin, M. Barbic, T. J. Blanche, V. Bonin, J. Couto, B. Dutta, S. L. Gratiy, D. A. Gutnisky, M. Häusser, B. Karsh, P. Ledochowitsch, C. M. Lopez, C. Mitelut, S. Musa, M. Okun, M. Pachitariu, J. Putzeys, P. D. Rich, C. Rossant, W.-l. Sun, K. Svoboda, M. Carandini, K. D. Harris, C. Koch, J. O’Keefe and T. D. Harris. *Fully integrated silicon probes for high-density recording of neural activity*. Nature, 551(7679):232–236, November 2017. ISSN 1476-4687. doi:10.1038/nature24636. URL <https://www.nature.com/articles/nature24636>, number: 7679 Publisher: Nature Publishing Group.
- [29] L. Hirsch and R. Brenner. *Atlas of EEG in critical care*. John Wiley & Sons, 2011. ISBN 1-119-96483-0.
- [30] V. Emmenegger, M. E. J. Obien, F. Franke and A. Hierlemann. *Technologies to Study Action Potential Propagation With a Focus on HD-MEAs*. Frontiers in Cellular Neuroscience, 13, 2019. ISSN 1662-5102. doi:10.3389/fncel.2019.00159. URL <https://www.frontiersin.org/articles/10.3389/fncel.2019.00159/full>, publisher: Frontiers.

- [31] M. J. Nelson, P. Pouget, E. A. Nilsen, C. D. Patten and J. D. Schall. *Review of signal distortion through metal microelectrode recording circuits and filters*. Journal of Neuroscience Methods, 169(1):141–157, March 2008. ISSN 0165-0270. doi:10.1016/j.jneumeth.2007.12.010. URL <http://www.sciencedirect.com/science/article/pii/S0165027007006048>.
- [32] W. C. Stacey, S. Kellis, B. Greger, C. R. Butson, P. R. Patel, T. Assaf, T. Mihaylova and S. Glynn. *Potential for unreliable interpretation of EEG recorded with microelectrodes*. Epilepsia, 54(8):1391–1401, 2013. ISSN 1528-1167. Type: Journal Article.
- [33] C. Li, R. K. Narayan, P.-M. Wu, N. Rajan, Z. Wu, N. Mehan, E. V. Golanov, C. H. Ahn and J. A. Hartings. *Evaluation of microelectrode materials for direct-current electrocorticography*. Journal of neural engineering, 13(1):016008, 2015. ISSN 1741-2552. URL [jsessionid=868D7577EB35DFAC72622EEE0DD9F6FB.ip-10-40-1-105|http://jopscience.iop.org/article/10.1088/1741-2560/13/1/016008/meta](http://jopscience.iop.org/article/10.1088/1741-2560/13/1/016008/meta), type: Journal Article.
- [34] S. Genon, A. Reid, R. Langner, K. Amunts and S. B. Eickhoff. *How to Characterize the Function of a Brain Region*. Trends in Cognitive Sciences, 22(4):350–364, April 2018. ISSN 1364-6613. doi:10.1016/j.tics.2018.01.010. URL <http://www.sciencedirect.com/science/article/pii/S1364661318300238>.
- [35] S. Herculano-Houzel, B. Mota and R. Lent. *Cellular scaling rules for rodent brains*. Proceedings of the National Academy of Sciences of the United States of America, 103(32):12138–12143, August 2006. ISSN 0027-8424. doi:10.1073/pnas.0604911103. URL <https://www.ncbi.nlm.nih.gov/pmc/articles/PMC1567708/>.
- [36] S. Herculano-Houzel. *The Human Brain in Numbers: A Linearly Scaled-up Primate Brain*. Frontiers in Human Neuroscience, 3, November 2009. ISSN 1662-5161. doi:10.3389/neuro.09.031.2009. URL <https://www.ncbi.nlm.nih.gov/pmc/articles/PMC2776484/>.
- [37] E. T. Rolls. *Cerebral Cortex: Principles of Operation*. Oxford University Press, 2016. ISBN 978-0-19-878485-2. Google-Books-ID: on_ADAAAQBAJ.
- [38] K. Amunts and K. Zilles. *Architectonic Mapping of the Human Brain beyond Brodmann*. Neuron, 88(6):1086–1107, December 2015. ISSN 0896-6273. doi:10.1016/j.neuron.2015.12.001. URL [https://www.cell.com/neuron/abstract/S0896-6273\(15\)01072-7](https://www.cell.com/neuron/abstract/S0896-6273(15)01072-7), publisher: Elsevier.
- [39] L. Krubitzer, K. L. Campi and D. F. Cooke. *All Rodents Are Not the Same: A Modern Synthesis of Cortical Organization*. Brain, Behavior and Evolution, 78(1):51–93, 2011. ISSN 0006-8977, 1421-9743. doi:10.1159/000327320. URL <https://www.karger.com/Article/FullText/327320>, publisher: Karger Publishers.
- [40] M. Häusser. *The Hodgkin-Huxley theory of the action potential*. Nature Neuroscience, 3(11):1165–1165, November 2000. ISSN 1546-1726. doi:10.1038/81426. URL https://www.nature.com/articles/nn1100_1165, number: 11 Publisher: Nature Publishing Group.
- [41] J.-F. Poulin, B. Tasic, J. Hjerling-Leffler, J. M. Trimarchi and R. Awatramani. *Disentangling neural cell diversity using single-cell transcriptomics*. Nature Neuroscience, 19(9):1131–1141, September 2016. ISSN 1546-1726. doi:10.1038/nn.4366. URL <https://www.nature.com/articles/nn.4366>, number: 9 Publisher: Nature Publishing Group.
- [42] L. J. Gentet, M. Avermann, F. Matyas, J. F. Staiger and C. C. H. Petersen. *Membrane Potential Dynamics of GABAergic Neurons in the Barrel Cortex of Behaving Mice*. Neuron, 65(3):422–435, February 2010. ISSN 0896-6273. doi:10.1016/j.neuron.2010.01.006. URL <http://www.sciencedirect.com/science/article/pii/S0896627310000115>.

- [43] C. C. H. Petersen. *Sensorimotor processing in the rodent barrel cortex*. Nature Reviews Neuroscience, 20(9):533–546, September 2019. ISSN 1471-0048. doi:10.1038/s41583-019-0200-y. URL <https://www.nature.com/articles/s41583-019-0200-y>, number: 9 Publisher: Nature Publishing Group.
- [44] G. Dallérac, O. Chever and N. Rouach. *How do astrocytes shape synaptic transmission? Insights from electrophysiology*. Frontiers in Cellular Neuroscience, 7, 2013. ISSN 1662-5102. doi:10.3389/fncel.2013.00159. URL <https://www.frontiersin.org/articles/10.3389/fncel.2013.00159/full>, publisher: Frontiers.
- [45] H. Lindén, T. Tetzlaff, T. Potjans, K. Pettersen, S. Grün, M. Diesmann and G. Einevoll. *Modeling the Spatial Reach of the LFP*. Neuron, 72(5):859–872, December 2011. ISSN 0896-6273. doi:10.1016/j.neuron.2011.11.006. URL <http://www.sciencedirect.com/science/article/pii/S0896627311010051>.
- [46] O. Herreras. *Local field potentials: myths and misunderstandings*. Frontiers in neural circuits, 10:101, 2016. ISSN 1662-5110. Type: Journal Article.
- [47] H. Lindén, E. Hagen, S. Leski, E. S. Norheim, K. H. Pettersen and G. T. Einevoll. *LFPy: a tool for biophysical simulation of extracellular potentials generated by detailed model neurons*. Frontiers in Neuroinformatics, 7, 2014. ISSN 1662-5196. doi:10.3389/fninf.2013.00041. URL <https://www.frontiersin.org/articles/10.3389/fninf.2013.00041/full>, publisher: Frontiers.
- [48] E. Hagen, S. Næss, T. V. Ness and G. T. Einevoll. *Multimodal Modeling of Neural Network Activity: Computing LFP, ECoG, EEG, and MEG Signals With LFPy 2.0*. Frontiers in Neuroinformatics, 12, 2018. ISSN 1662-5196. doi:10.3389/fninf.2018.00092. URL <https://www.frontiersin.org/articles/10.3389/fninf.2018.00092/full>, publisher: Frontiers.
- [49] O. Herreras, J. Makarova and V. A. Makarov. *New uses of LFPs: Pathway-specific threads obtained through spatial discrimination*. Neuroscience, 310:486–503, December 2015. ISSN 0306-4522. doi:10.1016/j.neuroscience.2015.09.054. URL <http://www.sciencedirect.com/science/article/pii/S0306452215008817>.
- [50] F. M. Ashcroft. *Ion Channels and Disease*. Academic Press, October 1999. ISBN 978-0-08-053521-0.
- [51] V. S. Sohal and J. L. R. Rubenstein. *Excitation-inhibition balance as a framework for investigating mechanisms in neuropsychiatric disorders*. Molecular Psychiatry, 24(9):1248–1257, September 2019. ISSN 1476-5578. doi:10.1038/s41380-019-0426-0. URL <https://www.nature.com/articles/s41380-019-0426-0>, number: 9 Publisher: Nature Publishing Group.
- [52] G. Buzsáki and A. Draguhn. *Neuronal Oscillations in Cortical Networks*. Science, 304(5679):1926–1929, June 2004. ISSN 0036-8075, 1095-9203. doi:10.1126/science.1099745. URL <https://science.sciencemag.org/content/304/5679/1926>, publisher: American Association for the Advancement of Science Section: Review.
- [53] T. H. Bullock, M. C. Mcclune and J. T. Enright. *Are the electroencephalograms mainly rhythmic? Assessment of periodicity in wide-band time series*. Neuroscience, 121(1):233–252, September 2003. ISSN 0306-4522. doi:10.1016/S0306-4522(03)00208-2. URL <http://www.sciencedirect.com/science/article/pii/S0306452203002082>.
- [54] W. v. Drongelen. *Signal Processing for Neuroscientists*. Academic Press, April 2018. ISBN 978-0-12-810483-5. Google-Books-ID: Em89DwAAQBAJ.

- [55] A. V. Delgado, F. González-Caballero, R. J. Hunter, L. K. Koopal and J. Lyklema. *Measurement and Interpretation of Electrokinetic Phenomena (IUPAC Technical Report)*. Pure and Applied Chemistry, 77(10):1753–1805, January 2005. ISSN 0033-4545, 1365-3075. doi: 10.1351/pac200577101753. URL <https://www.degruyter.com/view/journals/pac/77/10/article-p1753.xml>, publisher: De Gruyter Section: Pure and Applied Chemistry.
- [56] L. R. Faulkner and A. J. Bard. *Electrochemical methods: fundamentals and applications*. John Wiley and Sons, 2002. ISBN 0-471-40521-3.
- [57] H. Du, X. Lin, Z. Xu and D. Chu. *Electric double-layer transistors: a review of recent progress*. Journal of Materials Science, 50(17):5641–5673, September 2015. ISSN 1573-4803. doi:10.1007/s10853-015-9121-y. URL <https://doi.org/10.1007/s10853-015-9121-y>.
- [58] C. Cea, G. D. Spyropoulos, P. Jastrzebska-Perfect, J. J. Ferrero, J. N. Gelinas and D. Khodagholy. *Enhancement-mode ion-based transistor as a comprehensive interface and real-time processing unit for in vivo electrophysiology*. Nature Materials, pages 1–8, March 2020. ISSN 1476-4660. doi:10.1038/s41563-020-0638-3. URL <https://www.nature.com/articles/s41563-020-0638-3>, publisher: Nature Publishing Group.
- [59] R. J. Baker. *CMOS circuit design, Layout and simulation 3rd Edition*. IEEE press, 2010.
- [60] K. A. Ludwig, R. M. Miriani, N. B. Langhals, M. D. Joseph, D. J. Anderson and D. R. Kipke. *Using a common average reference to improve cortical neuron recordings from microelectrode arrays*. Journal of neurophysiology, 101(3):1679, 2009. Type: Journal Article.
- [61] A. J. Williams, M. Trumpis, B. Bent, C. Chiang and J. Viventi. *A Novel micro-ECoG Electrode Interface for Comparison of Local and Common Averaged Referenced Signals*. In *2018 40th Annual International Conference of the IEEE Engineering in Medicine and Biology Society (EMBC)*, pages 5057–5060. July 2018. doi:10.1109/EMBC.2018.8513432. ISSN: 1558-4615.
- [62] A. Hassibi, R. Navid, R. W. Dutton and T. H. Lee. *Comprehensive study of noise processes in electrode electrolyte interfaces*. Journal of Applied Physics, 96(2):1074–1082, June 2004. ISSN 0021-8979. doi:10.1063/1.1755429. URL <https://aip.scitation.org/doi/abs/10.1063/1.1755429>, publisher: American Institute of Physics.
- [63] R. Sarpeshkar, T. Delbruck and C. A. Mead. *White noise in MOS transistors and resistors*. IEEE Circuits and Devices Magazine, 9(6):23–29, November 1993. ISSN 1558-1888. doi: 10.1109/101.261888. Conference Name: IEEE Circuits and Devices Magazine.
- [64] M. M. Sorkhabi, M. Benjaber, P. Brown and T. Denison. *Physiological Artefacts and the Implications for Brain-Machine-Interface Design*. bioRxiv, page 2020.05.22.111609, May 2020. doi:10.1101/2020.05.22.111609. URL <https://www.biorxiv.org/content/10.1101/2020.05.22.111609v1>, publisher: Cold Spring Harbor Laboratory Section: New Results.
- [65] D. Kuzum, H. Takano, E. Shim, J. C. Reed, H. Juul, A. G. Richardson, J. Vries, H. Bink, M. A. Dichter, T. H. Lucas, D. A. Coulter, E. Cubukcu and B. Litt. *Transparent and flexible low noise graphene electrodes for simultaneous electrophysiology and neuroimaging*. Nature communications, 5:5259, January 2014. ISSN 2041-1723. doi:10.1038/ncomms6259.
- [66] D. Khodagholy, J. Rivnay, M. Sessolo, M. Gurfinkel, P. Leleux, L. H. Jimison, E. Stavrinidou, T. Herve, S. Sanaur, R. M. Owens and G. G. Malliaras. *High transconductance organic electrochemical transistors*. Nature Communications, 4:1575, 2013. ISSN 2041-1723. doi:10.1038/ncomms3133.

- [67] B. M. Blaschke, N. Tort-Colet, A. Guimerà-Brunet, J. Weinert, L. Rousseau, A. Heimann, S. Drieschner, O. Kempfski, R. Villa, M. V. Sanchez-Vives and J. A. Garrido. *Mapping brain activity with flexible graphene micro-transistors*. 2D Materials, 4(2):025040, February 2017. ISSN 2053-1583. doi:10.1088/2053-1583/aa5eff. URL <https://doi.org/10.1088/2053-1583/aa5eff>, publisher: IOP Publishing.
- [68] A. Suarez-Perez, G. Gabriel, B. Rebollo, X. Illa, A. Guimerà-Brunet, J. Hernández-Ferrer, M. T. Martínez, R. Villa and M. V. Sanchez-Vives. *Quantification of Signal-to-Noise Ratio in Cerebral Cortex Recordings Using Flexible MEAs With Co-localized Platinum Black, Carbon Nanotubes, and Gold Electrodes*. Frontiers in Neuroscience, 12, 2018. ISSN 1662-453X. doi:10.3389/fnins.2018.00862. URL <https://www.frontiersin.org/articles/10.3389/fnins.2018.00862/full>, publisher: Frontiers.
- [69] B. I. Turetsky, J. Raz and G. Fein. *Noise and signal power and their effects on evoked potential estimation*. Electroencephalography and Clinical Neurophysiology/Evoked Potentials Section, 71(4):310–318, July 1988. ISSN 0168-5597. doi:10.1016/0168-5597(88)90032-9. URL <http://www.sciencedirect.com/science/article/pii/0168559788900329>.
- [70] O. Özdamar and R. E. Delgado. *Measurement of signal and noise characteristics in ongoing auditory brainstem response averaging*. Annals of Biomedical Engineering, 24(6):702–715, November 1996. ISSN 1573-9686. doi:10.1007/BF02684183. URL <https://doi.org/10.1007/BF02684183>.
- [71] C. Boehler, S. Carli, L. Fadiga, T. Stieglitz and M. Asplund. *Tutorial: guidelines for standardized performance tests for electrodes intended for neural interfaces and bioelectronics*. Nature Protocols, pages 1–22, October 2020. ISSN 1750-2799. doi:10.1038/s41596-020-0389-2. URL <https://www-nature-com-443.webvpn.jnu.edu.cn/articles/s41596-020-0389-2>, publisher: Nature Publishing Group.
- [72] M. Mierzejewski, H. Steins, P. Kshirsagar and P. D. Jones. *The noise and impedance of microelectrodes*. Journal of Neural Engineering, 17(5):052001, October 2020. ISSN 1741-2552. doi:10.1088/1741-2552/abb3b4. URL <https://doi.org/10.1088/1741-2552/abb3b4>, publisher: IOP Publishing.
- [73] S. F. Cogan. *Neural Stimulation and Recording Electrodes*. Annual Review of Biomedical Engineering, 10(1):275–309, 2008. doi:10.1146/annurev.bioeng.10.061807.160518. URL <https://doi.org/10.1146/annurev.bioeng.10.061807.160518>, _eprint: <https://doi.org/10.1146/annurev.bioeng.10.061807.160518>.
- [74] D. Khodagholy, T. Doublet, M. Gurfinkel, P. Quilichini, E. Ismailova, P. Leleux, T. Herve, S. Sanaur, C. Bernard and G. G. Malliaras. *Highly Conformable Conducting Polymer Electrodes for In Vivo Recordings*. Advanced Materials, 23(36):H268–H272, 2011. ISSN 1521-4095. doi:10.1002/adma.201102378. URL <https://onlinelibrary.wiley.com/doi/abs/10.1002/adma.201102378>, _eprint: <https://onlinelibrary.wiley.com/doi/pdf/10.1002/adma.201102378>.
- [75] C. Boehler, T. Stieglitz and M. Asplund. *Nanostructured platinum grass enables superior impedance reduction for neural microelectrodes*. Biomaterials, 67:346–353, 2015. ISBN: 0142-9612 Publisher: Elsevier.
- [76] C. Boehler, D. M. Vieira, U. Egert and M. Asplund. *NanoPt—A Nanostructured Electrode Coating for Neural Recording and Microstimulation*. ACS Applied Materials & Interfaces, 12(13):14855–14865, April 2020. ISSN 1944-8244. doi:10.1021/acsami.9b22798. URL <https://doi.org/10.1021/acsami.9b22798>, publisher: American Chemical Society.

- [77] P. Bergveld, J. Wiersma and H. Meertens. *Extracellular Potential Recordings by Means of a Field Effect Transistor Without Gate Metal, Called OSFET*. IEEE Transactions on Biomedical Engineering, BME-23(2):136–144, March 1976. ISSN 1558-2531. doi:10.1109/TBME.1976.324574. Conference Name: IEEE Transactions on Biomedical Engineering.
- [78] C. Leighton. *Electrolyte-based ionic control of functional oxides*. Nature Materials, 18(1):13–18, January 2019. ISSN 1476-4660. doi:10.1038/s41563-018-0246-7. URL <https://www.nature.com/articles/s41563-018-0246-7>, number: 1 Publisher: Nature Publishing Group.
- [79] M. Krause, S. Ingebrandt, D. Richter, M. Denyer, M. Scholl, C. Sprössler and A. Ofenhäusser. *Extended gate electrode arrays for extracellular signal recordings*. Sensors and Actuators B: Chemical, 70(1):101–107, November 2000. ISSN 0925-4005. doi:10.1016/S0925-4005(00)00568-2. URL <http://www.sciencedirect.com/science/article/pii/S0925400500005682>.
- [80] D. Khodagholy, T. Doublet, P. Quilichini, M. Gurfinkel, P. Leleux, A. Ghestem, E. Ismailova, T. Hervé, S. Sanaur, C. Bernard and G. G. Malliaras. *In vivo recordings of brain activity using organic transistors*. Nature Communications, 4(1):1575, March 2013. ISSN 2041-1723. doi:10.1038/ncomms2573. URL <https://www.nature.com/articles/ncomms2573>, number: 1 Publisher: Nature Publishing Group.
- [81] J. Rivnay, S. Inal, A. Salleo, R. M. Owens, M. Berggren and G. G. Malliaras. *Organic electrochemical transistors*. Nature Reviews Materials, 3(2):1–14, January 2018. ISSN 2058-8437. doi:10.1038/natrevmats.2017.86. URL <https://www.nature.com/articles/natrevmats201786>, number: 2 Publisher: Nature Publishing Group.
- [82] J. T. Friedlein, M. J. Donahue, S. E. Shaheen, G. G. Malliaras and R. R. McLeod. *Microsecond Response in Organic Electrochemical Transistors: Exceeding the Ionic Speed Limit*. Advanced Materials, 28(38):8398–8404, 2016. ISSN 1521-4095. Type: Journal Article.
- [83] M. Dankerl, M. V. Hauf, A. Lippert, L. H. Hess, S. Birner, I. D. Sharp, A. Mahmood, P. Mallet, J.-Y. Veuillen, M. Stutzmann and J. A. Garrido. *Graphene Solution-Gated Field-Effect Transistor Array for Sensing Applications*. Advanced Functional Materials, 20(18):3117–3124, 2010. ISSN 1616-3028. doi:10.1002/adfm.201000724. URL <http://onlinelibrary.wiley.com/store/10.1002/adfm.201000724/asset/3117ftp.pdf?v=1&t=immcgdi&s=8c703f178e10c357bfe6bf01a6cc625893849c7>, type: Journal Article.
- [84] A. Fabbro, D. Scaini, V. León, E. Vázquez, G. Cellot, G. Privitera, L. Lombardi, F. Torrisi, F. Tomarchio, F. Bonaccorso, S. Bosi, A. C. Ferrari, L. Ballerini and M. Prato. *Graphene-Based Interfaces Do Not Alter Target Nerve Cells*. ACS Nano, 10(1):615–623, January 2016. ISSN 1936-0851. doi:10.1021/acsnano.5b05647. URL <https://doi.org/10.1021/acsnano.5b05647>, publisher: American Chemical Society.
- [85] K. Kostarelos, M. Vincent, C. Hebert and J. A. Garrido. *Graphene in the Design and Engineering of Next-Generation Neural Interfaces*. Advanced Materials, 29(42):1700909, 2017. ISSN 1521-4095. doi:10.1002/adma.201700909. URL <https://onlinelibrary.wiley.com/doi/abs/10.1002/adma.201700909>, [_eprint: https://onlinelibrary.wiley.com/doi/pdf/10.1002/adma.201700909](https://onlinelibrary.wiley.com/doi/pdf/10.1002/adma.201700909).
- [86] M. J. Allen, V. C. Tung and R. B. Kaner. *Honeycomb Carbon: A Review of Graphene*. Chemical Reviews, 110(1):132–145, January 2010. ISSN 0009-2665. doi:10.1021/cr900070d. URL <https://doi.org/10.1021/cr900070d>, publisher: American Chemical Society.

- [87] R. Podeszwa. *Interactions of graphene sheets deduced from properties of polycyclic aromatic hydrocarbons*. The Journal of Chemical Physics, 132(4):044704, January 2010. ISSN 0021-9606. doi:10.1063/1.3300064. URL <https://aip.scitation.org/doi/10.1063/1.3300064>, publisher: American Institute of Physics.
- [88] A. K. Geim. *Graphene prehistory*. Physica Scripta, T146:014003, January 2012. ISSN 1402-4896. doi:10.1088/0031-8949/2012/T146/014003. URL <https://doi.org/10.1088/2F0031-8949/2F2012/2Ft146/2F014003>, publisher: IOP Publishing.
- [89] *The Nobel Prize in Physics 2010*. URL <https://www.nobelprize.org/prizes/physics/2010/summary/>, library Catalog: www.nobelprize.org.
- [90] D. A. C. Brownson and C. E. Banks. *The electrochemistry of CVD graphene: progress and prospects*. Physical Chemistry Chemical Physics, 14(23):8264–8281, May 2012. ISSN 1463-9084. doi:10.1039/C2CP40225D. URL <https://pubs.rsc.org/en/content/articlelanding/2012/cp/c2cp40225d>, publisher: The Royal Society of Chemistry.
- [91] C. Lee, X. Wei, J. W. Kysar and J. Hone. *Measurement of the Elastic Properties and Intrinsic Strength of Monolayer Graphene*. Science, 321(5887):385–388, July 2008. ISSN 0036-8075, 1095-9203. doi:10.1126/science.1157996. URL <https://science.sciencemag.org/content/321/5887/385>, publisher: American Association for the Advancement of Science Section: Report.
- [92] R. R. Nair, P. Blake, A. N. Grigorenko, K. S. Novoselov, T. J. Booth, T. Stauber, N. M. R. Peres and A. K. Geim. *Fine Structure Constant Defines Visual Transparency of Graphene*. Science, 320(5881):1308–1308, June 2008. ISSN 0036-8075, 1095-9203. doi:10.1126/science.1156965. URL <https://science.sciencemag.org/content/320/5881/1308>, publisher: American Association for the Advancement of Science Section: Brevia.
- [93] A. H. Castro Neto, F. Guinea, N. M. R. Peres, K. S. Novoselov and A. K. Geim. *The electronic properties of graphene*. Reviews of Modern Physics, 81(1):109–162, January 2009. doi:10.1103/RevModPhys.81.109. URL <https://link.aps.org/doi/10.1103/RevModPhys.81.109>, publisher: American Physical Society.
- [94] L. H. Hess, M. V. Hauf, M. Seifert, F. Speck, T. Seyller, M. Stutzmann, I. D. Sharp and J. A. Garrido. *High-transconductance graphene solution-gated field effect transistors*. Applied Physics Letters, 99(3):033503, July 2011. ISSN 0003-6951. doi:10.1063/1.3614445. URL <https://aip.scitation.org/doi/abs/10.1063/1.3614445>, publisher: American Institute of PhysicsAIP.
- [95] X. Li, W. Cai, J. An, S. Kim, J. Nah, D. Yang, R. Piner, A. Velamakanni, I. Jung, E. Tutuc, S. K. Banerjee, L. Colombo and R. S. Ruoff. *Large-Area Synthesis of High-Quality and Uniform Graphene Films on Copper Foils*. Science, 324(5932):1312–1314, June 2009. ISSN 0036-8075, 1095-9203. doi:10.1126/science.1171245. URL <https://science.sciencemag.org/content/324/5932/1312>, publisher: American Association for the Advancement of Science Section: Report.
- [96] X. Du, L. Wu, J. Cheng, S. Huang, Q. Cai, Q. Jin and J. Zhao. *Graphene microelectrode arrays for neural activity detection*. Journal of biological physics, 41(4):339–47, September 2015. ISSN 1573-0689. doi:10.1007/s10867-015-9382-3.
- [97] A. T. Valota, I. A. Kinloch, K. S. Novoselov, C. Casiraghi, A. Eckmann, E. W. Hill and R. A. W. Dryfe. *Electrochemical Behavior of Monolayer and Bilayer Graphene*. ACS Nano, 5(11):8809–8815, November 2011. ISSN 1936-0851. doi:10.1021/nn202878f. URL <https://doi.org/10.1021/nn202878f>, publisher: American Chemical Society.

- [98] J. Xia, F. Chen, J. Li and N. Tao. *Measurement of the quantum capacitance of graphene*. Nat Nano, 4(8):505–509, 2009. ISSN 1748-3387. doi:http://www.nature.com/nnano/journal/v4/n8/supinfo/nnano.2009.177_S1.html. URL <http://dx.doi.org/10.1038/nnano.2009.177>, type: Journal Article.
- [99] S. Drieschner, A. Guimerà, R. G. Cortadella, D. Viana, E. Makrygiannis, B. M. Blaschke, J. Vieten and J. A. Garrido. *Frequency response of electrolyte-gated graphene electrodes and transistors*. Journal of Physics D: Applied Physics, 50(9):095304, February 2017. ISSN 0022-3727. doi:10.1088/1361-6463/aa5443. URL <https://doi.org/10.1088/2F1361-6463/2Faa5443>, publisher: IOP Publishing.
- [100] D. A. C. Brownson, S. A. Varey, F. Hussain, S. J. Haigh and C. E. Banks. *Electrochemical properties of CVD grown pristine graphene: monolayer- vs. quasi-graphene*. Nanoscale, 6(3):1607–1621, 2014. ISSN 2040-3372. doi:10.1039/c3nr05643k.
- [101] A. Kaplan, Z. Yuan, J. D. Benck, A. G. Rajan, X. S. Chu, Q. H. Wang and M. S. Strano. *Current and future directions in electron transfer chemistry of graphene*. Chemical Society Reviews, 46(15):4530–4571, July 2017. ISSN 1460-4744. doi:10.1039/C7CS00181A. URL <https://pubs.rsc.org/en/content/articlelanding/2017/cs/c7cs00181a>, publisher: The Royal Society of Chemistry.
- [102] A. García-Miranda Ferrari, C. W. Foster, D. A. C. Brownson, K. A. Whitehead and C. E. Banks. *Exploring the reactivity of distinct electron transfer sites at CVD grown monolayer graphene through the selective electrodeposition of MoO₂ nanowires*. Scientific Reports, 9(1):12814, September 2019. ISSN 2045-2322. doi:10.1038/s41598-019-48022-6. URL <https://www.nature.com/articles/s41598-019-48022-6>, number: 1 Publisher: Nature Publishing Group.
- [103] P. Bergveld. *Development, operation, and application of the ion-sensitive field-effect transistor as a tool for electrophysiology*. IEEE Transactions on Biomedical Engineering, (5):342–351, 1972. ISSN 0018-9294. Type: Journal Article.
- [104] A. Goldman. *Electrostatic Gating of Ultrathin Films*. Annual Review of Materials Research, 44(1):45–63, 2014. doi:10.1146/annurev-matsci-070813-113407. URL <https://doi.org/10.1146/annurev-matsci-070813-113407>, _eprint: <https://doi.org/10.1146/annurev-matsci-070813-113407>.
- [105] T. C. Cristarella, A. J. Chinderle, J. Hui and J. Rodríguez-López. *Single-Layer Graphene as a Stable and Transparent Electrode for Nonaqueous Radical Annihilation Electrogenenerated Chemiluminescence*. Langmuir, 31(13):3999–4007, April 2015. ISSN 0743-7463. doi:10.1021/la5050317. URL <https://doi.org/10.1021/la5050317>, publisher: American Chemical Society.
- [106] M. K. Blees, A. W. Barnard, P. A. Rose, S. P. Roberts, K. L. McGill, P. Y. Huang, A. R. Ruyack, J. W. Kevek, B. Kobrin, D. A. Muller and P. L. Mceuen. *Graphene kirigami*. Nature Letter, 524:204–207, 2015. doi:10.1038/nature14588.
- [107] D.-W. Park, A. A. Schendel, S. Mikael, S. K. Brodnick, T. J. Richner, J. P. Ness, M. R. Hayat, F. Atry, S. T. Frye, R. Pashaie, S. Thongpang, Z. Ma and J. C. Williams. *Graphene-based carbon-layered electrode array technology for neural imaging and optogenetic applications*. Nature Communications, 5(1):5258, October 2014. ISSN 2041-1723. doi:10.1038/ncomms6258. URL <https://www.nature.com/articles/ncomms6258>, number: 1 Publisher: Nature Publishing Group.

- [108] P. Ledochowitsch, E. Olivero, T. Blanche and M. M. Maharbiz. *A transparent microECoG array for simultaneous recording and optogenetic stimulation*. In *2011 Annual International Conference of the IEEE Engineering in Medicine and Biology Society*, pages 2937–2940. August 2011. doi:10.1109/IEMBS.2011.6090808. ISSN: 1558-4615.
- [109] X. Guo, X. Liu, F. Lin, H. Li, Y. Fan and N. Zhang. *Highly Conductive Transparent Organic Electrodes with Multilayer Structures for Rigid and Flexible Optoelectronics*. Scientific Reports, 5(1):10569, May 2015. ISSN 2045-2322. doi:10.1038/srep10569. URL <https://www.nature.com/articles/srep10569>, number: 1 Publisher: Nature Publishing Group.
- [110] X. Duan, R. Gao, P. Xie, T. Cohen-Karni, Q. Qing, H. S. Choe, B. Tian, X. Jiang and C. M. Lieber. *Intracellular recordings of action potentials by an extracellular nanoscale field-effect transistor*. Nature Nanotechnology, 7(3):174–179, March 2012. ISSN 1748-3395. doi:10.1038/nnano.2011.223. URL <https://www.nature.com/articles/nnano.2011.223>, number: 3 Publisher: Nature Publishing Group.
- [111] C. Mackin, L. H. Hess, A. Hsu, Y. Song, J. Kong, J. A. Garrido and T. Palacios. *A Current-Voltage Model for Graphene Electrolyte-Gated Field-Effect Transistors*. IEEE Transactions on Electron Devices, 61(12):3971–3977, 2014. ISSN 0018-9383. doi:10.1109/TED.2014.2360660.
- [112] S. Adam, E. H. Hwang, V. M. Galitski and S. Das Sarma. *A self-consistent theory for graphene transport*. PNAS, 104(47):18392–18397, 2007.
- [113] E. Masvidal Codina. *Current–Voltage Model for Graphene Solution-Gated Field-Effect Transistors*, July 2020. doi:10.5281/zenodo.3938679. URL <https://zenodo.org/record/3938679#.XwhGeOexXU9>, language: eng.
- [114] A. A. Balandin. *Low-frequency $1/f$ noise in graphene devices*. Nature Nanotechnology, 8(8):549–555, August 2013. ISSN 1748-3395. doi:10.1038/nnano.2013.144. URL <https://www.nature.com/articles/nnano.2013.144>, number: 8 Publisher: Nature Publishing Group.
- [115] N. Mavredakis, R. G. Cortadella, A. B. Calia, J. A. Garrido and D. Jiménez. *Understanding the bias dependence of low frequency noise in single layer graphene FETs*. Nanoscale, 10(31):14947–14956, August 2018. ISSN 2040-3372. doi:10.1039/C8NR04939D. URL <https://pubs.rsc.org/en/content/articlelanding/2018/nr/c8nr04939d>, publisher: The Royal Society of Chemistry.
- [116] Y.-M. Lin, K. A. Jenkins, A. Valdes-Garcia, J. P. Small, D. B. Farmer and P. Avouris. *Operation of Graphene Transistors at Gigahertz Frequencies*. Nano Letters, 9(1):422–426, January 2009. ISSN 1530-6984. doi:10.1021/nl803316h. URL <https://doi.org/10.1021/nl803316h>, publisher: American Chemical Society.
- [117] A. Pirkle, J. Chan, A. Venugopal, D. Hinojos, C. Magnuson, S. McDonnell, L. Colombo, E. Vogel, R. Ruoff and R. Wallace. *The effect of chemical residues on the physical and electrical properties of chemical vapor deposited graphene transferred to SiO₂*. Applied Physics Letters, 99(12):122108, 2011. ISSN 0003-6951. Type: Journal Article.
- [118] N. Schaefer, R. Garcia-Cortadella, A. B. Calia, N. Mavredakis, X. Illa, E. Masvidal-Codina, J. d. I. Cruz, E. d. Corro, L. Rodríguez, E. Prats-Alfonso, J. Bousquet, J. Martínez-Aguilar, A. P. Pérez-Marín, C. Hébert, R. Villa, D. Jiménez, A. Guimerà-Brunet and J. A. Garrido. *Improved metal-graphene contacts for low-noise, high-density micro-transistor arrays for neural sensing*. Carbon, 161:647–655, May 2020. ISSN 0008-6223. doi:10.1016/j.carbon.2020.01.066. URL <http://www.sciencedirect.com/science/article/pii/S0008622320300737>.

- [119] F. Giubileo and A. Di Bartolomeo. *The role of contact resistance in graphene field-effect devices*. Progress in Surface Science, 92(3):143–175, August 2017. ISSN 0079-6816. doi:10.1016/j.progsurf.2017.05.002. URL <http://www.sciencedirect.com/science/article/pii/S0079681617300126>.
- [120] G. Giovannetti, P. A. Khomyakov, G. Brocks, V. M. Karpan, J. van den Brink and P. J. Kelly. *Doping Graphene with Metal Contacts*. Physical Review Letters, 101(2):026803, July 2008. doi:10.1103/PhysRevLett.101.026803. URL <https://link.aps.org/doi/10.1103/PhysRevLett.101.026803>, publisher: American Physical Society.
- [121] S. M. Song, J. K. Park, O. J. Sul and B. J. Cho. *Determination of work function of graphene under a metal electrode and its role in contact resistance*. Nano Letters, 12(8):3887–3892, 2012. ISSN 15306984. doi:10.1021/nl300266p.
- [122] A. Allain, J. Kang, K. Banerjee and A. Kis. *Electrical contacts to two-dimensional semiconductors*. Nature Materials, 14(12):1195–1205, 2015. ISSN 1476-1122. doi:10.1038/nmat4452. Publisher: Nature Publishing Group.
- [123] V. Viswam, M. E. J. Obien, F. Franke, U. Frey and A. Hierlemann. *Optimal Electrode Size for Multi-Scale Extracellular-Potential Recording From Neuronal Assemblies*. Frontiers in Neuroscience, 13, 2019. ISSN 1662-453X. doi:10.3389/fnins.2019.00385. URL <https://www.frontiersin.org/articles/10.3389/fnins.2019.00385/full>, publisher: Frontiers.
- [124] E. Masvidal-Codina, X. Illa, M. Dasilva, A. B. Calia, T. Dragojević, E. E. Vidal-Rosas, E. Prats-Alfonso, J. Martínez-Aguilar, J. M. D. I. Cruz, R. Garcia-Cortadella, P. Godignon, G. Rius, A. Camassa, E. D. Corro, J. Bousquet, C. Hébert, T. Durduran, R. Villa, M. V. Sanchez-Vives, J. A. Garrido and A. Guimerà-Brunet. *High-resolution mapping of infraslow cortical brain activity enabled by graphene microtransistors*. Nature Materials, 18(3):280–288, March 2019. ISSN 1476-4660. doi:10.1038/s41563-018-0249-4. URL <https://www.nature.com/articles/s41563-018-0249-4>.
- [125] R. Garcia-Cortadella, E. Masvidal-Codina, J. M. D. I. Cruz, N. Schäfer, G. Schweisig, C. Jeschke, J. Martinez-Aguilar, M. V. Sanchez-Vives, R. Villa, X. Illa, A. Sirota, A. Guimerà and J. A. Garrido. *Distortion-Free Sensing of Neural Activity Using Graphene Transistors*. Small, 16(16):1906640, 2020. ISSN 1613-6829. doi:10.1002/smll.201906640. URL <https://onlinelibrary.wiley.com/doi/abs/10.1002/smll.201906640>, [_eprint: https://onlinelibrary.wiley.com/doi/pdf/10.1002/smll.201906640](https://onlinelibrary.wiley.com/doi/pdf/10.1002/smll.201906640).
- [126] C. Hébert, E. Masvidal-Codina, A. Suarez-Perez, A. B. Calia, G. Piret, R. Garcia-Cortadella, X. Illa, E. D. C. Garcia, J. M. D. I. C. Sanchez, D. V. Casals, E. Prats-Alfonso, J. Bousquet, P. Godignon, B. Yvert, R. Villa, M. V. Sanchez-Vives, A. Guimerà-Brunet and J. A. Garrido. *Flexible Graphene Solution-Gated Field-Effect Transistors: Efficient Transducers for Micro-Electrocorticography*. Advanced Functional Materials, 28(12):1703976, 2018. ISSN 1616-3028. doi:10.1002/adfm.201703976. URL <https://onlinelibrary.wiley.com/doi/abs/10.1002/adfm.201703976>, [_eprint: https://onlinelibrary.wiley.com/doi/pdf/10.1002/adfm.201703976](https://onlinelibrary.wiley.com/doi/pdf/10.1002/adfm.201703976).
- [127] N. Lago, D. Ceballos, F. J. Rodríguez, T. Stieglitz and X. Navarro. *Long term assessment of axonal regeneration through polyimide regenerative electrodes to interface the peripheral nerve*. Biomaterials, 26(14):2021–2031, May 2005. ISSN 0142-9612. doi:10.1016/j.biomaterials.2004.06.025.
- [128] J. D. Yeager, D. J. Phillips, D. M. Rector and D. F. Bahr. *Characterization of flexible ECoG electrode arrays for chronic recording in awake rats*. Journal of Neuroscience Methods, 173(2):279–285, August 2008. ISSN 0165-0270. doi:10.1016/j.jneumeth.2008.06.024.

- [129] A. Altuna, E. Bellistri, E. Cid, P. Aivar, B. Gal, J. Berganzo, G. Gabriel, A. Guimerà, R. Villa and L. J. Fernández. *SU-8 based microprobes for simultaneous neural depth recording and drug delivery in the brain*. Lab on a Chip, 13(7):1422–1430, 2013. Type: Journal Article.
- [130] R. Chen, A. Canales and P. Anikeeva. *Neural recording and modulation technologies*. Nature Reviews Materials, 2(2):1–16, January 2017. ISSN 2058-8437. doi:10.1038/natrevmats.2016.93. URL <https://www.nature.com/articles/natrevmats201693>, number: 2 Publisher: Nature Publishing Group.
- [131] M. Vomero, M. F. Porto Cruz, E. Zucchini, F. Ciarpella, E. Delfino, S. Carli, C. Boehler, M. Asplund, D. Ricci, L. Fadiga and T. Stieglitz. *Conformable polyimide-based μ ECOGs: Bringing the electrodes closer to the signal source*. Biomaterials, 255:120178, October 2020. ISSN 0142-9612. doi:10.1016/j.biomaterials.2020.120178. URL <http://www.sciencedirect.com/science/article/pii/S0142961220304245>.
- [132] J. Kang, D. Shin, S. Bae, B. H. Hong, D. Shin, B. H. Hong, S. J. Chae, X.-S. Li, A. Benayad, D. D. Loc., F. Gunes, Y. H. Lee, J.-Y. Choi, Z. F. Liu, L. M. Peng, C. A. Richter and Y. P. Chen. *Graphene transfer: key for applications*. Nanoscale, 4(18):5527, 2012. ISSN 2040-3364. doi:10.1039/c2nr31317k. Publisher: The Royal Society of Chemistry.
- [133] L. G. P. Martins, Y. Song, T. Zeng, M. S. Dresselhaus, J. Kong and P. T. Araujo. *Direct transfer of graphene onto flexible substrates*. Proceedings of the National Academy of Sciences, 110(44):17762–17767, October 2013. ISSN 0027-8424, 1091-6490. doi:10.1073/pnas.1306508110. URL <https://www.pnas.org/content/110/44/17762>, publisher: National Academy of Sciences Section: Physical Sciences.
- [134] M. Kim, A. Shah, C. Li, P. Mustonen, J. Susoma, F. Manoocheri, J. Riikonen and H. Lipsanen. *Direct transfer of wafer-scale graphene films*. 2D Materials, 4(3):035004, June 2017. ISSN 2053-1583. doi:10.1088/2053-1583/aa780d. URL <https://doi.org/10.1088/2F2053-1583/2Faa780d>, publisher: IOP Publishing.
- [135] C. J. L. de la Rosa, J. Sun, N. Lindvall, M. T. Cole, Y. Nam, M. Löffler, E. Olsson, K. B. K. Teo and A. Yurgens. *Frame assisted H₂O electrolysis induced H₂ bubbling transfer of large area graphene grown by chemical vapor deposition on Cu*. Applied Physics Letters, 102(2):022101, January 2013. ISSN 0003-6951. doi:10.1063/1.4775583. URL <https://aip.scitation.org/doi/10.1063/1.4775583>, publisher: American Institute of Physics.
- [136] L.-P. Ma, W. Ren and H.-M. Cheng. *Transfer Methods of Graphene from Metal Substrates: A Review*. Small Methods, 3(7):1900049, 2019. ISSN 2366-9608. doi:10.1002/smt.201900049. URL <https://onlinelibrary.wiley.com/doi/abs/10.1002/smt.201900049>, _eprint: <https://onlinelibrary.wiley.com/doi/pdf/10.1002/smt.201900049>.
- [137] H. H. Gatzten, V. Saile and J. Leuthold. *Micro and Nano Fabrication: Tools and Processes*. Springer, January 2015. ISBN 978-3-662-44395-8. Google-Books-ID: qzwLBgAAQBAJ.
- [138] G. Liu, S. Rumyantsev, M. Shur and A. A. Balandin. *Graphene thickness-graded transistors with reduced electronic noise*. Applied Physics Letters, 100(3), 2012. ISSN 00036951. doi:10.1063/1.3676277.
- [139] W. S. Leong, C. T. Nai and J. T. L. Thong. *What Does Annealing Do to Metal–Graphene Contacts?* Nano Letters, 14(7):3840–3847, 2014. ISSN 1530-6984. doi:10.1021/nl500999r. Publisher: American Chemical Society.

- [140] A. Gahoi, V. Passi, S. Kataria, S. Wagner, A. Bablich and M. Lemme. *Systematic comparison of metal contacts on CVD graphene*. In *2015 45th European Solid State Device Research Conference (ESSDERC)*, pages 184–187. IEEE, 2015. ISBN 978-1-4673-7133-9. doi:10.1109/ESSDERC.2015.7324744.
- [141] K. Nagashio, T. Nishimura, K. Kita and A. Toriumi. *Contact resistivity and current flow path at metal/graphene contact*. *Applied Physics Letters*, 97(14):143514, 2010. ISSN 0003-6951. doi:10.1063/1.3491804. Publisher: American Institute of Physics.
- [142] A. Venugopal, L. Colombo and E. M. Vogel. *Contact resistance in few and multilayer graphene devices*. *Applied Physics Letters*, 96(1):013512, 2010. ISSN 0003-6951. doi:10.1063/1.3290248. Publisher: American Institute of Physics.
- [143] W. S. Leong, H. Gong and J. T. L. Thong. *Low-Contact-Resistance Graphene Devices with Nickel-Etched-Graphene Contacts*. *ACS Nano*, 8(1):994–1001, 2014. ISSN 1936-0851. doi:10.1021/nn405834b. Publisher: American Chemical Society.
- [144] H. Y. Park, W. S. Jung, D. H. Kang, J. Jeon, G. Yoo, Y. Park, J. Lee, Y. H. Jang, J. Lee, S. Park, H. Y. Yu, B. Shin, S. Lee and J. H. Park. *Extremely Low Contact Resistance on Graphene through n-Type Doping and Edge Contact Design*. *Advanced Materials*, 28(5):864–870, 2016. ISSN 15214095. doi:10.1002/adma.201503715.
- [145] J. T. Smith, A. D. Franklin, D. B. Farmer and C. D. Dimitrakopoulos. *Reducing Contact Resistance in Graphene Devices through Contact Area Patterning*. *ACS Nano*, 7(4):3661–3667, 2013. ISSN 1936-0851. doi:10.1021/nn400671z. Publisher: American Chemical Society.
- [146] X. Yan, K. Jia, Y. Su, Y. Ma, J. Luo, H. Zhu and Y. Wei. *Edge-Contact Formed by Oxygen Plasma and Rapid Thermal Annealing to Improve Metal-Graphene Contact Resistance*. *ECS Journal of Solid State Science and Technology*, 7(2):M11–M15, 2018. ISSN 2162-8769. doi:10.1149/2.0251802jss.
- [147] S.-H. Cho, H. M. Lu, L. Cauller, M. I. Romero-Ortega, J.-B. Lee and G. A. Hughes. *Biocompatible SU-8-based microprobes for recording neural spike signals from regenerated peripheral nerve fibers*. *Ieee Sensors Journal*, 8(11):1830–1836, 2008. ISSN 1530-437X. Type: Journal Article.
- [148] K. V. Nemani, K. L. Moodie, J. B. Brennick, A. Su and B. Gimi. *In vitro and in vivo evaluation of SU-8 biocompatibility*. *Materials Science and Engineering: C*, 33(7):4453–4459, 2013. ISSN 0928-4931. Type: Journal Article.
- [149] J. Ortigoza-Diaz, K. Scholten, C. Larson, A. Cobo, T. Hudson, J. Yoo, A. Baldwin, A. Weltman Hirschberg and E. Meng. *Techniques and Considerations in the Microfabrication of Parylene C Microelectromechanical Systems*. *Micromachines*, 9(9):422, September 2018. doi:10.3390/mi9090422. URL <https://www.mdpi.com/2072-666X/9/9/422>, number: 9 Publisher: Multidisciplinary Digital Publishing Institute.
- [150] B. Mailly-Giacchetti, A. Hsu, H. Wang, V. Vinciguerra, F. Pappalardo, L. Occhipinti, E. Guidetti, S. Coffa, J. Kong and T. Palacios. *pH sensing properties of graphene solution-gated field-effect transistors*. *Journal of Applied Physics*, 114(8):084505, 2013. doi:doi:http://dx.doi.org/10.1063/1.4819219. URL <http://scitation.aip.org/docserver/fulltext/aip/journal/jap/114/8/1.4819219.pdf?expires=1459862382&id=id&accname=2109340&checksum=B595864B461416D56BB2B27D36BB9C76>, type: Journal Article.

- [151] W. Fu, C. Nef, O. Knopfmacher, A. Tarasov, M. Weiss, M. Calame and C. Schönenberger. *Graphene Transistors Are Insensitive to pH Changes in Solution*. Nano Letters, 11(9):3597–3600, September 2011. ISSN 1530-6984. doi:10.1021/nl201332c. URL <https://doi.org/10.1021/nl201332c>, publisher: American Chemical Society.
- [152] L. Zuccaro, J. Krieg, A. Desideri, K. Kern and K. Balasubramanian. *Tuning the isoelectric point of graphene by electrochemical functionalization*. Scientific Reports, 5(1):11794, July 2015. ISSN 2045-2322. doi:10.1038/srep11794. URL <https://www.nature.com/articles/srep11794>, number: 1 Publisher: Nature Publishing Group.
- [153] B. M. Blaschke. *Graphene solution-gated field-effect transistors*. Master’s thesis, Technische Universität München, München, 2012.
- [154] E. Masvidal Codina. *pH and ionic strength graphene charge neutrality point model*, July 2020. doi:10.5281/zenodo.3938518. URL <https://zenodo.org/record/3938518#.Xwg0PuexXU9>, language: eng.
- [155] A. A. Balandin. *Low-frequency 1/f noise in graphene devices*. Nature Nanotechnology, 8(8):549–555, 2013. ISSN 17483395. doi:10.1038/nnano.2013.144. ISBN: 1748-3387 Publisher: Nature Publishing Group.
- [156] B. Pellegrini, P. Marconcini, M. Macucci, G. Fiori and G. Basso. *Carrier density dependence of 1/f noise in graphene explained as a result of the interplay between band-structure and inhomogeneities*. Journal of Statistical Mechanics: Theory and Experiment, 2016(5):054017, 2016. ISSN 1742-5468. doi:10.1088/1742-5468/2016/05/054017. Publisher: IOP Publishing.
- [157] A. N. Pal, S. Ghatak, V. Kochat, E. S. Sneha, A. Sampathkumar, S. Raghavan and A. Ghosh. *Microscopic Mechanism of 1/f Noise in Graphene: Role of Energy Band Dispersion*. ACS Nano, 5(3):2075–2081, 2011. ISSN 1936-0851. doi:10.1021/nn103273n. Publisher: American Chemical Society.
- [158] B. Razavi and R. Behzad. *RF microelectronics*, volume 2. Prentice Hall New York, 2012.
- [159] S. Rodriguez, A. Smith, S. Vaziri, M. Ostling, M. C. Lemme and A. Rusu. *Static Non-linearity in Graphene Field Effect Transistors*. IEEE Transactions on Electron Devices, 61(8):3001–3003, August 2014. ISSN 1557-9646. doi:10.1109/TED.2014.2326887. Conference Name: IEEE Transactions on Electron Devices.
- [160] M. Mukovski, S. Chauvette, I. Timofeev and M. Volgushev. *Detection of active and silent states in neocortical neurons from the field potential signal during slow-wave sleep*. Cerebral Cortex, 17(2):400–414, 2007. ISSN 10473211. doi:10.1093/cercor/bhj157.
- [161] M. Mattia and M. Sanchez-Vives. *Exploring the spectrum of dynamical regimes and timescales in spontaneous cortical activity*. Cognitive Neurodynamics, 6(3):239–250, 2012. ISSN 18714080. doi:10.1007/s11571-011-9179-4.
- [162] M. Ruiz-Mejias, L. Ciria-Suarez, M. Mattia and M. Sanchez-Vives. *Slow and fast rhythms generated in the cerebral cortex of the anesthetized mouse*. Journal of Neurophysiology, 106(6):2910–2921, December 2011. ISSN 0022-3077. doi:10.1152/jn.00440.2011.
- [163] R. Reig, M. Sanchez-Vives, A. Duque, Y. Yu and D. McCormick. *Synaptic Transmission and Plasticity in an Active Cortical Network*. PLoS ONE, 2(8):e670, August 2007. ISSN 1932-6203. doi:10.1371/journal.pone.0000670.

- [164] A. Guimerà-Brunet, E. Masvidal-Codina, X. Illa, M. Dasilva, A. Bonaccini-Calia, E. Prats-Alfonso, J. Martínez-Aguilar, J. De la Cruz, R. Garcia-Cortadella, N. Schaefer, A. Barbero, P. Godignon, G. Rius, E. Del Corro, J. Bousquet, C. Hébert, R. Wykes, M. V. Sanchez-Vives, R. Villa and J. A. Garrido. *Neural interfaces based on flexible graphene transistors: A new tool for electrophysiology*. In *2019 IEEE International Electron Devices Meeting (IEDM)*, pages 18.3.1–18.3.4. December 2019. doi:10.1109/IEDM19573.2019.8993433. ISSN: 2156-017X.
- [165] A. B. Schwartz, X. T. Cui, D. Weber and D. W. Moran. *Brain-Controlled Interfaces: Movement Restoration with Neural Prosthetics*. *Neuron*, 52(1):205–220, October 2006. ISSN 08966273. doi:10.1016/j.neuron.2006.09.019.
- [166] S. Ahn, K. Kim and S. C. Jun. *Steady-State Somatosensory Evoked Potential for Brain-Computer Interface-Present and Future*. *Frontiers in human neuroscience*, 9:716, 2015. ISSN 1662-5161. doi:10.3389/fnhum.2015.00716.
- [167] Y. Wang, X. Gao, B. Hong, C. Jia and S. Gao. *Brain-Computer Interfaces Based on Visual Evoked Potentials*. *IEEE Engineering in Medicine and Biology Magazine*, 27(5):64–71, September 2008. ISSN 0739-5175. doi:10.1109/EMEMB.2008.923958.
- [168] L. Muller, L. S. Hamilton, E. Edwards, K. E. Bouchard and E. F. Chang. *Spatial resolution dependence on spectral frequency in human speech cortex electrocorticography*. *Journal of Neural Engineering*, 13(5):056013, October 2016. ISSN 1741-2560. doi:10.1088/1741-2560/13/5/056013.
- [169] K. J. Miller, K. E. Weaver and J. G. Ojemann. *Direct electrophysiological measurement of human default network areas*. *Proceedings of the National Academy of Sciences of the United States of America*, 106(29):12174–7, July 2009. ISSN 1091-6490. doi:10.1073/pnas.0902071106.
- [170] T. J. Abel, A. E. Rhone, K. Nourski, M. A. Granner, H. Oya, T. D. Griffiths, D. T. Tranel, H. Kawasaki, M. A. Howard and III. *Mapping the temporal pole with a specialized electrode array: technique and preliminary results*. *Physiological measurement*, 35(3):323–37, March 2014. ISSN 1361-6579. doi:10.1088/0967-3334/35/3/323.
- [171] N. Schaefer, R. Garcia-Cortadella, J. Martínez-Aguilar, G. Schwesig, X. Illa, A. M. Lara, S. Santiago, C. Hébert, G. Guirado, R. Villa, A. Sirota, A. Guimerà-Brunet and J. A. Garrido. *Multiplexed neural sensor array of graphene solution-gated field-effect transistors*. *2D Materials*, 7(2):025046, March 2020. ISSN 2053-1583. doi:10.1088/2053-1583/ab7976. URL <https://doi.org/10.1088/2F2053-1583/2Fab7976>, publisher: IOP Publishing.
- [172] R. Garcia-Cortadella, N. Schäfer, J. Cisneros-Fernandez, L. Ré, X. Illa, G. Schwesig, A. Moya, S. Santiago, G. Guirado, R. Villa, A. Sirota, F. Serra-Graells, J. A. Garrido and A. Guimerà-Brunet. *Switchless Multiplexing of Graphene Active Sensor Arrays for Brain Mapping*. *Nano Letters*, 20(5):3528–3537, May 2020. ISSN 1530-6984. doi:10.1021/acs.nanolett.0c00467. URL <https://doi.org/10.1021/acs.nanolett.0c00467>, publisher: American Chemical Society.
- [173] S. W. Hughes, M. L. Lőrincz, H. R. Parri and V. Crunelli. *Chapter 10 - Infralow (<0.1Hz) oscillations in thalamic relay nuclei: basic mechanisms and significance to health and disease states*. In E. J. W. Van Someren, Y. D. Van Der Werf, P. R. Roelfsema, H. D. Mansvelder and F. H. Lopes Da Silva, editors, *Progress in Brain Research*, volume 193, pages 145–162. Elsevier, 2011. ISBN 0079-6123. doi:10.1016/B978-0-444-53839-0.00010-7. URL <http://www.sciencedirect.com/science/article/pii/B9780444538390000107>, type: Book Section.

- [174] A. Mitra, A. Kraft, P. Wright, B. Acland, A. Z. Snyder, Z. Rosenthal, L. Czerniewski, A. Bauer, L. Snyder, J. Culver, J.-M. Lee and M. E. Raichle. *Spontaneous Infra-slow Brain Activity Has Unique Spatiotemporal Dynamics and Laminar Structure*. *Neuron*, 98(2):297–305.e6, April 2018. ISSN 0896-6273. doi:10.1016/j.neuron.2018.03.015. URL <http://www.sciencedirect.com/science/article/pii/S0896627318301922>.
- [175] S. Lecci, L. M. Fernandez, F. D. Weber, R. Cardis, J.-Y. Chatton, J. Born and A. Lüthi. *Coordinated infraslow neural and cardiac oscillations mark fragility and offline periods in mammalian sleep*. *Science Advances*, 3(2):e1602026, 2017. ISSN 2375-2548. Type: Journal Article.
- [176] A. Mitra, A. Z. Snyder, E. Tagliazucchi, H. Laufs and M. E. Raichle. *Propagated infra-slow intrinsic brain activity reorganizes across wake and slow wave sleep*. *Elife*, 4, 2015. Type: Journal Article.
- [177] T. Hiltunen, J. Kantola, A. A. Elseoud, P. Lepola, K. Suominen, T. Starck, J. Nikkinen, J. Remes, O. Tervonen and S. Palva. *Infra-slow EEG fluctuations are correlated with resting-state network dynamics in fMRI*. *Journal of Neuroscience*, 34(2):356–362, 2014. ISSN 0270-6474. Type: Journal Article.
- [178] D. A. Leopold, Y. Murayama and N. K. Logothetis. *Very slow activity fluctuations in monkey visual cortex: implications for functional brain imaging*. *Cerebral cortex*, 13(4):422–433, 2003. ISSN 1460-2199. Type: Journal Article.
- [179] A. C. Kelly, L. Q. Uddin, B. B. Biswal, F. X. Castellanos and M. P. Milham. *Competition between functional brain networks mediates behavioral variability*. *Neuroimage*, 39(1):527–537, 2008. ISSN 1053-8119. Type: Journal Article.
- [180] D. Y. Chung and C. Ayata. *Chapter 30 - Spreading Depolarizations A2 - Caplan, Louis R.* In J. Biller, M. C. Leary, E. H. Lo, A. J. Thomas, M. Yenari and J. H. Zhang, editors, *Primer on Cerebrovascular Diseases (Second Edition)*, pages 149–153. Academic Press, San Diego, 2017. ISBN 978-0-12-803058-5. doi:10.1016/B978-0-12-803058-5.00030-8. URL <https://www.sciencedirect.com/science/article/pii/B9780128030585000308>, type: Book Section.
- [181] J. A. Hartings, C. W. Shuttleworth, S. A. Kirov, C. Ayata, J. M. Hinzman, B. Foreman, R. D. Andrew, M. G. Boutelle, K. Brennan and A. P. Carlson. *The continuum of spreading depolarizations in acute cortical lesion development: examining Leão’s legacy*. *Journal of Cerebral Blood Flow & Metabolism*, 37(5):1571–1594, 2017. ISSN 0271-678X. Type: Journal Article.
- [182] J. P. Dreier. *The role of spreading depression, spreading depolarization and spreading ischemia in neurological disease*. *Nat Med*, 17(4):439–447, 2011. ISSN 1078-8956. URL <http://www.nature.com/nm/journal/v17/n4/pdf/nm.2333.pdf>, type: Journal Article.
- [183] J. P. Dreier and C. Reiffurth. *The Stroke-Migraine Depolarization Continuum*. *Neuron*, 86(4):902–922, 2015. ISSN 0896-6273. doi:<https://doi.org/10.1016/j.neuron.2015.04.004>. URL <http://www.sciencedirect.com/science/article/pii/S0896627315003335>, type: Journal Article.
- [184] M. Lauritzen, J. P. Dreier, M. Fabricius, J. A. Hartings, R. Graf and A. J. Strong. *Clinical relevance of cortical spreading depression in neurological disorders: migraine, malignant stroke, subarachnoid and intracranial hemorrhage, and traumatic brain injury*. *Journal of Cerebral Blood Flow & Metabolism*, 31(1):17–35, 2011. ISSN 0271-678X. Type: Journal Article.

- [185] J. A. Hartings, C. Li, J. M. Hinzman, C. W. Shuttleworth, G. L. Ernst, J. P. Dreier, J. A. Wilson, N. Andaluz, B. Foreman and A. P. Carlson. *Direct current electrocorticography for clinical neuromonitoring of spreading depolarizations*. Journal of Cerebral Blood Flow & Metabolism, 37(5):1857–1870, 2017. ISSN 0271-678X. Type: Journal Article.
- [186] J. P. Dreier, M. Fabricius, C. Ayata, O. W. Sakowitz, C. W. Shuttleworth, C. Dohmen, R. Graf, P. Vajkoczy, R. Helbok and M. Suzuki. *Recording, analysis, and interpretation of spreading depolarizations in neurointensive care: review and recommendations of the COSBID research group*. Journal of Cerebral Blood Flow & Metabolism, page 0271678X16654496, 2016. ISSN 0271-678X. Type: Journal Article.
- [187] S. Kovac, E.-J. Speckmann and A. Gorji. *Uncensored EEG: The role of DC potentials in neurobiology of the brain*. Progress in Neurobiology, 2018. ISSN 0301-0082. doi:<https://doi.org/10.1016/j.pneurobio.2018.02.001>. URL <http://www.sciencedirect.com/science/article/pii/S0301008217301648>, type: Journal Article.
- [188] S. Vanhatalo, J. Voipio and K. Kaila. *Full-band EEG (FbEEG): an emerging standard in electroencephalography*. Clinical Neurophysiology, 116(1):1–8, 2005. ISSN 1388-2457. doi:<http://dx.doi.org/10.1016/j.clinph.2004.09.015>. URL <http://www.sciencedirect.com/science/article/pii/S1388245704003748>, type: Journal Article.
- [189] S. Vanhatalo, J. M. Palva, M. Holmes, J. Miller, J. Voipio and K. Kaila. *Infraslow oscillations modulate excitability and interictal epileptic activity in the human cortex during sleep*. Proceedings of the National Academy of Sciences of the United States of America, 101(14):5053–5057, 2004. ISSN 0027-8424. Type: Journal Article.
- [190] C. Ayata and M. Lauritzen. *Spreading depression, spreading depolarizations, and the cerebral vasculature*. Physiological reviews, 95(3):953–993, 2015. ISSN 0031-9333. URL <http://physrev.physiology.org/content/physrev/95/3/953.full.pdf>, type: Journal Article.
- [191] S. S. Stensaas and L. J. Stensaas. *Histopathological evaluation of materials implanted in the cerebral cortex*. Acta Neuropathologica, 41(2):145–155, 1978. ISSN 1432-0533. doi:10.1007/bf00689766. URL <http://dx.doi.org/10.1007/BF00689766>, type: Journal Article.
- [192] T. Deneux, A. Kaszas, G. Szalay, G. Katona, T. Lakner, A. Grinvald, B. Rózsa and I. Vanzetta. *Accurate spike estimation from noisy calcium signals for ultrafast three-dimensional imaging of large neuronal populations in vivo*. Nature Communications, 7:12190, 2016. doi:10.1038/ncomms12190<https://www.nature.com/articles/ncomms12190#supplementary-information>. URL <http://dx.doi.org/10.1038/ncomms12190>, type: Journal Article.
- [193] H. Fang, K. J. Yu, C. Gloschat, Z. Yang, E. Song, C.-H. Chiang, J. Zhao, S. M. Won, S. Xu and M. Trumpis. *Capacitively coupled arrays of multiplexed flexible silicon transistors for long-term cardiac electrophysiology*. Nature biomedical engineering, 1(3):0038, 2017. ISSN 2157-846X. Type: Journal Article.
- [194] P. Heremans, A. K. Tripathi, A. de Jamblinne de Meux, E. C. Smits, B. Hou, G. Pourtois and G. H. Gelinck. *Mechanical and electronic properties of thin-film transistors on plastic, and their integration in flexible electronic applications*. Advanced Materials, 28(22):4266–4282, 2016. ISSN 1521-4095. Type: Journal Article.
- [195] B. J. Kim, H. Jang, S.-K. Lee, B. H. Hong, J.-H. Ahn and J. H. Cho. *High-Performance Flexible Graphene Field Effect Transistors with Ion Gel Gate Dielectrics*. Nano Letters, 10(9):3464–3466, 2010. ISSN 1530-6984. doi:10.1021/nl101559n. URL <http://dx.doi.org/10.1021/nl101559n>, type: Journal Article.

- [196] S. Canals, I. Makarova, L. Lopez-Aguado, C. Largo, J. M. Ibarz and O. Herreras. *Longitudinal depolarization gradients along the somatodendritic axis of CA1 pyramidal cells: a novel feature of spreading depression*. Journal of neurophysiology, 94(2):943–951, 2005. ISSN 0022-3077. URL <http://jn.physiology.org/content/jn/94/2/943.full.pdf>, type: Journal Article.
- [197] W. Yang and R. Yuste. *In vivo imaging of neural activity*. Nature Methods, 14:349, 2017. doi:10.1038/nmeth.4230<https://www.nature.com/articles/nmeth.4230#supplementary-information>. URL <http://dx.doi.org/10.1038/nmeth.4230>, type: Journal Article.
- [198] J. Woitzik, N. Hecht, A. Pinczolits, N. Sandow, S. Major, M. K. Winkler, S. Weber-Carstens, C. Dohmen, R. Graf, A. J. Strong, J. P. Dreier and P. Vajkoczy. *Propagation of cortical spreading depolarization in the human cortex after malignant stroke*. Neurology, 80(12):1095–1102, 2013. doi:10.1212/WNL.0b013e3182886932. URL <http://n.neurology.org/content/neurology/80/12/1095.full.pdf>, type: Journal Article.
- [199] S. Baillet. *Magnetoencephalography for brain electrophysiology and imaging*. Nature Neuroscience, 20:327, 2017. doi:10.1038/nn.4504. URL <http://dx.doi.org/10.1038/nn.4504>, type: Journal Article.
- [200] M. Eiselt, F. Gießler, D. Platzek, J. Haueisen, U. Zwiener and J. Röther. *Inhomogeneous propagation of cortical spreading depression—detection by electro-and magnetoencephalography in rats*. Brain research, 1028(1):83–91, 2004. ISSN 0006-8993. Type: Journal Article.
- [201] X. Illa, B. Rebollo, G. Gabriel, M. V. Sánchez-Vives and R. Villa. *A SU-8-based flexible microprobe for close and distal recordings from the cortical network*. In *SPIE Microtechnologies*, pages 951803–951803–6. International Society for Optics and Photonics. Type: Conference Proceedings.
- [202] C. P. Valdes, H. M. Varma, A. K. Kristoffersen, T. Dragojevic, J. P. Culver and T. Durduran. *Speckle contrast optical spectroscopy, a non-invasive, diffuse optical method for measuring microvascular blood flow in tissue*. Biomedical optics express, 5(8):2769–2784, 2014. ISSN 2156-7085. Type: Journal Article.
- [203] D. A. Boas and A. K. Dunn. *Laser speckle contrast imaging in biomedical optics*. Journal of biomedical optics, 15(1):011109, 2010. ISSN 1083-3668. Type: Journal Article.
- [204] R. Bandyopadhyay, A. Gittings, S. Suh, P. Dixon and D. J. Durian. *Speckle-visibility spectroscopy: A tool to study time-varying dynamics*. Review of scientific instruments, 76(9):093110, 2005. ISSN 0034-6748. Type: Journal Article.
- [205] D. M. Rosenberg and C. C. Horn. *Neurophysiological analytics for all! Free open-source software tools for documenting, analyzing, visualizing, and sharing using electronic notebooks*. Journal of Neurophysiology, 116(2):252–262, April 2016. ISSN 0022-3077. doi:10.1152/jn.00137.2016. URL <https://journals.physiology.org/doi/full/10.1152/jn.00137.2016>, publisher: American Physiological Society.
- [206] C. Capone, B. Rebollo, A. Muñoz, X. Illa, P. Del Giudice, M. V. Sanchez-Vives and M. Matia. *Slow Waves in Cortical Slices: How Spontaneous Activity is Shaped by Laminar Structure*. Cerebral Cortex, pages 1–17, 2017. Type: Journal Article.
- [207] M. W. Shinwari, D. Zhitomirsky, I. A. Deen, P. R. Selvaganapathy, M. J. Deen and D. Landheer. *Microfabricated Reference Electrodes and their Biosensing Applications*. Sensors, 10(3):1679, 2010. ISSN 1424-8220. URL <http://www.mdpi.com/1424-8220/10/3/1679>, type: Journal Article.

- [208] S. Chen, Y. Liu and J. Chen. *Heterogeneous electron transfer at nanoscopic electrodes: importance of electronic structures and electric double layers*. Chemical Society Reviews, 43(15):5372–5386, 2014. Type: Journal Article.
- [209] D. A. C. Brownson, L. J. Munro, D. K. Kampouris and C. E. Banks. *Electrochemistry of graphene: not such a beneficial electrode material?* RSC Advances, 1(6):978, 2011. ISSN 2046-2069. doi:10.1039/c1ra00393c. Type: Journal Article.
- [210] M. Shibata and N. Suzuki. *Exploring the role of microglia in cortical spreading depression in neurological disease*. Journal of Cerebral Blood Flow & Metabolism, 37(4):1182–1191, 2017. doi:10.1177/0271678x17690537. URL <http://journals.sagepub.com/doi/abs/10.1177/0271678x17690537>, type: Journal Article.
- [211] A. Mitra and M. E. Raichle. *How networks communicate: propagation patterns in spontaneous brain activity*. Phil. Trans. R. Soc. B, 371(1705):20150546, 2016. ISSN 0962-8436. Type: Journal Article.
- [212] M. Massimini, R. Huber, F. Ferrarelli, S. Hill and G. Tononi. *The sleep slow oscillation as a traveling wave*. Journal of Neuroscience, 24(31):6862–6870, 2004. ISSN 0270-6474. Type: Journal Article.
- [213] A. P. Carlson, C. William Shuttleworth, B. Mead, B. Burlbaw, M. Krasberg and H. Yonas. *Cortical spreading depression occurs during elective neurosurgical procedures*. Journal of neurosurgery, 126(1):266–273, 2017. ISSN 0022-3085. Type: Journal Article.
- [214] D. R. Kramer, T. Fujii, I. Ohiorhenuan and C. Y. Liu. *Interplay between Cortical Spreading Depolarization and Seizures*. Stereotactic and Functional Neurosurgery, 95(1):1–5, 2017. ISSN 1011-6125, 1423-0372. doi:10.1159/000452841. URL <https://www.karger.com/Article/FullText/452841>, publisher: Karger Publishers.
- [215] J. P. Dreier, C. L. Lemale, V. Kola, A. Friedman and K. Schoknecht. *Spreading depolarization is not an epiphenomenon but the principal mechanism of the cytotoxic edema in various gray matter structures of the brain during stroke*. Neuropharmacology, 134:189–207, May 2018. ISSN 0028-3908. doi:10.1016/j.neuropharm.2017.09.027. URL <http://www.sciencedirect.com/science/article/pii/S0028390817304446>.
- [216] I. Aiba and J. L. Noebels. *Spreading depolarization in the brainstem mediates sudden cardiorespiratory arrest in mouse SUDEP models*. Science Translational Medicine, 7(282):282ra46–282ra46, April 2015. ISSN 1946-6234, 1946-6242. doi:10.1126/scitranslmed.aaa4050. URL <https://stm.sciencemag.org/content/7/282/282ra46>, publisher: American Association for the Advancement of Science Section: Research Article.
- [217] A. C. Charles and S. M. Baca. *Cortical spreading depression and migraine*. Nature Reviews Neurology, 9(11):637–644, November 2013. ISSN 1759-4766. doi:10.1038/nrneuro1.2013.192. URL <https://www.nature.com/articles/nrneuro1.2013.192>, number: 11 Publisher: Nature Publishing Group.
- [218] C. Ayata. *Cortical spreading depression triggers migraine attack: pro*. Headache: The Journal of Head and Face Pain, 50(4):725–730, 2010. ISBN: 0017-8748 Publisher: Wiley Online Library.
- [219] D. Pietrobon and M. A. Moskowitz. *Chaos and commotion in the wake of cortical spreading depression and spreading depolarizations*. Nature Reviews Neuroscience, 15(6):379–393, June 2014. ISSN 1471-0048. doi:10.1038/nrn3770. URL <https://www.nature.com/articles/nrn3770>, number: 6 Publisher: Nature Publishing Group.

- [220] B. Blaschke. *Graphene Transistors for Bioelectronic Applications*. Dissertation, Technische Universität München, München, 2018.
- [221] C. Ayata. *Pearls and pitfalls in experimental models of spreading depression*. Cephalalgia, May 2013. doi:10.1177/0333102412470216. URL <https://journals.sagepub.com/doi/10.1177/0333102412470216>, publisher: SAGE PublicationsSage UK: London, England.
- [222] D. Y. Chung, H. Sadeghian, T. Qin, S. Lule, H. Lee, F. Karakaya, S. Goins, F. Oka, M. A. Yaseen and T. Houben. *Determinants of Optogenetic Cortical Spreading Depolarizations*. Cerebral Cortex, 2018. Type: Journal Article.
- [223] T. Houben, I. C. Loonen, S. M. Baca, M. Schenke, J. H. Meijer, M. D. Ferrari, G. M. Terwindt, R. A. Voskuyl, A. Charles, A. M. van den Maagdenberg and E. A. Tolner. *Optogenetic induction of cortical spreading depression in anesthetized and freely behaving mice*. Journal of Cerebral Blood Flow & Metabolism, 37(5):1641–1655, May 2017. ISSN 0271-678X. doi:10.1177/0271678X16645113. URL <https://doi.org/10.1177/0271678X16645113>, publisher: SAGE Publications Ltd STM.
- [224] C. Ikonomidou and L. Turski. *Why did NMDA receptor antagonists fail clinical trials for stroke and traumatic brain injury?* The Lancet Neurology, 1(6):383–386, October 2002. ISSN 1474-4422. doi:10.1016/S1474-4422(02)00164-3. URL <http://www.sciencedirect.com/science/article/pii/S1474442202001643>.
- [225] C. Kudo, A. Nozari, M. A. Moskowitz and C. Ayata. *The impact of anesthetics and hyperoxia on cortical spreading depression*. Experimental Neurology, 212(1):201–206, July 2008. ISSN 0014-4886. doi:10.1016/j.expneurol.2008.03.026. URL <http://www.sciencedirect.com/science/article/pii/S0014488608001465>.
- [226] G. Köhr. *NMDA receptor antagonists: tools in neuroscience with promise for treating CNS pathologies*. The Journal of physiology, 581(Pt 1):1, 2007. Publisher: Wiley-Blackwell.
- [227] K. Eikermann-Haerter, J. H. Lee, N. Yalcin, E. S. Yu, A. Daneshmand, Y. Wei, Y. Zheng, A. Can, B. Sengul, M. D. Ferrari, A. M. J. M. van den Maagdenberg and C. Ayata. *Migraine prophylaxis, ischemic depolarizations, and stroke outcomes in mice*. Stroke, 46(1):229–236, January 2015. ISSN 1524-4628. doi:10.1161/STROKEAHA.114.006982.
- [228] A. Nasretdinov, N. Lotfullina, D. Vinokurova, J. Lebedeva, G. Burkhanova, K. Chernova, A. Zakharov and R. Khazipov. *Direct Current Coupled Recordings of Cortical Spreading Depression Using Silicone Probes*. Frontiers in Cellular Neuroscience, 11, 2017. ISSN 1662-5102. doi:10.3389/fncel.2017.00408. URL <https://www.frontiersin.org/articles/10.3389/fncel.2017.00408/full>, publisher: Frontiers.
- [229] H. Krüger, U. Heinemann and H. J. Luhmann. *Effects of ionotropic glutamate receptor blockade and 5-HT1A receptor activation on spreading depression in rat neocortical slices*. NeuroReport, 10(12):2651–2656, August 1999. ISSN 0959-4965. URL https://journals.lww.com/neuroreport/Abstract/1999/08200/Effects_of_ionotropic_glutamate_receptor_blockade.39.aspx.
- [230] J. Hernández-Cáceres, R. Macías-González, G. Brožek and J. Bureš. *Systemic ketamine blocks cortical spreading depression but does not delay the onset of terminal anoxic depolarization in rats*. Brain Research, 437(2):360–364, December 1987. ISSN 0006-8993. doi:10.1016/0006-8993(87)91652-0. URL <http://www.sciencedirect.com/science/article/pii/0006899387916520>.

- [231] A. Rashidy-Pour, Z. Motaghd-Larijani and J. Bures. *Tolerance to ketamine-induced blockade of cortical spreading depression transfers to MK-801 but not to AP5 in rats*. Brain Research, 693(1):64–69, September 1995. ISSN 0006-8993. doi:10.1016/0006-8993(95)00692-J. URL <http://www.sciencedirect.com/science/article/pii/000689939500692J>.
- [232] M. Fabricius, S. Fuhr, L. Willumsen, J. P. Dreier, R. Bhatia, M. G. Boutelle, J. A. Hartings, R. Bullock, A. J. Strong and M. Lauritzen. *Association of seizures with cortical spreading depression and peri-infarct depolarisations in the acutely injured human brain*. Clinical Neurophysiology, 119(9):1973–1984, September 2008. ISSN 1388-2457. doi:10.1016/j.clinph.2008.05.025. URL <http://www.sciencedirect.com/science/article/pii/S1388245708005543>.
- [233] T. Takizawa, T. Qin, A. Lopes de Morais, K. Sugimoto, J. Y. Chung, L. Morsett, I. Mulder, P. Fischer, T. Suzuki, M. Anzabi, M. Böhm, W.-s. Qu, T. Yanagisawa, S. Hickman, J. E. Khoury, M. J. Whalen, A. M. Harriott, D. Y. Chung and C. Ayata. *Non-invasively triggered spreading depolarizations induce a rapid pro-inflammatory response in cerebral cortex*. Journal of Cerebral Blood Flow & Metabolism, 40(5):1117–1131, May 2020. ISSN 0271-678X. doi:10.1177/0271678X19859381. URL <https://doi.org/10.1177/0271678X19859381>, publisher: SAGE Publications Ltd STM.
- [234] Sugimoto Kazutaka, Chung David Y., Böhm Maximilian, Fischer Paul, Takizawa Tsubasa, Aslihan Aykan Sanem, Qin Tao, Yanagisawa Takeshi, Harriott Andrea, Oka Fumiaki, Yaseen Mohammad A., Sakadžić Sava and Ayata Cen. *Peri-Infarct Hot-Zones Have Higher Susceptibility to Optogenetic Functional Activation-Induced Spreading Depolarizations*. Stroke, 51(8):2526–2535, August 2020. doi:10.1161/STROKEAHA.120.029618. URL <https://www.ahajournals.org/doi/10.1161/STROKEAHA.120.029618>, publisher: American Heart Association.
- [235] J. L. Nathanson, Y. Yanagawa, K. Obata and E. M. Callaway. *Preferential labeling of inhibitory and excitatory cortical neurons by endogenous tropism of adeno-associated virus and lentivirus vectors*. Neuroscience, 161(2):441–450, June 2009. ISSN 0306-4522. doi:10.1016/j.neuroscience.2009.03.032. URL <http://www.sciencedirect.com/science/article/pii/S0306452209003923>.
- [236] G. Nagel, M. Brauner, J. F. Liewald, N. Adeishvili, E. Bamberg and A. Gottschalk. *Light Activation of Channelrhodopsin-2 in Excitable Cells of Caenorhabditis elegans Triggers Rapid Behavioral Responses*. Current Biology, 15(24):2279–2284, December 2005. ISSN 0960-9822. doi:10.1016/j.cub.2005.11.032. URL <http://www.sciencedirect.com/science/article/pii/S0960982205014077>.
- [237] T. Matsuura and J. Bureš. *The minimum volume of depolarized neural tissue required for triggering cortical spreading depression in rat*. Experimental Brain Research, 12(3):238–249, April 1971. ISSN 1432-1106. doi:10.1007/BF00237916. URL <https://link.springer.com/article/10.1007/BF00237916>, company: Springer Distributor: Springer Institution: Springer Label: Springer Number: 3 Publisher: Springer-Verlag.
- [238] H. Kager, W. J. Wadman and G. G. Somjen. *Conditions for the Triggering of Spreading Depression Studied With Computer Simulations*. Journal of Neurophysiology, 88(5):2700–2712, November 2002. ISSN 0022-3077. doi:10.1152/jn.00237.2002. URL <https://journals.physiology.org/doi/full/10.1152/jn.00237.2002>, publisher: American Physiological Society.

- [239] A. Tuttle, J. R. Diaz and Y. Mori. *A computational study on the role of glutamate and NMDA receptors on cortical spreading depression using a multidomain electrodiffusion model*. PLOS Computational Biology, 15(12):e1007455, December 2019. ISSN 1553-7358. doi:10.1371/journal.pcbi.1007455. URL <https://journals.plos.org/ploscompbiol/article?id=10.1371/journal.pcbi.1007455>, publisher: Public Library of Science.
- [240] H. Nakamura, A. J. Strong, C. Dohmen, O. W. Sakowitz, S. Vollmar, M. Sué, L. Kracht, P. Hashemi, R. Bhatia, T. Yoshimine, J. P. Dreier, A. K. Dunn and R. Graf. *Spreading depolarizations cycle around and enlarge focal ischaemic brain lesions*. Brain, 133(7):1994–2006, July 2010. ISSN 0006-8950. doi:10.1093/brain/awq117. URL <https://academic.oup.com/brain/article/133/7/1994/325471>, publisher: Oxford Academic.
- [241] D. von Bornstädt, T. Houben, J. L. Seidel, Y. Zheng, E. Dilekoz, T. Qin, N. Sandow, S. Kura, K. Eikermann-Haerter, M. Endres, D. Boas, M. Moskowitz, E. Lo, J. Dreier, J. Woitzik, S. Sakadžić and C. Ayata. *Supply-Demand Mismatch Transients in Susceptible Peri-infarct Hot Zones Explain the Origins of Spreading Injury Depolarizations*. Neuron, 85(5):1117–1131, March 2015. ISSN 0896-6273. doi:10.1016/j.neuron.2015.02.007. URL <http://www.sciencedirect.com/science/article/pii/S0896627315000963>.
- [242] B. Donmez-Demir, c. E. Erdener, H. Karatas, Z. Kaya, I. Ulusoy and T. Dalkara. *KCl-induced cortical spreading depression waves more heterogeneously propagate than optogenetically-induced waves in lissencephalic brain: an analysis with optical flow tools*. Scientific Reports, 10(1):12793, July 2020. ISSN 2045-2322. doi:10.1038/s41598-020-69669-6. URL <https://www.nature.com/articles/s41598-020-69669-6>, number: 1 Publisher: Nature Publishing Group.
- [243] Y. Kitahara, K. Taga, H. Abe and K. Shimoji. *The Effects of Anesthetics on Cortical Spreading Depression Elicitation and c-fos Expression in Rats*. Journal of Neurosurgical Anesthesiology, 13(1):26–32, January 2001. ISSN 0898-4921. URL https://journals.lww.com/jnsa/Fulltext/2001/01000/The_Effects_of_Anesthetics_on_Cortical_Spreading.5.aspx.
- [244] A. Klass, R. Sánchez-Porras and E. Santos. *Systematic review of the pharmacological agents that have been tested against spreading depolarizations*. Journal of Cerebral Blood Flow & Metabolism, April 2018. doi:10.1177/0271678X18771440. URL <https://journals.sagepub.com/doi/10.1177/0271678X18771440>, publisher: SAGE PublicationsSage UK: London, England.
- [245] A. P. Carlson, M. Abbas, R. L. Alunday, F. Qeadan and C. W. Shuttleworth. *Spreading depolarization in acute brain injury inhibited by ketamine: a prospective, randomized, multiple crossover trial*. Journal of neurosurgery, pages 1–7, May 2018. ISSN 0022-3085. doi:10.3171/2017.12.JNS171665. URL <https://www.ncbi.nlm.nih.gov/pmc/articles/PMC6279620/>.
- [246] Petzold Gabor C., Windmüller Olaf, Haack Stephan, Major Sebastian, Buchheim Katharina, Megow Dirk, Gabriel Siegrun, Lehmann Thomas-Nicolas, Drenckhahn Christoph, Peters Oliver, Meierkord Hartmut, Heinemann Uwe, Dirnagl Ulrich and Dreier Jens P. *Increased Extracellular K⁺ Concentration Reduces the Efficacy of N-methyl-D-aspartate Receptor Antagonists to Block Spreading Depression-Like Depolarizations and Spreading Ischemia*. Stroke, 36(6):1270–1277, June 2005. doi:10.1161/01.STR.0000166023.51307.e0. URL <https://www.ahajournals.org/doi/full/10.1161/01.str.0000166023.51307.e0>, publisher: American Heart Association.

- [247] I. C. M. Loonen, N. A. Jansen, S. M. Cain, M. Schenke, R. A. Voskuyl, A. C. Yung, B. Bohnet, P. Kozłowski, R. D. Thijs, M. D. Ferrari, T. P. Snutch, A. M. J. M. van den Maagdenberg and E. A. Tolner. *Brainstem spreading depolarization and cortical dynamics during fatal seizures in Cacna1a S218L mice*. *Brain*, 142(2):412–425, February 2019. ISSN 0006-8950. doi:10.1093/brain/awy325. URL <https://academic.oup.com/brain/article/142/2/412/5288800>, publisher: Oxford Academic.
- [248] A. Seto, S. Taylor, D. Trudeau, I. Swan, J. Leung, P. Reeson, K. R. Delaney and C. E. Brown. *Induction of ischemic stroke in awake freely moving mice reveals that isoflurane anesthesia can mask the benefits of a neuroprotection therapy*. *Frontiers in Neuroenergetics*, 6:1, 2014. ISSN 1662-6427. doi:10.3389/fnene.2014.00001.
- [249] M. J. Prescott and K. Lidster. *Improving quality of science through better animal welfare: the NC3Rs strategy*. *Lab Animal*, 46(4):152, 2017. ISBN: 1548-4475 Publisher: Nature Publishing Group.
- [250] X. Gong, D. Mendoza-Halliday, J. T. Ting, T. Kaiser, X. Sun, A. M. Bastos, R. D. Wimmer, B. Guo, Q. Chen, Y. Zhou, M. Pruner, C. W. H. Wu, D. Park, K. Deisseroth, B. Barak, E. S. Boyden, E. K. Miller, M. M. Halassa, Z. Fu, G. Bi, R. Desimone and G. Feng. *An Ultra-Sensitive Step-Function Opsin for Minimally Invasive Optogenetic Stimulation in Mice and Macaques*. *Neuron*, 107(1):38–51.e8, July 2020. ISSN 0896-6273. doi:10.1016/j.neuron.2020.03.032. URL <https://www.sciencedirect.com/science/article/pii/S0896627320302397>.
- [251] G. Martín-Vázquez, J. Makarova, V. A. Makarov and O. Herreras. *Determining the True Polarity and Amplitude of Synaptic Currents Underlying Gamma Oscillations of Local Field Potentials*. *PLOS ONE*, 8(9):e75499, September 2013. ISSN 1932-6203. doi:10.1371/journal.pone.0075499. URL <https://journals.plos.org/plosone/article?id=10.1371/journal.pone.0075499>, publisher: Public Library of Science.
- [252] J. A. Hartings, T. Watanabe, J. P. Dreier, S. Major, L. Vendelbo and M. Fabricius. *Recovery of Slow Potentials in AC-Coupled Electrocorticography: Application to Spreading Depolarizations in Rat and Human Cerebral Cortex*. *Journal of Neurophysiology*, 102(4):2563–2575, June 2009. ISSN 0022-3077. doi:10.1152/jn.00345.2009. URL <https://journals.physiology.org/doi/full/10.1152/jn.00345.2009>, publisher: American Physiological Society.
- [253] K. Kanazawa, R. Matsumoto, H. Imamura, M. Matsushashi, T. Kikuchi, T. Kunieda, N. Mikuni, S. Miyamoto, R. Takahashi and A. Ikeda. *Intracranially recorded ictal direct current shifts may precede high frequency oscillations in human epilepsy*. *Clinical Neurophysiology*, 126(1):47–59, January 2015. ISSN 1388-2457. doi:10.1016/j.clinph.2014.05.028. URL <http://www.sciencedirect.com/science/article/pii/S1388245714003034>.
- [254] N. Aladjalova. *Infra-slow rhythmic oscillations of the steady potential of the cerebral cortex*. *Nature*, 179(4567):957, 1957. ISSN 1476-4687. Type: Journal Article.
- [255] M. D. Fox and M. E. Raichle. *Spontaneous fluctuations in brain activity observed with functional magnetic resonance imaging*. *Nature Reviews Neuroscience*, 8(9):700–711, September 2007. ISSN 1471-0048. doi:10.1038/nrn2201. URL <https://www.nature.com/articles/nrn2201>, number: 9 Publisher: Nature Publishing Group.
- [256] J. L. Vincent, G. H. Patel, M. D. Fox, A. Z. Snyder, J. T. Baker, D. C. Van Essen, J. M. Zempel, L. H. Snyder, M. Corbetta and M. E. Raichle. *Intrinsic functional architecture in the anaesthetized monkey brain*. *Nature*, 447(7140):83–86, May 2007. ISSN 1476-4687. doi:10.1038/nature05758. URL <https://www.nature.com/articles/nature05758>, number: 7140 Publisher: Nature Publishing Group.

- [257] S. Monto, S. Palva, J. Voipio and J. M. Palva. *Very Slow EEG Fluctuations Predict the Dynamics of Stimulus Detection and Oscillation Amplitudes in Humans*. *Journal of Neuroscience*, 28(33):8268–8272, August 2008. ISSN 0270-6474, 1529-2401. doi:10.1523/JNEUROSCI.1910-08.2008. URL <https://www.jneurosci.org/content/28/33/8268>, publisher: Society for Neuroscience Section: Brief Communications.
- [258] M. Penttonen, N. Nurminen, R. Miettinen, J. Sirviö, D. A. Henze, J. Csicsvári and G. Buzsáki. *Ultra-slow oscillation (0.025 Hz) triggers hippocampal afterdischarges in Wistar rats*. *Neuroscience*, 94(3):735–743, October 1999. ISSN 0306-4522. doi:10.1016/S0306-4522(99)00367-X. URL <http://www.sciencedirect.com/science/article/pii/S030645229900367X>.
- [259] J. K. Grooms, G. J. Thompson, W.-J. Pan, J. Billings, E. H. Schumacher, C. M. Epstein and S. D. Keilholz. *Infraslow Electroencephalographic and Dynamic Resting State Network Activity*. *Brain Connectivity*, 7(5):265–280, May 2017. ISSN 2158-0014. doi:10.1089/brain.2017.0492. URL <https://www.liebertpub.com/doi/10.1089/brain.2017.0492>, publisher: Mary Ann Liebert, Inc., publishers.
- [260] W.-J. Pan, G. J. Thompson, M. E. Magnuson, D. Jaeger and S. Keilholz. *Infraslow LFP correlates to resting-state fMRI BOLD signals*. *NeuroImage*, 74:288–297, July 2013. ISSN 1053-8119. doi:10.1016/j.neuroimage.2013.02.035. URL <http://www.sciencedirect.com/science/article/pii/S1053811913001626>.
- [261] M. V. Sanchez-Vives. *Origin and dynamics of cortical slow oscillations*. *Current Opinion in Physiology*, 15:217–223, June 2020. ISSN 2468-8673. doi:10.1016/j.cophys.2020.04.005. URL <http://www.sciencedirect.com/science/article/pii/S2468867320300365>.
- [262] M. C. Walker. *Clinical advances in the understanding, diagnosis, and treatment of epilepsy*. *Current Opinion in Neurology*, 33(2):161–162, April 2020. ISSN 1350-7540. doi:10.1097/WCO.0000000000000804. URL https://journals.lww.com/co-neurology/Citation/2020/04000/Clinical_advances_in_the_understanding,_diagnosis,.2.aspx.
- [263] G. G. Somjen. *Electrogenesis of sustained potentials*. *Progress in Neurobiology*, 1:199–237, January 1973. ISSN 0301-0082. doi:10.1016/0301-0082(73)90012-9. URL <http://www.sciencedirect.com/science/article/pii/0301008273900129>.
- [264] A. Gorji and E.-J. Speckmann. *Epileptiform EEG Spikes and Their Functional Significance*. *Clinical EEG and Neuroscience*, October 2009. doi:10.1177/155005940904000404. URL <https://journals.sagepub.com/doi/10.1177/155005940904000404>, publisher: SAGE PublicationsSage CA: Los Angeles, CA.
- [265] E. Rodin and P. Modur. *Ictal intracranial infraslow EEG activity*. *Clinical Neurophysiology*, 119(10):2188–2200, October 2008. ISSN 1388-2457. doi:10.1016/j.clinph.2008.07.222. URL <http://www.sciencedirect.com/science/article/pii/S1388245708008560>.
- [266] M. Avoli, M. Barbarosie, A. Lücke, T. Nagao, V. Lopantsev and R. Köhling. *Synchronous GABA-Mediated Potentials and Epileptiform Discharges in the Rat Limbic System In Vitro*. *Journal of Neuroscience*, 16(12):3912–3924, June 1996. ISSN 0270-6474, 1529-2401. doi:10.1523/JNEUROSCI.16-12-03912.1996. URL <https://www.jneurosci.org/content/16/12/3912>, publisher: Society for Neuroscience Section: Articles.
- [267] V. K. Jirsa, W. C. Stacey, P. P. Quilichini, A. I. Ivanov and C. Bernard. *On the nature of seizure dynamics*. *Brain*, 137(8):2210–2230, August 2014. ISSN 0006-8950. doi:10.1093/brain/awu133. URL <https://academic.oup.com/brain/article/137/8/2210/2847958>, publisher: Oxford Academic.

- [268] M. Eickhoff, S. Kovac, P. Shahabi, M. Khaleghi Ghadiri, J. P. Dreier, W. Stummer, E.-J. Speckmann, H.-C. Pape and A. Gorji. *Spreading depression triggers ictal activity in partially disinhibited neuronal tissues*. *Experimental Neurology*, 253:1–15, March 2014. ISSN 0014-4886. doi:10.1016/j.expneurol.2013.12.008. URL <https://www.sciencedirect.com/science/article/pii/S0014488613003749>.
- [269] N. Tort-Colet, C. Capone, M. V. Sanchez-Vives and M. Mattia. *Attractor competition enriches cortical dynamics during awakening from anesthesia*. bioRxiv, page 517102, January 2019. doi:10.1101/517102. URL <https://www.biorxiv.org/content/10.1101/517102v1>, publisher: Cold Spring Harbor Laboratory Section: New Results.
- [270] S. Tétrault, O. Chever, A. Sik and F. Amzica. *Opening of the blood–brain barrier during isoflurane anaesthesia*. *European Journal of Neuroscience*, 28(7):1330–1341, 2008. ISSN 1460-9568. doi:10.1111/j.1460-9568.2008.06443.x. URL <https://onlinelibrary.wiley.com/doi/abs/10.1111/j.1460-9568.2008.06443.x>, eprint: <https://onlinelibrary.wiley.com/doi/pdf/10.1111/j.1460-9568.2008.06443.x>.
- [271] D. J. Sandstrom. *Isoflurane Reduces Excitability of Drosophila Larval Motoneurons by Activating a Hyperpolarizing Leak Conductance*. *Anesthesiology: The Journal of the American Society of Anesthesiologists*, 108(3):434–446, March 2008. ISSN 0003-3022. doi:10.1097/ALN.0b013e318164cfda. URL <https://anesthesiology.pubs.asahq.org/article.aspx?articleid=1932069>, publisher: The American Society of Anesthesiologists.
- [272] N. Kokita, T. A. Stekiel, M. Yamazaki, Z. J. Bosnjak, J. P. Kampine and W. J. Stekiel. *Potassium Channel-mediated Hyperpolarization of Mesenteric Vascular Smooth Muscle by Isoflurane*. *Anesthesiology: The Journal of the American Society of Anesthesiologists*, 90(3):779–788, March 1999. ISSN 0003-3022. URL <https://anesthesiology.pubs.asahq.org/article.aspx?articleid=1946501>, publisher: The American Society of Anesthesiologists.
- [273] Ohta Kouichi, Graf Rudolf, Rosner Gerd and Heiss Wolf-Dieter. *Calcium Ion Transients in Peri-Infarct Depolarizations May Deteriorate Ion Homeostasis and Expand Infarction in Focal Cerebral Ischemia in Cats*. *Stroke*, 32(2):535–543, February 2001. doi:10.1161/01.STR.32.2.535. URL <https://www.ahajournals.org/doi/full/10.1161/01.str.32.2.535>, publisher: American Heart Association.
- [274] J. M. Hinzman, V. A. DiNapoli, E. J. Mahoney, G. A. Gerhardt and J. A. Hartings. *Spreading depolarizations mediate excitotoxicity in the development of acute cortical lesions*. *Experimental Neurology*, 267:243–253, May 2015. ISSN 0014-4886. doi:10.1016/j.expneurol.2015.03.014. URL <http://www.sciencedirect.com/science/article/pii/S0014488615000825>.
- [275] J. A. Hartings, J. York, C. P. Carroll, J. M. Hinzman, E. Mahoney, B. Krueger, M. K. L. Winkler, S. Major, V. Horst, P. Jahnke, J. Woitzik, V. Kola, Y. Du, M. Hagen, J. Jiang and J. P. Dreier. *Subarachnoid blood acutely induces spreading depolarizations and early cortical infarction*. *Brain*, 140(10):2673–2690, October 2017. ISSN 0006-8950. doi:10.1093/brain/awx214. URL <https://academic.oup.com/brain/article/140/10/2673/4102114>, publisher: Oxford Academic.
- [276] A. I. Oliveira-Ferreira, D. Milakara, M. Alam, D. Jorks, S. Major, J. A. Hartings, J. Lückl, P. Martus, R. Graf, C. Dohmen, G. Bohner, J. Woitzik, J. P. Dreier and f. t. C. s. group. *Experimental and Preliminary Clinical Evidence of an Ischemic Zone with Prolonged Negative*

- DC Shifts Surrounded by a Normally Perfused Tissue Belt with Persistent Electrocortico-graphic Depression*. Journal of Cerebral Blood Flow & Metabolism, March 2010. doi:10.1038/jcbfm.2010.40. URL <https://journals.sagepub.com/doi/10.1038/jcbfm.2010.40>, publisher: SAGE PublicationsSage UK: London, England.
- [277] A. P. Carlson, C. W. Shuttleworth, S. Major, C. L. Lemale, J. P. Dreier and J. A. Hartings. *Terminal spreading depolarizations causing electrocortical silencing prior to clinical brain death: case report*. Journal of Neurosurgery, 131(6):1773–1779, December 2018. ISSN 1933-0693, 0022-3085. doi:10.3171/2018.7.JNS181478. URL <https://thejns.org/view/journals/j-neurosurg/131/6/article-p1773.xml>, publisher: American Association of Neurological Surgeons Section: Journal of Neurosurgery.
- [278] J. P. Dreier, S. Major, B. Foreman, M. K. L. Winkler, E.-J. Kang, D. Milakara, C. L. Lemale, V. DiNapoli, J. M. Hinzman, J. Woitzik, N. Andaluz, A. Carlson and J. A. Hartings. *Terminal spreading depolarization and electrical silence in death of human cerebral cortex*. Annals of Neurology, 83(2):295–310, 2018. ISSN 1531-8249. doi:10.1002/ana.25147. URL <https://onlinelibrary.wiley.com/doi/abs/10.1002/ana.25147>, _eprint: <https://onlinelibrary.wiley.com/doi/pdf/10.1002/ana.25147>.
- [279] B.-J. Zandt, B. t. Haken, M. J. A. M. v. Putten and M. A. Dahlem. *How does spreading depression spread? Physiology and modeling*. Reviews in the Neurosciences, 26(2):183–198, April 2015. ISSN 2191-0200, 0334-1763. doi:10.1515/revneuro-2014-0069. URL <https://www.degruyter.com/view/journals/revneuro/26/2/article-p183.xml>, publisher: De Gruyter Section: Reviews in the Neurosciences.
- [280] E. Macé, G. Montaldo, I. Cohen, M. Baulac, M. Fink and M. Tanter. *Functional ultrasound imaging of the brain*. Nature Methods, 8(8):662–664, August 2011. ISSN 1548-7105. doi:10.1038/nmeth.1641. URL <https://www.nature.com/articles/nmeth.1641>.
- [281] B. Lu, S. Zheng, B. Q. Quach and Y.-C. Tai. *A study of the autofluorescence of parylene materials for microTAS applications*. Lab on a Chip, 10(14):1826–1834, June 2010. ISSN 1473-0189. doi:10.1039/B924855B. URL <https://pubs.rsc.org/en/content/articlelanding/2010/1c/b924855b>, publisher: The Royal Society of Chemistry.
- [282] B. L. Sabatini and L. Tian. *Imaging Neurotransmitter and Neuromodulator Dynamics In Vivo with Genetically Encoded Indicators*. Neuron, 108(1):17–32, October 2020. ISSN 0896-6273. doi:10.1016/j.neuron.2020.09.036. URL <https://www.sciencedirect.com/science/article/pii/S0896627320307601>.
- [283] A. Korovaichuk, J. Makarova, V. A. Makarov, N. Benito and O. Herreras. *Minor Contribution of Principal Excitatory Pathways to Hippocampal LFPs in the Anesthetized Rat: A Combined Independent Component and Current Source Density Study*. Journal of Neurophysiology, 104(1):484–497, May 2010. ISSN 0022-3077. doi:10.1152/jn.00297.2010. URL <https://journals.physiology.org/doi/full/10.1152/jn.00297.2010>, publisher: American Physiological Society.
- [284] A. I. Srienc, K. R. Biesecker, A. M. Shimoda, J. Kur and E. A. Newman. *Ischemia-induced spreading depolarization in the retina*. Journal of Cerebral Blood Flow & Metabolism, 36(9):1579–1591, September 2016. ISSN 0271-678X. doi:10.1177/0271678X16657836. URL <https://doi.org/10.1177/0271678X16657836>, publisher: SAGE Publications Ltd STM.
- [285] G. Tse, E. T. H. Lai, J. M. Yeo, V. Tse and S. H. Wong. *Mechanisms of Electrical Activation and Conduction in the Gastrointestinal System: Lessons from Cardiac Electrophysiology*. Frontiers in Physiology, 7, 2016. ISSN 1664-042X. doi:10.3389/fphys.2016.

00182. URL <https://www.frontiersin.org/articles/10.3389/fphys.2016.00182/full>, publisher: Frontiers.
- [286] C. Andronescu and W. Schuhmann. *Graphene-based field effect transistors as biosensors*. *Current Opinion in Electrochemistry*, 3(1):11–17, June 2017. ISSN 2451-9103. doi:10.1016/j.coelec.2017.03.002. URL <https://www.sciencedirect.com/science/article/pii/S2451910316300217>.
- [287] T. Stieglitz. *Of Man and Mice: Translational Research in Neurotechnology*. *Neuron*, 105(1):12–15, January 2020. ISSN 0896-6273. doi:10.1016/j.neuron.2019.11.030. URL [https://www.cell.com/neuron/abstract/S0896-6273\(19\)31039-6](https://www.cell.com/neuron/abstract/S0896-6273(19)31039-6), publisher: Elsevier.
- [288] J. A. Hartings. *How slow can you go?* *Nature Materials*, 18(3):194–196, March 2019. ISSN 1476-4660. doi:10.1038/s41563-018-0272-5. URL <https://www.nature.com/articles/s41563-018-0272-5>, number: 3 Publisher: Nature Publishing Group.
- [289] H. Ji, X. Zhao, Z. Qiao, J. Jung, Y. Zhu, Y. Lu, L. L. Zhang, A. H. MacDonald and R. S. Ruoff. *Capacitance of carbon-based electrical double-layer capacitors*. *Nature Communications*, 5(1):3317, February 2014. ISSN 2041-1723. doi:10.1038/ncomms4317. URL <https://www.nature.com/articles/ncomms4317>, number: 1 Publisher: Nature Publishing Group.
- [290] *Graphene Science Handbook*. Routledge Handbooks Online, April 2016. ISBN 978-1-4665-9127-1 978-1-4665-9128-8. doi:10.1201/b19606. URL <https://www.routledgehandbooks.com/doi/10.1201/b19606>.
- [291] A. Ismach, C. Druzgalski, S. Penwell, A. Schwartzberg, M. Zheng, A. Javey, J. Bokor and Y. Zhang. *Direct Chemical Vapor Deposition of Graphene on Dielectric Surfaces*. *Nano Letters*, 10(5):1542–1548, May 2010. ISSN 1530-6984. doi:10.1021/nl9037714. URL <https://doi.org/10.1021/nl9037714>, publisher: American Chemical Society.
- [292] H. Kim, I. Song, C. Park, M. Son, M. Hong, Y. Kim, J. S. Kim, H.-J. Shin, J. Baik and H. C. Choi. *Copper-Vapor-Assisted Chemical Vapor Deposition for High-Quality and Metal-Free Single-Layer Graphene on Amorphous SiO₂ Substrate*. *ACS Nano*, 7(8):6575–6582, August 2013. ISSN 1936-0851. doi:10.1021/nn402847w. URL <https://doi.org/10.1021/nn402847w>, publisher: American Chemical Society.
- [293] X. Li, L. Colombo and R. S. Ruoff. *Synthesis of Graphene Films on Copper Foils by Chemical Vapor Deposition*. *Advanced Materials*, 28(29):6247–6252, 2016. ISSN 1521-4095. doi:10.1002/adma.201504760. URL <https://onlinelibrary.wiley.com/doi/abs/10.1002/adma.201504760>, _eprint: <https://onlinelibrary.wiley.com/doi/pdf/10.1002/adma.201504760>.
- [294] E. H. Hwang, S. Adam and S. D. Sarma. *Carrier Transport in Two-Dimensional Graphene Layers*. *Physical Review Letters*, 98(18):186806, May 2007. doi:10.1103/PhysRevLett.98.186806. URL <https://link.aps.org/doi/10.1103/PhysRevLett.98.186806>, publisher: American Physical Society.
- [295] L. Wang, I. Meric, P. Y. Huang, Q. Gao, Y. Gao, H. Tran, T. Taniguchi, K. Watanabe, L. M. Campos, D. A. Muller, J. Guo, P. Kim, J. Hone, K. L. Shepard and C. R. Dean. *One-Dimensional Electrical Contact to a Two-Dimensional Material*. *Science*, 342(6158):614–617, 2013.
- [296] M. Nesladek, A. Bogdan, W. Deferme, N. Tranchant and P. Bergonzo. *Charge transport in high mobility single crystal diamond*. *Diamond and Related Materials*, 17(7-10):1235–1240, 2008. ISSN 09259635. doi:10.1016/j.diamond.2008.03.015.

- [297] E. C. H. Kyle, S. W. Kaun, P. G. Burke, F. Wu, Y.-R. Wu and J. S. Speck. *High-electron-mobility GaN grown on free-standing GaN templates by ammonia-based molecular beam epitaxy*. Journal of Applied Physics, 115(19):193702, 2014. ISSN 0021-8979. doi: 10.1063/1.4874735. Publisher: American Institute of Physics.
- [298] S. Bae, H. Kim, Y. Lee, X. Xu, J.-S. Park, Y. Zheng, J. Balakrishnan, T. Lei, H. Ri Kim, I. Y. Song, Y.-J. Kim, K. S. Kim, B. ?zyilmaz, J.-H. Ahn, B. H. Hong and S. Iijima. *Roll-to-roll production of 30-inch graphene films for transparent electrodes*. Nature Nanotechnology, 5(8):574–578, 2010. ISSN 1748-3387. doi:10.1038/nnano.2010.132.
- [299] X. Wu, G. Zhong, L. D’Arsié, H. Sugime, S. Esconjauregui, A. W. Robertson and J. Robertson. *Growth of Continuous Monolayer Graphene with Millimeter-sized Domains Using Industrially Safe Conditions*. Scientific reports, 6:21152, 2016. ISSN 2045-2322. doi: 10.1038/srep21152. Publisher: Nature Publishing Group.
- [300] T. Kobayashi, M. Bando, N. Kimura, K. Shimizu, K. Kadono, N. Umez, K. Miyahara, S. Hayazaki, S. Nagai, Y. Mizuguchi, Y. Murakami and D. Hobara. *Production of a 100-m-long high-quality graphene transparent conductive film by roll-to-roll chemical vapor deposition and transfer process*. Applied Physics Letters, 102(2):023112, 2013. ISSN 0003-6951. doi:10.1063/1.4776707. Publisher: American Institute of Physics.
- [301] P. Blake, E. W. Hill, A. H. Castro Neto, K. S. Novoselov, D. Jiang, R. Yang, T. J. Booth and A. K. Geim. *Making graphene visible*. Applied Physics Letters, 91(6):063124, August 2007. ISSN 0003-6951. doi:10.1063/1.2768624. URL <https://aip.scitation.org/doi/10.1063/1.2768624>, publisher: American Institute of Physics.
- [302] *Introduction, Basic Theory and Principles*. In *Modern Raman Spectroscopy – A Practical Approach*, pages 1–21. John Wiley & Sons, Ltd, 2005. ISBN 978-0-470-01183-6. doi:10.1002/0470011831.ch1. URL <https://onlinelibrary.wiley.com/doi/abs/10.1002/0470011831.ch1>, section: 1 _eprint: <https://onlinelibrary.wiley.com/doi/pdf/10.1002/0470011831.ch1>.
- [303] *The Theory of Raman Spectroscopy*. In *Modern Raman Spectroscopy – A Practical Approach*, pages 71–92. John Wiley & Sons, Ltd, 2005. ISBN 978-0-470-01183-6. doi:10.1002/0470011831.ch3. URL <https://onlinelibrary.wiley.com/doi/abs/10.1002/0470011831.ch3>, section: 3 _eprint: <https://onlinelibrary.wiley.com/doi/pdf/10.1002/0470011831.ch3>.
- [304] P.-H. Tan, editor. *Raman Spectroscopy of Two-Dimensional Materials*. Springer Series in Materials Science. Springer Singapore, 2019. ISBN 9789811318276. doi:10.1007/978-981-13-1828-3. URL <https://www.springer.com/gp/book/9789811318276>.
- [305] *The Raman Experiment – Raman Instrumentation, Sample Presentation, Data Handling and Practical Aspects of Interpretation*. In *Modern Raman Spectroscopy – A Practical Approach*, pages 23–70. John Wiley & Sons, Ltd, 2005. ISBN 978-0-470-01183-6. doi:10.1002/0470011831.ch2. URL <https://onlinelibrary.wiley.com/doi/abs/10.1002/0470011831.ch2>, section: 2 _eprint: <https://onlinelibrary.wiley.com/doi/pdf/10.1002/0470011831.ch2>.
- [306] H. Zhang, J. Huang, Y. Wang, R. Liu, X. Huai, J. Jiang and C. Anuso. *Atomic force microscopy for two-dimensional materials: A tutorial review*. Optics Communications, 406:3–17, January 2018. ISSN 0030-4018. doi:10.1016/j.optcom.2017.05.015. URL <http://www.sciencedirect.com/science/article/pii/S0030401817303887>.